

University of Kentucky

UKnowledge

Theses and Dissertations--Chemistry

Chemistry


2020

STRUCTURE, SURFACE, AND INTERFACIAL MODIFICATIONS OF CARBON AND SUPPORTED-METAL ELECTRODES FOR ELECTROCHEMICAL CARBON DIOXIDE CONVERSION

Namal Wanninayake

University of Kentucky, namal.wanninayakejob@gmail.com

Author ORCID Identifier:

 <https://orcid.org/0000-0002-8875-8726>

Digital Object Identifier: <https://doi.org/10.13023/etd.2020.484>

[Right click to open a feedback form in a new tab to let us know how this document benefits you.](#)

Recommended Citation

Wanninayake, Namal, "STRUCTURE, SURFACE, AND INTERFACIAL MODIFICATIONS OF CARBON AND SUPPORTED-METAL ELECTRODES FOR ELECTROCHEMICAL CARBON DIOXIDE CONVERSION" (2020). *Theses and Dissertations--Chemistry*. 136.
https://uknowledge.uky.edu/chemistry_etds/136

This Doctoral Dissertation is brought to you for free and open access by the Chemistry at UKnowledge. It has been accepted for inclusion in Theses and Dissertations--Chemistry by an authorized administrator of UKnowledge. For more information, please contact UKnowledge@lsv.uky.edu.

STUDENT AGREEMENT:

I represent that my thesis or dissertation and abstract are my original work. Proper attribution has been given to all outside sources. I understand that I am solely responsible for obtaining any needed copyright permissions. I have obtained needed written permission statement(s) from the owner(s) of each third-party copyrighted matter to be included in my work, allowing electronic distribution (if such use is not permitted by the fair use doctrine) which will be submitted to UKnowledge as Additional File.

I hereby grant to The University of Kentucky and its agents the irrevocable, non-exclusive, and royalty-free license to archive and make accessible my work in whole or in part in all forms of media, now or hereafter known. I agree that the document mentioned above may be made available immediately for worldwide access unless an embargo applies.

I retain all other ownership rights to the copyright of my work. I also retain the right to use in future works (such as articles or books) all or part of my work. I understand that I am free to register the copyright to my work.

REVIEW, APPROVAL AND ACCEPTANCE

The document mentioned above has been reviewed and accepted by the student's advisor, on behalf of the advisory committee, and by the Director of Graduate Studies (DGS), on behalf of the program; we verify that this is the final, approved version of the student's thesis including all changes required by the advisory committee. The undersigned agree to abide by the statements above.

Namal Wanninayake, Student

Dr. Doo Young Kim, Major Professor

Dr. Yinan Wei, Director of Graduate Studies

STRUCTURE, SURFACE, AND INTERFACIAL MODIFICATIONS OF CARBON
AND SUPPORTED-METAL ELECTRODES FOR ELECTROCHEMICAL CARBON
DIOXIDE CONVERSION

DISSERTATION

A dissertation submitted in partial fulfillment of the
requirements for the degree of Doctor of Philosophy in the
College of Arts and Sciences
at the University of Kentucky

By
Namal Wanninayake
Lexington, Kentucky
Director: Dr. Doo Young Kim, Professor of Chemistry
Lexington, Kentucky
2020

Copyright © Namal Wanninayake 2020
<https://orcid.org/0000-0002-8875-8726>

ABSTRACT OF DISSERTATION

STRUCTURE, SURFACE, AND INTERFACIAL MODIFICATIONS OF CARBON AND SUPPORTED-METAL ELECTRODES FOR ELECTROCHEMICAL CARBON DIOXIDE CONVERSION

Currently, the global emission of greenhouse CO₂ is over 36 billion tons per year. Consequently, the atmosphere's CO₂ concentrations have exceeded 400 ppm, which is the highest reported in the last three million years. The accumulation of CO₂ is the most critical origin for today's climate change; thus, closing the carbon cycle is vital to reverse the detrimental impacts of climate change. Under this goal, the electrochemical reduction of CO₂ into commodity fuels and chemicals via renewable energy is one of the most promising strategies to recycle CO₂. Despite significant progress made in electrocatalysis, currently there are no commercial-grade catalysts or reactor systems that meet projected benchmarks for CO₂ electroreduction. Therefore, more efficient catalysts and electrochemical reactors should be developed by understanding catalytic processes, local microenvironments, and underlying interfacial phenomena and chemistry.

This thesis will address the effects of structure, surface, and interfacial modifications of nanomaterials that endow selective, efficient, and stable electrocatalysts for CO₂ conversion. Since the catalyst performance and the electrode architecture are two critical factors in determining the overall efficiency of a system, this thesis will first showcase the impact of heteroatom-doped carbon catalysts toward electrochemical CO₂ conversion to CO, with the examples of nitrogen-doped ultrananocrystalline diamond and nitrogen and sulfur co-doped carbon nano onions (CNOs). The atomic-scale visualization of heteroatom dopants in CNOs will also be highlighted. Experimental studies in parallel with theoretical calculations will be presented to gain an in-depth insight into reaction mechanisms. In the latter part of this thesis, the improvement of electrode microstructures and interfaces will be presented. These changes have significantly enhanced the selectivity and activity toward CO₂ electroreduction to ethanol. Thus, this thesis will demonstrate how nitrogen-doped CNOs (N-CNOs) can alter the local electronic properties of copper catalysts and improve the composite catalyst's interfacial properties to boost ethanol selectivity. Furthermore, the construction of scalable and durable electrode architecture using N-CNOs and copper will also be presented. Ultimately, this thesis uncovers the underlying importance of tailoring the microstructures, surface chemistries, and electrode interfaces of heteroatom-doped carbon to improve efficiency and selectivity for CO₂ electroreduction. These results provide valuable insights into the development of more efficient catalysts in the future.

KEYWORDS: Electrochemical CO₂ Reduction, Ultrananocrystalline Diamond, Carbon Nano Onions, Heteroatom Doping, Copper, Gas Diffusion Electrodes

Namal Wanninayake

(Name of Student)

11/10/2020

Date

STRUCTURE, SURFACE, AND INTERFACIAL MODIFICATIONS OF
CARBON AND SUPPORTED-METAL ELECTRODES FOR
ELECTROCHEMICAL CARBON DIOXIDE CONVERSION

By
Namal Wanninayake

Dr. Doo Young Kim

Director of Dissertation

Dr. Yinan Wei

Director of Graduate Studies

11/10/2020

Date

DEDICATION

To my wife, daughter, parents, brother, and sister.

ACKNOWLEDGMENTS

This dissertation includes the research work I conducted under the guidance of Prof. Doo Young Kim at the Chemistry Department of the University of Kentucky. This work is supported by University of Kentucky Start-up Fund, Kentucky Science & Engineering Foundation, NSF KY EPSCoR - Membrane Pillar, and NASA KY EPSCoR awards. I would like to thank my advisor Prof. Doo Young Kim, for molding me to who I am today. I am grateful for his kindness and patience towards me. He is very understanding and always enthusiastic about our research. His knowledge of electrochemistry piqued my interest in electrochemistry and electrochemical engineering. His curiosity always helped me to think about my research critically. Also, I would like to appreciate my committee members Prof. Dong-Sheng Yang, Prof. Dibakar Bhattacharyya, and Prof. John Anthony, for their support and guidance throughout these years.

I would also like to thank my wonderful collaborators over these years. Our computational “go-to” group, Prof. Chad Risko, and Qianxiang Ai, always helped me when I need theoretical insights. Prof. Marcelo Guzman, Ariful Hoque, and Ruixin Zhou for their continuous support on gas chromatography analysis. Prof. Beth Guiton and Melonie Thomas for their assistance on electron microscopy. Wasif Zaheer and Prof. Sarbajit Banerjee from the Texas A&M University for their assistance on XAS measurements. Furthermore, I learned a lot regarding titanium dioxide materials by working with Prof. Stephen Rankin and Syed Islam. I am also fortunate to work with Prof. Dibakar Bhattacharyya and Andrew Colburn and expand my knowledge regarding membranes.

I am also grateful for Dr. Justin Mobley, Prof. Anne-Frances Miller, Taylor Varner, and Raphael Ryan for their assistance on NMR analysis. I would like to thank Prof. Yang-Tse Cheng, Dr. Dali Qian, Dr. Nicolas Briot, and Jillian Cramer for their assistance and support on XPS and electron microscopy analysis. Furthermore, I sincerely appreciate the generosity of Prof. Kenneth Graham for letting me use their airbrush and assistance from his student, Alex Boehm on UPS measurements. I am also grateful for Amrit Kaphle for the training and assistance on sputtering experiments. In particular, I am appreciative of the help given by Piya Amara Palamure, when I struggle to figure out MATLAB codes.

I specifically want to thank Steven Maynard for helping me to build flow cell reactors. Furthermore, Arthur Sebesta for fixing anything electronic. I cannot imagine how much money you saved for us by your wisdom. Many thanks will also go to Jeff Babbitt, who runs the glass shop at the chemistry department. You are a true master of your craft.

I also want to thank my wonderful lab mates: past members - Yiyang Liu, Yan Zhang, Sin Hea Yeom, Allen Reed, Josiah Roberts, Tim little pillar, and Rosemary Calabro as well as present members – Udari Kodithuwakku, Nadeesha Kothalawala, Michael Moore and Collan Henderson. I always enjoyed the talks and discussions we had attending conferences and in the group meeting. Furthermore, I genuinely appreciate their support and encouragement every step of the way we work together in the lab.

I would also like to acknowledge my wife, Thilini Abeywasnsha, for being my strength during every hurdle we came upon. Also, to my sweet little daughter, Leona, for keeping me sane over the past three years. I cannot imagine getting through grad school without your love and encouragement. Aside from all these wonderful people, I deeply

appreciate the encouragement from my parents, my siblings, and my friends although you are ten thousand miles away from us. I love you all very much and thank you from the bottom of my heart for all that you do.

TABLE OF CONTENTS

ACKNOWLEDGMENTS	iii
TABLE OF CONTENTS.....	vi
LIST OF TABLES.....	xii
LIST OF FIGURES	xiii
CHAPTER 1. INTRODUCTION AND LITERATURE REVIEW	1
1.1 Climate change and world's energy needs.....	1
1.2 Current challenges in renewable energy storage and chemical energy storage.....	5
1.2.1 Chemical energy storage.....	8
1.3 CO ₂ utilization and CO ₂ reduction electrocatalysis.....	9
1.3.1 CO ₂ utilization methods for sustainable development.....	9
1.3.2 Physicochemical properties of CO ₂	10
1.3.3 Electrocatalysis.....	14
1.3.3.1 Electrochemical reaction.....	15
1.3.3.2 Thermodynamic and kinetic aspects of electrode reactions	17
1.3.3.3 The heat of adsorption and Volcano plots	19
1.3.3.4 Effects of mass transport.....	20
1.3.4 Introduction to electrochemical CO ₂ reduction.....	23
1.4 Review of CO ₂ electroreduction.....	27
1.4.1 Metal-free catalysts for CO ₂ electroreduction.....	29
1.4.2 Metal-based catalysts for CO ₂ electroreduction.....	33
1.5 System design for CO ₂ electroreduction.....	36

1.6 Objectives of this dissertation.....	38
CHAPTER 2. UNDERSTANDING THE EFFECT OF HOST STRUCTURE OF	
NITROGEN DOPED ULTRANANOCRYSTALLINE DIAMOND ELECTRODE ON	
ELECTROCHEMICAL CARBON DIOXIDE REDUCTION	40
2.1 Introduction.....	40
2.2 Experimental.....	44
2.2.1 Microwave Assisted Chemical Vapor Deposition (MACVD) of Carbon Thin Films	44
2.2.2 Electrode Preparation.....	45
2.2.3 Material Characterization.....	45
2.2.4 Electrochemical Cell Configuration	46
2.2.5 Electrolysis.....	47
2.2.6 Product Analysis	48
2.3 Results and discussion	49
2.3.1 Control of Carbon Phase and Microstructure in Carbon Thin Films by MACVD.....	49
2.3.2 Characterization of Nitrogen-doped Carbon Films.....	50
2.3.3 Electrochemical Reduction of CO ₂	57
2.3.4 CO ₂ Catalysis Models.....	63
2.4 Summary	67
2.5 Supplementary information	68
2.5.1 Indexing Selected Area Electron Diffraction (SAED) patterns.....	69

2.5.2	Calculation of Electrochemical Surface Area (ECSA).....	72
2.5.3	Calculation of Faradaic Efficiency (FE) for gaseous and liquid products....	75
2.5.4	Computational Methods.....	78
CHAPTER 3. NITROGEN AND SULFUR DOPED CARBON NANO ONIONS FOR EFFICIENT ELECTROREDUCTION OF CO ₂		84
3.1	Introduction.....	84
3.2	Experimental.....	88
3.2.1	Synthesis, oxidation, and doping of CNOs.....	88
3.2.1.1	Synthesis of CNOs.....	88
3.2.1.2	Oxidation of CNOs	88
3.2.1.3	Synthesis of N-CNOs.....	89
3.2.1.4	Synthesis of S-CNOs	89
3.2.1.5	Synthesis of NS-CNOs	90
3.2.2	Electrode preparation.....	90
3.2.2.1	Preparation of electrodes for H-cell experiments	90
3.2.2.2	Preparation of a rotating ring disk electrode (RRDE)	91
3.2.2.3	Preparation of electrodes in an electrochemical cell with a flow cell configuration.....	91
3.2.3	Material characterization	91
3.2.3.1	Micro-Raman spectroscopy	91
3.2.3.2	X-ray Diffraction (XRD) analysis	91
3.2.3.3	Brunauer–Emmett–Teller (BET) measurement.....	91
3.2.3.4	Fourier-transform infrared spectroscopy (FT-IR).....	92

3.2.3.5	Scanning transmission electron microscopy (STEM).....	92
3.2.3.5.1	Stem sample preparation and characterization	92
3.2.3.5.2	Fourier filtering.....	92
3.2.3.6	X-ray absorption spectroscopy (XAS).....	92
3.2.3.7	X-ray photoelectron spectroscopy (XPS)	93
3.2.4	Electrochemical cell configuration	93
3.2.4.1	Electrochemical tests with an H-cell configuration	93
3.2.4.2	Configuration of the gas diffusion flow cell electrochemical setup	94
3.2.5	Electrolysis.....	94
3.2.6	Product analysis	95
3.2.6.1	Gas chromatography analysis	95
3.2.6.2	NMR analysis for liquid products.....	95
3.2.7	Computational methods	96
3.2.8	Evaluation of local CO ₂ species concentration.....	96
3.3	Results and discussion	97
3.3.1	Synthesis	97
3.3.2	Material Characterization.....	98
3.3.3	Electrochemical Characterization	104
3.3.4	Theoretical evaluation of the activity of NS-CNO catalyst	112
3.3.5	Performance Comparison.....	114
3.4	Summary	119
3.5	Supplementary information	120
3.5.1	NMR quantification of formic acid.....	120

3.5.2	Calculation of faradaic efficiencies (FE's) for liquid and gaseous products	120
3.5.3	Raman spectroscopic analysis.....	122
3.5.4	XRD analysis	126
3.5.5	BET isotherms and pore size distribution.....	126
3.5.6	A summary of XPS results.....	127
3.5.7	NEXAFS spectroscopy analysis	128
3.5.8	FT-IR analysis.....	130
3.5.9	Faradaic efficiencies of N-CNO and NS-CNO prepared at 600 °C and 800 °C.....	131
3.5.10	Schematics of the H-cell electrochemical setup and the flow electrochemical setup.....	132
3.5.11	Computational methods	133
3.5.11.1	Defect/configuration Generation	133
3.5.12	Characterization of a catalyst after electrolysis	135
3.5.13	Comparison of NS-CNO(700) performance with metal-based catalysts	138
CHAPTER 4. CO ₂ ELECTROREDUCTION TO MUTICARBON PRODUCTS BY SUPPORTED COPPER ON NITROGEN-DOPED CARBON NANO ONIONS		141
4.1	Introduction.....	141
4.2	Experimental.....	143
4.2.1	Synthesis of nitrogen doped CNOs and supported copper on N-CNOs.	143
4.2.2	Preparation of gas diffusion electrodes.....	144
4.2.3	Material characterizations.....	145

4.2.4	Simulation of local electrode conditions.....	145
4.2.5	Electrochemical test.....	146
4.2.5.1	A flow-type cell configuration.....	146
4.2.5.2	Electrochemical test and electrolysis.....	146
4.3	Results and discussion	147
4.4	Summary.....	163
4.5	Supplementary information	164
4.5.1	Calculation of crystalline domain size.....	165
CHAPTER 5. CONCLUSIONS AND FUTURE DIRECTIONS		167
APPENDIX: MODELING LOCAL ELECTRODE CONDITIONS WITH MATLAB		
USING REACTION DIFFUSION MODEL.....		171
REFERENCES		186
VITA.....		208

LIST OF TABLES

Table 1. 1 Physical and chemical properties of CO ₂ (Adapted from Song, C., Global challenges and strategies for control, conversion and utilization of CO ₂ for sustainable development involving energy, catalysis, adsorption and chemical processing. Catalysis Today 2006, 115 (1), 2-32. Copyright (2006), with permission from Elsevier) ²¹	11
Table 1. 2 Standard Gibbs free energy and standard potential for half-cell electrochemical reduction of CO ₂	18
Table 2. 1 Experimental parameters used for the MACVD of 8 carbon thin films	45
Table 2. 2 The summary of elemental composition and chemical states in each electrode	57
Table S2. 1 Periodic boundary conditions for the computational models.	79
Table 3. 1 Statistical analysis of dopant distribution on S-CNO(700), N-CNO(700) and NS-CNO(700). ⁷⁷	102
Table 3. 2 Performance comparison of NS-CNO(700) electrode with other CO generating metal-free catalysts(The table summarizes experimental conditions and the details of the performance for each catalyst).....	118
Table S3. 1 Parameters determined from Raman spectroscopic analysis.....	122
Table S3. 2 A summary of XPS results	127
Table S3. 3 Performance comparison of NS-CNO(700) electrode with other CO generating catalysts (The table summarizes experimental conditions and the details of the performance for each catalyst).....	138
Table 4. 1 Elemental composition of CNO-based catalyst/composite.	155
Table 4. 2 Comparison of ethanol FE for catalysts with current density higher than 10 mA cm ⁻²	162

LIST OF FIGURES

Figure 1. 1 (a) Global greenhouse gas emissions based on global emissions from 2010 ¹ and (b) global atmospheric CO ₂ concentrations. ²	2
Figure 1. 2 Annual total CO ₂ emissions, based on the world region. ³	3
Figure 1. 3 The year 2018 US CO ₂ emissions, by source. ⁷	4
Figure 1. 4 US primary energy consumption according to the energy source. Source: U.S. Energy Information Administration (April 2020). ¹⁰	5
Figure 1. 5 Renewable energy curtailment in the state of California in 2016. SOURCE: California ISO (Teodros Hailye/KQED). ¹⁵	6
Figure 1. 6 Energy storage methods and their discharge times and capacities (Reprinted from Dincer, I.; Ezan, M. A., Energy Storage Methods. In Heat Storage: A Unique Solution For Energy Systems, Springer International Publishing: Cham, 2018; pp 35-56. Copyright (2018), with permission from Springer). ¹⁷	7
Figure 1. 7 Energy density comparison between chemical fuel vs. batteries.	8
Figure 1. 8 Various pathways for CO ₂ utilization and removal. (Adapted from Hepburn, C.; Adlen, E.; Beddington, J.; Carter, E. A.; Fuss, S.; Mac Dowell, N.; Minx, J. C.; Smith, P.; Williams, C. K., The technological and economic prospects for CO ₂ utilization and removal. Nature 2019, 575 (7781), 87-97. Copyright (2019), with permission from Nature). ¹⁹	10
Figure 1. 9 (a) Molecular orbital diagram of CO ₂ (Expanded from Miessler et al. and Francke et al.), ^{24, 25} (b) Change in total energy as a function of OCO angle, (c) change in C-O distance as a function OCO angle, (d) Walsh diagram for CO ₂ bending and (e) molecular orbitals of CO ₂ at various OCO angles. (Reprinted from Mondal, B.; Song, J.; Neese, F.; Ye, S., Bio-inspired mechanistic insights into CO ₂ reduction. Current Opinion in Chemical Biology 2015, 25, 103-109. Copyright (2015), with permission from Elsevier). ²³	14
Figure 1. 10 Potential energy diagram corresponds to the catalyst effect on the hypothetical exothermic reaction X+Y→Z.	15
Figure 1. 11 A schematic diagram of the electrolysis cell.....	16
Figure 1. 12 The general electrochemical pathway.	16
Figure 1. 13 Schematic representation of the Sabatier principle. (Reprinted from Medford, A. J.; Vojvodic, A.; Hummelshøj, J. S.; Voss, J.; Abild-Pedersen, F.; Studt, F.; Bligaard, T.; Nilsson, A.; Nørskov, J. K., From the Sabatier principle to a predictive theory of transition-metal heterogeneous catalysis. Journal of Catalysis 2015, 328, 36-42. Copyright (2015), with permission from Elsevier). ³²	20
Figure 1. 14 Modes of mass transport. (Reprinted from Perez, N., Mass Transport by Diffusion and Migration. In Electrochemistry and Corrosion Science, Perez, N., Ed. Springer International Publishing: Cham, 2016; pp 151-197. Copyright (2016), with permission from Springer). ³³	21
Figure 1. 15 Nernst diffusion layer model. ²⁹	23
Figure 1. 16 CO ₂ utilization via electrochemical CO ₂ conversion.	23

Figure 1. 17 Economics and energetics of CO₂ electroreduction products(Lines represent minimum cost of production of CO₂ utilizing electricity, the circle size indicates the logarithmic representation of the current market size of each product, and both axes are normalized to the mass of the carbon). Adapted with permission from (Nitopi, S.; Bertheussen, E.; Scott, S. B.; Liu, X.; Engstfeld, A. K.; Horch, S.; Seger, B.; Stephens, I. E. L.; Chan, K.; Hahn, C.; Nørskov, J. K.; Jaramillo, T. F.; Chorkendorff, I., Progress and Perspectives of Electrochemical CO₂ Reduction on Copper in Aqueous Electrolyte. Chemical Reviews 2019, 119 (12), 7610-7672. Copyright (2019) American Chemical Society).⁶..... 24

Figure 1. 18 Possible mechanistic pathways of CO₂ electroreduction. Adapted with permission from (Nitopi, S.; Bertheussen, E.; Scott, S. B.; Liu, X.; Engstfeld, A. K.; Horch, S.; Seger, B.; Stephens, I. E. L.; Chan, K.; Hahn, C.; Nørskov, J. K.; Jaramillo, T. F.; Chorkendorff, I., Progress and Perspectives of Electrochemical CO₂ Reduction on Copper in Aqueous Electrolyte. Chemical Reviews 2019, 119 (12), 7610-7672. Copyright (2019) American Chemical Society).⁶..... 28

Figure 1. 19 Allotropes of carbon. Adapted from (Tripathi, A.C.; Saraf, S.A.; Saraf, S.K. Carbon Nanotropes: A Contemporary Paradigm in Drug Delivery. Materials 2015, 8, 3068-3100).⁴²..... 30

Figure 1. 20 Common bonding configurations of N doped carbon. Adapted with permission from (Wei, D.; Liu, Y.; Wang, Y.; Zhang, H.; Huang, L.; Yu, G., Synthesis of N-Doped Graphene by Chemical Vapor Deposition and Its Electrical Properties. Nano Letters 2009, 9 (5), 1752-1758). Copyright (2009) American Chemical Society)⁴⁹..... 32

Figure 1. 21 (a) Main effects of the carbon support and (b) d- π interactions leading to charge transfer between metal and the support(Reprinted from Navalon, S.; Dhakshinamoorthy, A.; Alvaro, M.; Garcia, H., Metal nanoparticles supported on two-dimensional graphenes as heterogeneous catalysts. Coordination Chemistry Reviews 2016, 312, 99-148. Copyright (2016), with permission from Elsevier).⁷²..... 36

Figure 1. 22 (a) Schematics of traditional H-cell and (b) gas diffusion electrolyzer (WE, RE and CE correspond to the working electrode, reference electrode and counter electrode, respectively-Figures adapted from Hernandez-Aldave et al.).⁷⁴..... 37

Figure 2. 1 Representative SEM images of (a) NDC-1, (b) NDC-2, (c) NDC-3, (d) NDC-4, and high resolution TEM images of (e) NDC-1, (f) NDC-2, (g) NDC-3, (h) NDC-4 films. Insets in the bottom-left corner of each TEM image represents SAED patterns. Diamond related indexes are denoted with a (D), and Graphite related indexes are denoted with a (G)...... 51

Figure 2. 2 XPS analyses of samples: (a) high-resolution C1s spectra and (b) high-resolution N1s spectra..... 56

Figure 2. 3 Linear sweep voltammetric (LSV) curves recorded for (a) NDC-X and (b) UDC-X. The LSV curves were recorded after the 0.1 M KHCO₃ electrolyte solution was saturated with CO₂. 59

Figure 2. 4 Faradaic efficiency of each product as a function of potential (a) NDC-1, (b) NDC-2, (c) NDC-3, and (d) NDC-4. 62

Figure 2. 5 Surface structures investigated in this study. The carbon (C) subscript in the P structure labels denotes the atomic layer in which the carbon atom resides. The resulting G and P structures are labeled with Kröger–Vink notations. 65

Figure 2. 6 (a) Free energy diagrams for the formation of CO on various surface (possible reaction pathways are highlighted with dotted lines) and (b) Intermediates with lowest energy pathways among P and G structures. C, N, O and H atoms represent by gray, blue, red, and white colors, respectively. All intermediate structures can be found in Figures S2.13-S2.16.....	66
Figure S2. 1 A schematic of the electrochemical cell and experimental setup used in this work (Top left inset – Photograph of a flow cell reactor).....	68
Figure S2. 2 Representative SEM images of (a) UDC-1, (b) UDC-2, (c) UDC-3, (d) UDC-4, and TEM (e) UDC-1, (f) UDC-2, (g) UDC-3, (h) UDC-4 catalysts.....	68
Figure S2. 3 Representative SEM cross-sectional images of (a) NDC-1, (b) NDC-2, (c) NDC-3, (d) NDC-4, (e) UDC-1, (f) UDC-2, (g) UDC-3, and (h) UDC-4.....	69
Figure S2. 4 SAED pattern of NDC-4. (2R = diameter of the ring, a (G) = 1 st diffraction line from the graphite phase and, b (D) = 1 st diffraction line from the diamond phase) ..	69
Figure S2. 5 Raman spectra of (a) NDC-X and (b) UDC-X.....	71
Figure S2. 6 XPS survey spectra of (a) NDC-X and (b) UDC-X. (c) high-resolution XPS C1s spectra of UDC-X.....	72
Figure S2. 7 Measurements for determining electrochemically active surface area (a) Cyclic voltammograms of NDC-4 in the non-faradaic region at various scan rates (0.1 V window around the OCP), (b) Anodic and cathodic charging currents measured for NDC-4 at OCP vs. Ag/AgCl plotted as a function of scan rate(inset – NDC-4 electrode, geometric surface area 2.01 cm ²) and (c) the calculated electrochemical surface area (ECSA) of NDC-X and UDC-X.	74
Figure S2. 8 Chrono-amperometric currents recorded for (a) NDC-X and (b) UDC-X while the fixed potential at -1.10 V vs. RHE is held.	74
Figure S2. 9 Faradaic efficiency of each product as a function of potential for (a) UDC-1, (b) UDC-2, (c) UDC-3 and (d) UDC-4.....	77
Figure S2. 10 Possible pathways for the electrochemical production of CO from CO ₂ ...	77
Figure S2. 11 Basic structures for simulating surface structures. The graphite slab for NDC-4 (left) and the diamond (111) surface with Pandey’s reconstruction for NDC-1 (right).	79
Figure S2. 12 Free energy diagrams for HER on various model surfaces.....	81
Figure S2. 13 Optimized *COOH intermediate structures for (from left to right) G1, G2, G3, G4, G5 structures from Figure 2.6(a).....	82
Figure S2. 14 Optimized *CO intermediate structures for (from left to right) G1, G2, G3, G4, G5 structures from Figure 2.6(a).....	82
Figure S2. 15 Optimized *COOH intermediate structures for (from left to right) P1, P2, P3, P4 structures from Figure 2.6(a).....	83
Figure S2. 16 Optimized *CO intermediate structures for (from left to right) P1, P2, P3, P4 structures from Figure 2.6(a).	83
Figure 3. 1 (a) Thermal conversion of ND to CNO and (b) synthetic process of Ox-CNO, N-CNO, S-CNO and NS-CNO.	98
Figure 3. 2 (a) STEM HAADF micrographs of S-CNO [i], N-CNO [ii], and NS-CNO [iii] samples and their Fourier filtered images [iv, v, vi], (b) HAADF micrograph [i], Fourier filtered image [ii], and false colored filtered image [iii] (red = CNO, yellow = dopants) of NS-CNO(700) showing the configuration of dopants.	101
Figure 3. 3 High-resolution XPS characterization of (a) S-CNO(700)-(S2p), (b) N-CNO(700)-(N1s), (C) NS-CNO(700)-(S2p), (d) NS-CNO(700)-(N1s), (e) calculated	

percentages of N and S configurations and X-ray Absorption Spectroscopy (XAS) of (f) C K-edge, (g) N K-edge and (h) O K-edge of samples.	104
Figure 3. 4 Cyclic voltammograms of (a) pristine CNO, (b) S-CNO(700), (c) N-CNO(700), and (d) NS-CNO(700) in aqueous electrolyte saturated with CO ₂ gas at the scan rate of 50 mV s ⁻¹ . For the comparison, cyclic voltammogram of each catalyst was also recorded in saturated N ₂	105
Figure 3. 5 RRDE measurements of (a) CNO, (b) S-CNO(700), (c) N-CNO(700), and (d) NS-CNO(700) to determine the onset potential of CO formation in the presence of CO ₂ gas at a scan rate of 50 mV s ⁻¹ (1000 rpm). The potential at the Pt ring was scanned from 0.10 V to 1.20 V (vs. RHE), while a fixed potential was held at the disk.	108
Figure 3. 6 Faradaic efficiencies for gaseous and liquid products in (a) CNO, (b) S-CNO(700), (c) N-CNO(700), and (d) NS-CNO(700).	110
Figure 3. 7 Possible mechanistic pathways of CO ₂ reduction to CO and HCOOH. Legend at the top-right indicates the implication of the lines that connecting intermediates: Blue-Kortlever et al., ²²³ Orange-Feaster et al., ²²¹ Green-Chernyshova et al., ²²⁴ Black-Hori et al., ¹⁶⁰ Red-Peterson et al., ¹⁵⁴ Adapted from the mechanistic pathway by Chorkendorff et al.. ⁶	113
Figure 3. 8 (a) Colored bar chart of the 50 lowest MIG calculated based on different configurations. The bars are colored blue, red, yellow for N-doped, N, S-doped, S-doped structures, respectively. (b) A colored scatter plot of free energy changes in CO/COOH desorption processes for various configurations, where a color code is inherited from (a) except that the gray markers denote the configurations excluded from the bar chart. ...	114
Figure 3. 9 (a) Availability of CO ₂ in 0.1 M KHCO ₃ (H-cell configuration at -0.92 mA cm ⁻² current density, x=0 represents the surface of the planar electrode), (b) availability of CO ₂ in 1 M KHCO ₃ (GDE configuration at -12 mA cm ⁻² current density, x=0 refers to the base of the GDE where gas-liquid boundary exists), (c) durability test of NS-CNO(700) and (d) performance comparison of NS-CNO(700) electrode with other CO generating metal-free catalysts(numbers refer to the catalysts listed in Table 3.2, The magnitude of the current density at each data point is represented by various color intensities).	118
Figure S3. 1 (a) 1D ¹ H NMR spectrum of a sample containing the formic acid analyte. (b) a calibration plot of formic acid using phenol as an internal standard (a relative peak area = area of formic acid (peak at 8.33 ppm) / Area of phenol (peak at 7.24 ppm)). Phenol and DMSO are internal standards.	120
Figure S3. 2 Raman spectra of CNO, Ox-CNO, N-CNO(700), S-CNO(700) and NS-CNO(700).	122
Figure S3. 3 The plots of (a) I _D /I _G , (b) I _{2D} /I _G , (c) D-band position, (d) G-band position, (e) 2D band position, and (f) 2D band FWHM determined from Raman spectra.	123
Figure S3. 4 XRD of CNO, Ox-CNO, N-CNO(700), S-CNO(700) and NS-CNO(700).	126
Figure S3. 5 (a) BET isotherms and (b) the pore size distributions of all samples. A plot of BET surface-areas is shown in the inset.	126
Figure S3. 6 A summary of dopant configurations in all samples determined by XPS analyses.	127
Figure S3. 7 FT-IR spectra of samples of interest.	130
Figure S3. 8 Faradaic efficiencies of N-CNO and NS-CNO prepared at 600 °C and 800 °C.	131

Figure S3. 9 Schematics of a H-cell and a flow-type cell (with gas-diffusion electrodes) used in this study.....	132
Figure S3. 10 Base structure with 10 sites haloed for defect generation.....	134
Figure S3. 11 Images of the 8 most active configurations as predicted by the theoretical calculations (activity follows the order 1-high:8-low. Grey, Blue, Yellow and White color represents Carbon, Nitrogen, Sulfur, and Hydrogen. In each structure, the adsorption site is haloed in yellow).....	135
Figure S3. 12 Photographs of NS-CNO(700) before (a) and after 30-hour electrolysis (b)	135
Figure S3. 13 XPS characterizations of NS-CNO(700) before and after electrolysis: XPS survey spectra of before (a) and after electrolysis (b), high-resolution XPS N1s scan before (c) and after electrolysis (d), and high-resolution XPS S2p scan before (e) and after electrolysis (f).....	136
Figure S3. 14 The area plot (top) compares the performance of NS-CNO(700) with metallic catalysts for CO production in terms of FE, overpotential, and current density(The numbers refer to the catalysts listed in Table S3.3). Various color intensities represent the magnitude of the current density at each data point.	138
Figure 4. 1 Electrode-catalyst optimization and triple-phase boundary of the integrated system (Carbon, nitrogen, and Cu are denoted as black, blue, and red-orange colors)..	143
Figure 4. 2 (a) The local pH, (b) CO ₂ concentration in the absence of nafion, and (c) CO ₂ in the presence of nafion layer (thickness: 5 μm) calculated by a reaction-diffusion model. 0 μm represents the base of the porous electrode, and 500 μm corresponds to the liquid diffusion thickness. The colors indicate the pH or CO ₂ concentration.....	148
Figure 4. 3 Schematic of the electrode fabrication process.	149
Figure 4. 4 SEM images of (a) PTFE-Cu, (b) a top view of Cu_N-CNO-Cu(700), (c) a cross-sectional image of Cu_N-CNO-Cu(700)_Nf and (d) HAADF-STEM-EDS mapping of N-CNO-Cu(700) and (e)-(f) high resolution TEM images of N-CNO-Cu(700) where circled regions indicate Cu nanoparticles.	152
Figure 4. 5 XRD of (a) N-CNO(700), (b) N-CNO-Cu(700), (c) PTFE_Cu and (d) Cu (simulated by Mercury software). ³⁰¹	153
Figure 4. 6 XPS characterization of electrode substrate and catalyst composite.....	155
Figure 4. 7 Linear sweep voltammograms of each electrode under CO ₂	156
Figure 4. 8 Faradaic efficiencies of (a) Cu_Nf, (b) Cu_CNO_Nf, (c) Cu_N-CNO(700)_Nf and (d) Cu_N-CNO-Cu(700)_Nf.....	158
Figure 4. 9 (a) Ethylene vs. ethanol pathways, (b) confinement of reactants between N-CNO and sputtered Cu, and (c) electronic structure modulation of Cu by N-CNO.	160
Figure 4. 10 (a) Comparison of current density and FE _{Ethanol} of all electrodes at -0.9 V vs. RHE and (b) correlation between catalyst loading, catalyst thickness, and J _{Ethanol} at -0.9 V vs. RHE of Cu_N-CNO-Cu(700)_Nf electrode.....	161
Figure 4. 11 (a) Durability test of Cu_N-CNO-Cu(700)_Nf electrode at -0.9 V vs. RHE and (b) comparison of performance with other reported catalysts that grant current densities >10 mA cm ⁻²	162
Figure S4. 1 Digital photographs of (a) PTFE-Cu, (b) PTFE-Cu-Nafion, and PTFE-Cu-(Nafion+Catalyst) electrodes.	164
Figure S4. 2 TEM of (a) CNO, (b) N-CNO(700) and (c)-(d) N-CNO-Cu(700), three Cu particles are circled in the inset of (d).....	164

Figure S4. 3 High-resolution XPS of acid leached N-CNO-Cu(700).....	165
Figure S4. 4 ¹ H-NMR of Cu_N-CNO-Cu(700)_Nf catholyte after electrolysis at -0.9 V vs. RHE for 30 minutes. DMSO and phenol are internal standards.....	166

CHAPTER 1. INTRODUCTION AND LITERATURE REVIEW

1.1 Climate change and world's energy needs.

The climate of the earth is significantly affected by energy from the sun. The earth absorbs solar energy ($\sim 100 \text{ mW cm}^{-2}$ at sea level) and reflects part of it to space. During this process, certain gaseous molecules called greenhouse gases (GHGs) in the atmosphere can trap the radiated energy, heating the earth's surface. This greenhouse effect is a natural phenomenon. However, after the industrial revolution, anthropogenic GHGs were added into the atmosphere affecting a natural carbon cycle.¹ GHGs include carbon dioxide (CO_2), methane (CH_4), nitrous oxide (N_2O), and fluorinated gases. Figure 1.1 (a) and (b) show global GHG emissions in 2018 and the change of CO_2 concentration in the atmosphere for the past 300 years, respectively. Based on this chart, CO_2 is the major origin of climate change.

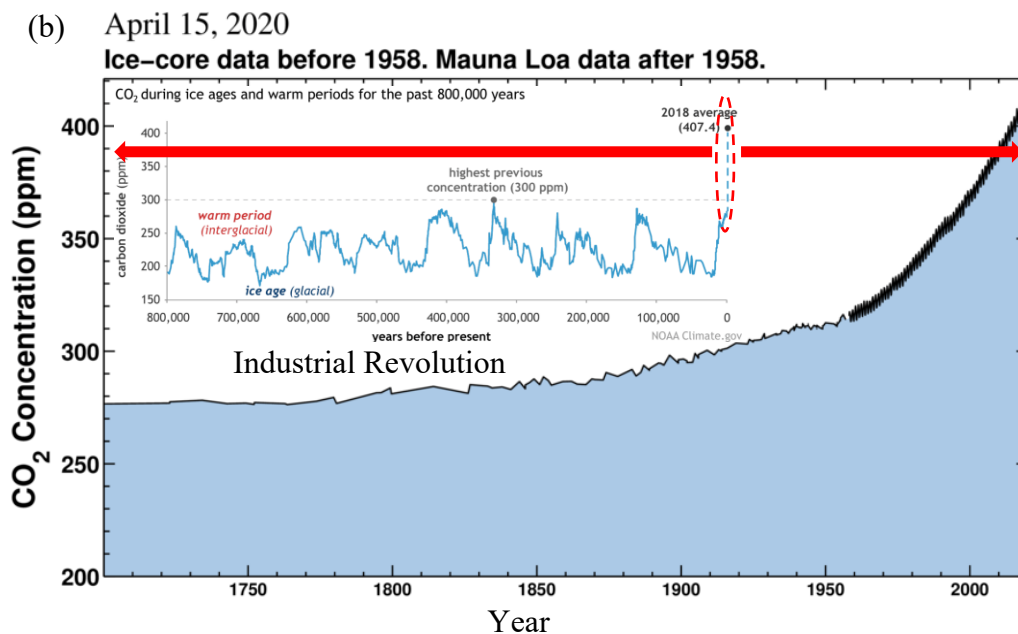
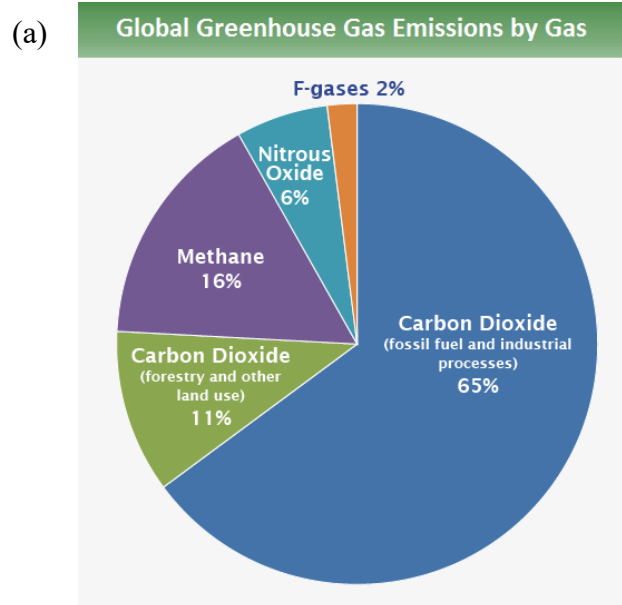


Figure 1. 1 (a) Global greenhouse gas emissions based on global emissions from 2010¹ and (b) global atmospheric CO₂ concentrations.²

As of today, more than 36 billion tons of CO₂ is being generated globally per year. Among all countries, the major emitters of CO₂ are China and the United States (US), which are responsible for 27 % and 15 % of the global emissions, respectively (Figure

1.2).³ Consequently, the CO₂ concentrations in the atmosphere have exceeded 400 ppmv, which is the highest value in the last three million years (Figure 1.1).³ It has been predicted that the concentration of CO₂ will reach 590 ppmv by the year 2100, raising the global temperature by 1.9 °C.^{4, 5} Therefore, reversing the trend of CO₂ emissions is extremely important to minimize detrimental impacts on the climate change.⁶

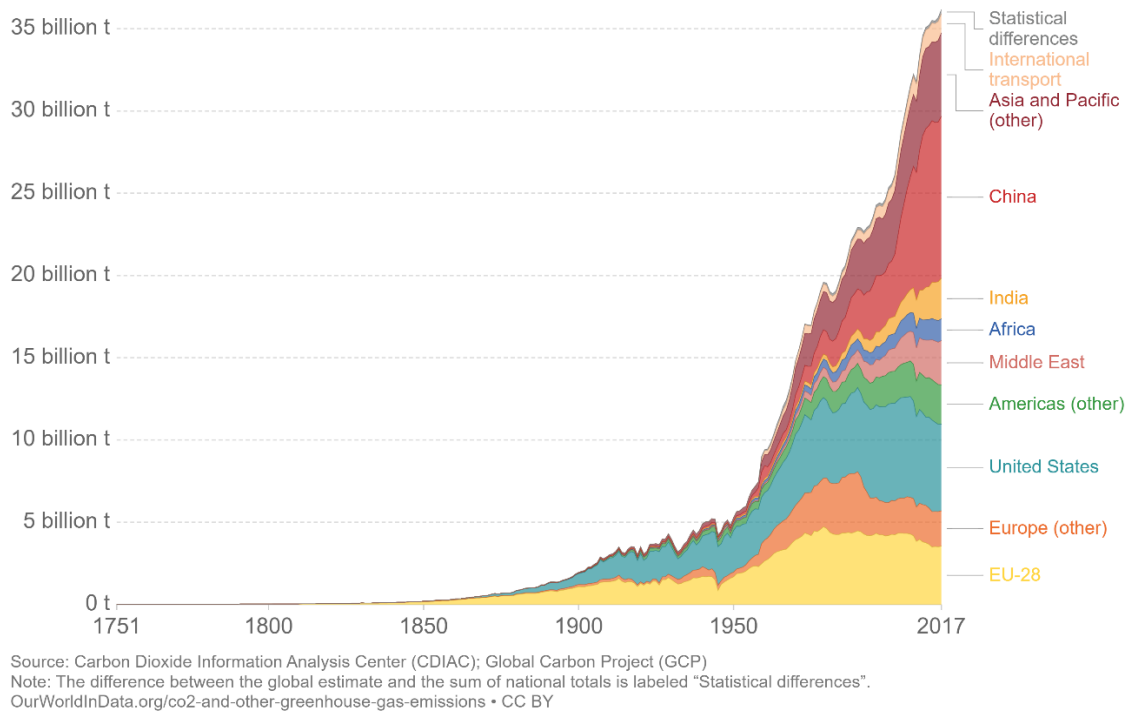


Figure 1. 2 Annual total CO₂ emissions, based on the world region.³

Out of the GHG emissions from US in 2018, anthropogenic CO₂ is almost 80 %.⁷ The primary source of CO₂ is the combustion of fossil fuel (coal, natural gas, and oil) for energy and transportation applications. Industrial processes also emit CO₂ with or without fossil fuel consumption. Figure 1.3 illustrates the year 2018 US CO₂ emissions based on the emitted source. Transportations account for about 34 % of the total CO₂ emissions through the combustion of gasoline and diesel. Electricity generation to power homes,

businesses, and industries is the second biggest source (32 %). Industries are the third (15 %). These industrial processes involve the combustion of fossil fuels or other chemical reactions that generate CO₂.⁷

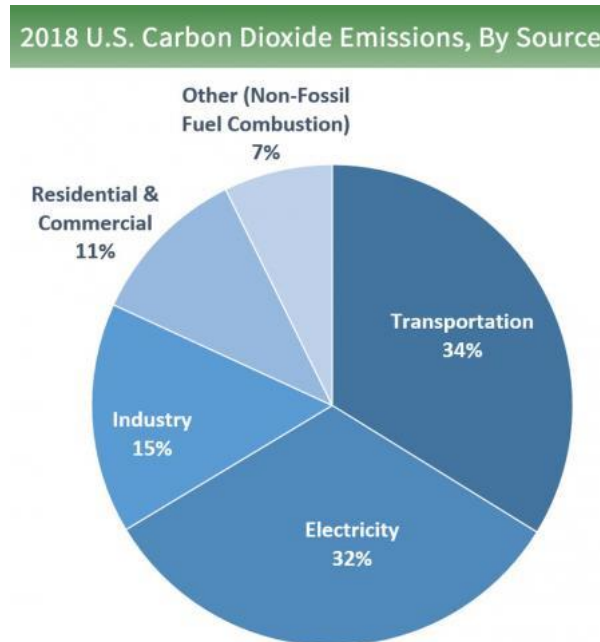


Figure 1. 3 The year 2018 US CO₂ emissions, by source.⁷

A takeaway from the above reports is that it is challenging to eliminate anthropogenic CO₂ emissions because most of the processes evolving CO₂ are essential for our day-to-day activities. Fossil fuels have been the holy grail of energy for the past 200 years, but their reserves may run out in 50 years if we keep burning them at the current rate. As stated in the Paris agreement on climate change, it is essential to leave 75-85 % of fossil fuel reserves untouched in order to keep the global temperature increase below 2 °C above the pre-industrial level.⁸

1.2 Current challenges in renewable energy storage and chemical energy storage.

Renewable energy is the "energy that is produced by natural resources—such as sunlight, wind, rain, waves, tides, and geothermal heat—that are naturally replenished within a time span of a few years."⁹ Figure 1.4 illustrates the US primary energy consumption by energy sources in 2019. The contribution of the renewables to US energy consumption is about 11%,¹⁰ while a renewable energy contribution in Europe is ~19% in 2018.¹¹ Although the portion of renewable energy in the US is lower than that of Europe, renewable energy is a rapidly expanding sector in the US, and it will continue to increase. In the near future, renewable energy will be one of the leading sources of energy.¹²

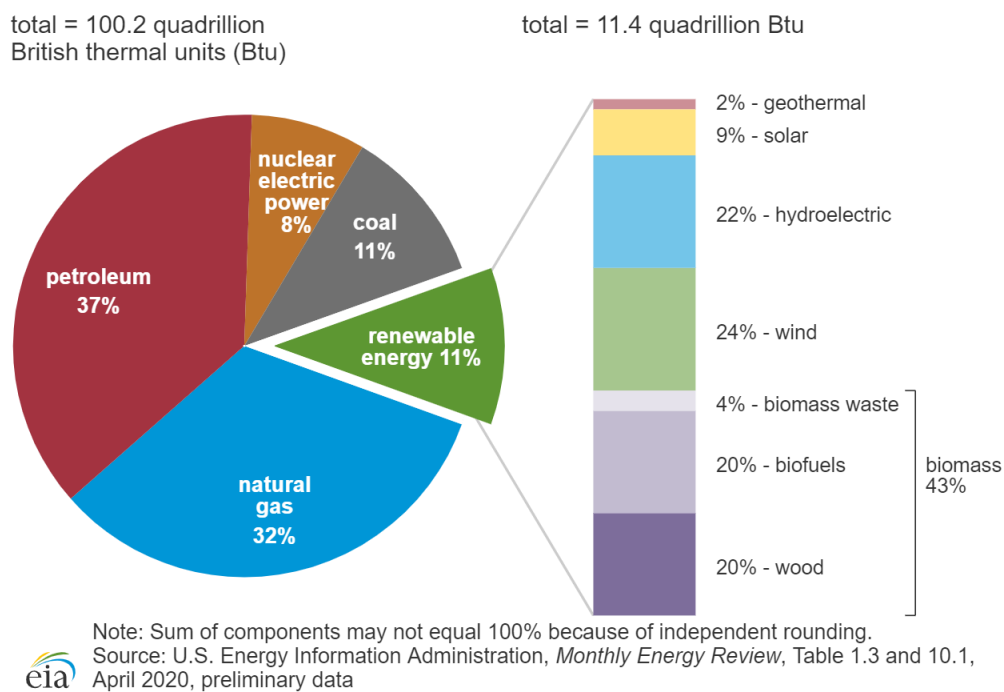


Figure 1. 4 US primary energy consumption according to the energy source. Source: U.S. Energy Information Administration (April 2020).¹⁰

However, the main limitation of renewable energy is intermittency, particularly wind and solar energy. Therefore, there is a great demand for technologies to overcome

renewable energy curtailment.¹³ Renewable energy curtailment occurs when more renewable energy is supplied than the amount of energy grid.¹⁴ Figure 1.5 illustrates an example of renewable energy curtailment in the state of California.¹⁵ When solar resources are added to the grid, there is excessive power generated during daylight hours and remain unutilized. On the contrary, after sunsets, more power is needed for peoples' needs, such as meal preparation and the use of electronic devices. Typically, about 13 000 MW of electricity is needed in a Spring day of California after 4 pm to replenish within 3 hours to meet the electrical deficit of solar power.¹⁶ Therefore, it is imperative to develop methods that can efficiently capture excess renewable energy so it can be supplied on demand.

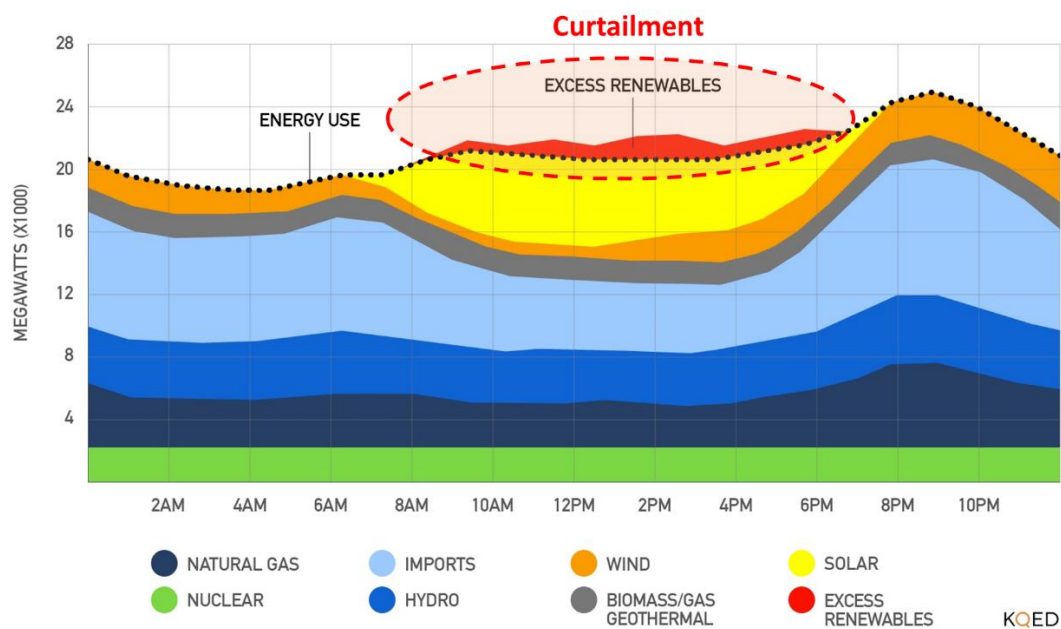


Figure 1. 5 Renewable energy curtailment in the state of California in 2016. SOURCE: California ISO (Teodros Hailye/KQED).¹⁵

Energy can be stored in various ways. Figure 1.6 summarizes common technologies for energy storage (ES), including chemical, electrical, electrochemical, mechanical, and thermal routes.¹⁷ Depending upon an ES method, the rate of discharging is varied from

seconds to hours, and its output power is scalable from kW to GW. While flywheels and supercapacitors are suitable for short-term electricity supply, hydroelectric power and chemical storages are more viable to back up a shortage of larger electricity. One significant drawback of hydroelectric power is its limited or unavailability in some regions of the US, hindering the distribution of electrical power. Therefore, chemical methods are versatile to serve for energy transmission and grid support.¹⁷

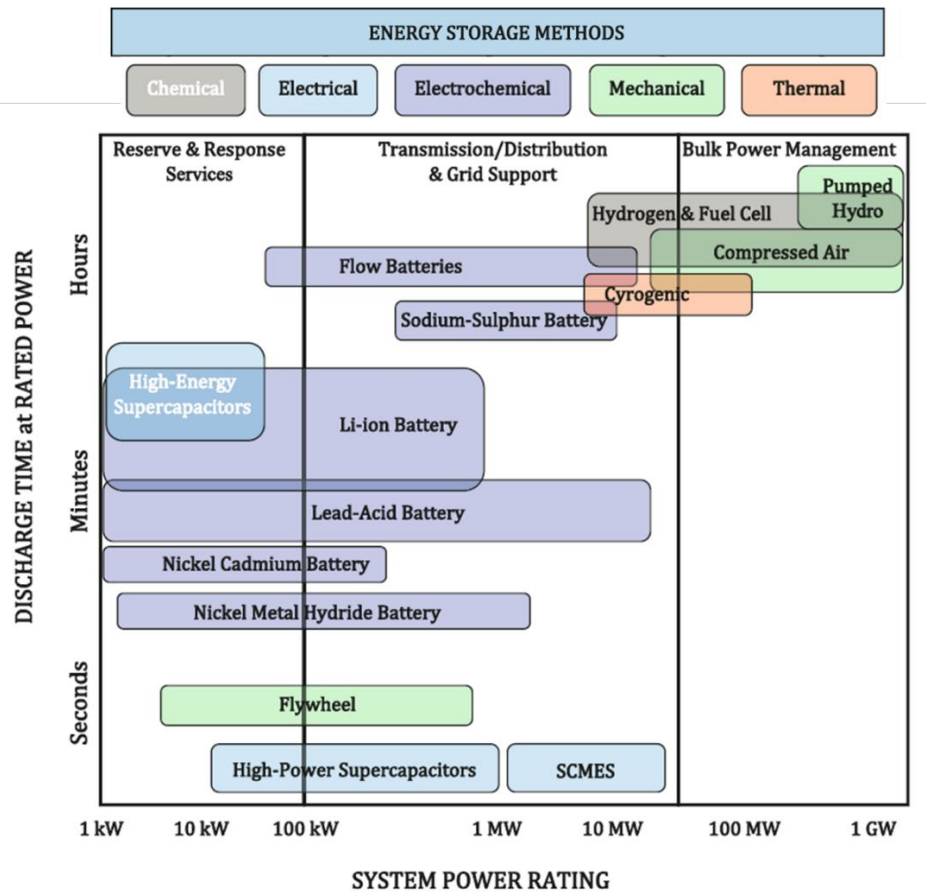


Figure 1. 6 Energy storage methods and their discharge times and capacities (Reprinted from Dincer, I.; Ezan, M. A., Energy Storage Methods. In Heat Storage: A Unique Solution For Energy Systems, Springer International Publishing: Cham, 2018; pp 35-56. Copyright (2018), with permission from Springer).¹⁷

1.2.1 Chemical energy storage.

Chemical reactions involve the release or absorption of energy as chemical bonds in molecules are broken or reformed to generate new molecules. Energy stored in chemical fuels such as gasoline, natural gas, ethylene, ethanol, hydrogen, etc. can be recovered on demand. These fuels are stable and portable to a long distance. Hence, chemical fuels are a great way to store renewable energy. Figure 1.7 compares the energy densities of various types of chemical fuels and batteries.¹⁸ Chemical fuels are superior to Li-ion batteries in terms of both volumetric and gravimetric energy densities. For example, the volumetric energy density of gasoline is about 100 times higher than that of Li-ion batteries. For hydrogen molecules, it has a remarkable gravimetric energy density, but its volumetric energy density is much lower than most hydrocarbon fuels. Furthermore, hydrogen requires special and costly units for storage. For this reason, chemical fuels, particularly hydrocarbon fuels are an excellent choice for both short-term and long-term energy needs.¹⁸ If hydrocarbon fuels are converted from anthropogenic CO₂, it can simultaneously mitigate global warming and renewable energy curtailment.¹⁹

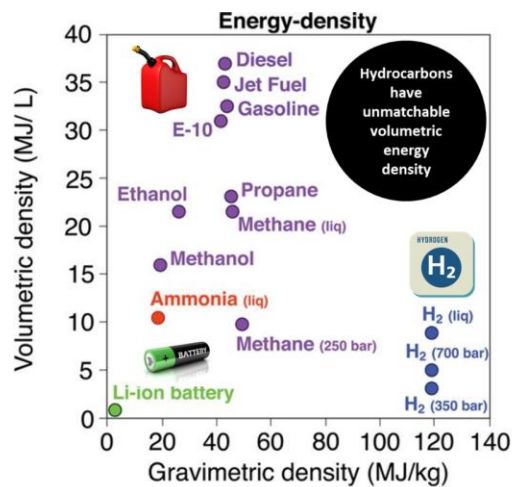


Figure 1. 7 Energy density comparison between chemical fuel vs. batteries.

1.3 CO₂ utilization and CO₂ reduction electrocatalysis.

1.3.1 CO₂ utilization methods for sustainable development.

CO₂ molecules can be utilized directly or indirectly as a feedstock in industrial or chemical processes to produce value-added carbon-containing products.¹⁹ Figure 1.8 illustrates 10 possible pathways of CO₂ utilization: (1) Production of CO₂-based chemicals; (2) production of CO₂ based-fuels; (3) microalgae fuels/products; (4) concrete building materials; (5) CO₂-enhanced oil recovery; (6) bio-energy with carbon capture and storage; (7) geoengineering approaches to enhance weathering; (8) forestry techniques; (9) land management via soil carbon sequestration; (10) synthesis of biochar.¹⁹ Among these, our primary focus is on the production of CO₂ based fuels/chemicals. This route includes biochemical, radiochemical, thermochemical, photochemical, and electrochemical reduction of CO₂.²⁰ Among various methods, an electrochemical approach is promising due to several advantages, including (1) the ease of coupling with renewable energy sources, (2) operation under ambient temperature and pressure, 3) control of rates and products by tuning applied voltage and electrolyte and (4) economic and engineering feasibility.^{6,20}

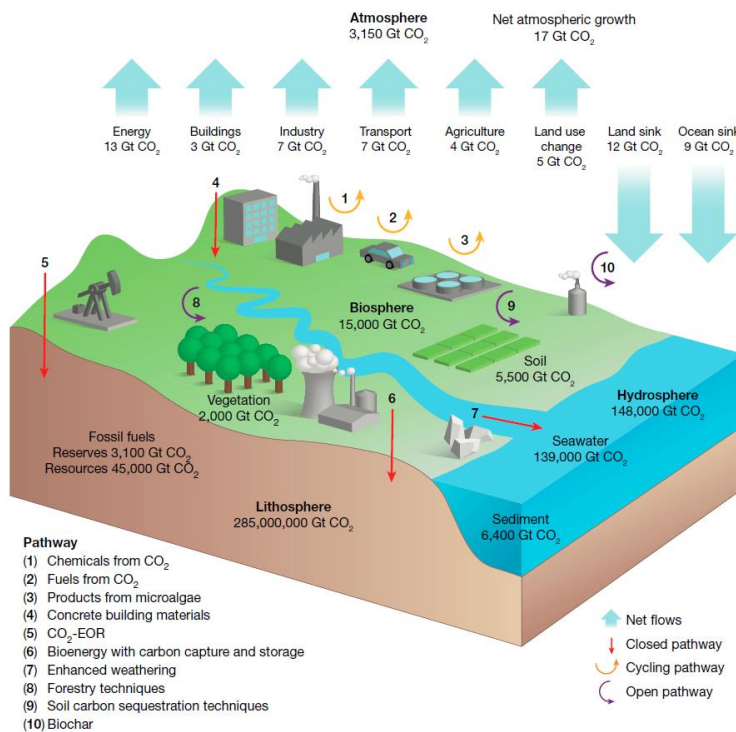


Figure 1. 8 Various pathways for CO₂ utilization and removal. (Adapted from Hepburn, C.; Adlen, E.; Beddington, J.; Carter, E. A.; Fuss, S.; Mac Dowell, N.; Minx, J. C.; Smith, P.; Williams, C. K., The technological and economic prospects for CO₂ utilization and removal. *Nature* 2019, 575 (7781), 87-97. Copyright (2019), with permission from Nature).¹⁹

1.3.2 Physicochemical properties of CO₂.

CO₂ is a gas with no color or odor. It is soluble in water, ethanol, and acetone. Chemical and physical properties of CO₂ are listed in Table 1.1.²¹ In the ground state, CO₂ is linear in geometry and nonpolar. The C atom on the center forms double bonds with O atoms at both ends (C=O bond strength: 750 kJ mol⁻¹).²² Its C=O bond length is ~1.17 Å. The oxidation state of C atom in CO₂ is (+4), the highest oxidation number of carbon. Due to the above facts, CO₂ possesses high thermodynamic stability, making CO₂ utilization an energy-intensive process.²³

Table 1. 1 Physical and chemical properties of CO₂ (Adapted from Song, C., Global challenges and strategies for control, conversion and utilization of CO₂ for sustainable development involving energy, catalysis, adsorption and chemical processing. *Catalysis Today* 2006, 115 (1), 2-32. Copyright (2006), with permission from Elsevier)²¹

Property	Value and unit
Molecular weight	44.01 g/mol
Sublimation point at 1 atm (101.3 kPa)	-78.5 °C
Triple point at 5.1 atm (518 kPa)	-56.5 °C
Triple point pressure	5.1 atm
Critical temperature (T _c)	31.04 °C
Critical pressure (P _c)	7383 kPa
Critical density (ρ _c)	0.468 g/l
Gas density at 0 °C and 1 atm	1.976 g/l
Liquid density at 0 °C and 1 atm	928 g/l
Solid density	1560 g/l
Specific volume at 1 atm and 21 °C	0.546 m ³ /kg
Latent heat of vaporization at the triple point (-78.5 °C) at 0 °C	353.4 J/g 231.3 J/g
Viscosity at 25 °C and 1 atm CO ₂	0.015 cP
Solubility in water at 0 °C and 1 atm 25 °C and 1 atm	0.3346 g/100g-H ₂ O 0.1449 g/100g-H ₂ O
Heat of formation at 25 °C, ΔH° gas	-393.5 kJ/mol
Entropy of formation at 25 °C, S° gas	213.6 kJ/mol
Gibbs free energy of formation at 25 °C, ΔG° gas	-394.3 kJ/mol
Heat capacity under constant pressure at 25 °C	37.1 J/(mol °C)
Heat capacity under constant volume at 25 °C	28.1 J/(mol °C)
Thermal conductivity	14.65 mW/(m K)
Viscosity at 0 °C	0.0001372 Poise
Electron affinity (E _a)	-0.6 eV ²⁴
First Ionization potential (I _p)	13.8 eV ²⁴

Understanding the electronic properties of CO₂ is essential for CO₂ utilization. Figure 1.9 (a) depicts the molecular orbital (MO) diagram of CO₂ in which ¹π_g and ²π_u are HOMO and LUMO, respectively.^{24, 25} In the non-bonding HOMO, electrons are localized at the terminals of oxygen atoms, while empty LUMO orbitals are placed on the carbon center. CO₂ is amphoteric since the oxygen atoms act as Lewis bases, and the carbon atom acts as a Lewis acid. Considering slightly negative electron affinity (-0.6 eV) and the first

ionization potential (13.8 eV) of CO₂, electrophilic character of C is more dominant than the nucleophilic character of O in CO₂.²⁴ Therefore, certain reactivity is expected due to lone pairs and pi-electron density between C=O bonds. When LUMO of CO₂ is filled with an electron, the CO₂ molecule becomes bent.²³ This bending decreases the OCO bond angle and elongates the C-O bond, splitting in-plane LUMO from out-of-plane LUMO (Figure 1.9 (b-e)). Due to this geometric distortion, subsequent electron-transfer events occur more easily to complete CO₂ reduction.^{23, 24} However, the first step to shuttle an electron to a neutral CO₂ is energy-intensive as large negative potential (-1.9 V) is required to form the bent CO₂^{•-} radical anion. Due to the first rate-determining step, the overall CO₂ reduction is kinetically sluggish.²³

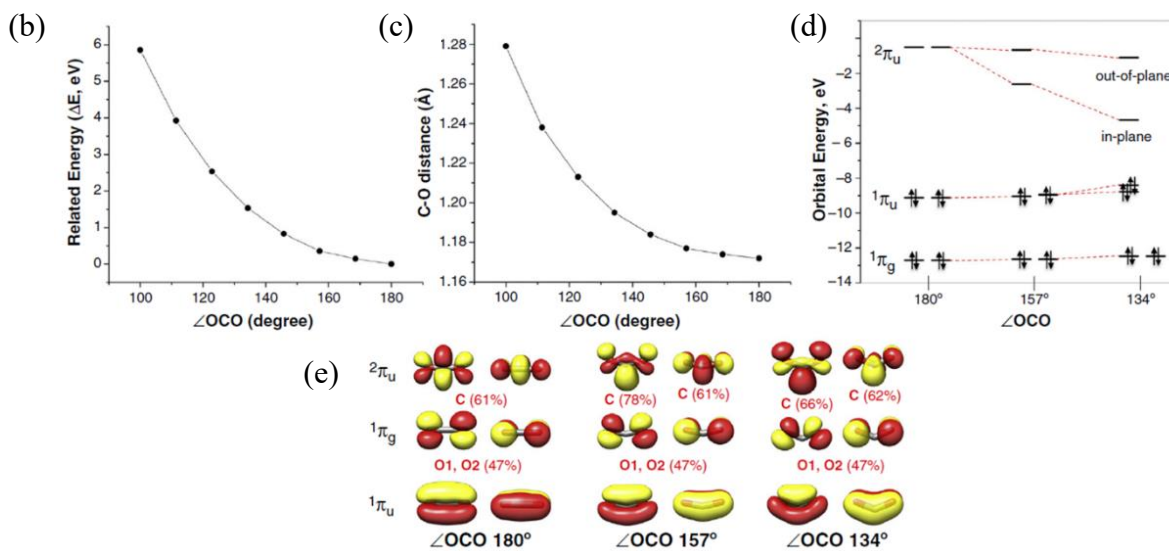
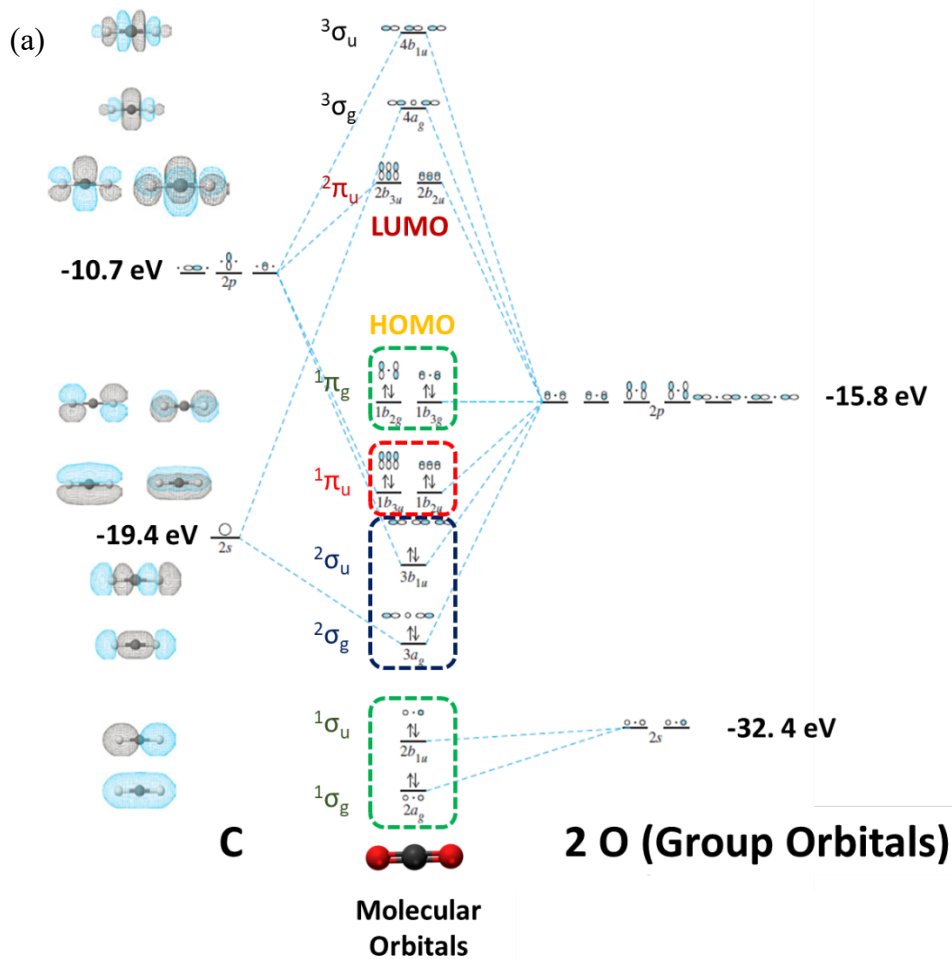


Figure 1. 9 (a) Molecular orbital diagram of CO₂ (Expanded from Miessler et al. and Francke et al.),^{24, 25} (b) Change in total energy as a function of OCO angle, (c) change in C-O distance as a function OCO angle, (d) Walsh diagram for CO₂ bending and (e) molecular orbitals of CO₂ at various OCO angles. (Reprinted from Mondal, B.; Song, J.; Neese, F.; Ye, S., Bio-inspired mechanistic insights into CO₂ reduction. *Current Opinion in Chemical Biology* 2015, 25, 103-109. Copyright (2015), with permission from Elsevier).²³

1.3.3 Electrocatalysis.

The concept of catalysis was first introduced by the Swedish chemist Jöns Jacob Berzelius in 1835. A catalyst is a substance that enhances the rate of a chemical reaction without being consumed.²⁶ Figure 1.10 illustrates the effect of a catalyst in a hypothetical exothermic reaction $X+Y\rightarrow Z$.²⁷ In the diagram, the reaction proceeds through an alternative pathway with low activation energy when the catalyst is present. The scope of catalysts can be extended to electrocatalysis. Thus, an electrocatalyst refers to a material that interacts with reactants and increases the rate of an electrochemical reaction without being altered.²⁸

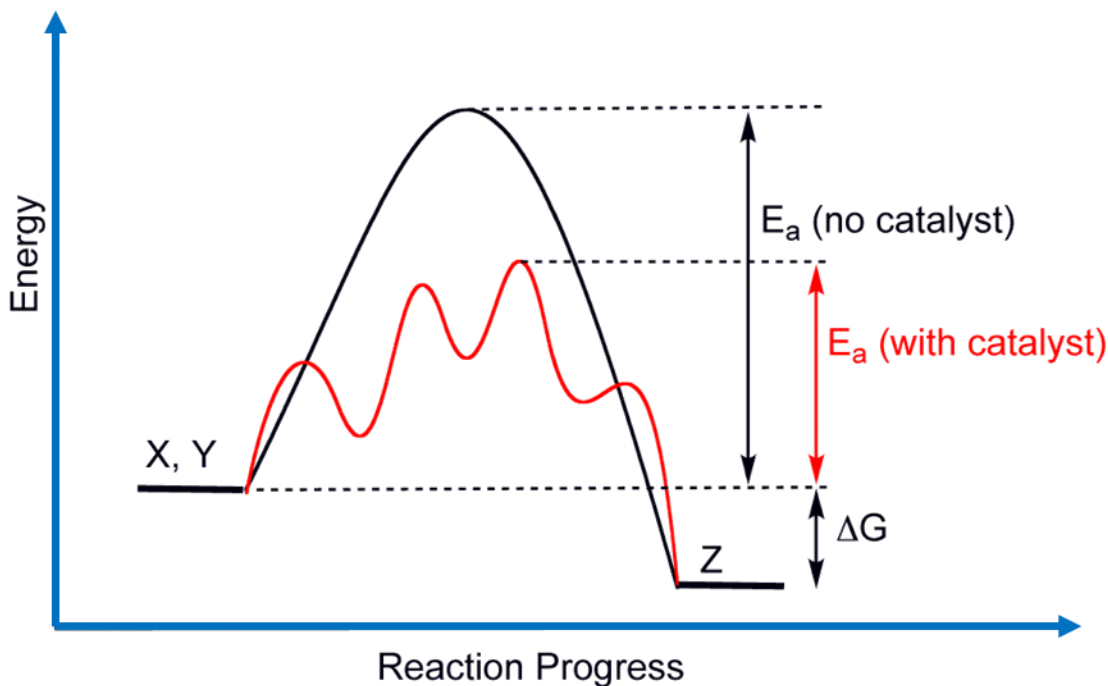


Figure 1. 10 Potential energy diagram corresponds to the catalyst effect on the hypothetical exothermic reaction $X+Y \rightarrow Z$.

1.3.3.1 Electrochemical reaction

In an electrochemical reaction, charge species, electrons and ions, are transferred across interfaces. An electrochemical reaction involves electron transfer occurring at an interface between a conductive solid and an electrolyte. Typically, the electrode reactions include two half-reactions, namely cathodic and anodic reactions. The electron transfer is driven by potential energy gradients developed at cathode and anode.²⁹ Following examples showcase electrochemical reactions that occur during the electrochemical conversion of CO_2 to carbon monoxide (CO) in an electrolysis cell (Figure 1.11).

At cathode (reduction): $CO_{2(aq)} + 2H_{(aq)}^+ + 2e^- \rightarrow CO_{(g)} + H_2O_{(l)}$; $E^\circ_c = -0.106 \text{ V}$

At anode (oxidation): $\frac{1}{2}O_{2(g)} + 2H_{(aq)}^+ + 2e^- \rightarrow H_2O_{(l)}$; $E^\circ_a = +1.229 \text{ V}$

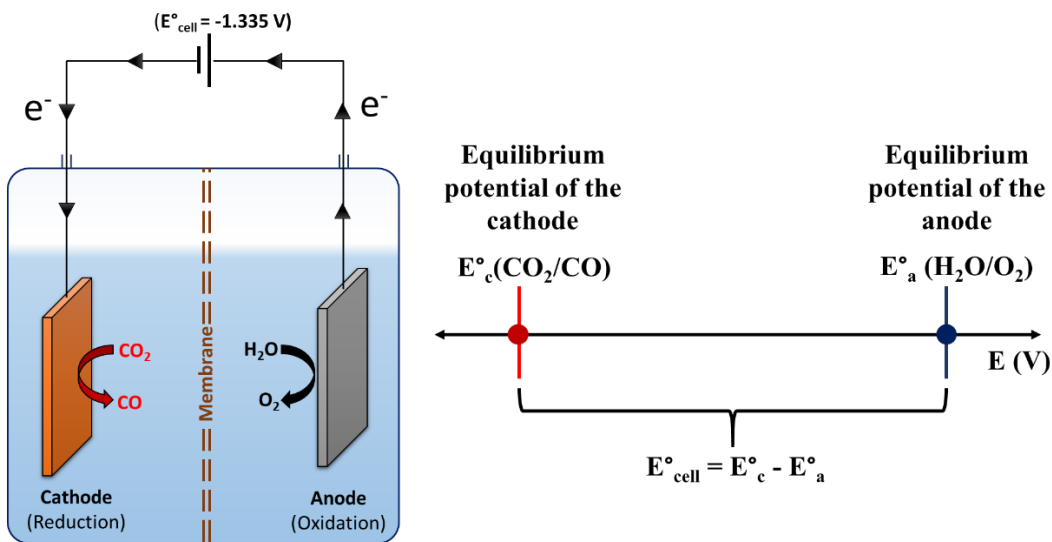
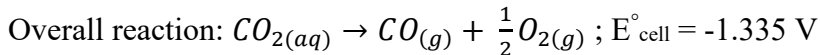


Figure 1. 11 A schematic diagram of the electrolysis cell.

The above process suggests that to drive the overall reaction, a minimum of -1.335 V needs to be applied across electrodes. In Figure 1.11, CO_2 conversion and water oxidation occur on cathode and anode, respectively. Both reactions take place within molecular distances from the electrode surface, and in most instances, reactants need to form chemical bonds with electrodes for electron transfer events to occur.

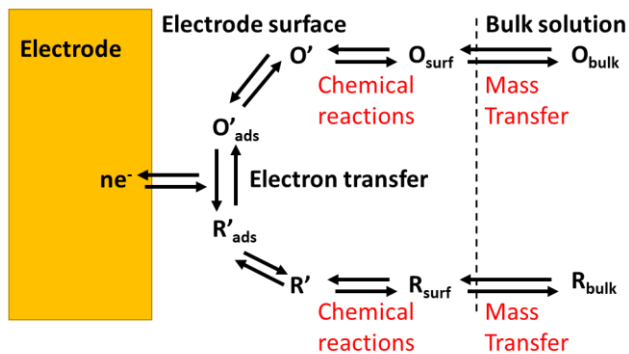


Figure 1. 12 The general electrochemical pathway.

Figure 1.12 describes the general electrochemical pathways for a simple reaction $O + ne^- \leftrightarrow R$.³⁰ Besides electron transfer and mass transfer, several fundamental steps may take place during the electrode reactions. These steps include (i) adsorption of reactants through electrostatic interaction or by forming a covalent bond, (ii) chemical reactions through cleavage or formation of chemical bonds, (iii) phase formation (formation of gas/oxide layer in metals, etc.), (iv) multiple electron transfer (electron transfer separated by chemical reactions).²⁹ To gain an insight into a complicated electrode reaction process, thermodynamic and kinetic aspects of each elementary step should be understood.

1.3.3.2 Thermodynamic and kinetic aspects of electrode reactions

The thermodynamics of electrochemical reactions can be related to Gibbs free energy difference (ΔG) between products and reactants. As a rule of thumb, we can predict the spontaneity of the reaction based on the sign of ΔG . If,

$\Delta G < 0$; the reaction is spontaneous

$\Delta G = 0$; the reaction is in equilibrium

$\Delta G > 0$; the reaction is nonspontaneous.

At equilibrium, the standard Gibbs free energy change (ΔG°) can be related to the equilibrium potential, E° as follows.³¹

$$\Delta G^\circ = -nFE^\circ$$

where n = number of electrons and $F = 96485.33212 \text{ C mol}^{-1}$, Faraday constant. Based on this relation, the standard Gibbs free energy and the standard reduction potential of several CO_2 reduction processes are tabulated in table 1.2.

Table 1. 2 Standard Gibbs free energy and standard potential for half-cell electrochemical reduction of CO₂.

Half Reaction	ΔG° (kJ mol ⁻¹) ^a	E° (V) vs. SHE
$CO_{2(aq)} + e^- \rightarrow CO_2^{*-}$	183.32	-1.90
$CO_{2(aq)} + 2H_{(aq)}^+ + 2e^- \rightarrow CO_{(g)} + H_2O_{(l)}$	19.88	-0.10
$CO_{2(aq)} + 2H_{(aq)}^+ + 2e^- \rightarrow HCOOH_{(aq)}$	38.40	-0.20
$CO_{2(aq)} + 6H_{(aq)}^+ + 6e^- \rightarrow CH_3OH_{(aq)} + H_2O_{(l)}$	-17.95	+0.03
$CO_{2(aq)} + 8H_{(aq)}^+ + 8e^- \rightarrow CH_{4(g)} + 2H_2O_{(l)}$	-130.40	+0.17
$2CO_{2(aq)} + 12H_{(aq)}^+ + 12e^- \rightarrow C_2H_{4(g)} + 4H_2O_{(l)}$	-40.52	+0.07
$2CO_{2(aq)} + 12H_{(aq)}^+ + 12e^- \rightarrow C_2H_5OH_{(aq)} + 3H_2O_{(l)}$	-49.21	+0.085
$3CO_{2(aq)} + 18H_{(aq)}^+ + 18e^- \rightarrow C_3H_7OH_{(aq)} + 5H_2O_{(l)}$	-52.1	+0.09

^a Gibbs free energy of reaction for a mole of CO₂ at 298 K, 1 atm in 1M solution.

Although thermodynamics suggests that reactions in Table 1.2 occur at relatively similar potentials, these reactions are governed by kinetics as they involve multiple steps. The kinetic aspects of electrode reactions establish the relation between Faradaic current and overpotential (η). For a given electrochemical reaction, the term, overpotential (η), is defined as the "electrode potential necessary to drive a certain current," which is the difference between the applied potential (E) and equilibrium potential (E_e); $\eta = E - E_e$.²⁷ The overpotential may originate from two major sources; 1) Activation overpotential (η_a) - related to activation energy of coupled electrochemical reactions, 2) Concentration overpotential (η_c) – ensue from mass transport limitation. An ohmic loss in the cell (due to electrolyte and external electrical contact) also contributes to the Overpotential, which is called IR drop (η_o). It is possible to keep η_c and η_o can be kept minimum by carefully engineering the electrochemical cell. Therefore, one of the main goals of electrocatalysis studies is to discover electrode materials at which η_a is minimum.²⁷ With negligible η_c and

η_o , the relationship between current (i) and activation overpotential (η_a) can be derived for one step-one electron reaction as follows:

$$i = i_0 \left\{ e^{\left[\frac{-(\alpha)F\eta_a}{RT} \right]} - e^{\left[\frac{(1-\alpha)F\eta_a}{RT} \right]} \right\}$$

The above equation is known as the Butler-Volmer (BV) equation. α is the transfer coefficient and i_0 is defined as the exchange current density- an indication of electron transfer rate at equilibrium potential. i is the net current as the first and second exponential terms correspond to cathodic and anodic terms, respectively. When the system operates farther from equilibrium, i.e $|\eta_a| > 50 \text{ mV}$, the BV equation is reduced to the Tafel equation. As an example, when the reduction reaction is dominant, the following linear relationship is obtained.

$$i_c = i_0 e^{\left[\frac{-(\alpha)F\eta_a}{RT} \right]}$$

$$\log |i_c| = - \left(\frac{(\alpha)F}{RT} \right) \eta_a + \log (i_0)$$

The Tafel equation can be used to evaluate the activity of the catalyst. If a CO_2 electrocatalyst exhibits a large i_c with a smaller η_a , that catalyst facilitates a smaller activation barrier and fast reaction kinetics.

1.3.3.3 The heat of adsorption and Volcano plots

Various electrodes show vastly different activities under the same potential and reaction conditions. These differences originate from the varying heat of adsorption energy of educts, intermediates, or products on the electrode.²⁷ The heat of adsorption depends on the chemical nature of the electrode. The plot that correlates adsorption energy of key reaction intermediates and reaction rates exhibits a volcano-shaped dependence. French

chemist Paul Sabatier introduced this concept in the early 1900s. According to the Sabatier principle, the best catalyst will adsorb key intermediate species moderately on its surface, neither too weakly nor too strongly.²⁷ This concept can be extended for electrocatalysis, and the qualitative representation of Sabatier principle is shown in Figure 1.13.³² In this principle, the reaction rate is either limited by strongly bound intermediates causing the deactivation of electrode surface or weakly bound intermediates which easily desorb from the catalyst surface without undergoing reaction. Therefore, finding the Sabatier optimum for a catalytic reaction has been the hallmark of catalysis studies.

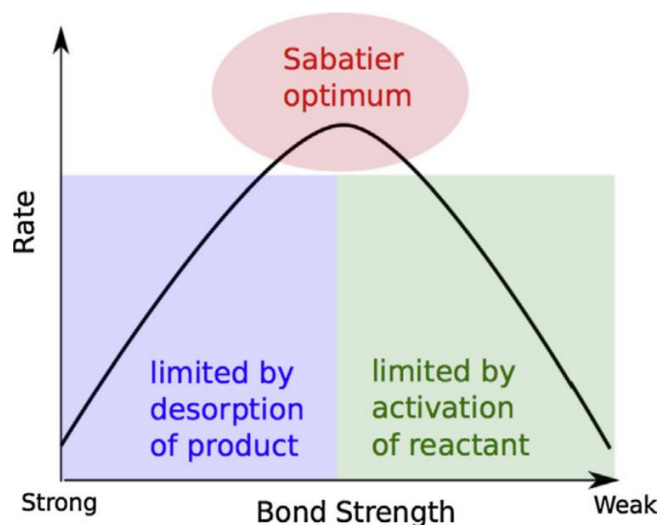


Figure 1. 13 Schematic representation of the Sabatier principle. (Reprinted from Medford, A. J.; Vojvodic, A.; Hummelshøj, J. S.; Voss, J.; Abild-Pedersen, F.; Studt, F.; Bligaard, T.; Nilsson, A.; Nørskov, J. K., From the Sabatier principle to a predictive theory of transition-metal heterogeneous catalysis. *Journal of Catalysis* 2015, 328, 36-42. Copyright (2015), with permission from Elsevier).³²

1.3.3.4 Effects of mass transport.

The first requirement of any electrochemical reaction is that the proximal availability of reactants to assist the electron transfer. Therefore, the mass transfer of species to the electrode surface is a critical factor. In section 1.3.3.2, the concept of

concentration overpotential (η_c), which arises from the mass transport limit, was briefly discussed. In order to keep the minimum η_c , however, it is imperative to understand three forms of mass transport, diffusion, migration, and convection (Figure 1.14).²⁹

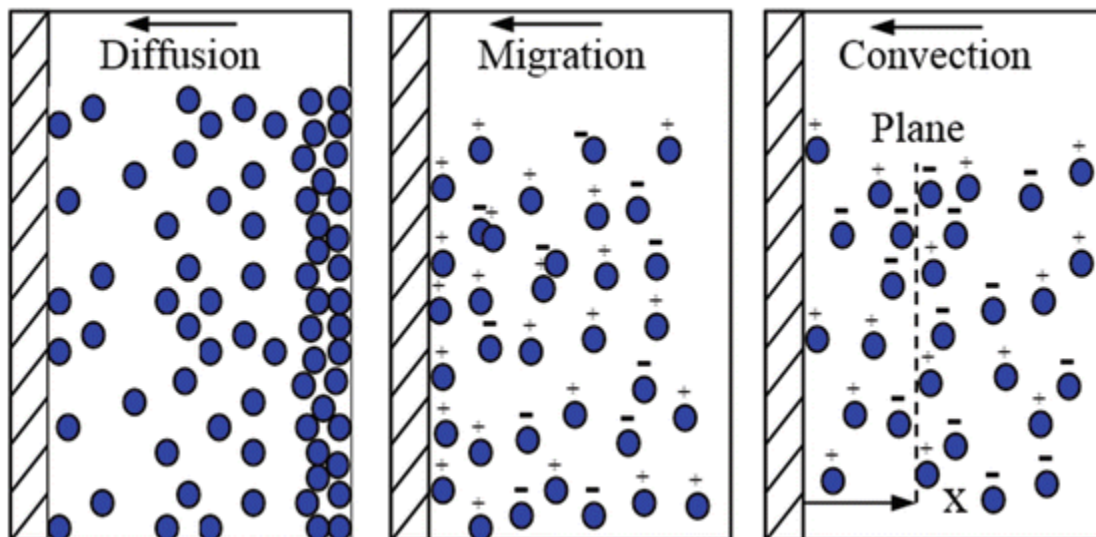


Figure 1. 14 Modes of mass transport. (Reprinted from Perez, N., Mass Transport by Diffusion and Migration. In *Electrochemistry and Corrosion Science*, Perez, N., Ed. Springer International Publishing: Cham, 2016; pp 151-197. Copyright (2016), with permission from Springer).³³

Diffusion is the movement of species due to the concentration gradient. Diffusion takes place from regions with high concentration to low concentration until the system obtains a uniform concentration.³⁴ This process is unavoidable in most catalytic systems as the electron transfer occurs on the electrode surface and lowers the concentration of reactants in the interfacial region. Migration is the movement of charged species due to an electric field. In an electrochemical cell, the current is passing through two electrodes; thus, there is an existing potential gradient to drive the reactants via electrostatic forces. However, typical experiments involve a large concentration of electrolyte shielding the electrostatic force. Therefore, migration is not a dominant mode of mass transport. Convection occurs when species move due to external mechanical forces such as moving electrode, stirring,

and sparging solution with gas.²⁹ When the experiment involves forced convection, it dominates the diffusion process. Therefore, it is crucial to quantify the convective region. As an example, for the rotating disk electrode (RDE), the thickness of the boundary layer (δ) is given by:

$$\delta = \frac{1.61 \nu^{1/6} D^{1/3}}{\omega^{1/2}}$$

Where ν , D , and ω are kinematic viscosity (i.e., viscosity/density) of the solution, diffusion coefficient of the species, and rotation rate of the disk, respectively. Overall, all three modes of mass transport are integrated into the Nernst-Planck equation as follows:

$$J_i = -D_i \frac{\partial C_i}{\partial x} + \frac{z_i F D_i C_i}{RT} \frac{\partial \phi(x)}{\partial x} + C_i v(x)$$

Where,

$$J_i = \text{molar flux} (\text{mol cm}^{-2} \text{s}^{-1})$$

$$C_i = \text{Concentration}$$

$$z_i = \text{Charge of species}$$

$$D_i = \text{Diffusion Coefficient}$$

$$\phi(x) = \text{electric potential}$$

$$v(x) = \text{solution velocity along } x \text{ direction}$$

Regardless, in the proximity to the electrode surface, the convection is diminished due to the electrode rigidity and frictional forces. Therefore, diffusional transport is the only transport mode in this region, which is known as the Nernst diffusion layer. Schematic representation of the Nernst diffusion layer is depicted in Figure 1. 15.²⁹

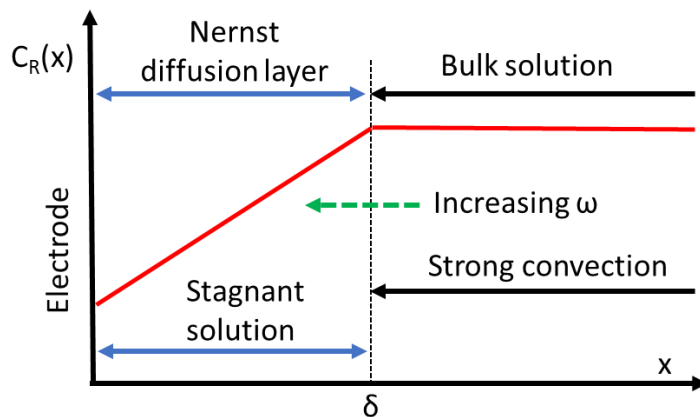


Figure 1. 15 Nernst diffusion layer model.²⁹

1.3.4 Introduction to electrochemical CO₂ reduction.

As stated earlier, the primary motivation for CO₂ electroreduction is to reduce the carbon footprint and efficiently convert renewable energy into usable chemicals and fuels.

This process is summarized in Figure 1.16.

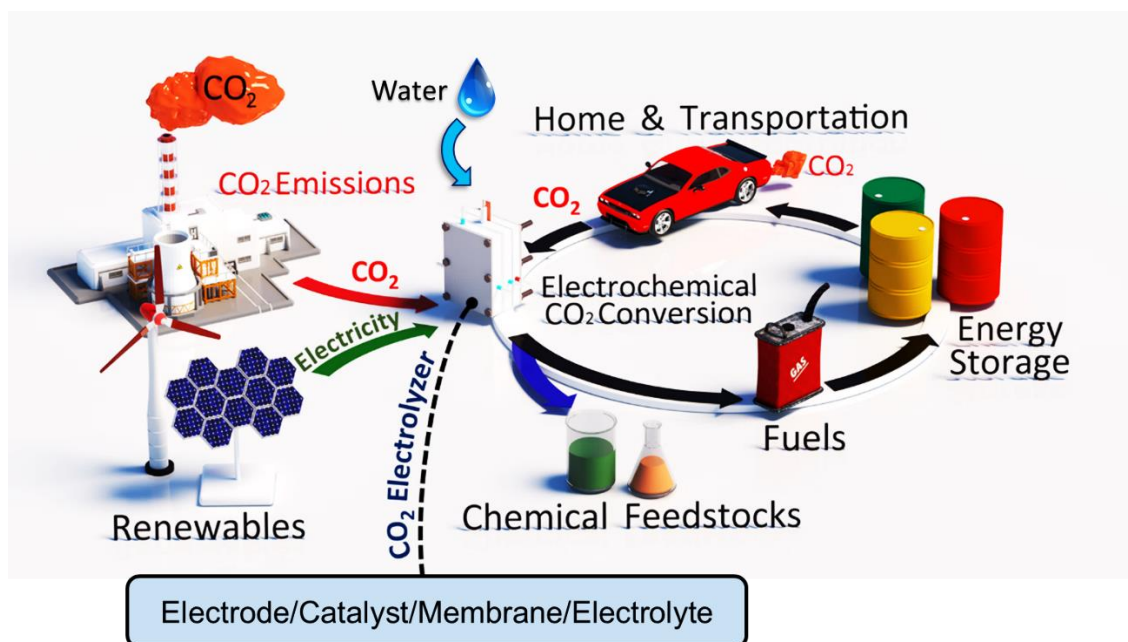
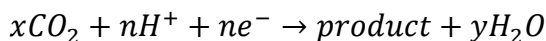


Figure 1. 16 CO₂ utilization via electrochemical CO₂ conversion.

It is important to note that the CO₂ reduction takes place at the cathode side of the CO₂ electrolyzer. The cathodic reaction for electrochemical CO₂ reduction has the following general form:



The choice of possible CO₂ electroreduction products ultimately comes down to the technoeconomics and energetics.^{6, 35-37} Figure 1. 17 shows the correlation between the approximate market price of viable CO₂ reduction products and the minimum energy needed for their production balanced by oxygen evolution reaction (OER).

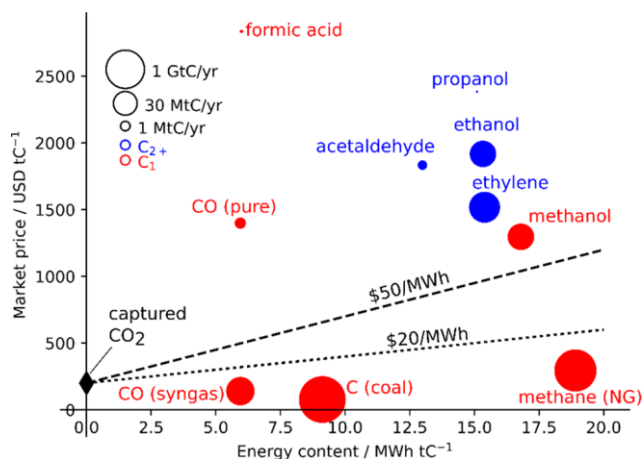


Figure 1. 17 Economics and energetics of CO₂ electroreduction products (Lines represent minimum cost of production of CO₂ utilizing electricity, the circle size indicates the logarithmic representation of the current market size of each product, and both axes are normalized to the mass of the carbon). Adapted with permission from (Nitopi, S.; Bertheussen, E.; Scott, S. B.; Liu, X.; Engstfeld, A. K.; Horch, S.; Seger, B.; Stephens, I. E. L.; Chan, K.; Hahn, C.; Nørskov, J. K.; Jaramillo, T. F.; Chorkendorff, I., Progress and Perspectives of Electrochemical CO₂ Reduction on Copper in Aqueous Electrolyte. Chemical Reviews 2019, 119 (12), 7610-7672. Copyright (2019) American Chemical Society).⁶

The dashed and dotted lines represent the minimum cost for captured CO₂ from concentrated sources. This cost is estimated to be \$200/tC from a power plant. \$50 and \$20/MWh are estimated current and future solar installation costs, respectively. This plot

suggests that any products appear above two lines may be economically feasible, excluding capital and other expenses. Therefore, specialty chemicals such as formic acid, industrial precursors such as carbon monoxide as well as ethylene, and energy-dense fuels such as ethanol give a better chance of achieving economic feasibility.⁶ Therefore, it is imperative to develop catalysts and design systems that can produce these products efficiently.

Catalysts are developed and evaluated in terms of three primary figures of merit: activity, stability, and selectivity. Kibria et al. recently set several technoeconomic targets for CO₂ electroreduction performance, including 1) high selectivity of catalysts >90%, 2) current density >300 mA cm⁻², and 3) stability of >80,000 h.³⁷ However, none of the catalytic systems simultaneously meet these stringent requirements so far. Thus, there is vast room for the development of catalysts, electrodes, and electrolyzer designs for the CO₂ electroreduction.

In the laboratory scale, the very first parameter to evaluate is the catalyst selectivity, which is measured in terms of faradaic efficiency (FE)/current efficiency. FE is the ratio between electrons involved in the target product vs. total electron input. FE is calculated according to the following formula:⁵

$$FE = \frac{Q_{Experimental}}{Q_{Theoretical}} \%$$

$$FE = \frac{z \times n \times F \times 100}{Q} \%$$

Where,

$Q = \text{Total number of electron input}$

$z = \text{Number of mols of the product of interest}$

$n = \text{Number of electrons required to produce the product of interest}$

$F = \text{Faraday constant}$

Using the FE, the energy conversion efficiency in terms of the cathodic half cell ($EE_{cathodic\ half-cell}$) and full-cell energy efficiency ($EE_{full-cell}$) can also be validated considering OER counter-reaction as follows:³⁸

$$EE_{cathodic\ half-cell} = \frac{(1.23 + (-E_{product})) \times FE_{product}}{(1.23 + (-E_{applied}))} (\%) \quad 1.18$$

$$EE_{full-cell} = \frac{(1.23 + (-E_{product})) \times FE_{product}}{-E_{full-cell\ applied}} (\%) \quad 1.19$$

Where,

$E_{product}$ = Thermodynamic potential for CO₂ reduction (vs. RHE)

$FE_{product}$ = Faradaic efficiency of product of interest

$E_{applied}$ = Applied potential (vs. RHE)

$E_{full-cell\ applied}$ = Full cell potential applied across cathode and anode

Since we mostly focus on the development of the cathode, it is highly desirable to use a universal reference system when reporting data. Typically, during the experiment, the potential of the cathode is measured against a reference electrode such as Ag/AgCl. Ultimately, to compare this data from one laboratory to another, it is recommended to report the potentials thermodynamically relevant and pH-independent reversible hydrogen electrode (RHE) scale.⁶ Therefore, all the potentials that were measured against the Ag/AgCl electrode in this work are converted to the RHE scale using the following formula.

$$V\ vs.\ (RHE) = V\ vs.\ (Ag/AgCl) + 0.222 + 0.059 \times pH_{electrolyte} \quad 1.20$$

1.4 Review of CO₂ electroreduction.

Electrochemical CO₂ reduction is a complicated and kinetically sluggish process that involves the coupling of multiple electrons and protons on the catalyst surface. Figure 1.18 summarizes the possible pathways of CO₂ electroreduction to produce both C1 and C2 products.⁶ These pathways were proposed based on both experimental and theoretical studies. To gain knowledge of mechanistic pathways and molecular interactions on the catalytic surface is crucial to develop efficient catalysts that meet our needs in the future. For example, the most common pathway of converting CO₂ to CO involves the formation of *COOH intermediate. Therefore, to produce CO efficiently, *COOH should bind tightly, and CO should bind weakly to the electrode surface. This knowledge can be used to tune the size, structure, and composition of the catalyst, such that the binding energies of reactants can be tailored to enhance the catalyst performance further.³⁹

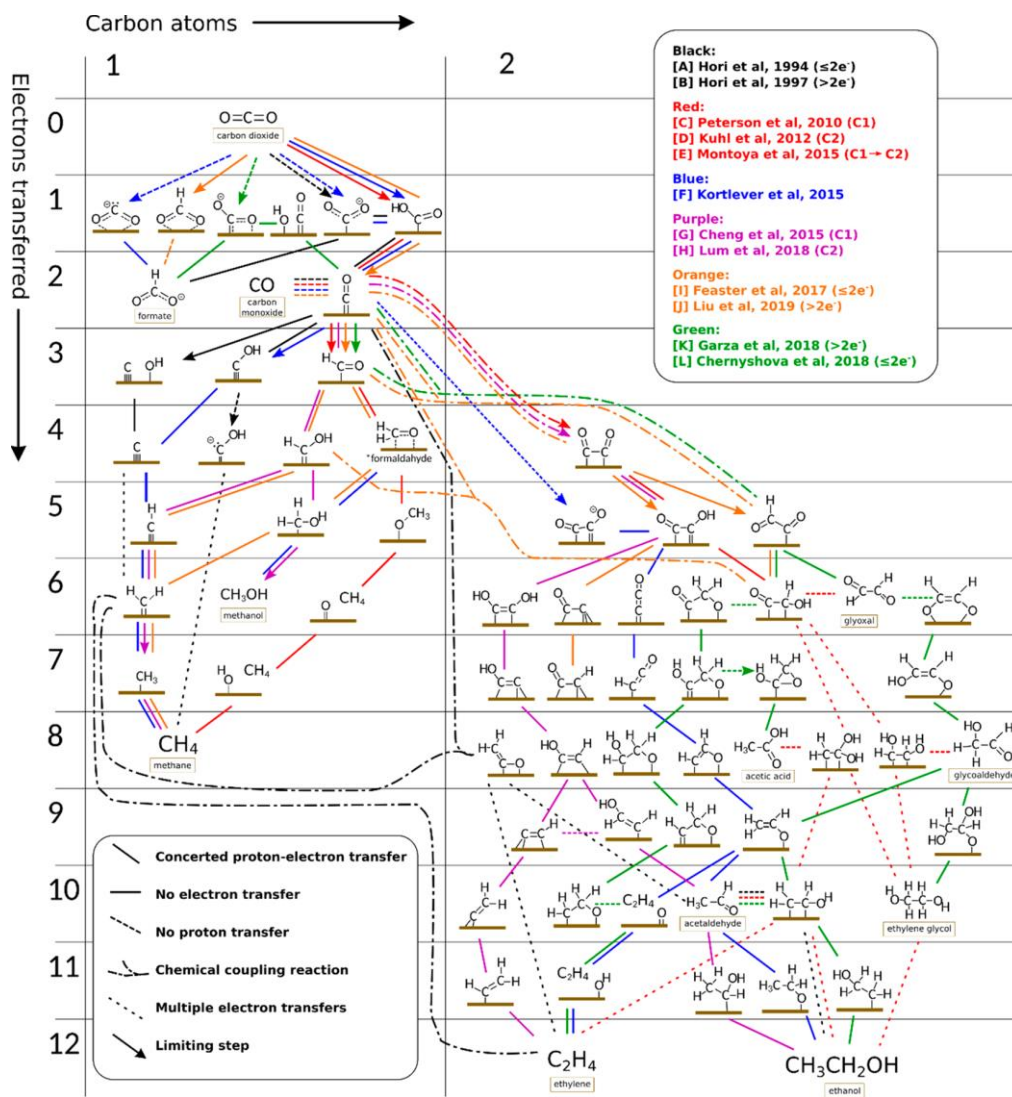


Figure 1. 18 Possible mechanistic pathways of CO₂ electroreduction. Adapted with permission from (Nitopi, S.; Bertheussen, E.; Scott, S. B.; Liu, X.; Engstfeld, A. K.; Horch, S.; Seger, B.; Stephens, I. E. L.; Chan, K.; Hahn, C.; Nørskov, J. K.; Jaramillo, T. F.; Chorkendorff, I., Progress and Perspectives of Electrochemical CO₂ Reduction on Copper in Aqueous Electrolyte. *Chemical Reviews* 2019, 119 (12), 7610-7672. Copyright (2019) American Chemical Society).⁶

Over the recent years, there is a rapid inclination of the electrochemical CO₂ reduction technologies. Interestingly, several industries are currently working on the commercialization of this technology by establishing pilot-plants and performing scale-up studies.⁴⁰ This technology development is mainly driven by two key sectors, 1) catalyst

engineering and 2) electrochemical cell engineering (electrolyzer configuration).²² As for catalysts, there are two main categories: (1) metal-free carbon-based catalysis and 2) metallic catalysis. Both types of catalysts will be extensively discussed in the following sections.

1.4.1 Metal-free catalysts for CO₂ electroreduction.

Carbon-based metal-free electrocatalysts are especially alluring to CO₂ electroreduction due to their unique properties such as chemical stability, ease of structure modification, and low-cost bulk production.⁴¹ The ability of carbon to adopt various hybridizations (sp, sp², and sp³) can result in forming bulk carbon allotropes such as diamond and graphite. Diamond is made of a three-dimensional sp³-hybridized carbon network and graphite consisting of stacked sp²-hybridized layers of carbon. Interestingly, in the nanoscale, other allotropes of carbon such as nanodiamond, carbon nano onions, carbon nanotubes (CNT), fullerenes, and graphene (Figure 1.19) emerge.^{42, 43} These allotropes possess unique properties such as high surface area, high conductivity, and high controllability over the surface as well as electronic structures that are highly desirable for catalyst applications.⁴⁴ Although most of the pristine carbon allotropes are electrochemically inactive towards CO₂ reduction, heteroatom-doping, defect engineering and curving of carbon structure have been used to manipulate p-orbital polarization, electron charge and spin densities.⁴⁴ These modifications generate active sites and tune the adsorption energy of reactants as well as intermediates during CO₂ electroreduction.

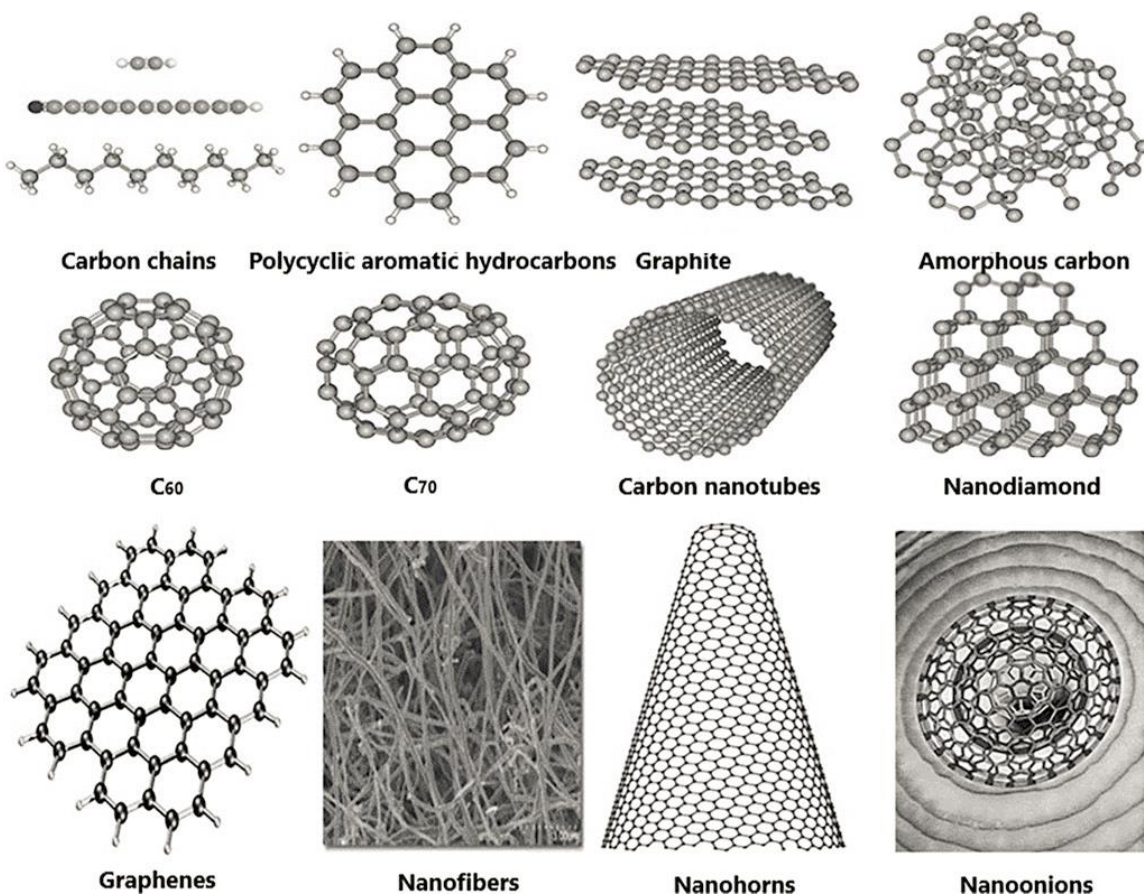


Figure 1. 19 Allotropes of carbon. Adapted from (Tripathi, A.C.; Saraf, S.A.; Saraf, S.K. Carbon Nanotropes: A Contemporary Paradigm in Drug Delivery. *Materials* 2015, 8, 3068-3100).⁴²

Carbon nanostructures can also be engineered to attain a wide spectrum of pore sizes; micropores (<2 nm), mesopores (2-50 nm), and macropores (>50 nm). For activated carbon, for instance, most of the modifications occur on micropores. However, mesopores and macropores play a crucial role by serving as channels for the passage of reactants to the micropores.⁴⁵ Therefore, in addition to the tunability of electronic properties, the structure tunability of carbon nanomaterials is beneficial to enhance the mass transfer of reactants/products during electrocatalysis.

The most common approach to tune the selectivity of carbon materials toward electrochemical CO₂ reduction is made by doping with heteroatoms such as B, N, F, P, S, etc.⁴⁴ N, and B doping has been investigated for diamond-based catalysis. Liu et al. synthesized nitrogen-doped nanodiamond via microwave assisted chemical vapor deposition (MACVD) technique. They reported acetate FE of ~77% at -0.8V vs. RHE.⁴⁶ In one of their recent study, they further investigated the effect of both N and B co-doped nanodiamond for CO₂ electroreduction. This specific catalyst generated ethanol with high selectivity (~93%) at -1.0 V vs. RHE.⁴⁷ In another study, Tomisaki et al. studied B-doped diamond and reported HCOOH faradaic efficiency of 70% at -2.1 V vs. Ag/AgCl in the KCl electrolyte.⁴⁸ However, the major bottleneck of diamond-based electrodes is the low current density.

Among graphitic carbon materials, nitrogen (N) is the most extensively studied dopant. N dopant may be involved with three chemical configurations; pyridinic-N, pyrrolic-N, and graphitic-N (Figure 1.20).⁴⁹ Due to similar bond lengths of C-N (1.41 Å) and C-C (1.42 Å), pyridinic and graphitic N do not significantly alter the graphitic structure. The stability and chemical environment of these configurations also play a crucial role in catalyst applications. Most of the nitrogen doping is done by thermal treatment methods where it involves annealing with nitrogen precursors such as urea, ammonia, melamine or dicyandiamide. It has been reported that the N functional groups introduced above 500 °C exhibit high thermal stabilities, particularly graphitic N.⁵⁰

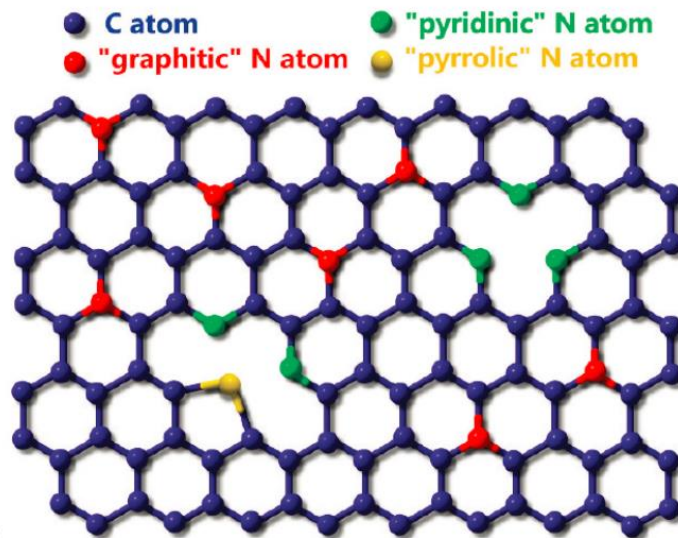


Figure 1. 20 Common bonding configurations of N doped carbon. Adapted with permission from (Wei, D.; Liu, Y.; Wang, Y.; Zhang, H.; Huang, L.; Yu, G., Synthesis of N-Doped Graphene by Chemical Vapor Deposition and Its Electrical Properties. Nano Letters 2009, 9 (5), 1752-1758). Copyright (2009) American Chemical Society⁴⁹

The catalytic activity of N-doped carbon is governed by its electronic properties. The electronegativity differences between N (3.04) and C (2.55) create polarization in the carbon network. Furthermore, the nitrogen configuration also influences the n- or p-type behavior of the carbon. Graphitic-N injects π electrons to the carbon network.⁵¹ Therefore, the Fermi level (an indicator which determines how the energy levels are occupied) is upshifting towards the conduction band and exhibits n-type behavior.⁵¹ However, pyridinic and pyrrolic N impose p-doping effect due to the withdrawal of electrons from carbon.⁵² These electronic structure modulations alter the interactions between CO₂ and N-doped carbon. In principle, the active sites are identified by the point of CO₂ adsorption and activation. Therefore, the interactions between HOMO of N-doped carbon and LUMO of CO₂ are used to deduce the active sites. For instance, it has been proposed that, when the

catalyst sites occupy high level of electronic density of states (DOS) at or just below the Fermi level, favorable interactions may occur between the active site and CO₂.⁴⁴

Several studies have proposed that the N itself or the carbon atom adjacent to it may act as active sites for the CO₂ electroreduction. However, the exact origin for the activity of N-doped carbon is still under debate. Recent studies by Ajayan and coworkers have proposed that the pyridinic-N is the primary active site for the CO₂ electroreduction based on both experimental and theoretical evaluations.⁵³⁻⁵⁵ Nevertheless, there are other studies that suggest pyrrolic or graphitic N could be the active site.⁵⁶⁻⁵⁸ The main reason for these contradictory conclusions is the structural heterogeneity and complexity of doped carbon materials. Therefore, it is imperative to perform a thorough structure analysis and integrate those findings with theoretical calculations to obtain an in-depth understanding.

Sulfur is another dopant that can promote CO₂ electroreduction.⁵⁹ Although C(2.55) and S(2.58) have similar electronegativities, they have different sizes. This size mismatch creates nonuniform spin densities on the host structure, which endow catalytic properties.⁵² These catalytic properties can be further enhanced by co-doping with N and S. However, to understand the nature of the catalyst sites and activity, active sites should be generated on a well-defined host structure.

1.4.2 Metal-based catalysts for CO₂ electroreduction.

Metal-based catalysts are the major stream in the area of electrochemical CO₂ reduction. Particularly, the activity of bulk metals was well studied and reviewed by Hori and coworkers in 2008.⁶⁰ Metal-based catalysts were classified into three major categories, depending on the binding energy of CO₂ reduction intermediate and the product selectivity.

Group 1 includes p-block metals such as Sn, In, Pb, Ti, Hg, Cd, and Bi, which predominately produce formate. On these catalysts, $^*CO_2^{\delta-}$ intermediate weakly chemisorbs and generate formate through *HCOO intermediate (bounds to the surface via oxygen atoms). Surface structuring has been used to improve metal catalysts. Zheng et al. showed that formate selectivity could be enhanced by three times by using S modified Sn catalyst (Sn(S)/Au) over (Sn/Au) catalyst. They confer activity owing to the undercoordinated Sn sites induced by S. This catalyst showed formate FE of 93% at -0.75 V vs. RHE for more than 40 hr stability exhibiting 55 mA cm^{-2} current density.⁶¹ Group 2 includes metals such as Au and Ag, which forms CO as the primary product. On these metals, the reaction follows via $^*CO_2^{\delta-}$ intermediate then followed by strong binding with *COOH for subsequent reduction to *CO . This weakly bonded *CO leads to the formation of CO.³⁷ CO selectivity has also been improved by nanostructuring strategies. Ma et al. reported that the oxide derived (OD) Ag catalyst outperforms the polycrystalline Ag catalyst. With OD Ag, Overpotential was reduced by 0.49 V, and that catalyst achieved 80% CO FE at -0.6 V vs. RHE. This reduced overpotential is attributed to the low-coordinated surface sites of OD Ag.⁶² Beyond group 2, single-atom transition-metal catalysis have been studied for CO₂ electroreduction to CO. Strasser et al., and Wang et al. showed that single Ni atomic sites are highly active than metallic Ni. Notably, the unique electronic structure of single atomic catalysts suppresses the HER and selectively promote CO₂ electroreduction to CO.^{63, 64} Group 3 includes catalysts that moderately bind *CO intermediate and further reduce it to form hydrocarbons and oxygenates by enabling C-C coupling. As of today, Cu is the only catalyst that can produce up to sixteen different products due to its ability to bind *CO intermediate moderately.⁶⁵ Therefore, the lack of

selectivity has been the greatest challenge in Cu catalysis. Various strides have been made to tune the product selectivity of Cu, including surface and compositional changes. Particularly, OD Cu has been demonstrated to generate multicarbon products at low Overpotential with high selectivity.⁶⁶⁻⁷⁰ Several studies have reported that OD Cu has an abundance of grain boundaries, which can stabilize CO to form multicarbon products. Other than these approaches, tuning crystalline size, facets, strain, and local pH has been employed to promote multicarbon products with high selectivity.³⁷ For instance, Dinh et al. showed that by performing CO₂ electroreduction on Cu using 10 M KOH, ethylene FE can be increased up to 70% while suppressing HER.⁷¹

Other than these studies, supported metal catalysts have also been investigated for CO₂ electroreduction. The nature of support materials plays a crucial role in catalysis. Particularly, carbon-based materials endow new opportunities for the advancement of supported metal catalysts. These unique advantages of carbon support can be stated as follows (Figure 1.21 (a)): (1) carbon support provides a large surface area for the metal particles to allow adsorption of reactants near metal particle, (2) carbon support enhances strong metal-support interaction due to overlap between π orbitals of carbon and d orbitals of the metal (Figure 1.21 (b)), (3) the support provides or withdraws electrons from the metal and modulate the electron density of metal particle and (4) the support can provide cooperative active sites such as dopants or defects which can act as additional catalytic sites.⁷²

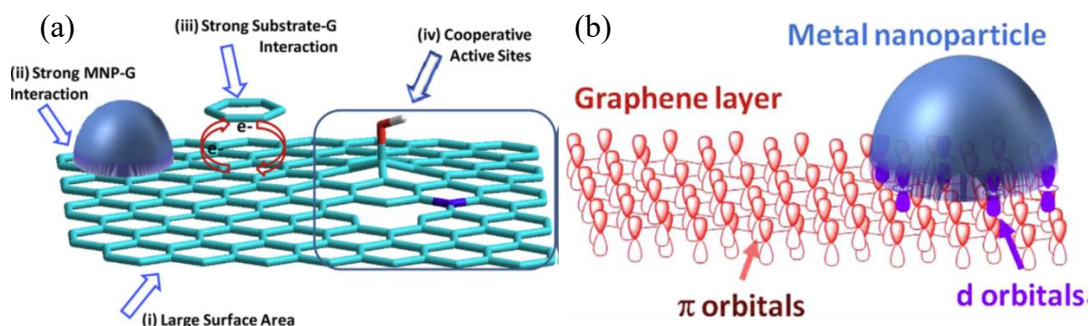


Figure 1. 21 (a) Main effects of the carbon support and (b) d- π interactions leading to charge transfer between metal and the support (Reprinted from Navalon, S.; Dhakshinamoorthy, A.; Alvaro, M.; Garcia, H., *Metal nanoparticles supported on two-dimensional graphenes as heterogeneous catalysts*. *Coordination Chemistry Reviews* 2016, 312, 99-148. Copyright (2016), with permission from Elsevier).⁷²

These concepts have been explored regarding electrochemical CO₂ reduction. Song et al. prepared a highly-textured carbon nano spike (CNS) support by a chemical vapor deposition technique and nucleated Cu nanoparticles on CNS via electrodeposition method.⁷³ This catalyst generated ethanol at 63% FE at -1.2 V vs. RHE. They attribute this activity to the simultaneous interactions exerted on OCCO intermediate by the proximal N-doped sites and Cu particles. Ultimately, these interactions lead to a complete reduction of OCCO intermediate on the Cu end to -CH₃ and partial reduction to -CH₂OH from CNS's end, granting high selectivity towards ethanol.⁷³ However, the mechanistic aspect of the reaction is still obscure.

1.5 System design for CO₂ electroreduction.

Although most of the studies have focused on the improvement of the catalyst, the optimization of a CO₂ electrolyzer is a highly important factor in enhancing the economic feasibility.³⁷ Typically, a catalyst testing is done in H-cell reactors, where the reacting CO₂ is dissolved in the liquid electrolyte (Figure 1.22 (a)).^{37, 74} In H-cell condition, the reaction

is limited by the solubility of CO_2 ($\sim 34 \text{ mM}$); thus, the current densities are limited to $\sim 35 \text{ mA cm}^{-2}$ under typical reaction conditions.⁷⁵ Since the current density is not enough for industrial adoption ($>200 \text{ mA}$), it is highly desired to design an electrolysis systems to boost current densities.⁷⁵ Consequently, gas-fed, gas diffusion electrodes (GDE) are actively being explored (Figure 1.22 (b)). GDE consists of a porous catalyst layer and diffusion media to assist the transport as well as the distribution of reactants. In GDEs, CO_2 gas is delivered to the cathode in the vapor phase where it can overcome the diffusion limitations as the CO_2 diffusion in the air is $\sim 8,000$ times greater than that of aqueous solution.⁷⁶

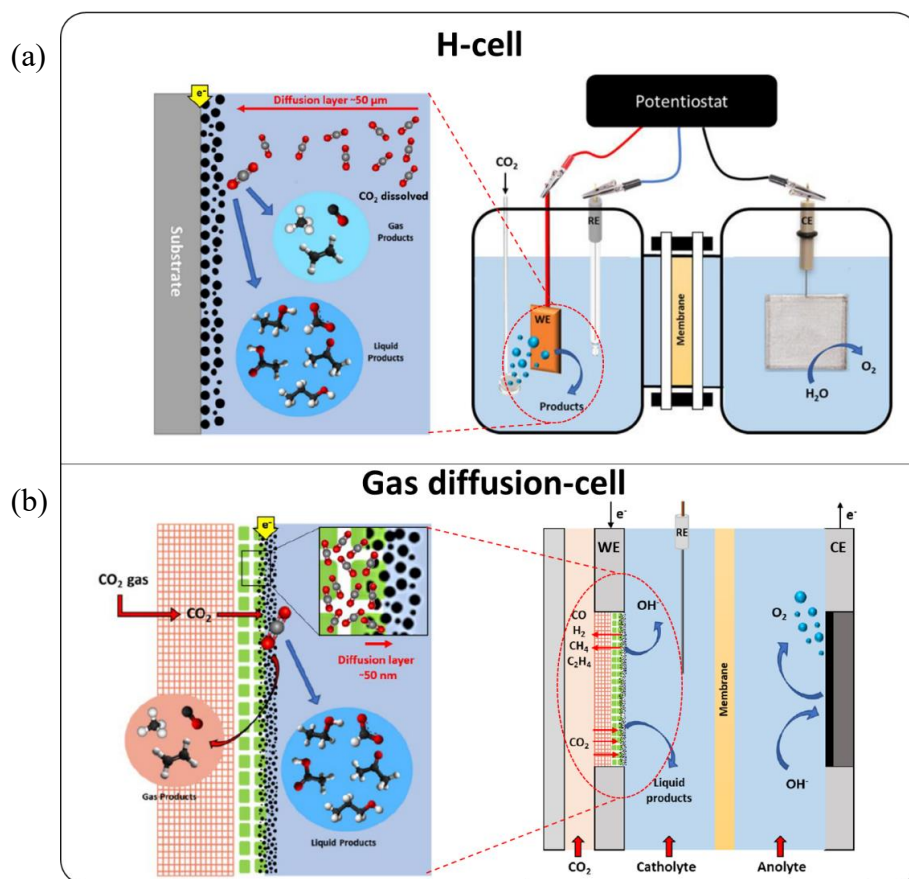


Figure 1. 22 (a) Schematics of traditional H-cell and (b) gas diffusion electrolyzer (WE, RE and CE correspond to the working electrode, reference electrode and counter electrode, respectively-Figures adapted from Hernandez-Aldave et al.).⁷⁴

Current GDE systems however exhibit some disadvantages, including electrolyte flooding and carbonate salt formation. These issues need to be solved by careful GDE engineering.⁶⁹

1.6 Objectives of this dissertation.

Compared to metal-based catalysts, heteroatom-doped carbon-based catalysts bring unique advantages to CO₂ electroreduction. However, their overall activity regarding selectivity, overpotential, and current density should be further improved. Also, the effect of support curvature and heteroatom dopants on the supported metal is not clearly understood. To develop better catalysis, therefore, a fundamental understanding of catalyst sites and reaction mechanisms should be investigated. In order to achieve activities and current densities relevant to industrial adoptions, an electrolysis reactor and electrodes need to be advanced.

Driven by the challenges and opportunities listed above, this dissertation includes research activities to advance the current state of CO₂ electroreduction catalysis. The second chapter explores the effect of nitrogen-doped ultrananocrystalline host structure on the product selectivity of CO₂ electroreduction.⁵ In this work, catalysts were prepared using a microwave-assisted CVD technique, and the electrode activity was investigated in a custom-made electrochemical cell. Furthermore, electrode microstructure analysis is performed using X-ray photoelectron spectroscopy (XPS), transmission electron spectroscopy (TEM), and scanning electron microscopy (SEM) techniques. For mechanistic understanding, theoretical models for active sites were developed, and reaction energies were evaluated using density functional theory (DFT) studies.

The third chapter investigates both N and S doped carbon nano onions (CNO) for the electrochemical CO₂ reduction. In this work, N, S, and NS co-doped CNO were prepared

via thermal treatment procedure. The onset potentials of catalysts were evaluated via a rotating ring disk electrode (RRDE), and electrolysis experiments were conducted using a custom-made electrochemical cell. The durability of the NS co-doped catalyst was evaluated on GDE, and catalytic performance was compared to other metal-free and metal-based electrocatalysts. To visualize the chemical structure of active sites, catalysts were analyzed by scanning transmission electron microscopy (STEM) technique.⁷⁷ Chemical information extracted from the STEM images and XPS/FTIR results provided chemical structures of active sites for theoretical modeling to gain a mechanistic understanding of activities and selectivities of heteroatom doped CNO.

The fourth chapter investigates the electronic effect of the catalyst support and discovers methods to improve the durability as well as the current density of GDE based electrodes for CO₂ electroreduction. Conventional GDE used in CO₂ electrolyzers has the limitation of insufficient CO₂ mass transfer due to water flooding during an elongated operation. To resolve these issues, conventional GDE was replaced by a customized GDE. This novel GDL was prepared by sputtering a thin layer of Cu on a polytetrafluoroethylene (PTFE) membrane. Then, the electronic properties of copper catalysts were further tuned by utilizing heteroatom doped CNO as catalyst support. For this purpose, the composites of Cu catalyst/CNO were deposited on the conductive GDE with an ionomer. The local catalytic environment was also simulated using macroscopic modeling via MATLAB programming. Finally, the role of heteroatoms in C₂ production activities/selectivity's of copper was further understood.

CHAPTER 2. UNDERSTANDING THE EFFECT OF HOST STRUCTURE OF NITROGEN DOPED ULTRANANOCRYSTALLINE DIAMOND ELECTRODE ON ELECTROCHEMICAL CARBON DIOXIDE REDUCTION

This chapter is adapted from the original publication of this work: Wanninayake, N.; Ai, Q.; Zhou, R.; Hoque, M. A.; Herrell, S.; Guzman, M. I.; Risko, C.; Kim, D. Y., Understanding the effect of host structure of nitrogen doped ultrananocrystalline diamond electrode on electrochemical carbon dioxide reduction. *Carbon* **2020**, *157*, 408-419.⁵ Reproduced with permission.

(In the following work, computational calculations were conducted by Qianxiang Ai under the guidance of Prof. Chad Risko; Gas chromatography analysis was conducted by Ariful Hoque under the guidance of Prof. Marcelo Guzman)

2.1 Introduction

The level of atmospheric carbon dioxide (CO₂) has dramatically increased since the industrial revolution, as the burning of fossil fuels has served as the primary energy source to spur this societal change.⁷⁸ Elevated atmospheric CO₂ concentrations are a major environmental concern due to the climate change associated with the greenhouse effect of CO₂.⁷⁹ Notably, the level of CO₂ in the atmosphere is predicted to increase from 400 ppmv (parts per million by volume) to 590 ppmv by the year 2100, potentially raising the average global temperature by 1.9 °C.⁴

Electrocatalytic reduction of CO₂ has emerged as a promising solution to CO₂ conversion because of its potential to readily convert CO₂ emitted from fossil fuel combustion into valuable fuels and chemicals with high efficiency while being powered by renewable energy sources.⁸⁰ As seawater is abundant and conductive, it has been suggested

that seawater is a desirable medium in which such an electrocatalytic conversion is carried out.⁶⁵ Hence, the development of electrocatalysts operating in such aqueous environments needs to consider several requirements: (i) high activity (cathodic current density ~ 1000 mA cm⁻²),⁸¹ (ii) high product selectivity by suppressing competing reactions such as hydrogen evolution reaction (HER) in aqueous electrolyte, (iii) excellent electrochemical stability during prolonged operation. However, no catalyst currently meets these stringent requirements for the electrocatalytic conversion of CO₂.^{65, 82}

Metal-based catalysts have been extensively studied for electrochemical conversion of CO₂, with copper (Cu) being one of the most studied metal catalysts for the CO₂ reduction reaction (CO₂RR). Although Cu shows attractive properties, such as CO₂ reduction products spanning hydrocarbons and alcohols, it suffers from poor selectivity and fast deactivation of catalytic activity.⁶⁵ Tin (Sn) shows excellent selectivity ($\sim 95\%$ Faradaic efficiency (FE)) towards CO₂RR for the formation of formate in 0.1 M Na₂SO₄ solution.⁸³ However, the performance of Sn-based electrodes rapidly decays during the first 30 minutes of operation.^{65, 81} Additionally, it has been a great challenge to suppress the involvement of HER in aqueous electrolyte and thereby to enhance the overall selectivity and FE for CO₂RR.⁸⁴

Therefore, the search for environmentally friendly, inexpensive, highly selective, and stable electrocatalysts for CO₂ conversion endures. Carbon-based nanostructures showcase promising features as electrocatalysts, including cost-effective synthesis, excellent electrochemical stability, and easy modification of the electrode surface.^{85, 86} Electrodes based on carbon nanomaterials have demonstrated high electrical conductivity, excellent mechanical strength, high surface area, and remarkable chemical and

electrochemical stabilities.⁸⁷ Although pristine carbon materials exhibit negligible activity, heteroatom-doped (including B, N, P, and S as potential dopants) carbon materials possess high catalytic activity, presumably due to asymmetric charge distributions along the electrode surface induced by dopants.^{46, 88, 89} These catalytic sites facilitate the adsorption of CO₂ and CO₂RR intermediates lowering the activation barriers.^{46, 87}

Recently, metal-free, nitrogen-doped carbon-based catalysts demonstrated promising features as alternative electrocatalysts for CO₂RR.^{87, 90} These materials can be categorized into graphitic carbon-based (*sp*²-carbon rich) or diamond-based (*sp*³-carbon rich) catalysts. In graphitic carbon structures, nitrogen in the carbon can be present as pyridinic, pyrrolic, graphitic, amine, nitro, or a mixture of these configurations. Various forms of nitrogen-doped *sp*²-carbon materials have been investigated, including nitrogen-doped carbon nanotubes,^{91, 92} nitrogen-doped graphene quantum dots,^{46, 55} and nitrogen-doped graphene foam.⁵⁴ Several experimental and theoretical studies suggest that pyridinic and graphitic nitrogen species are particularly active adsorption sites for CO₂RR.^{57, 58, 86} Most of these electrodes were reported to convert CO₂ to carbon monoxide (CO) over 80 % FE at low overpotential. In addition to *sp*²-carbon electrodes, nitrogen or boron-doped diamond has also been reported to demonstrate excellent catalytic performance.^{46, 47} For example, Natsui et al. reported the FE of 94.7 % for the production of formic acid with boron-doped diamond catalyst.⁹³ Liu et al. reported the catalytic performance of a nitrogen doped diamond array built on the Si array that shows the conversion of CO₂ to acetate with a 90% FE.⁴⁶ Furthermore, Liu et al. recently demonstrated both nitrogen and boron co-doped diamond catalyst generates ethanol with a 92% FE.⁴⁷ Despite of remarkable performance of heteroatom-doped diamond electrocatalysts, the origin of the catalytic

activity is unclear. Also, the nature of nitrogen dopants incorporated in sp^3 -bonded carbon is not thoroughly understood.^{46, 47}

In the present study, we conducted in-depth and systematic investigations of carbon-based materials for their CO₂RR activities. To determine the roles of nitrogen dopants and the host structure in catalytic performance, nitrogen dopants were incorporated in either grain boundaries of ultrananocrystalline diamond (UNCD) or the graphitic carbon network. This synthetic process was controlled by varying the composition of CH₄ and Ar gases in the source gas mixture during microwave-assisted chemical vapor deposition (MACVD) growth. The morphology, microstructure, and chemical states of nitrogen-doped electrocatalysts were characterized by scanning electron microscopy (SEM), transmission electron microscopy (TEM), Raman spectroscopy, and X-ray photoelectron spectroscopy (XPS). Electrochemical tests and DFT calculations were performed to evaluate catalytic performance and to track the possible catalytic pathways, respectively.

Our results indicate that both the chemical states of nitrogen dopant and the carbon host structure play important roles in determining the electrocatalytic performance of the nitrogen-doped carbon electrode. Based on our experimental and computational results, we conclude that the catalytic role of nitrogen is significantly enhanced when nitrogen atoms are incorporated in the graphitic carbon host as compared to being doped in the diamond-rich carbon. These findings provide new insights into understanding the electrocatalytic activity of graphitic and diamond hybrid electrodes toward CO₂RR.

2.2 Experimental

2.2.1 Microwave Assisted Chemical Vapor Deposition (MACVD) of Carbon Thin Films

Carbon thin films were deposited on boron-doped, p-type conductive (0.001-0.005 Ω .cm) Si wafers <100> by MACVD using a reactor system (Seki Diamond Systems, AX5010, 2.45 GHz) as described previously.^{94,95} Before deposition, the Si substrates were first ultrasonically cleaned with acetone, methanol, piranha solution, and then deionized (DI) water. Then, the Si substrate was pretreated by ultrasonication with nanodiamond powder suspension (Dynamene NB50) to increase the number of nucleation sites. Excessive diamond powders were removed by rinsing with DI water. Next, the Si substrate was placed on a stage in the reaction chamber, and the chamber was evacuated to a base pressure of 60 mTorr by a mechanical pump (PASCAL, 2021 SD; Adixen). Subsequently, the microwave plasma was ignited under the flow of high purity (Scott-Gross, 99.999%) Ar, CH₄, and N₂ source gases. The plasma was adjusted 1 mm above the Si substrate while maintaining a chamber pressure of 100 Torr. For each deposition, flow rates of the reaction gases were controlled by mass flow controllers (MKS). Four nitrogen-doped carbon thin films and four undoped carbon thin films were prepared to determine their electrocatalytic performances. Table 2.1 summarizes the experimental parameters, including microwave power, chamber pressure, and growth time, and source gas compositions for the growth of each film.

Table 2. 1 Experimental parameters used for the MACVD of 8 carbon thin films

Sample	Ar ^a	CH ₄ ^a	N ₂ ^a	Power (W)	Pressure (Torr)	Time (min)
NDC-1	79	1	20	1000	100	70
NDC-2	78	2	20	1000	100	65
NDC-3	77	3	20	1000	100	60
NDC-4	76	4	20	1000	100	60
UDC-1	99	1	0	1000	100	90
UDC-2	98	2	0	1000	100	80
UDC-3	97	3	0	1000	100	70
UDC-4	96	4	0	1000	100	65

^a Gas flow rate in sccm

2.2.2 Electrode Preparation

After CVD growth, each carbon film on the Si substrate was cut into a 2 cm × 1 cm size using a LatticeScriber. In each film, a corner was gently scratched, and a drop of indium metal was applied to make electrical contact with a Cu wire. The contact was secured by applying the conductive silver epoxy resin, and subsequently an epoxy adhesive to isolate the electrical contacts and back of the electrode from the electrolyte. The surface area of the electrode exposed to electrolyte was estimated by the *ImageJ 1.51J8* software.

2.2.3 Material Characterization

The morphology, microstructure, and phase of the carbon films were characterized by scanning electron microscopy (SEM) equipped with a focused ion beam (FIB, Helios Nanolab 660, FEI). For SEM characterization, a sample was cut into 0.5 cm x 0.5 cm square and mounted on a stage using conductive carbon tape. FIB was used to slice off a film for

its cross-sectional view, and transmission electron microscopy (TEM) (FEI Talos F200X) was used to obtain high-resolution images. Raman spectra were obtained with a DXR micro-Raman instrument (Thermo Scientific). A diode-pumped Nd:YVO₄ laser was used as an excitation source (532 nm excitation) for Raman characterization. Elemental compositions and the chemical states of elements present in each carbon film were analyzed by X-ray photoelectron spectroscopy (XPS) using a Thermo Scientific K-Alpha photoelectron spectrometer. Before analyses, samples were cleaned with ethanol and dried under vacuum for 24 hours. XPS measurements were performed by focusing on monochromatic Al K- α radiation (energy of 1486.6 eV) onto a sample. The focused spot diameter was 400 μm .

2.2.4 Electrochemical Cell Configuration

Electrochemical characterizations were conducted with a customized electrochemical cell with 3 electrodes (Figure S2.1). The electrochemical cell was separated into two compartments, where the working electrode (WE) was immersed in one compartment, and the counter electrode (CE) in the other (about 10 cm apart). A platinum foil was used for CE and was placed parallel to the WE to achieve a uniform voltage around the WE. In each experiment, a carbon thin film prepared by CVD was used as the WE, and an Ag/AgCl electrode (CH Instruments) was used as the reference electrode (RE). The distance between the WE and RE was about 6 mm. A Luggin capillary (1.5 mm diameter) was used to reduce the electrical resistance between WE and RE, and to obtain a precise sensing point. The capillary tip was designed to face the WE and placed about 3 mm away from the WE to avoid any shielding errors. To block the re-oxidation of liquid products

formed at WE, a Selemion anion exchange membrane (AGC Inc.) was installed between two compartments. Both compartments were filled with 10 mL of 0.1 M KHCO₃ solution (Aldrich, BioUltra, ≥ 99.5 %). When filled with electrolyte, each compartment had a gas headspace volume of about 4 mL. Before electrolysis, the electrolyte in each compartment was purged with CO₂ (Scott-Gross, 4.8 research grade, 99.998% purity) gas at 20 sccm (MKS-GE50A mass flow controller) for 30 minutes. The pH of the electrolyte was equilibrated to 6.80. Each electrolysis was performed under the continuous flow of CO₂. All recorded currents were normalized by the electrochemical surface area of each electrode.

2.2.5 Electrolysis

Electrochemical experiments were conducted with a CHI 660D potentiostat (CH Instruments). Electrochemical data recorded with respect to Ag/AgCl RE were converted to a reversible hydrogen electrode (RHE) scale using the following formula:

$$V_{(85\% \text{ IR corrected}) \text{ vs } (RHE)} = V_{\text{measured } (85\% \text{ IR corrected}) \text{ vs. } (Ag/AgCl)} + 0.222 + 0.059 \times 6.80_{(pH \text{ electrolyte})}$$

An error in the potential originates from a solution resistance/uncompensated resistance (Ru), and it was corrected by the potentiostat's IR compensation function. Although it is possible to compensate for the entire resistance, 100 % IR compensation leads to an oscillation of the potentiostat.^{65, 96} Therefore, 85% of the Ru was compensated by the potentiostat and the rest of 15% was manually corrected using the following formula after data collection.

$$V_{(100\% \text{ IR corrected}) \text{ vs } (RHE)} = V_{(85\% \text{ IR corrected}) \text{ vs } (RHE)} - 15\% \times Ru \text{ (Ohms)} \times I_{\text{Average}}$$

Each electrolysis was performed by applying a constant potential to WE, while an amperometric *i-t* curve is recorded for 60 minutes.

2.2.6 Product Analysis

During electrolysis, gas samples were intermittently collected to analyze gaseous products. Gaseous products were collected into gas sampling bags (NDEV83Z- Dalian Hede Technology Co., Ltd). The quantification of gaseous products was performed by gas chromatography (GC, SRI 8610C) with two columns (a silica gel HaySep D as column 1 and a Mole-Sieve 13X as column 2), a thermal conductivity detector (TCD), and a flame ionization (FID) detector interfaced to a methanizer as described previously.⁹⁷ Gas samples (1 mL) were withdrawn through a septum from the gas sampling bag immediately before injection into the GC. The FID detector was used for the analyses of CO, CO₂, and CH₄ using N₂ (Scott-Gross, UHP) as the carrier gas (flow rate = 20 mL min⁻¹), and supplying H₂ gas (Scott-Gross, UHP) to FID/methanizer at a flow rate of 25 mL min⁻¹. The analysis of H₂ used a TCD detector. The oven temperature was maintained at 40 °C for 10 min and then increased to 200 °C using a ramp of 20 °C min⁻¹. After the completion of electrolysis, the resultant solution was analyzed by NMR (400 MHz Bruker Avance NEO) to identify liquid products. After each electrolysis, a sample for NMR analysis was prepared by mixing 700 µl electrolyte solution with 100 µl D₂O, 10 µl of 7 mM GdCl₃, and 10 µl of 8.4 mM dimethyl sulfoxide (DMSO) as well as 20 µl of 8.4 mM phenol as internal standards. Water peak was suppressed to increase the visibility of NMR signals.

2.3 Results and discussion

2.3.1 Control of Carbon Phase and Microstructure in Carbon Thin Films by MACVD

It is hypothesized that the carbon electrode host structure has a significant impact on the overall catalytic activity for the electrochemical reduction of CO₂. To explore this hypothesis, we attempted to control the phase and microstructure of the carbon electrode by employing MACVD. More specifically, we aimed to control the ratio of *sp*²-carbon (graphitic) phase to *sp*³-carbon (diamond-like) phase by varying the concentration of CH₄ gas in the source gas mixture (Ar, CH₄, and N₂). It is well established that reactive species formed in the plasma chamber under the flow of CH₄ gas are sensitive to the concentration of CH₄ gas.⁹⁸ High CH₄ concentrations yield C₂ radicals and preferentially form graphitic carbon phases, while for low CH₄ concentrations, the formation of C₂ radicals is suppressed, and the formation of CH₃ radicals is enhanced, allowing the concentrated CH₃ radicals in the reactor to promote the growth of *sp*³-bonded diamond phase.^{99,100} A delicate balance between CH₃ and C₂ radicals in the plasma, hence, determines the phase and microstructure of the carbon electrode.

To investigate how the combination of varied carbon host structure and the presence/absence of nitrogen dopants determine catalytic activity for electrochemical CO₂ reduction, eight carbon films were prepared by varying the concentrations of Ar, CH₄, and N₂ gases. The grown carbon thin films were labeled as NDC-1, NDC-2, NDC-3, NDC-4, UDC-1, UDC-2, UDC-3, and UDC-4, where NDC represents nitrogen-doped carbon films, and UDC represents undoped carbon films. For NDC-X and UDC-X, the X denotes the flow rate (in sccm) of the CH₄ source gas. Detailed growth parameters for the growth of the four-carbon films including the flow rates of source gases (Ar, CH₄, and N₂) are

presented in Table 2.1. It is well established that reaction gas mixtures dominated by argon gas result in the growth of ultra-nanocrystalline diamond (UNCD) films.^{101, 102}

2.3.2 Characterization of Nitrogen-doped Carbon Films

SEM and TEM images of NDC-1, NDC-2, NDC-3, and NDC-4 are shown in Figure 2.1. SEM and TEM images of UDC-1, UDC-2, UDC-3, and UDC-4 are shown in Figure S2.2. Visual inspection of the SEM and TEM images clearly indicate that the morphology of carbon films is strongly affected by both the nitrogen dopant and the varied concentration of CH₄ used in the reactions. As shown in Figure 2.1 and S2.2, 3-4% CH₄ (NDC-3, NDC-4, UDC-3, and UDC-4) results in multilayer graphitic (MLG) carbon films formed around the acicular UNCD grains, while 1-2 % CH₄ (NDC-1, NDC-2, UDC-1, and UDC-2) leads to the preferential formation of granular UNCD structures.¹⁰¹ During these reactions, the plasma temperature is elevated with increasing concentrations of CH₄ gas,¹⁰³ with higher chamber temperatures inducing graphitization, as observed for NDC-3, NDC-4, UDC-3, and UDC-4.¹⁰⁴ The presence of N₂ can further promote the formation of C₂ through CN by the dissociation of CH₄.¹⁰⁵ Thus, NDC-X films have a higher growth rate than UDC-X films. To obtain catalyst films with a similar thickness, the growth duration of each film was adjusted as shown in Table 2.1. Figure S2.3 represents the cross-sectional SEM image of each electrode. Overall, the films grown by MACVD are highly reproducible.

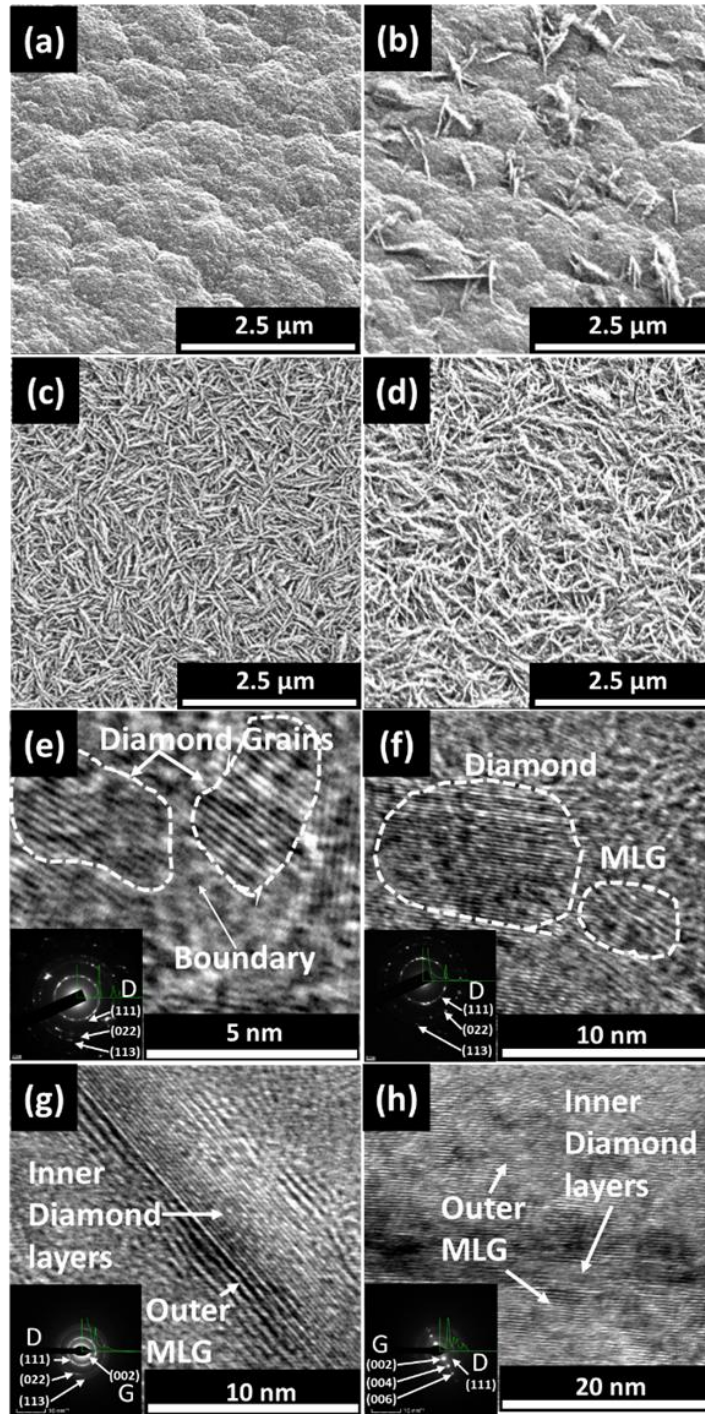


Figure 2. 1 Representative SEM images of (a) NDC-1, (b) NDC-2, (c) NDC-3, (d) NDC-4, and high resolution TEM images of (e) NDC-1, (f) NDC-2, (g) NDC-3, (h) NDC-4 films. Insets in the bottom-left corner of each TEM image represents SAED patterns. Diamond related indexes are denoted with a (D), and Graphite related indexes are denoted with a (G).

The nitrogen dopants also significantly influence the film surface morphologies. At high temperatures, the addition of nitrogen yields the formation of needle-like sp^2 -carbon structures, which is in agreement with the surface morphology of NDC-3 and NDC-4 found in this study.¹⁰⁶ In contrast, a granular morphology is found for NDC-1 and NDC-2 due to smaller amounts of sp^2 carbon. UDC-3 and UDC-4 also show asymmetric features (Figure S2.2 (c), (d)), but these surface features are not as pronounced as in NDC-3 and NDC-4 due to the absence of nitrogen.

Figure 2.1(e) shows that the average size of grains in the NDC-1 sample is ~5 nm and the size of grain boundaries is ~2-3 nm. Grains in this film consist of sp^3 bonded carbon, whereas the grain boundaries mainly contain amorphous sp^2 bonded carbon. It was reported that the electrical conductivity of NDC-1 mainly originated from these interconnected grain boundaries.¹⁰¹ Based on the results of previous molecular dynamic simulations, nitrogen incorporation at grain boundaries is thermodynamically more favored than its incorporation in the grains,^{99, 101} since the energy of nitrogen-doped grain boundaries is 3 to 5 eV lower than that of the nitrogen atom in the grains.¹⁰⁷ Compared to NDC-1, NDC-2 contained larger diamond grains, which are due to the increasing CH_4 concentration. The diamond grain size in NDC-2 is about 10 nm. Further increase in CH_4 concentration grows the diamond phase along any particular direction anisotropically.¹⁰⁸

As shown in Figure 2.1(c) and 2.1(d), both NDC-3 and NDC-4 exhibit a needle-like morphology, which contains acicular diamond grains embedded in multilayer graphitic carbon. The lattice spacing of the outer layers is close to that of graphite, indicating the presence of sp^2 carbon layers.¹⁰⁹ The main differences between NDC-3 and NDC-4 are the needle length and the number of MLG layers. The needles in NDC-4 are longer and contain

more MLG layers than those in NDC-3, reflecting that NDC-4 is more graphitic than NDC-3. It is noteworthy that Figure 2.1(g) and 2.1(h) clearly present outer MLG layers surrounding inner diamond layers. Selected area electron diffraction (SEAD) patterns obtained for NDC-X (insets of Figure 2.1(e)-(h)) demonstrate strong reflections of the cubic diamond (111) plane, indicating all structures contain the cubic diamond phase. The SAED patterns also reveal that NDC-3 and NDC-4 structures contain reflections from the hexagonal graphite phase. The full analysis of SAED patterns is given in Figure S2.4. These SAED reflections are evaluated by CrystBox software to confirm the corresponding crystalline phase.¹¹⁰

Figure S2.5 represents Raman spectra for (a) NDC-X and (b) UDC-X. All spectra consist of three main bands centered at 1134-1137 cm^{-1} , 1324-1352 cm^{-1} , and 1535-1600 cm^{-1} . These three bands are assigned to the *trans*-polyacetylene (TPA) band, D-band, and G-band, respectively. A Raman signal from the sp^3 carbon phase is obscured due to its low Raman cross-section (about 50-250 times lower than sp^2 carbon phase).^{111, 112} TPA segments are lying in the grain boundaries of UNCD.¹¹¹ It is evident that the intensity of TPA band decreases from NDC-1 to NDC-4 and from UDC-1 to UDC-4. This observation suggests that at high temperatures, the TPA phase is converted to the graphite phase. The G-band originates from stretching vibration between any pair of sp^2 carbon atoms while the D-band is a defect activated band.¹¹³ Any defect that breaks the symmetry of the graphite (such as sp^3 defects, vacancy sites, grain boundaries, and substitutional atoms) increases the intensity of D-band.¹¹⁴ It is notable that the G-band position in NDC-3, NDC-4, and UDC-3 and UDC-4 shifts toward higher wavenumber due to the graphitic carbon layers. Furthermore, the G-band intensity of NDC-4 is higher than that of D-band,

indicating that NDC-4 has a highly ordered MLG phase. This graphitic structure is further confirmed by the appearance of the 2D band at 2700 cm^{-1} .¹⁰³

Since Raman spectra cannot differentiate sp^2 and sp^3 phases, X-ray photoelectron spectroscopy (XPS) is employed to probe elemental compositions and the chemical states of all carbon film electrodes (Figure 2.2, and S2.6). XPS survey spectra, shown in Figure S2.6(a) and S2.6(b), indicate that all samples are free of impurities and contain only carbon, nitrogen, and oxygen. The atomic percentages of each element reported in Table 2.2 represent the average of three different measurements performed on the same film. In this study, the same concentration of N_2 source gas (20 %) is employed during the growth of the NDC-X samples. As a result, the NDC-X samples contain similar levels of nitrogen: 1.46, 1.40, 1.50, and 1.49 atomic % for NDC-1, NDC-2, NDC-3, and NDC-4, respectively (Table 2.2). The XPS spectra reveal the presence of oxygen in all samples, which may be introduced from the ambient environment during sample handling.⁹⁸ The high-resolution XPS C1s spectrum for each sample (Figure 2.2(a)) was deconvoluted into peaks centered around 284.45 eV,¹¹⁵⁻¹¹⁷ 285.00 eV,^{115, 116, 118, 119} 285.80 eV,^{120, 121} and 286.70 eV,^{120, 121} which correspond to the chemical states of C- sp^2 , C- sp^3 , C-N, and C-O, respectively. In order to quantify the sp^2 -C/ sp^3 -C ratio of each sample, peaks are deconvoluted by maintaining a FWHM value of 1.00 ± 0.05 eV. Based on the integrated area of each peak after deconvolution (Figure 2.2(a)), for NDC-X, the percentage of sp^2 carbon is 26.4%,¹²² 43.0%, 56.7% and 80.0% for NDC-1, NDC-2, NDC-3 and NDC-4, respectively; for UDC-X, the percentage of sp^2 carbon is 29.5%, 45.7%, 80.9% and 86.3% for UDC-1, UDC-2, UDC-3 and UDC-4, respectively (Table 2.2). These results reveal that the increased concentration of CH_4 source gas shifts the growth from diamond-like to graphitic structure.

For all NDC-X samples, observed XPS high-resolution N1s spectra were resembled to each other (Figure 2.2(b)). It is important to note that nitrogen configurations in NDC-1 at grain boundaries are different from nitrogen associated with MLG layers in NDC-4. However, due to the presence of a variety of nitrogen configurations and the limitation of the XPS measurement, these distinct configurations remain unresolved.¹²³ Therefore, N1s spectra of NDC-X were deconvoluted into three sub-peaks centered at 398.80 eV (N1), 399.90 eV (N2), and 401.60 eV (N3). Based upon the results obtained from TEM and Raman analyses in this study as well as the similar studies reported in the literature, we assigned the nitrogen chemical states for NDC-1 and NDC-4 as follows. For grain boundary nitrogen in NDC-1, N1, N2, and N3 were assigned to polyacetylene (C=N-C),^{104, 124} amine (NR₃),^{107, 125, 126} and protonated amine (NHR₃⁺)^{107, 127} configurations, respectively. For NDC-4, N1, N2, and N3 were assigned to pyridinic,^{128, 129} pyrrolic,^{128, 130} and graphitic^{128, 131} configurations, respectively. Based on this analysis, the majority of the nitrogen in NDC-1 (~70%) exists as polyacetylene type C=N-C in grain boundaries, whereas pyridinic nitrogen (~76%) is dominant in MLG layers of NDC-4. Since both NDC-2 and NDC-3 have mixed characteristics of *sp*² and *sp*³, it is assumed that NDC-2 contains more polyacetylene (C=N-C), and NDC-3 contains more pyridinic type nitrogen configurations. However, due to the mixed characteristics of *sp*²/*sp*³, it is difficult to assign nitrogen configurations for NDC-2 and NDC-3 quantitatively.

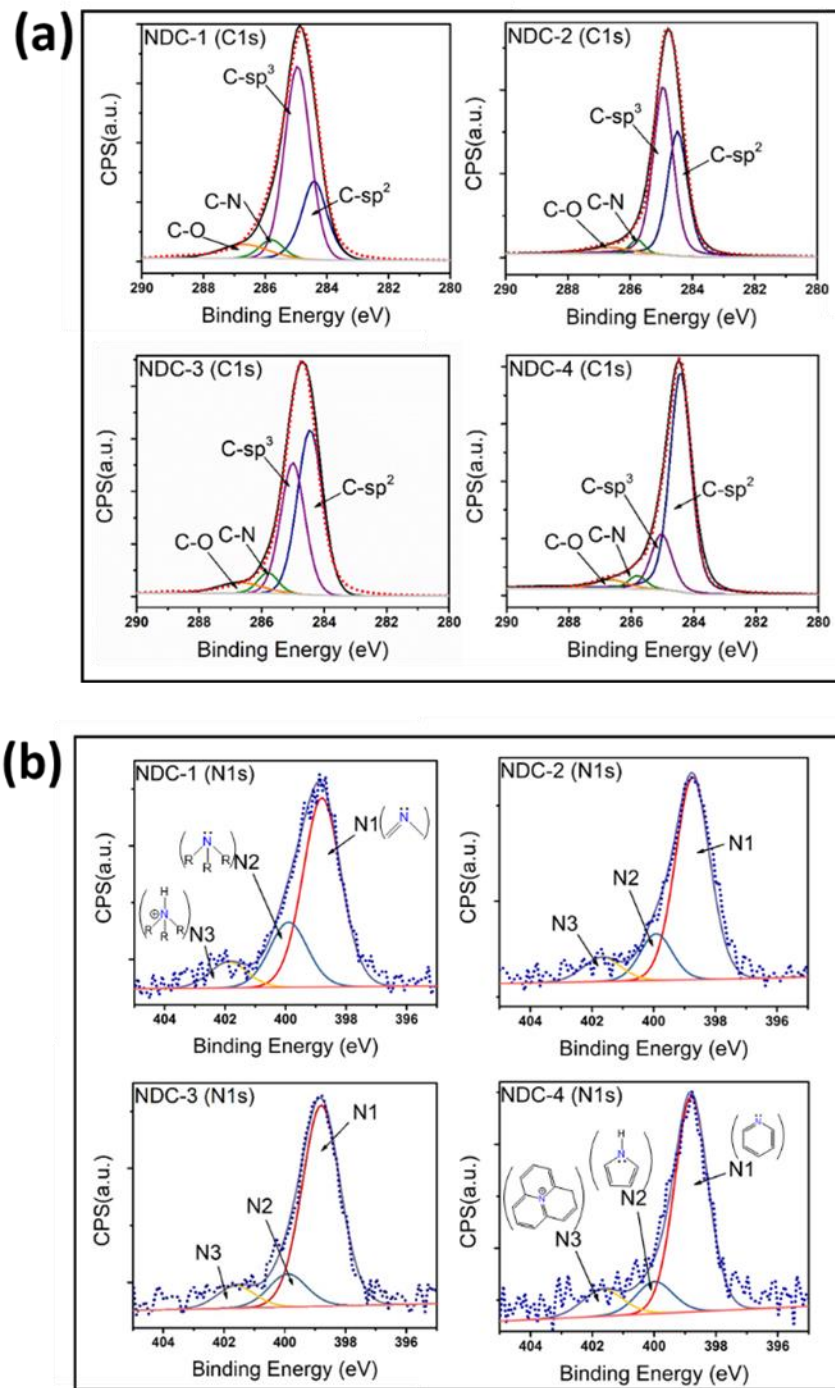


Figure 2. 2 XPS analyses of samples: (a) high-resolution C1s spectra and (b) high-resolution N1s spectra.

Table 2. 2 The summary of elemental composition and chemical states in each electrode

Sample	C1s ^a	C-sp ² ^b	C-sp ³ ^b	C-N ^b	C-O ^b	$\left(\frac{sp^2 \times 100\%}{sp^3 + sp^2}\right)^c$	N1s ^a	N1 ^b	N2 ^b	N3 ^b	O1s ^a
NDC-1	94.09 ± 0.85	23	64	5	8	26.4	1.46 ± 0.08	70	20	10	4.45 ± 0.15
NDC-2	95.87 ± 0.60	40	53	3	4	43.0	1.40 ± 0.09	74	15	11	2.73 ± 0.41
NDC-3	94.89 ± 0.75	51	39	5	6	56.7	1.50 ± 0.05	78	13	9	3.61 ± 0.25
NDC-4	94.96 ± 0.50	72	18	4	6	80.0	1.49 ± 0.06	76	12	12	3.55 ± 0.39
UDC-1	96.60 ± 0.92	28	67	-	5	29.5	0	-	-	-	3.40 ± 0.18
UDC-2	95.20 ± 0.81	42	50	-	8	45.7	0	-	-	-	4.80 ± 0.34
UDC-3	95.89 ± 0.23	76	18	-	5	80.9	0	-	-	-	4.11 ± 0.07
UDC-4	96.72 ± 0.45	82	13	-	5	86.3	0	-	-	-	3.28 ± 0.62

^a Atomic percentages.

^b Percentages based on the deconvoluted peak area.

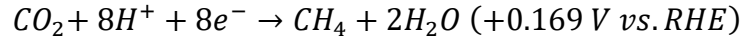
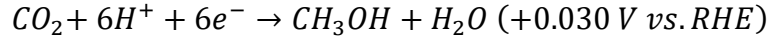
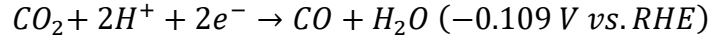
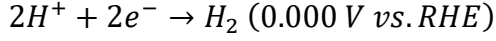
^c sp² carbon percentage out of total sp² and sp³ carbon content

2.3.3 Electrochemical Reduction of CO₂

The electrochemical behavior of each carbon film toward CO₂RR was examined in a two-compartment, three-electrode electrochemical cell. The schematic presentation of the electrochemical cell is shown in Figure S2.1. Prior to the electrochemical measurement

for CO₂RR, the electrochemical surface area (ECSA) of each electrode was determined by non-Faradaic capacitive current associated with the double layer charging in 0.1 M KOH solution. (Refer section 2.5.2 and Figure S7 for more details regarding the calculation). It is noted that the ECSA of all samples is larger than that of the geometric area, which is due to the surface roughness of each catalyst. Furthermore, NDC-X and UDC-X samples containing a similar percentage of *sp*² carbon showed similar ECSA. The ratios of ECSA/geometric area for NDC-1, NDC-2, NDC-3, and NDC-4 are 1.58, 1.78, 1.99, and 2.06, respectively. The ratios for UDC-1, UDC-2, UDC-3 and UDC-4 are 1.42, 1.75, 1.91 and 2.11, respectively. All current densities ($J_{\text{ECSA(DL)}}$) reported in this work are normalized by ECSA.

Figure 2.3(a) and 2.3(b) show linear sweep voltammograms (LSVs) recorded for NDC-X and UDC-X in the solution saturated with CO₂. The potential range was from 0.00 V to -1.70 V vs. RHE, and the potential sweep rate was 50 mV s⁻¹. In the LSV curves (Figure 2.3), the NDC-X samples have higher current densities than the UDC-X samples, indicating the critical role of nitrogen in CO₂RR. It is also noted that increasing the *sp*² carbon content of both NDC-X and UDC-X shift the onset potential to the positive direction. Onset potentials for the reduction currents found in NDC-1, NDC-2, NDC-3 and NDC-4 are -0.8 V, -0.7 V, -0.6 V, and -0.5 V vs. RHE, respectively. The onset of the reduction current noted in UDC-1, UDC-2, UDC-3, and UDC-4 are -1.1V, -0.9V, -0.8V, and -0.6V vs. RHE, respectively. When CO₂RR is performed in the aqueous electrolyte solution, the following reactions may take place.¹³²



Based on these reactions, the common CO₂ reduction routes always compete with HER. Therefore, the current observed in LSV is a combination of HER and CO₂RR. The LSV curves further suggest that increasing the *sp*² content of the catalyst catalyzes both CO₂RR and HER.

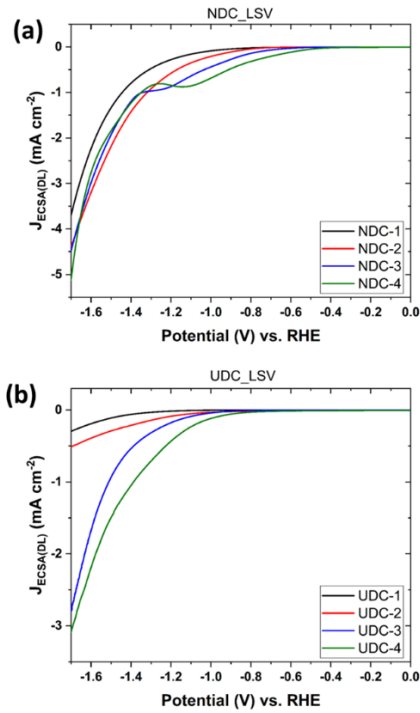


Figure 2. 3 Linear sweep voltammetric (LSV) curves recorded for (a) NDC-X and (b) UDC-X. The LSV curves were recorded after the 0.1 M KHCO₃ electrolyte solution was saturated with CO₂.

Among the electrodes studied, NDC-4 exhibits the highest current density and has the lowest overpotential, reflecting that its high activity may come from the pyridinic type nitrogen in MLG structure. In Figure 2.3, the LSV curves of both NDC-3 and NDC-4 have a hump in the potential range from -1.3 V to -0.4 V, which comes from the contribution of CO₂RR. NDC-3 has a cathodic peak at -1.3 V, and NDC-4 has a cathodic peak at -1.1 V. The positive shift of a cathodic peak in NDC-4 also indicates its highest electrocatalytic activity for CO₂RR. This observation is consistent with the plot of a product selectivity vs. potential shown in Figure 4. NDC-1 and NDC-2 electrodes show larger overpotential and lower current density, indicating their sluggish kinetics for CO₂RR.

Since the cathodic current has contributions from both HER and CO₂RR, the reaction products and the selectivity of each product cannot be determined solely by electrochemical measurements, but by combining electrochemical characterization with a product quantification. The product quantification was done by GC, and NMR.⁹¹ Figure S2.8 illustrates a current density–time ($i - t$) profile recorded for each electrode during electrolysis while the potential was held at -1.10 V vs. RHE for each film. For most samples and applied potentials, the current densities remain constant over the course of electrolysis. As shown in Figure S2.8, the current densities of NDC-4 are significantly larger than that of NDC-1, reflecting the promoted activity of NDC-4 toward CO₂RR. At -1.10 V, the maximal current of NDC-4 is about 6x larger than that of NDC-1 (0.14 mA/cm² for NDC-1 and 0.83 mA/cm² for NDC-4). During electrolysis, gaseous products were intermittently collected and analyzed by GC. The NDC-X electrodes primarily generate CO and H₂ but also produce a small amount of HCOOH, CH₄, and CH₃OH as minor products. In contrast, the UDC-X electrodes primarily generate H₂, reflecting the key role of nitrogen dopants in

activating the CO₂ reduction pathway. Except for UDC-1, all UDC-X electrodes formed a small quantity of CO, which may originate from defect sites present.¹³³

The Faradaic efficiency (FE) for the generation of each gaseous product was determined by the ratio of total electrons required to form the quantity of the product (from GC analysis) over the number of total electrons consumed at the electrolysis (from the chronoamperometric current - see the section 2.5.3 for more information). The FEs of products determined for NDC-X samples as a function of applied potential are plotted in Figure 2.4. The FEs for UDC-X samples are shown in Figure S2.9. Ideally, the sum of FEs at the given potential should be 100%, though ohmic losses between anode and cathode often yield FE less than 100%.¹³⁴

As shown in Figure 4(a), NDC-1 predominantly generates H₂ (In the potential range from -0.9 V to -1.8 V). The FE for the conversion of CO₂ to CO in NDC-1 is less than 10%. Overall, NDC-1 shows a poor selectivity for the generation of CO. In NDC-4 (Figure 2.4(d)), the FEs for CO rapidly increases, with the maximal FE of around 82% at -1.10 V vs. RHE. This observation demonstrates that the NDC-4 electrode is more catalytically active and selective for the generation of CO than NDC-1. The comparison between NDC-1 and NDC-4 clearly demonstrates that nitrogen dopants are much more catalytic when they are incorporated in the sp²-bonded MLG carbon network rather than grain boundaries in UNCD. It is also noted that the activity of NDC-3 is greater than that of NDC-2. Overall, the results imply that the effectiveness of nitrogen dopants for enhancing CO₂RR is enhanced with the increasing content of sp²- carbon.

When a more negative potential is applied to both NDC-3 and NDC-4, the FE of CO is suppressed, and H₂ evolution regains dominance. This is due to the mass transfer

limitation of CO₂ at high overpotential and depleted concentration of CO₂ at the electrode-electrolyte interface.¹³⁵ It is known that a quiescent cell usually suffers from mass transport limitations.⁶⁵ Therefore, it is crucial to design an electrochemical cell that can support the sufficient flux of CO₂ toward the electrode surface even at high reduction rates.

All UDC-X electrodes predominantly generate H₂, reflecting the critical role of nitrogen in activating CO₂RR in this series of carbon-based catalysts. An onset potential for HER in UDC-1 is about 0.4 V more negative than UDC-4. This is in good agreement with previous reports that graphitic carbon-rich electrodes catalyze HER.¹³⁶

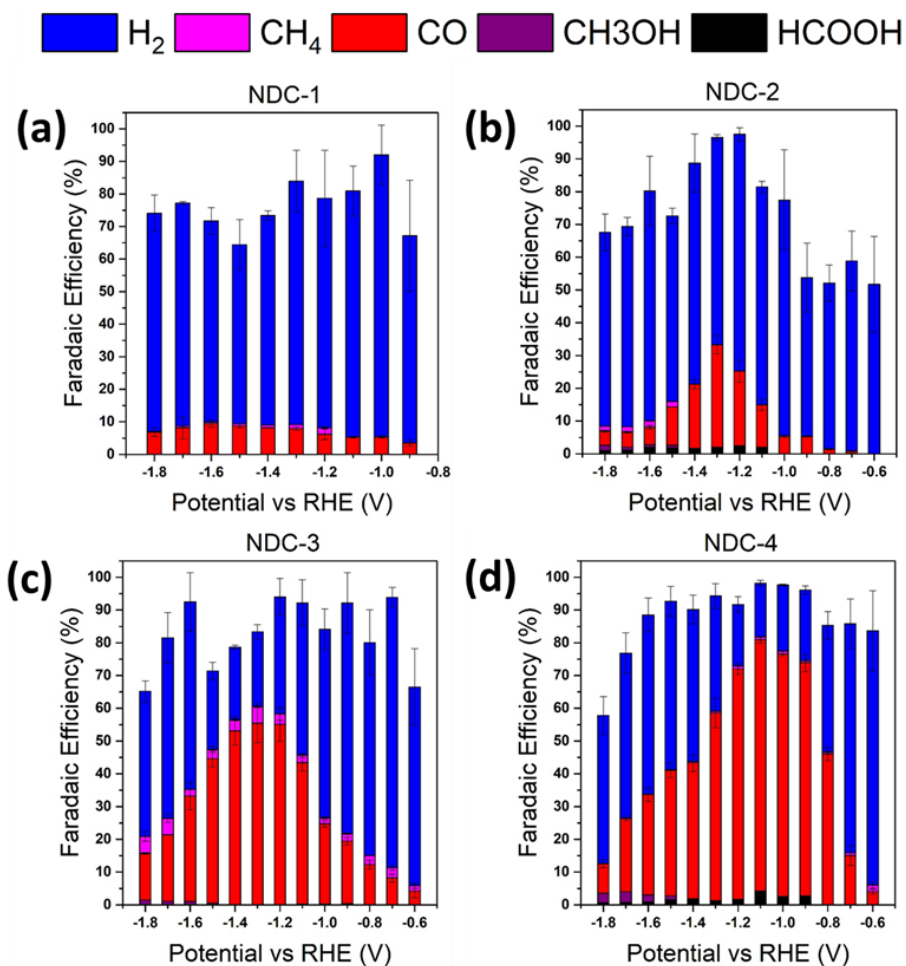


Figure 2. 4 Faradaic efficiency of each product as a function of potential (a) NDC-1, (b) NDC-2, (c) NDC-3, and (d) NDC-4.

2.3.4 CO₂ Catalysis Models

DFT calculations were carried out to better understand the distinctive phenomena of the nitrogen dopants in sp^3 -carbon and sp^2 -carbon environments at the atomic level. Two possible pathways for the electrochemical reduction of CO₂ into CO are shown in Figure S2.10.⁹¹ In the first pathway, CO₂ proceeds to form a surface-adsorbed *COOH by concerted electron transfer and protonation, with the electrolyte presumed to provide the source of protons. In the second pathway, *COOH is formed sequentially, with surface adsorption of *COO followed by protonation. Regardless of the mechanism, surface-adsorbed *COOH formation is often considered as the rate-limiting step.^{137, 138} For both pathways, the adsorbed *COOH then takes another electron and proton to eventually release CO and H₂O. For high activity and selectivity toward the production of CO, the intermediate *COOH should be strongly adsorbed on the catalytic surface, and *CO should be weakly bound to the same active site.⁹¹ If the binding energy of the intermediates is too strong, substrate access to the catalytic surface sites will be blocked by the pre-adsorbed intermediates, and the catalytic activity will be deteriorated (i.e., the catalyst is said to be “poisoned”); if the binding is too weak, the substrates will desorb from the catalyst surface without further reaction. Such a situation is often referred to as the Goldilocks principle.

To account for the difference between NDC-1 and NDC-4 in terms of their catalytic activities, DFT calculations (full details of which are provided in the section 2.5.4) were performed starting with the intermediates *COOH or *CO adsorbed on various active sites.^{56, 91, 92} Model structures used to simulate NDC-1 were built from the diamond (111) surface using Pandey’s reconstruction (denoted as “P”), which structure correctly describes the sp^2 bonding behavior of the silicon (111) and diamond (111) surfaces; in this work, the

model is adapted for nitrogen-doped TPA chains in grain boundaries.¹³⁹ A multi-layered graphite (denoted as the “G” structure) configuration is used as a model for the NDC-4, as shown in Figure S2.11. Detailed surface structures used in the simulations are shown in Figure 2.5. Free energy diagrams for CO formation using the models are shown in Figure 2.6(a), from which the onset potential can be estimated as $\max(\Delta G_{0 \rightarrow 1}/e, \Delta G_{1 \rightarrow 2}/2e)$ where e is the elementary charge. It is noteworthy that the free energy change of an elementary reaction in Figure 2.6(a) only presents the lower limit of its activation energy. The free energy diagram here contains no information regarding reaction kinetics or transition states.

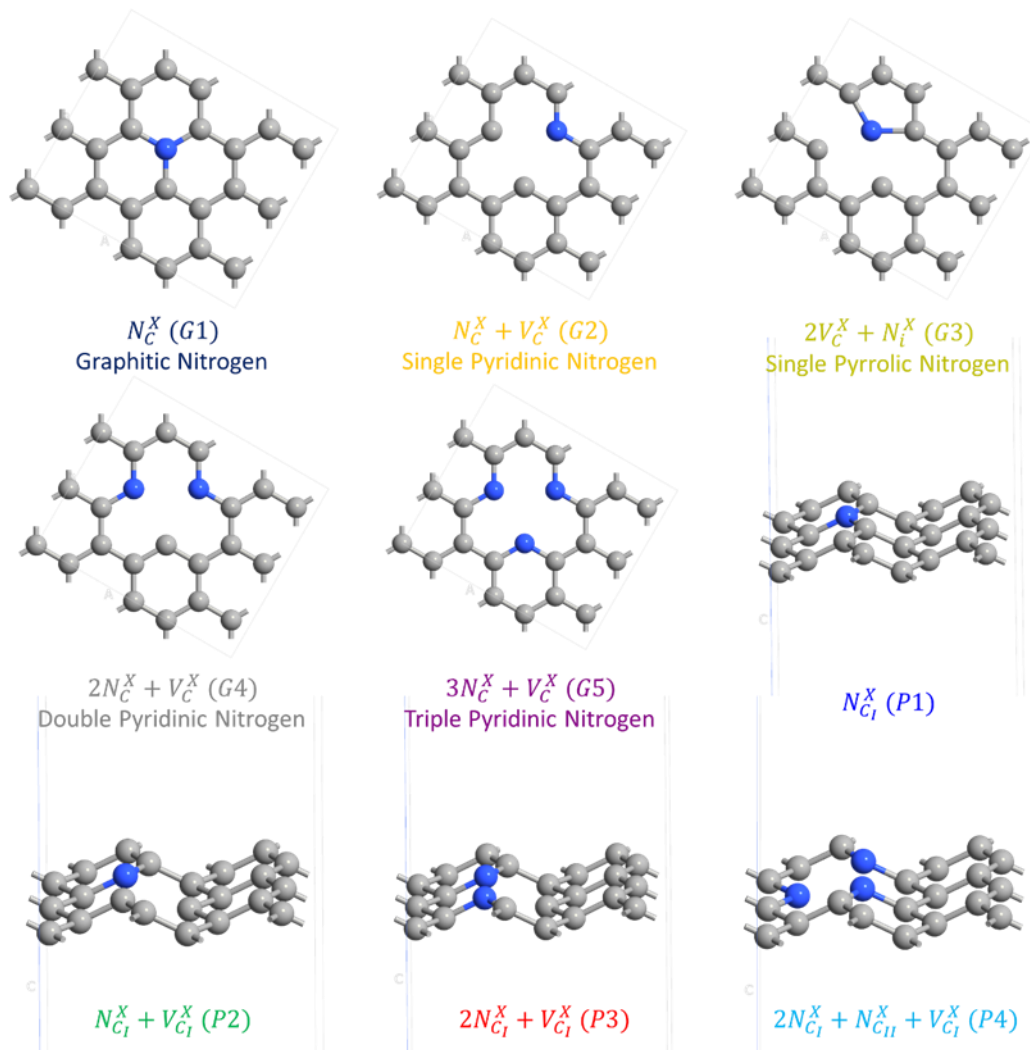


Figure 2. 5 Surface structures investigated in this study. The carbon (C) subscript in the P structure labels denotes the atomic layer in which the carbon atom resides. The resulting G and P structures are labeled with Kröger–Vink notations.

Among the models based on the P structure, with the exception of the one that contains only substitutional nitrogen, CO₂ reduction is blocked as the free energy of CO desorption (from reaction coordinate 2 to 2') is always positive with an arbitrarily applied potential. In other words, the *CO intermediate poisons and deactivates the surfaces. Only one type of defect (P1) is active for converting CO₂ to CO on the NDC-1 surface(Figure

2.6(b)), with the onset potential estimated as -1.85 V. The free energy difference of 1.85 eV for the conversion of CO₂ to CO (Figure 2.6(a), left) is much larger than that for HER (0.73 eV, Figure S2.12), indicating that the dominant process occurring on the active site is HER, not CO₂RR, which is in good agreement with the experimental results (*vide supra*).

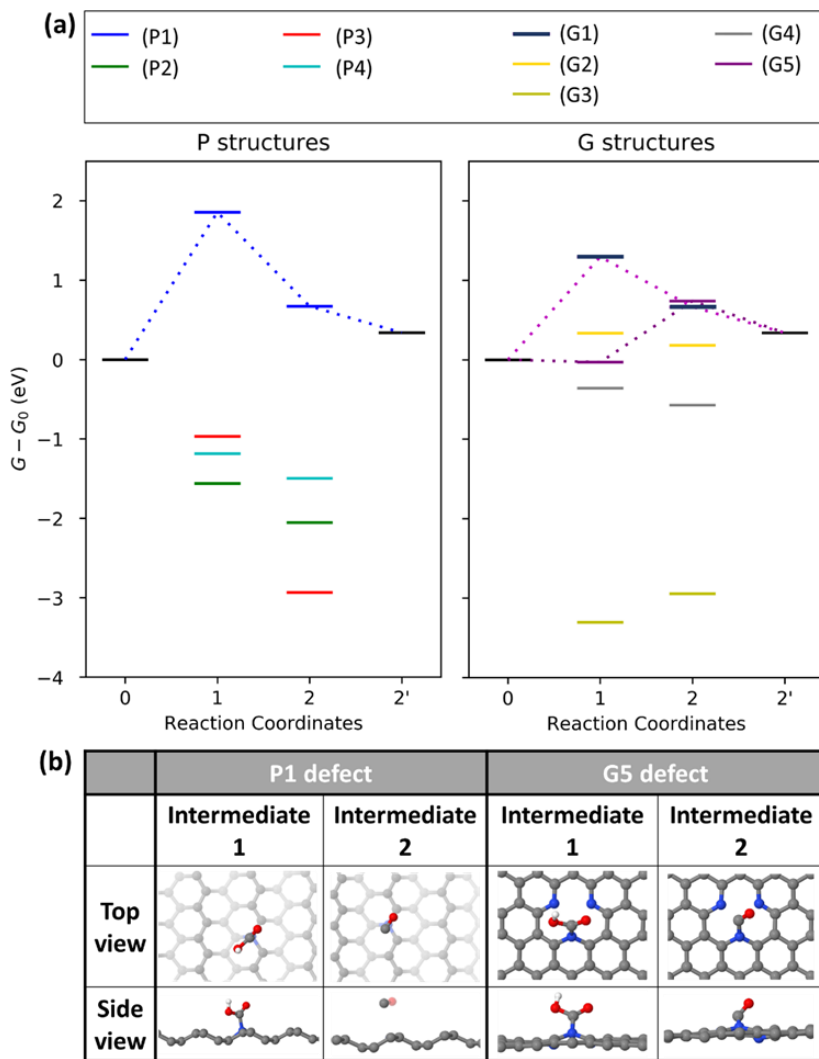


Figure 2. 6 (a) Free energy diagrams for the formation of CO on various surface (possible reaction pathways are highlighted with dotted lines) and (b) Intermediates with lowest energy pathways among P and G structures. C, N, O and H atoms represent by gray, blue, red, and white colors, respectively. All intermediate structures can be found in Figures S2.13-S2.16.

As for the graphite-based surface structures (G structures), graphitic nitrogen (G1), and triple pyridinic nitrogen (G5) defects are found to be thermodynamically favored for the reduction of CO₂ to CO. The onset potentials for CO₂RR determined by the DFT models are -1.29 V and -0.77 V for graphitic nitrogen and triple pyridinic nitrogen, respectively. The onset potential for HER is -0.80 V for a single pyridinic nitrogen surface (Figure S2.12). While both the CO₂RR and HER onset potentials from the models are close to the experimental value (-0.7 V), the dominant HER process at low bias revealed in the experiments indicates a higher reaction barrier for CO formation. Such discrepancy between computational and experimental results has been noted in previous studies,^{58, 92} and may arise from neglecting the presence of transition states and charged intermediates on the surface.¹⁴⁰⁻¹⁴²

2.4 Summary

This study reports the important roles of the carbon host structure and nitrogen dopants on the catalytic performance of nitrogen-doped UNCD thin-film electrodes for electrochemical CO₂ reduction. Our results confirm that the incorporation of nitrogen atoms enhances the catalytic activity of both NDC-1 (diamond-like) and NDC-4 (graphitic) in reducing CO₂ to CO. Importantly, the catalytic activity enhanced by nitrogen incorporation is much more dramatic in *sp*²-carbon (graphitic) structures when compared to grain boundary mediated *sp*³-carbon (diamond-like) structures. In NDC-1, the FE of CO generation is limited to ~10%, and HER is dominant over CO generation, while NDC-4 shows FE up to 82% with excellent activity and selectivity towards CO production. Critical aspects of the interplay among the host structure and dopant atoms are demonstrated by DFT calculations. The results reported here suggest that careful consideration is required

concerning different catalytic activities investigated for nitrogen-doped- UNCD and that the control of carbon host structure and heteroatom doping can have dramatic effects on catalytic activity and selectivity in CO₂RR.

2.5 Supplementary information

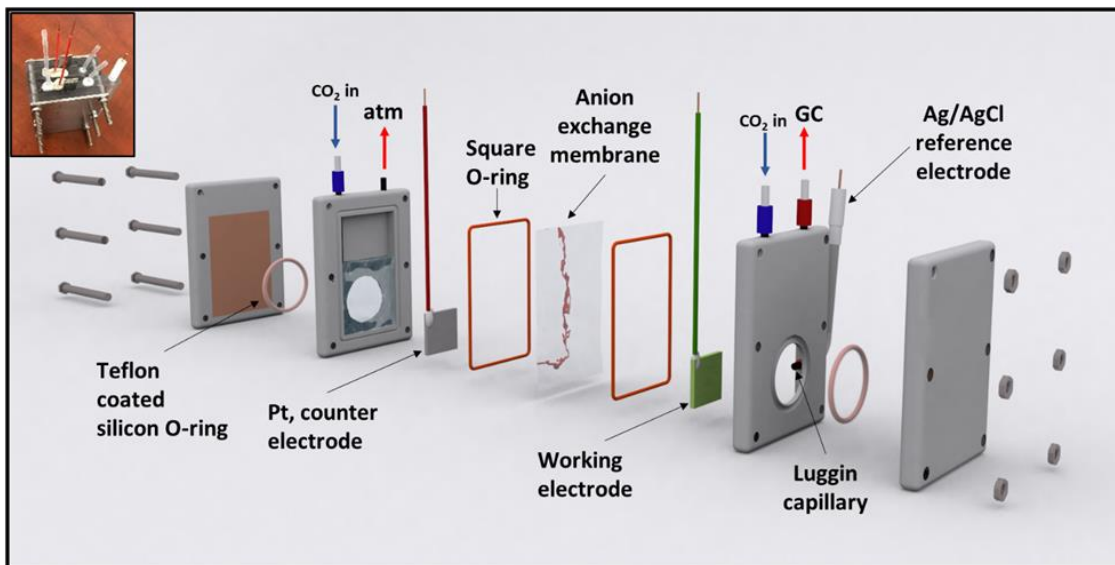


Figure S2. 1 A schematic of the electrochemical cell and experimental setup used in this work (Top left inset – Photograph of a flow cell reactor)

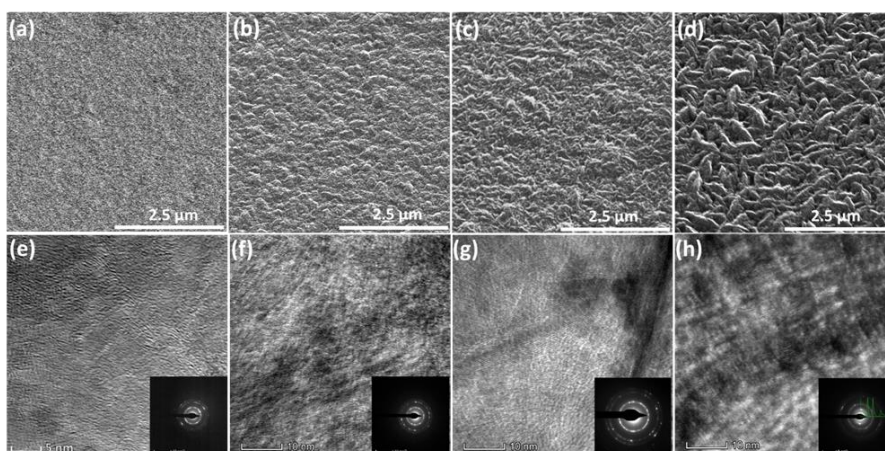


Figure S2. 2 Representative SEM images of (a) UDC-1, (b) UDC-2, (c) UDC-3, (d) UDC-4, and TEM (e) UDC-1, (f) UDC-2, (g) UDC-3, (h) UDC-4 catalysts.

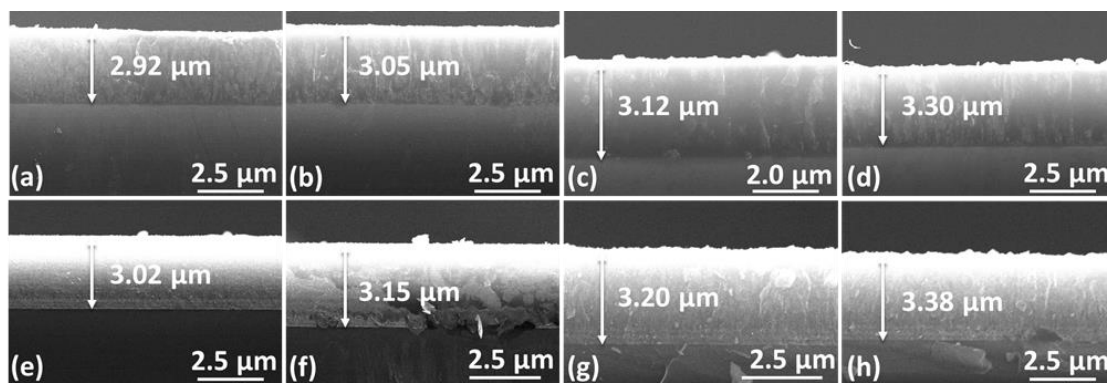


Figure S2. 3 Representative SEM cross-sectional images of (a) NDC-1, (b) NDC-2, (c) NDC-3, (d) NDC-4, (e) UDC-1, (f) UDC-2, (g) UDC-3, and (h) UDC-4.

2.5.1 Indexing Selected Area Electron Diffraction (SAED) patterns.

SAED patterns obtained from the TEM were indexed to identify the corresponding crystalline phases.

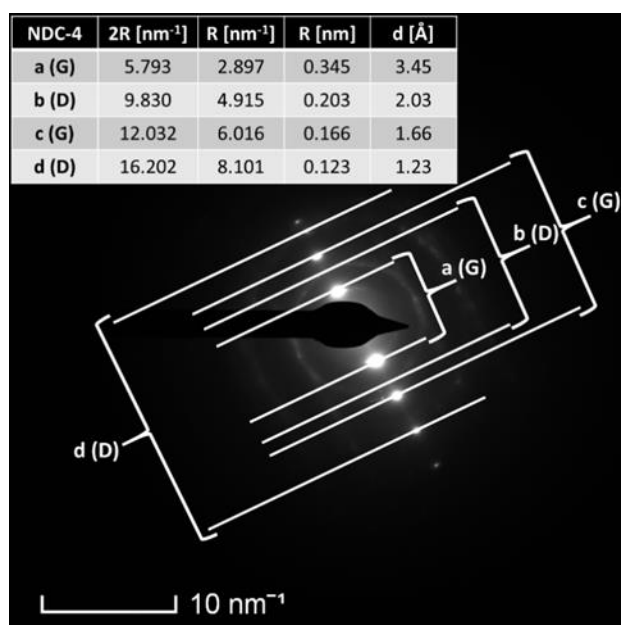


Figure S2. 4 SAED pattern of NDC-4. (2R = diameter of the ring, a (G) = 1st diffraction line from the graphite phase and, b (D) = 1st diffraction line from the diamond phase)

d- spacing calculated from the SAED patterns and the corresponding h,k,l planes were matched using the following procedure.

(1). For the cubic diamond phase,

$$\frac{1}{d^2} = \frac{h^2 + k^2 + l^2}{a^2}$$

Where,

$d = \text{Interplanar spacing}$

$h,k,l = \text{Miller indices}$

$a = \text{Lattice constant of diamond } (3.567 \text{ \AA})$

For b (D) diffraction line,

$$\frac{1}{d^2} = \frac{1}{2.03^2} = 0.243 \text{ \AA}^{-2}$$

$$\frac{h^2 + k^2 + l^2}{a^2} = \frac{1^2 + 1^2 + 1^2}{3.567^2} = 0.236 \text{ \AA}^{-2}$$

These numbers are approximately equal. Therefore, this plane corresponds to the cubic diamond (111) plane. Similarly, other planes were also indexed.

(2). For the hexagonal graphite phase,

$$\frac{1}{d^2} = \frac{4}{3} \left(\frac{h^2 + hk + k^2}{a^2} \right) + \frac{l^2}{c^2}$$

Where,

$d = \text{Interplanar spacing}$

$h,k,l = \text{Miller indices}$

$a =$ Lattice constant of graphite (3.567 \AA)

$c =$ Lattice constant of graphite (6.708 \AA)

For a (G) diffraction line,

$$\frac{1}{d^2} = \left(\frac{1}{3.45^2} \right) = 0.084 \text{ \AA}^{-2}$$

$$\frac{4}{3} \left(\frac{0^2 + 0 \cdot 0 + 0^2}{3.567^2} \right) + \frac{2^2}{6.708^2} = 0.088 \text{ \AA}^{-2}$$

These numbers are approximately equal. Therefore, this plane corresponds to the hexagonal graphite (002) plane. Similarly, other planes were also indexed.

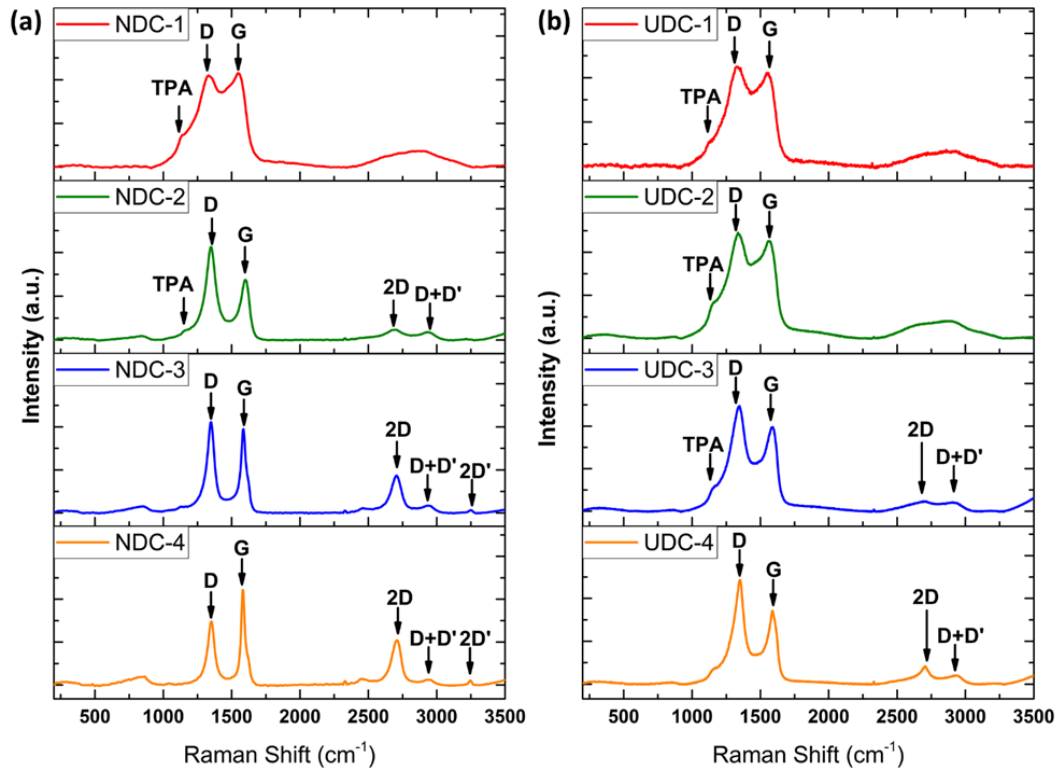


Figure S2. 5 Raman spectra of (a) NDC-X and (b) UDC-X.

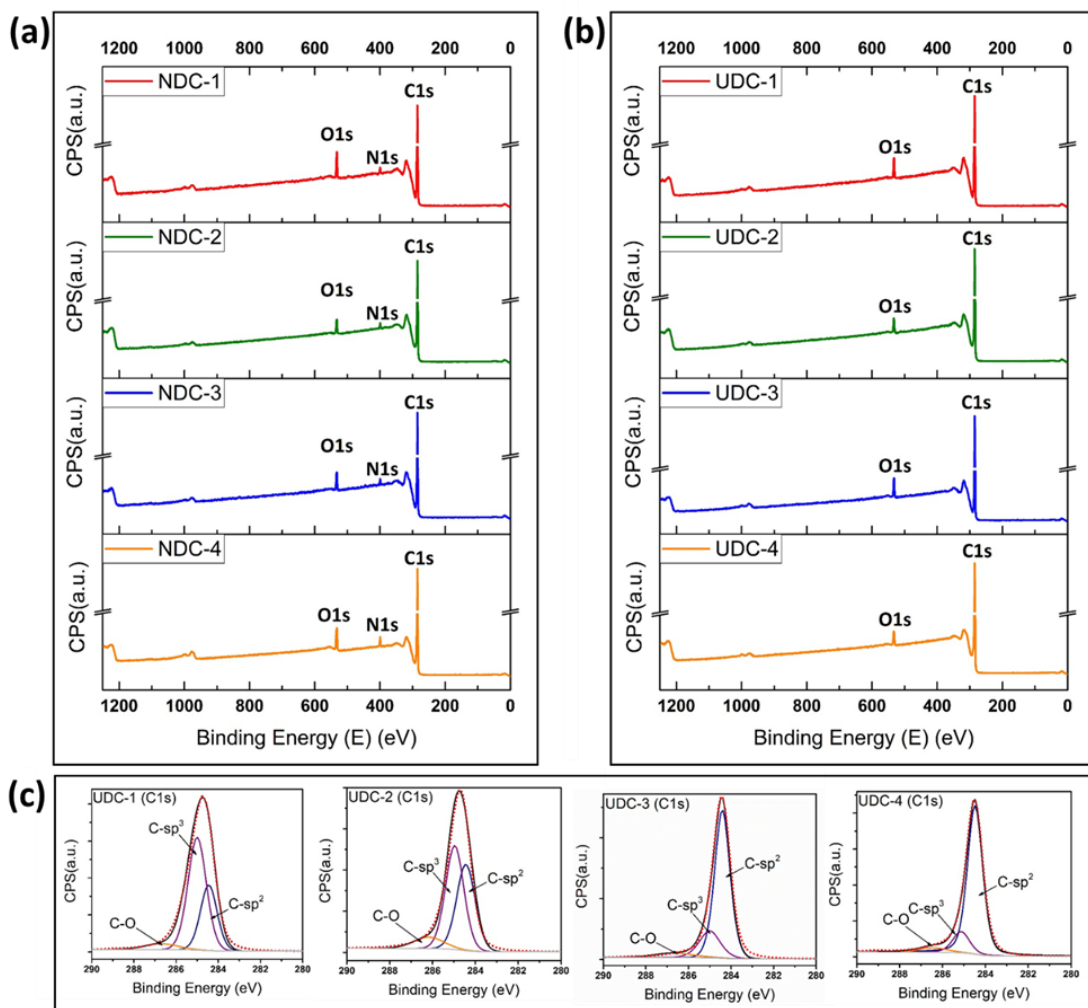


Figure S2. 6 XPS spectra of (a) NDC-X and (b) UDC-X. (c) high-resolution XPS C1s spectra of UDC-X.

2.5.2 Calculation of Electrochemical Surface Area (ECSA).

The electrochemically active surface area of each electrode is estimated from the electrochemical double-layer capacitance of the catalytic surface using 0.1 M KOH as the electrolyte.¹⁴³ In this approach, non-Faradaic capacitive current associated with the double layer charging CV cycles are recorded at various scan rates under nitrogen saturated electrolyte. As the non-Faradaic region, 0.1 V potential window centered at the open circuit

potential (OCP) vs. Ag/AgCl is chosen. The double layer charging current (i_c) in mA is given by,

$$i_c = C_{DL} \times v$$

Where,

C_{DL} = Double layer capacitance in μF (obtained by the slope of the charging current vs. scan rate plot)

v = scan rate (mV s^{-1})

Finally, the ECSA of the sample is given by,

$$ECSA = \frac{C_{DL}}{C_s}$$

Where,

C_s = specific capacitance of the sample ($\mu\text{F cm}^{-2}$)

C_s value is taken as $22 \mu\text{F cm}^{-2}$.¹⁴³

The current density obtained by the ECSA evaluated from the double layer charging is denoted as $J_{ECSA(DL)}$.

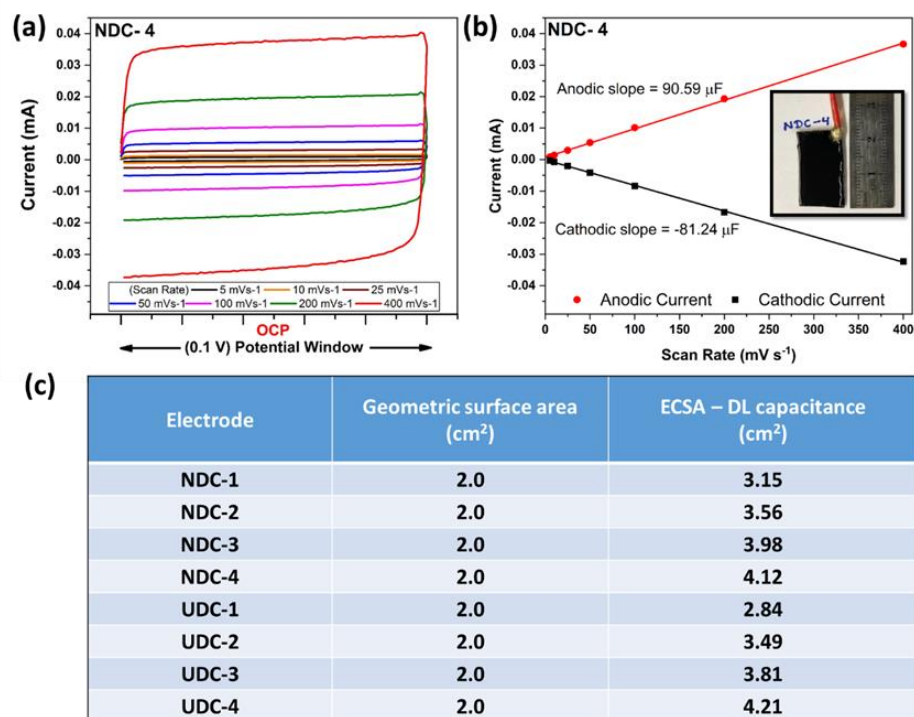


Figure S2. 7 Measurements for determining electrochemically active surface area (a) Cyclic voltammograms of NDC-4 in the non-faradaic region at various scan rates (0.1 V window around the OCP), (b) Anodic and cathodic charging currents measured for NDC-4 at OCP vs. Ag/AgCl plotted as a function of scan rate (inset – NDC-4 electrode, geometric surface area 2.01 cm²) and (c) the calculated electrochemical surface area (ECSA) of NDC-X and UDC-X.

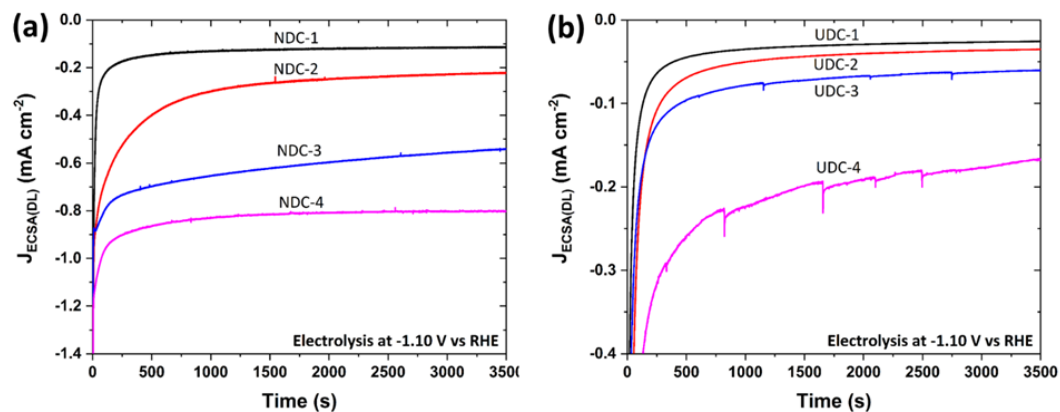


Figure S2. 8 Chrono-amperometric currents recorded for (a) NDC-X and (b) UDC-X while the fixed potential at -1.10 V vs. RHE is held.

2.5.3 Calculation of Faradaic Efficiency (FE) for gaseous and liquid products.

Faradaic efficiency for each gaseous product was calculated according to following equation.

$$\text{Faradaic efficiency} = \frac{e_{\text{output}} \times 100}{e_{\text{input}}} \%$$

$$\text{Faradaic efficiency} = \frac{x (\text{mol}) \times n_e \times F \times Q (\text{sccm}) \times 100\%}{I (\text{A}) \times V (\text{cm}^3) \times 60}$$

Where,

e_{output} = Number of electron moles produced from the specific gaseous product (mol)

e_{input} = Total number of electron moles provided into the electrode during the collection of V volume of gas (mol)

x = Number of specific gaseous product moles obtained from the GC measurement (mol)

n_e = Number electrons required to obtain 1 mol of specific gaseous product

F = Faraday constant (96485.3329 A s mol⁻¹)

Q = Carbon dioxide carrier gas flow rate (sccm)

I = Average chronoamperometric current recorded during the electrolysis experiment (A)

V = Volume of the gas inject into the GC (cm³)

Faradaic efficiency for each liquid product was calculated according to the following equation.

$$\text{Faradaic efficiency} = \frac{e_{\text{output}} \times 100}{e_{\text{input}}} \%$$

$$\text{Faradaic efficiency} = \frac{x (\text{mol}) \times n_e \times F \times 100\%}{I (\text{A}) \times t (\text{s})}$$

Where,

e_{output} = Number of electron moles produced from the specific liquid product (mol)

e_{input} = Total number of electron moles provided into the electrode during the electrolysis
(mol)

x = Number of specific liquid product moles quantified from the NMR measurement (mol)

n_e = Number electrons required to obtain 1 mol of specific liquid product

F = Faraday constant (96485.3329 A s mol⁻¹)

I = Average chronoamperometric current recorded during the electrolysis experiment (A)

t = Duration of the electrolysis experiment (s)

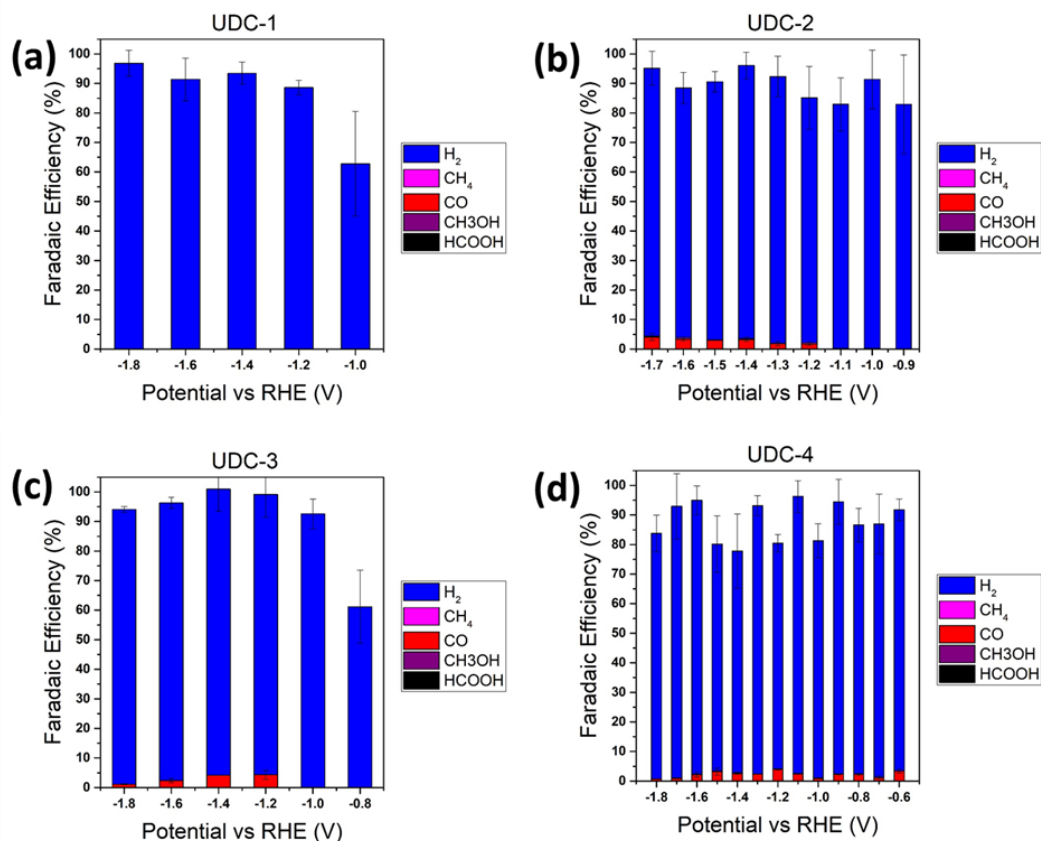


Figure S2. 9 Faradaic efficiency of each product as a function of potential for (a) UDC-1, (b) UDC-2, (c) UDC-3 and (d) UDC-4.

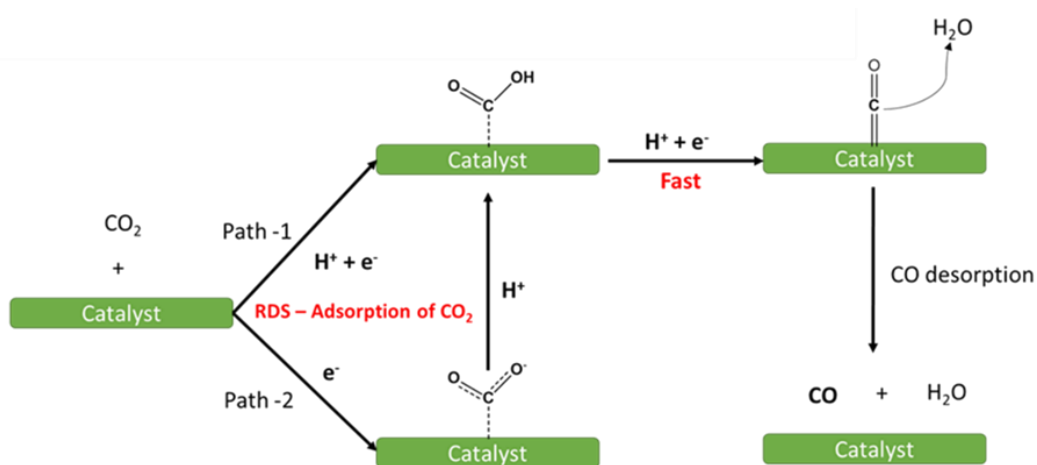


Figure S2. 10 Possible pathways for the electrochemical production of CO from CO₂.

2.5.4 Computational Methods

(DFT) calculations

Spin-polarized DFT calculations were carried out with the Vienna Ab-initio Simulation Package (VASP),¹⁴⁴⁻¹⁴⁷ making use of the Perdew, Burke, and Ernzerhof (PBE) exchange-correlation functional.¹⁴⁸ Electron-ion interactions were described with the projector augmented wave (PAW) method.¹⁴⁹ The kinetic energy cutoff for the plane-wave basis set was set to 520 eV, and a Methfessel-Paxton smearing with a width of 50 meV was employed. The D3 correction with BJ-damping was used to describe the dispersion forces.^{150, 151} The convergence criterion for the total energy was set to 10^{-5} eV in the self-consistent field loop, and that for forces during relaxation was set to 0.01 eV/Å. The Brillouin-zone was sampled with a $3\times 3\times 1$ Γ -centered grid. Solvation effects are considered under the implicit solvent model implemented by Hennig and Mathew.^{152, 153} The ground-state structures of slabs with adsorbates were obtained by finding the one with the lowest energy in configurations with different adsorption sites.

Slab models

Two basic models, the graphite slab (G) and diamond (111) surface with the reconstruction (P) proposed by Pandey,¹³⁹ were built to simulate the predominant surface structures in NDC-4 and NDC-1, respectively, as shown in Figure S2.11. 10 Å vacuum was inserted to block inter-slab interactions. Details concerning the boundary conditions are provided in Table S2.1. Starting from these base models, nitrogen atoms and vacancies were introduced into the first one and/or two atomic layers to simulate nitrogen-doped surfaces. The resulting structures, as shown in Figure 2.5, are labeled with Kröger–Vink notations, as well as the coordination state of nitrogen.

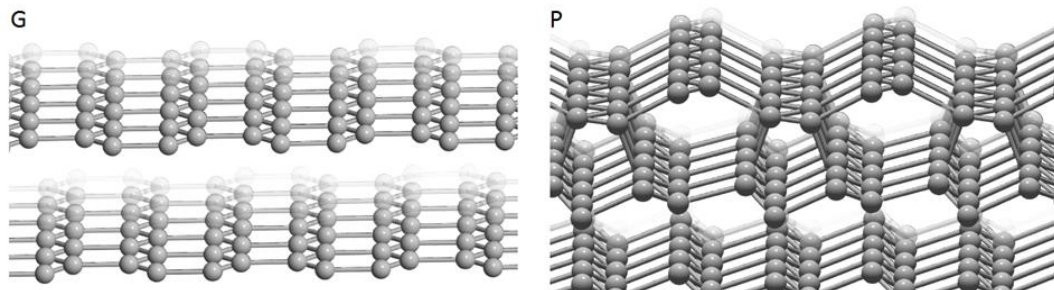


Figure S2. 11 Basic structures for simulating surface structures. The graphite slab for NDC-4 (left) and the diamond (111) surface with Pandey's reconstruction for NDC-1 (right).

Table S2. 1 Periodic boundary conditions for the computational models.

Basic Structure	Thickness (Å)	a (Å) \times b (Å)	Number of Atomic Layers Allowed to Relax
G	13.34	8.51×7.37	1
P	11.16	8.71×7.55	2

Free energy calculations

The free energy changes along the reaction pathway were calculated based on the computational hydrogen electrode (CHE) model.¹⁵⁴ The electrode potential was included in the free energy calculation by assuming the equilibrium of HER,

$$\mu(H^+) + \mu(e^-) = \frac{1}{2}\mu(H_2) - eU$$

where $\mu(H_2)$ is the chemical potential of gas phase hydrogen and U is the electrode potential vs. RHE.

The free energies of gas phase species were calculated by

$$G = E_{PBE} + E_{ZPE} + \int_0^T C_p dT - TS$$

where E_{PBE} is the electronic energy from DFT calculation, E_{ZPE} the zero point energy from frequency analysis assuming harmonic forces, T the experimental temperature 298K, C_p the heat capacity, and S the entropy. The last two terms, $\int_0^T C_p dT$ and $-TS$, were calculated from experimental data at 1 atm,¹⁵⁵ except for H₂O, which is done at both 1 atm and 0.035 atm (the latter is used for plotting free energy diagram in the main text). The calculated free energy change for the gas phase reaction (standard state) $CO_2 + H_2 = CO + H_2O$ is 0.424 eV, which is very close to the experimental value (0.427 eV).¹⁵⁵

For slabs with adsorbates, we adopt the approximation proposed by Jones,¹⁵⁶ in which the surface is assumed to be relatively rigid. We further assume that the free energy consists of vibrational and electronic contributions only, and the vibrational contribution can be obtained by a frequency analysis for the adsorbed species only. Thus, the free energy of the system is described by

$$G = E_{PBE}^{sys} + E_{ZPE}^{ads} + \int_0^T C_p^{ads,vib} dT - TS^{vib}$$

Where the superscripts originated from the approximations were made.¹⁵⁴ However, we stress that strictly speaking, the vibrational contributions to the free energy of the system cannot be addressed by only considering the adsorbates themselves, as they are now described by dispersive phonons. Thus, the aforementioned approximations need to be examined in future studies.

Free energy diagrams for HER

The free energy diagrams for HER are shown in Figure S2.12 where the color scheme follows that in Figure 2.6. The pathway with the lowest onset potential is highlighted with dotted lines.

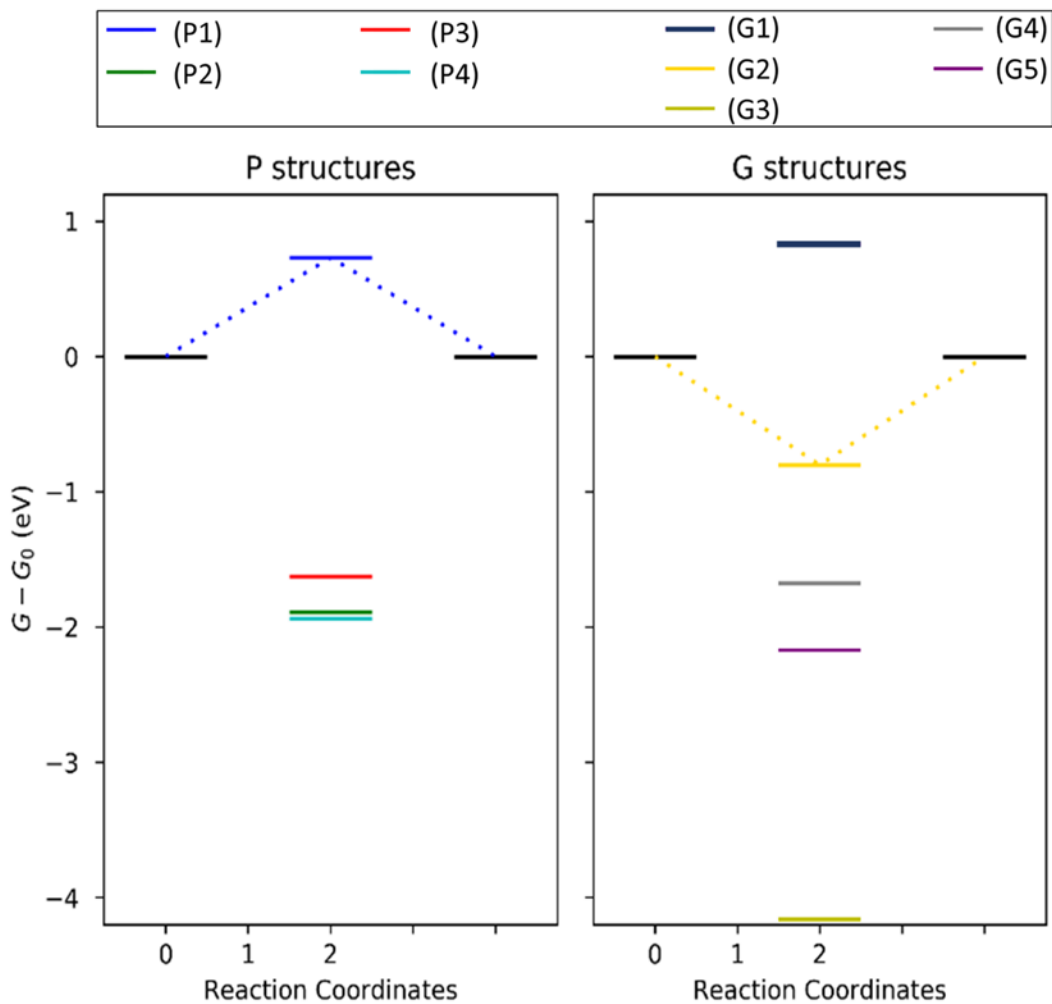


Figure S2. 12 Free energy diagrams for HER on various model surfaces.

CO₂RR reaction intermediates obtained for P and G structures

C, N, O, and H atoms represent by gray, blue, red, and white colors, respectively. Top view and side view of each intermediate is illustrated below. In the “P” structures, dark and light gray color TPA chains are located in two different planes as shown by the side view.

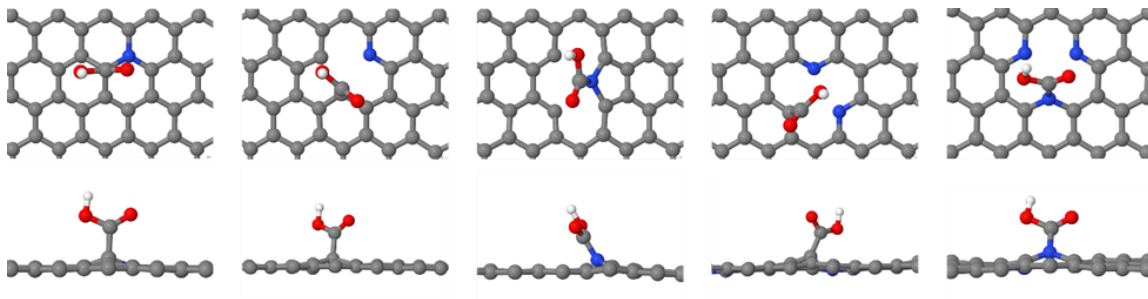


Figure S2. 13 Optimized *COOH intermediate structures for (from left to right) G1, G2, G3, G4, G5 structures from Figure 2.6(a).

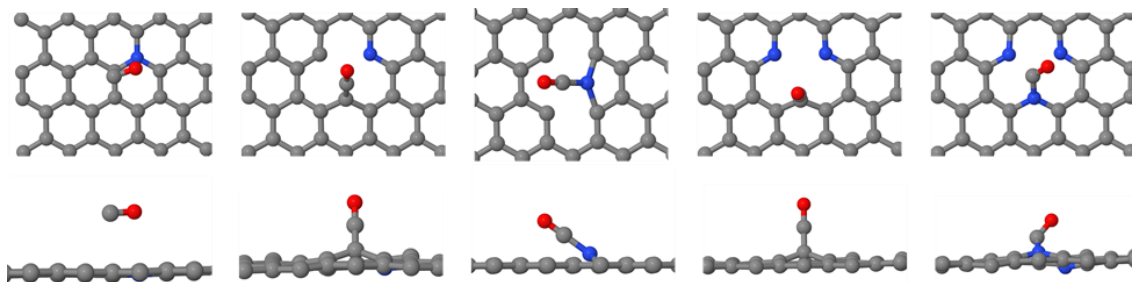


Figure S2. 14 Optimized *CO intermediate structures for (from left to right) G1, G2, G3, G4, G5 structures from Figure 2.6(a).

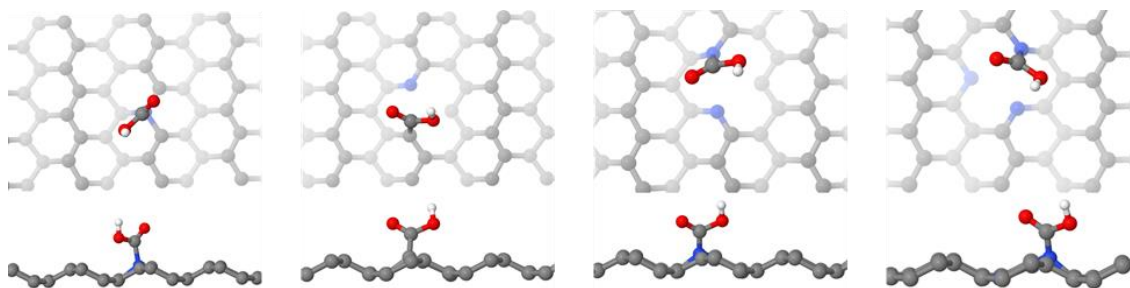


Figure S2. 15 Optimized *COOH intermediate structures for (from left to right) P1, P2, P3, P4 structures from Figure 2.6(a).

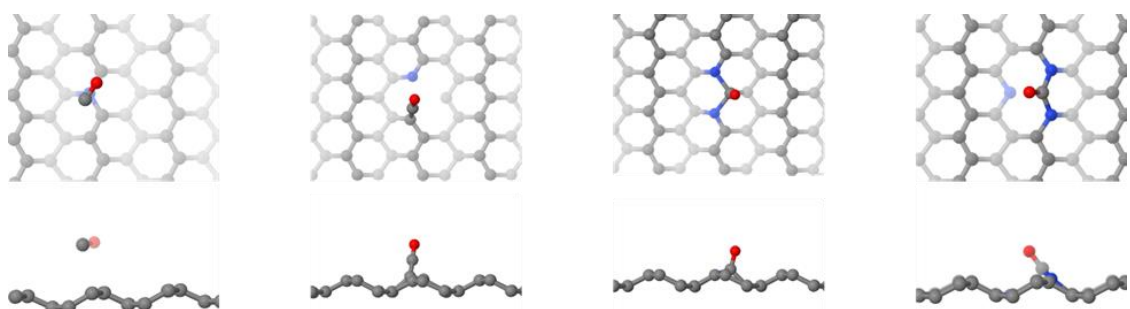


Figure S2. 16 Optimized *CO intermediate structures for (from left to right) P1, P2, P3, P4 structures from Figure 2.6(a).

CHAPTER 3. NITROGEN AND SULFUR DOPED CARBON NANO ONIONS FOR EFFICIENT ELECTROREDUCTION OF CO₂

(In the following work, computational calculations were conducted by Qianxiang Ai under the guidance of Prof. Chad Risko; Scanning transmission electron microscopy analyses were done by Melonie Thomas under the guidance of Prof. Beth Guiton; Gas chromatography analysis was conducted by Ariful Hoque under the guidance of Prof. Marcelo Guzman; BET measurements were conducted by Dr. Xin Gao from CAER; X-ray absorption spectroscopy measurements were conducted by Wasif Zaheer under the guidance of Prof. Sarbajit Banerjee from the Texas A&M University)

3.1 Introduction

Although renewable energy is a sustainable solution to mitigating the dependence on carbon-intensive energy sources, critical hurdles such as intermittency and geographical confinement remain unsolved for global adoption. Therefore, it is crucial to develop technologies that convert renewable energy into chemical energy forms that can be stored and transported.³⁶ For example, when powered by renewable energy, hydrogen via water electrolysis and hydrocarbons via CO₂ electrochemical reduction reaction (CERR), are valuable chemicals and fuels that are well suited to terawatt-scale storage.¹⁵⁷ In particular, CERR has a promising approach to store renewable energy since hydrocarbons have higher volumetric energy densities than batteries and compressed hydrogen.¹⁸

To improve the economic feasibility of CERR technology, several performance targets need to be hit: (i) current density of >300 mA cm⁻², (ii) faradaic efficiency (FE) of 80 % or higher at <1.8 V cell voltage, and (iii) a stable performance during a prolonged operation (>80,000 h).³⁷ Although no catalyst currently meets these requirements, recent

advances increased the industrial relevance of CERR.^{6, 36, 37, 158, 159} Techno-economic analyses have identified carbon monoxide (CO) and formic acid (HCOOH) as the most promising CERR products.^{35-37, 159} HCOOH has economic potential due to its high price.⁶ CO can be upgraded to diesel fuels through the Fischer-Tropsch process.³⁶ Therefore, electrocatalysts that efficiently convert CO₂ to CO or HCOOH are of utmost importance.

Metal-based CERR catalysts have been widely investigated.¹⁵⁸ Hori et al. classified metallic catalysts into four categories based on products:¹⁶⁰ (1) Zn, Ag, and Au to generate CO, (2) In, Sn, Hg, and Pb to generate HCOOH, (3) Ti, Fe, Ni and Pt to generate H₂, and (4) Cu or oxide-derived Cu to generate oxygenates and multicarbon products.¹⁵⁸ Overall, metallic catalysts have shown marked activities with low overpotentials. Especially, it was extraordinary that Cu or Cu derived catalysts generated multi-carbon products via C-C coupling. In pursuit of better activity and production of compelling hydrocarbons, metallic catalysts are aggressively being investigated through the modification of metals in oxidation states, strain and morphology, and crystallographic facets.^{6, 158} However, none of the metallic catalysts simultaneously achieved high activity, selectivity, and stability.

There are growing interests in metal-free catalysts due to their low cost, chemical inertness, and environmental friendliness.¹⁶¹ Unlike metallic catalysts, carbon electrodes have demonstrated stable performances without severe phase changes or reconstructions of catalytic sites.¹⁵⁸ The activity of carbon electrodes was significantly enhanced by incorporating heteroatoms such as boron (B), nitrogen (N), oxygen (O), fluorine (F), phosphorus (P), and sulfur (S). These dopants effectively modify local electronic properties in the vicinity of heteroatoms through charge and spin density distributions and create catalytic sites for CERR.¹⁵⁸

N is one of the most extensively studied dopants. For example, N-doped multiwall carbon nanotubes have shown a remarkable activity with high selectivity (FE of CO 80 %) at a low overpotential(-0.18 V), outperforming Au(FE of CO 12 %) and Ag(FE of CO 17%) catalysts under similar overpotentials.⁵³ The chemical identity of active sites, however, is controversial. Several experimental and theoretical studies showed that pyridinic-N sites acted as a major origin for activity while pyrrolic-N or graphitic-N had a minor role.⁵³⁻⁵⁵ A similar conclusion was reached in the study of N-doped ultrananocrystalline diamond films.⁵ More convincingly, Liu et al. showed that CERR activity had a linear trend with the content of pyridinic-N in a graphene nanoribbon.¹⁶² On the contrary, separate studies claimed that pyrrolic-N or graphitic-N as active sites.^{56, 163,}

164

The controversy on the identity of catalytic sites remained unsolved due to (i) the limitation in synthesis leading to the wide and non-uniform distribution of active sites associated with N (i.e., pyridinic-N, pyrrolic-N, and graphitic-N) and (ii) the intrinsic complexity of carbon host materials abundant with microstructural defects. Amal et al. reported an interesting experiment where nitrogen-doped mesoporous carbon was gradually annealed to generate defects and remove N atoms and proposed that edge defects such as Throrer-Stone-Wales (5-7-7-5) and point defects (5-8-5) may be more active than N chemical states.¹³³ Based on the above facts, it becomes more convincing that holistic approaches combining rigorous structure analyses, thorough electrochemical characterization, and theoretical calculations are essential to solving the mystery of catalytic sites.

The dual doping strategy of carbon has been recently explored to further tune the local electronic structure of a catalyst.^{52, 165} For example, S and N co-doping has shown to endow new catalytic sites for CERR through geometric and electronic benefits.¹⁶⁶ Due to the similar bond length between C-N (1.41 Å) and C-C (1.42 Å), pyridinic-N and graphitic-N has a negligible impact on the geometry of graphene, while pyrrolic-N may disrupt the planar structure of graphene.⁵² Electronic properties of graphene can be affected by polarization due to the dissimilar electronegativities between N (3.04) and C (2.55). S dopant creates a negligible polarization on the adjacent C atoms due to the similar electronegativity of S (2.58) to carbon. However, the size mismatch of C and S orbitals (bond length of C-S (1.78 Å) is about 25% longer than C-C) creates non-uniform spin density distributions leading to catalytic properties.^{167, 168}

While N, S co-doped carbons for CERR were reported in recent studies, the origin of activities remains unclear since rigorous structural and chemical analyses were missing in the studies.^{59, 169-172} The catalysts in the studies were mostly prepared by bottom-up pyrolysis, generating complicated and poorly defined carbon structures. These limitations have motivated us to investigate carbon nano onions (CNOs) as a substrate for co-doping. CNOs are relatively well-defined in microstructure since they consist of concentric shells of carbon atoms with a hollow core. Each CNO particle is typically 5-10 nm in diameter.¹⁷³ CNOs possess high electrical conductivity and large specific surface area. The curved morphology of graphene concentric layers in CNO shifts electron density to the outer surface, attracting CO₂ molecules for adsorption.¹⁷⁴⁻¹⁷⁶ CNOs provide a unique opportunity to investigate structure-property-activity relations for CERR.

Herein we systematically investigate high-surface-area CNOs doped with heteroatoms for CERR. CNOs are doped with N or S, or co-doped with N and S. To uncover the origin for CERR activity and to relate a mechanistic pathway to local chemical structures, thorough structural and chemical analyses, spectroscopy, and microscopic analysis were conducted in parallel with electrochemical characterizations. Local structures involving defects and dopants in doped CNOs are directly visualized by the aberration-corrected scanning transmission electron microscopy (STEM). Based on the STEM information and spectroscopic analyses, catalyst models are developed to unveil chemical interactions between adsorbed chemicals and active sites of catalysts as well as understand mechanistic pathways. The findings presented herein will pave a way to develop efficient and durable metal-free electrocatalysts for CERR.

3.2 Experimental

3.2.1 Synthesis, oxidation, and doping of CNOs

3.2.1.1 Synthesis of CNOs

CNOs were prepared from nanodiamond (ND) powders (~5 nm, (Dynamene NB50, Nanostructured & Amorphous Materials, Inc.). NDs were annealed in a graphitization furnace under the flow of helium gas at 1700 °C for 1 hour (at a 10 °C/min ramp rate). Subsequently, CNOs were further purified by annealing at 400 °C for 4 hours under air to remove any adventitious impurities.

3.2.1.2 Oxidation of CNOs

500 mg of CNOs were added in the mixture of 36 ml of concentrated HNO₃ (Fisher Scientific, Assay-69.5%) and 64 ml of deionized (DI) water (resistivity = 18.2 MΩ·cm) in

a 100 ml three-neck flask. After an ultrasonication for 15 minutes, the homogenized solution was refluxed at 105 °C for 4 hours. Afterward, the acid was removed by centrifugation, and CNO powders were washed with DI water until the pH becomes neutral. Oxidized CNOs (Ox-CNOs) were finally obtained by vacuum drying at 60 °C overnight.

3.2.1.3 Synthesis of N-CNOs

200 mg of Ox-CNOs, 1 g of urea (Sigma Aldrich, ACS reagent(99.0-100.5%), and 10 ml of methanol (Sigma Aldrich, anhydrous, 99.8%) were mixed and sonicated for 10 minutes. After evaporating methanol, the resulting solid was crushed into a powder. Then, the solid was placed on a quartz boat in a tube furnace (LINDBERG/BLUE M, Mini-Mite Tube Furnace). Under an argon environment (Scott-Gross, 99.999%), the furnace tube was heated to 600 °C, 700 °C, and 800 °C for 3 hours to obtain N-CNO(600), N-CNO(700), and N-CNO(800), respectively, where the annealing temperature of each N-CNO is shown in the parentheses). Then, solids were rinsed with DI water to remove any soluble species and dried at 60 °C overnight.

3.2.1.4 Synthesis of S-CNOs

60 mg of Ox-CNOs, 18 ml of dimethyl sulfoxide (DMSO, Sigma Aldrich, 99.9%), and 2 ml of DI water were added into a Teflon-lined container. Then, the solution was sonicated for 30 minutes. The container was capped and placed in a stainless-steel autoclave, then heated to 180 °C for 18 hours. Resultant solids were rinsed with ethanol (Sigma Aldrich, Reagent Alcohol 95%) and DI water several times and vacuum dried at 60 °C. Subsequently, the product was placed in a tube furnace and heated at 700 °C for 1

hour under 5 % hydrogen (Scott-Gross, ultra-pure 99.995%) in argon(Scott-Gross, 99.999%) to obtain S-CNO(700).

3.2.1.5 Synthesis of NS-CNOs

NS-CNO catalysts were prepared by the same procedure used to synthesize N-CNOs, but with thiourea (Sigma Aldrich, $\geq 99.999\%$ (metals basis)) instead of urea. Thiourea served as the nitrogen and sulfur donor. Finally, NS-CNO(600), NS-CNO(700), and NS-CNO(800) were obtained.

3.2.2 Electrode preparation

3.2.2.1 Preparation of electrodes for H-cell experiments

10 mg of a catalyst, 5 ml of DI water, and 50 μl Nafion (Sigma Aldrich, nafionTM 117 solution, ~ 5 wt%) were mixed and sonicated for 30 minutes to form a homogeneous catalyst ink solution (2 mg ml^{-1}). Then, a gas diffusion electrode (GDE, Sigracet 39BC, fuel cell store) was placed on a hot plate ($120 \text{ }^\circ\text{C}$), and the catalyst ink solution was airbrushed (Iwata Eclipse, IWATA HP-CS) onto the microporous layer of the GDE with the catalyst loading of $\sim 0.5 \text{ mg cm}^{-2}$. Subsequently, the electrode was further heat-treated in a vacuum oven at $130 \text{ }^\circ\text{C}$ for 30 minutes. After cooling down, the electrode was cut into pieces (each piece with the area of $1.5 \text{ cm} \times 1.5 \text{ cm}$), and a copper wire was attached using a silver epoxy resin. Finally, the electrical contacts and the back of the electrode were coated with an insulative epoxy adhesive. The surface area of a catalyst exposed to an electrolyte was estimated by the *ImageJ 1.51J8* software.

3.2.2.2 Preparation of a rotating ring disk electrode (RRDE)

A RRDE electrode with a glassy carbon disk (4 mm diameter) and a Pt ring was polished with alumina powder. Then, 40 μl of the prepared catalyst ink (2 mg ml^{-1}) was drop-casted on to the glassy carbon disk and dried at 60 $^{\circ}\text{C}$ overnight.

3.2.2.3 Preparation of electrodes in an electrochemical cell with a flow cell configuration

NS-CNO(700) catalyst was mounted on the GDE following the same method in section 2.2.1, but with 5% polyvinylidene difluoride (PVDF) instead of a Nafion binder to remove the interference from S. The loading of catalysts is 0.51 mg cm^{-2} . After heat treatment, the electrode is cut into 2.0 cm x 2.0 cm pieces, and they were directly used in a gas diffusion flow cell (Figure S3.9). The area of an electrode exposed to an electrolyte is 1.2 cm x 1.2 cm (Figure S3.12).

3.2.3 Material characterization

3.2.3.1 Micro-Raman spectroscopy

Raman spectroscopy was conducted with a DXR micro-Raman instrument (Thermo Scientific). Each spectrum was collected with a diode-pumped 532 nm Nd:YVO₄ laser as the excitation source (5 mW power with 3 second sample exposure time).

3.2.3.2 X-ray Diffraction (XRD) analysis

XRD patterns were acquired using BRUKER AXS D8 ADVANCE x-ray diffractometer equipped with CuK α radiation (1.54 \AA) and LYNXEYE (1D mode) detector, increment 0.01 $^{\circ}$.

3.2.3.3 Brunauer–Emmett–Teller (BET) measurement

BET surface area was analyzed by a gas adsorption analyzer (TRISTAR 3000, Micromeritics Instruments, Norcross, GA). Prior to the measurement, each 100 mg of the

sample was degassed at 160 °C overnight. Finally, the adsorption isotherms were obtained by using nitrogen as the probe gas.

3.2.3.4 Fourier-transform infrared spectroscopy (FT-IR)

FT-IR measurements were obtained with a spectrometer (Nicolet iS50, Thermo Fisher Scientific, Madison, WI) at a resolution of 4 cm⁻¹ for 32 scans in the range of 600 to 3500 cm⁻¹ using a Ge-ATR crystal

3.2.3.5 Scanning transmission electron microscopy (STEM)

3.2.3.5.1 Stem sample preparation and characterization

A small amount of each powdered S-, N-, and NS-CNO samples were sonicated in high purity isopropanol (Sigma-Aldrich) for 30 minutes, and 10 μL of each diluted solution was drop-cast on to three separate 300-mesh lacey-carbon TEM copper grids. The prepared TEM grids were annealed in a vacuum at 80 °C for 8 hours before inserting into the STEM. The STEM characterization was performed using a fifth-order aberration-corrected Nion UltraSTEM U100 at 100 kV (with a probe current of 0.5 nA).

3.2.3.5.2 Fourier filtering

The HAADF micrographs of interest were Fourier filtered to improve the signal to noise ratio with enhanced clarity. Using the Gatan Digital Micrograph® software, a fast Fourier transform (FFT) was performed for a particular HAADF image, followed by masking of the rings correspond to graphitic layers in FFTs to generate inverse FFT (IFFT) images.

3.2.3.6 X-ray absorption spectroscopy (XAS)

X-ray absorption spectroscopy (XAS) measurements were performed at the Beamline 8.0.1 of the Advanced Light Source (ALS). The beamline undulator and

spherical grating monochromator supply a linearly polarized photon beam. Before the measurement, powder samples were uniformly dispersed and pressed on a piece of copper tape. All the measurements were conducted under ultrahigh vacuum (UHV) conditions. The collected data were normalized to the beam flux measured by a clean gold mesh upstream of the end station. All XAS data presented in this work was collected in the total electron yield (TEY) mode.

3.2.3.7 X-ray photoelectron spectroscopy (XPS)

Elemental compositions and the atomic chemical states of catalysts were characterized by XPS with a Thermo Scientific K-Alpha photoelectron spectrometer. Monochromatic Al K- α radiation (energy of 1486.6 eV) was focused on the surface of each specimen. A typical spot size of the radiation was about 400 μm . During XPS, each specimen was exposed to an electron flood gun to reduce surface charging.

3.2.4 Electrochemical cell configuration

3.2.4.1 Electrochemical tests with an H-cell configuration

Electrochemical performances of catalysts were evaluated in a two-compartment three-electrode cell with an H-cell configuration. A platinum (Pt) foil and a catalyst were used for the counter electrode (CE) and the working electrode (WE), respectively. Two compartments were separated by an anion exchange membrane (Fumasep FAA-3-PK-130, fuel cell store). An Ag/AgCl electrode filled with 1 M KCl was used for the reference electrode (RE), and it was placed 5 mm away from WE. Each compartment held 12 ml of 0.1 M KHCO_3 (Aldrich, BioUltra, $\geq 99.5\%$) electrolyte. Before electrolysis, both compartments were purged with humidified CO_2 (Scott-Gross, 4.8 research-grade, 99.998% purity) gas at 50 sccm (MKS-GE50A mass flow controller) for 30 minutes. After

pH reached 6.80, electrolysis was initiated under a continuous flow of CO₂ and continued while the electrolyte is circulated through the cell using a dual-head peristaltic pump (PP-3, Binacaproducts) at a rate of 5 ml min⁻¹. All recorded currents were normalized by the geometric area of each electrode.

3.2.4.2 Configuration of the gas diffusion flow cell electrochemical setup

The durability test of NS-CNO(700) was performed in a cell with a gas diffusion electrode(GDE) configuration to enable faster CO₂ mass transfer. This cell contains two separate compartments for the WE(NS-CNO(700)-GDE) and the CE(Pt-mesh). Inside of the WE compartment, an Ag/AgCl RE was placed 5 mm away from the WE. Each compartment holds 15 ml of electrolyte (1 M KHCO₃), and they are separated by an anion exchange membrane (Fumasep FAA-3-PK-130, fuel cell store). The electrolyte was circulated through the electrochemical cell using a dual-head peristaltic pump(PP-3, Binacaproducts) at a rate of 5 ml min⁻¹. Gaseous CO₂ was introduced behind the NS-CNO(700)-GDE at a flow rate of 50 sccm. Throughout the electrochemical test, the pressure inside the WE gas channel was kept constant by a customized back-pressure regulator setup.

3.2.5 Electrolysis

Electrochemical studies were performed with a CHI 660D potentiostat (CHI instruments). The data collected with the Ag/AgCl reference electrode (RE) were later converted to the reversible hydrogen electrode (RHE) scale using the following formula:

$$V \text{ vs. (RHE)} = V \text{ vs. (Ag/AgCl)} + 0.222 \text{ V} + 0.059 \times \text{pH}_{(\text{electrolyte})}$$

For each electrolysis, amperometry was conducted for 1 hour under any applied potential.

3.2.6 Product analysis

3.2.6.1 Gas chromatography analysis

During electrolysis, gas samples were intermittently collected to analyze gaseous products. Gaseous products were collected in glass vials capped with a rubber septum. The quantification of gaseous products was performed by gas chromatography (GC, SRI 8610C) with two columns (a silica gel HaySep D as column 1 and a Mole-Sieve 13X as column 2), a thermal conductivity detector (TCD), and a flame ionization (FID) detector interfaced to a methanizer. Gas samples (1 mL) were withdrawn through a septum from the headspace of the vial containing the sample immediately before injection into the GC. The FID detector was used for the analyses of CO, CO₂, and CH₄ using N₂ (Scott-Gross, UHP) as the carrier gas (flow rate = 20 mL min⁻¹), and supplying H₂ gas (Scott-Gross, UHP) to FID/methanizer at a flow rate of 25 mL min⁻¹. The analysis of H₂ used a TCD detector. The oven temperature was maintained at 40 °C for 10 min and then increased to 200 °C using a ramp of 20 °C min⁻¹.

3.2.6.2 NMR analysis for liquid products

After the electrolysis, the electrolyte solution was analyzed by 400 MHz Bruker Avance NEO spectrometer to quantitatively identify the liquid products. NMR samples were prepared by mixing 700 µl electrolyte solution with 100 µl D₂O, 10 µl of GdCl₃ (7 mM) (relaxation agent) and 10 µl of dimethyl sulfoxide (DMSO, 8.4 mM) as well as 20 µl of phenol (8.4 mM) as internal standards. Each spectrum was collected by using 32 scans with a 10 second relaxation delay. The water peak was suppressed to increase the visibility of other peaks. Formic acid was quantified based on the integrated peak area of phenol. Quantitative correlation between formic and phenol is shown in Figure S3.1.

3.2.7 Computational methods

Semi-empirical PM7 Hamiltonian calculation as implemented in MOPAC2016 has been used throughout this study.¹⁷⁷⁻¹⁷⁹ Geometric optimizations are performed with the gradient criterion set to 0.5. The free energy changes along the reaction pathway were calculated based on the computational hydrogen electrode (CHE) model.¹⁸⁰ The electrode potential was included in the free energy calculation by assuming the equilibrium of HER (hydrogen evolution reaction). The calculated enthalpy change for the gas phase reaction (298K, standard state) $\text{CO}_2 + \text{H}_2 = \text{CO} + \text{H}_2\text{O}$ is 0.37 eV, which is ~50 meV lower the experimental value (0.42 eV).¹⁵⁵

3.2.8 Evaluation of local CO₂ species concentration

The CO₂ concentration at the electrode surface was calculated using the reaction-diffusion model for both planar and gas diffusion electrodes. Reaction-diffusion equations and rate constants were adopted from Gupta et al., and appropriate modifications were made to match the current system.¹⁸¹ The reaction-diffusion model accounts for interactions between CO₂, H⁺, OH⁻, HCO₃⁻ and CO₃²⁻. Based on these interactions, the concentration of CO₂ at the vicinity of the electrode surface can be evaluated at the current density of interest. For these calculations, a liquid diffusion thickness of 500 μm was assumed based on the epoxy thickness of the planar electrode and the depth of the Teflon groove where the GDE is recessed. Finally, time-dependent partial differential reaction-diffusion equations were solved by MATLAB programming to obtain local CO₂ concentration. Details of the reaction-diffusion model are available in the Appendix, Gupta et al.,¹⁸¹ Arquer et al.,¹⁸² and Dinh et al.¹⁸³

3.3 Results and discussion

3.3.1 Synthesis

CNOs are derived from detonation nanodiamonds (NDs) via annealing at 1700 °C (Figure 3.1(a)).¹⁸⁴ During this process, surface functional groups of NDs are removed, sp³-C bonds in NDs become graphitized and form concentric graphitic shells in CNOs.¹⁸⁵ Direct incorporation of heteroatoms in pristine CNOs is tedious due to the low surface energy of CNO.¹⁷³ Therefore, a prior introduction of defects such as oxygen functional groups is a critical step for heteroatom doping.¹⁸⁶ Nitric acid is commonly used to oxidize CNOs (Ox-CNOs).¹⁶¹ During the oxidation, chemisorbed NO₃⁻ ions form epoxides that are further oxidized to various oxygenated functional groups such as carbonyl, carboxylic, and lactones yielding Ox-CNOs (Figure 3.1(b)).¹⁸⁷ The oxygenated groups are entrance sites for the incorporation of heteroatoms.¹⁸⁸

S-CNOs are synthesized via a solvothermal treatment with DMSO, followed by annealing at 700 °C in a reducing environment (5 % hydrogen in argon). The annealing step removes oxygen functional groups of S-CNO. N-CNOs and NS-CNOs are obtained with urea and thiourea, respectively. The thermal decomposition of urea produces NH₃ and CO₂.¹⁸⁹ NH₃ reacts with oxygen functional groups in Ox-CNO to form C-N bonds.^{188, 190} The thermal decomposition of thiourea generates NH₃, HNCS (thiocyanic acid), H₂S and C(NH)₂(carbodiimide).¹⁹¹ These N and S containing gases react with oxygen functional groups of Ox-CNO, resulting in co-doped NS-CNOs (Figure 3.1(b)). N and S contents in CNOs are optimized by adjusting annealing temperature. In the present work, samples were prepared at 600 °C, 700 °C, and 800 °C. Mainly, the samples prepared at 700 °C are

discussed in chapter 3 results and discussion section. The results of the other samples are discussed in section 3.5.

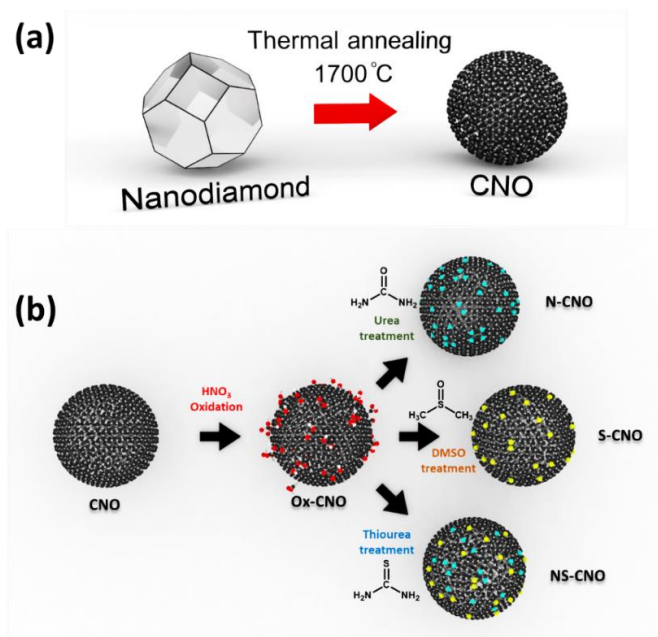


Figure 3. 1 (a) Thermal conversion of ND to CNO and (b) synthetic process of Ox-CNO, N-CNO, S-CNO and NS-CNO.

3.3.2 Material Characterization

Raman spectroscopy and XRD characterizations were conducted to analyze microstructure, electronic structure, local features, and crystallinity of undoped, oxidized, and doped CNOs. In Figure S3.2, Raman spectra of all samples exhibit three peaks centered around 1335 cm⁻¹, 1568 cm⁻¹, and 2663 cm⁻¹, which are assigned to D- band, G-band, and 2D-band, respectively. The G-band originates from the sp²-hybridized, in-plane stretching mode for both rings and chains.^{114, 192, 193} It is noteworthy that the G-bands of all CNOs are significantly shifted to lower wavenumbers (~1568 cm⁻¹) as compared to that of HOPG (~1580 cm⁻¹).¹⁹⁴ This shift is attributed to the tensile strain of CNOs due to their curvature.¹⁹⁵

The D-band arises from the breathing oscillation mode of sp^2 hybridized C-C rings.¹⁹² This mode becomes active in the presence of any defect that breaks the symmetry of graphite lattices such as heteroatoms, vacancies, sp^3 defects, and grain boundaries.¹¹⁴ Thus, the I_D/I_G ratio is the measure of a microstructural disorder in the graphitic material.¹⁹⁶ The calculated I_D/I_G ratios for CNO, Ox-CNO, N-CNO(700), S-CNO(700), and NS-CNO(700) are 0.95, 1.15, 1.28, 1.17, and 1.47, respectively. Undoped CNOs are the most ordered in microstructure, and subsequent treatments increase the microstructural disorder of CNOs. NS-CNOs are the most disordered due to the spread of defects associated with N and S dopants. Detailed Raman analyses and interpretations are in supplementary information section 3.5 (Table S3.1 and Figure S3.3). Notably, NS-CNO(700) has an n-type character with a significantly reduced work function compared to pristine and other doped CNOs.

In Figure S3.4, XRD patterns of all samples have peaks at 26.0° , 43.3° , 53.6° , and 78.7° that are characteristic of (002), (100), (004), and (110) crystalline planes of carbon materials, respectively. The peak observed at 26.0° in all samples corresponds to the graphitic (002) plane of CNOs. It implies that the crystallinity of CNOs is retained during the oxidation and doping processes.¹⁹⁷

The BET specific-surface-area and the pore-size distribution of each sample were determined through nitrogen adsorption-desorption measurements. In Figure S3.5(a), adsorption hysteresis loops of all samples imply a strong mesoporous nature.^{198, 199} This observation is consistent with the pore size distributions shown in Figure S3.5(b). In all samples, mesopores (2-50 nm) are dominant, as reported previously.²⁰⁰ Besides, a sharp peak at ~ 1.4 nm is found, indicating the presence of micropores associated with structural

vacancies. The calculated BET surface areas of CNO, Ox-CNO, N-CNO(700), S-CNO(700), and NS-CNO(700) are $626 \text{ m}^2 \text{ g}^{-1}$, $502 \text{ m}^2 \text{ g}^{-1}$, $424 \text{ m}^2 \text{ g}^{-1}$, $356 \text{ m}^2 \text{ g}^{-1}$, and $500 \text{ m}^2 \text{ g}^{-1}$, respectively (refer to the inset in Figure S3.5(b)). The oxidation and doping processes impacted the surface areas of CNOs. Notably, the specific-surface-area of NS-CNO(700) is significantly larger than those of N-CNO(700) and S-CNO(700) due to the increased mesoporous volume.

To track the origin of catalytic sites, it is crucial to probe the local structures and chemical configurations of dopants. For this purpose, the direct imaging of catalysts was accomplished in this study by employing a high-resolution STEM technique (Figure 3.2). All STEM images revealed the curved nature of CNOs with concentric multi-fullerene layers. The spacing between adjacent concentric layers in CNO is $0.34 \text{ nm} - 0.35 \text{ nm}$ (Figure 3.2(a) [iv,v,vi]), which is close to the interlayer spacing of graphite.²⁰¹ An EELS spectroscopy in our separate report has identified the elements C and S in S-CNO(700), C and N in N-CNO(700), and C, N, and S in NS-CNO(700). Oxygen was detected in the EELS of all samples and was attributed to leftover oxygen functional groups after doping processes.⁷⁷

Dopant atoms were statistically analyzed based on the number of atoms in groups and their proximity to defective sites (Table 3.1). N and S atoms are either isolated as individual atoms or clustered in CNOs, which is consistent with the literature reports.²⁰²⁻²⁰⁴ The clusters of 2 or 3 dopant atoms are more frequently observed in NS-CNO(700) than in other doped CNOs (Figure 3.2(b)). These clustered dopants maybe consisting of a combination of pyridinic-N, graphitic-N, and sulfide-S structures, which were predicted to be CERR active domains.⁵⁹ In the STEM images, these dopants preferentially occupy the

areas with sharp edges and on the curved regions of the CNOs. The detailed analysis of N-CNO(700), S-CNO(700), and NS-CNO(700) is published elsewhere, and this report also illustrates a superior oxygen reduction reaction(ORR) performance of co-doped NS-CNO.⁷⁷

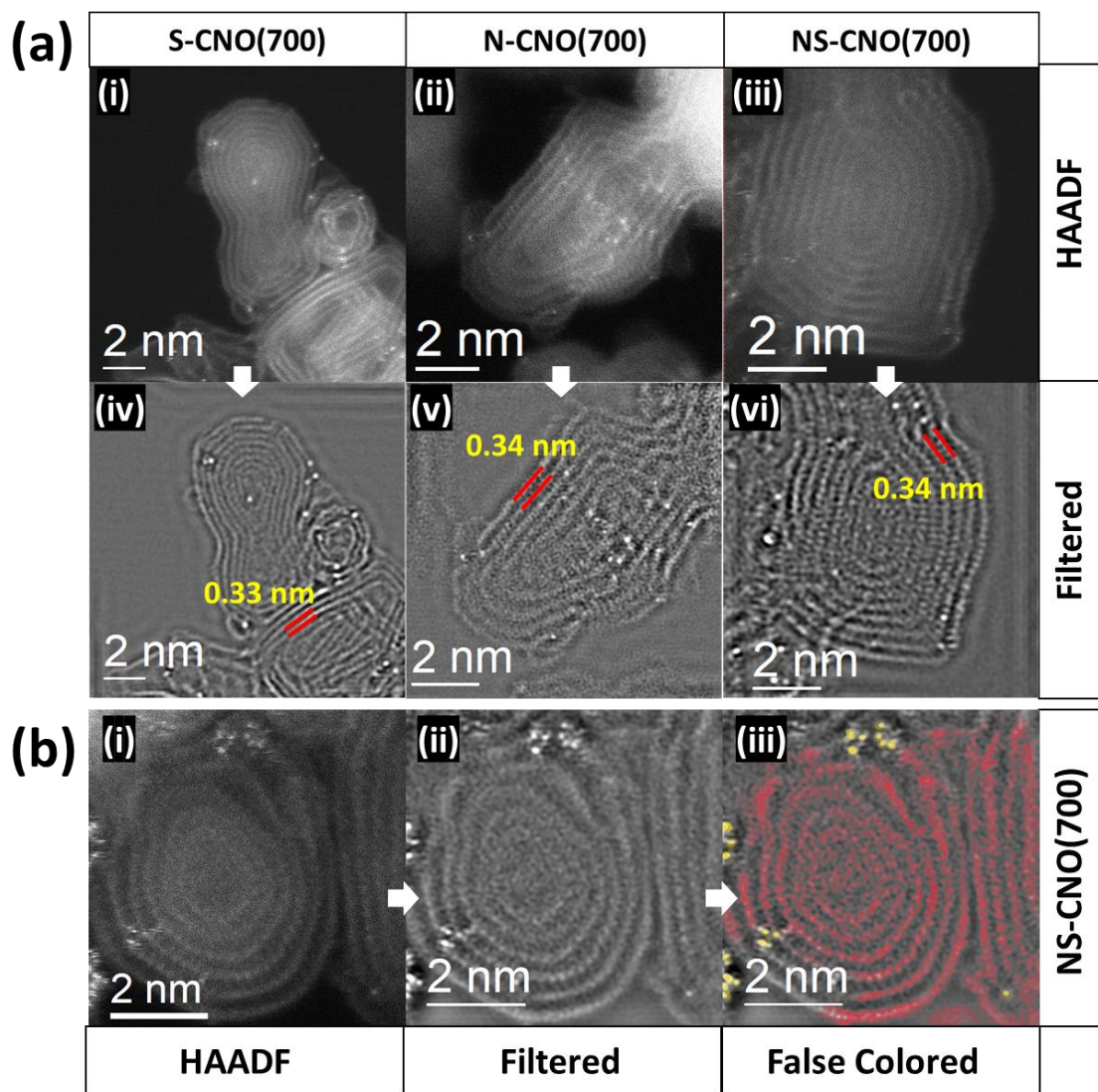


Figure 3. 2 (a) STEM HAADF micrographs of S-CNO [i], N-CNO [ii], and NS-CNO [iii] samples and their Fourier filtered images [iv, v, vi], (b) HAADF micrograph [i], Fourier filtered image [ii], and false colored filtered image [iii] (red = CNO, yellow = dopants) of NS-CNO(700) showing the configuration of dopants.

Table 3. 1 Statistical analysis of dopant distribution on S-CNO(700), N-CNO(700) and NS-CNO(700).⁷⁷

Type	Number of CNO	Number of dopants	Clusters				single atom dopants		Proximity to defect sites							
			2	3	>3	%			At the defect site		0-0.4 nm		0.41-0.7 nm		>0.7 nm	
NS-CNO	39	>209	23	10	3	42	121	58%	147	70%	34	16%	11	5%	17	8%
S-CNO	29	>82	7	3	1	32	55	67%	43	52%	4	5%	13	16%	22	27%
N-CNO	30	>67	8	4	-	42	39	58%	16	24%	3	4%	5	7%	43	64%

The CERR activity of a catalyst relies on its chemical structure, more specifically, chemical configurations of active sites for the adsorption of CO₂ molecules. XPS analyses were conducted to determine elemental contents and chemical states of dopants, N and S. The XPS results are presented in Figure 3.3(a)-(e), Table S3.2, and Figure S3.6. The survey XPS spectra indicate that all samples are free of impurities and mainly contain C, N, S, and O, confirming the successful process of doping (Table S3.2). The contents of S atoms in S-CNO(700), N-CNO(700), and NS-CNO(700) are 2.2, 0, and 2.1 at.%, respectively. The contents of N atoms in S-CNO(700), N-CNO(700), and NS-CNO(700) are 0, 2.3, and 2.2 at.%, respectively. Previous studies with planar graphene reported a much lower content of S than N due to a steric hindrance of bigger S atoms.⁵⁹ However, similar contents of N and S were found in the current study, and they were attributed to the curvature of CNOs that promotes the incorporation of S atoms.⁵²

High-resolution XPS S2p and N1s spectra of N-CNOs, S-CNOs, and NS-CNOs are presented in Figure 3.3(a)-(d). The deconvoluted XPS S2p spectra of S-CNO(700) and NS-CNO(700) show peaks at 163.9 eV, 165.2 eV, and ~168.2 eV, that correspond to S2p_{3/2}, S2p_{1/2}, and oxidized sulfur group, respectively.²⁰⁵ S may exist as sulfide (C-S-C), thiol (C-S-H), disulfide (C-S-S-C), and oxidized (C-SO_x-C) configurations. The oxidation states of S atoms are -2 for C-S-C/C-S-H, -1 for C-S-S-C, and ≥ 0 for C-SO_x-C. Because C-S-H

and C-S-S-C are excluded from FT-IR spectra (section 3.5, Figure S3.7), S dopants exist as (C-S-C) and (C-SO_x-C). S-CNO(700) and NS-CNO(700) contain similar portions of C-S-C (~82% and 78%) and lesser amounts of C-SO_x-C (18 and 22%) (Figure 3.3(e)).

Deconvoluted XPS N1s spectra of both N-CNO(700) and NS-CNO(700) result in four peaks at 398.3 eV, 399.7 eV, 401.3 eV, and ~403 eV, that are assigned to pyridinic-N, pyrrolic-N, graphitic-N, and oxidized N, respectively(Figure 3.3(b) and (d)).^{206, 207} The relative portions of pyridinic-N, pyrrolic-N, and graphitic-N in N-CNO(700) are 48 %, 35 %, and 11 %, indicating N dopants mostly exist in pyridinic and pyrrolic forms. In NS-CNO(700), however the relative portions of pyridinic-N, pyrrolic-N, and graphitic-N are 26 %, 28 %, and 40 %, respectively. Notably, the decrease of pyridinic-N content and the increase of graphitic-N content are observed when S and N dopants are co-present. While graphitic-N has a better thermostability and is typically formed at high annealing temperature, the promoted content of graphitic-N in the presence of S atom in NS-CNO(700) is attributable to the geometric effect of S.¹⁸⁸ It was previously reported that, although a direct bonding between S and N is not favored, the presence of either one in the neighboring rings could promote the incorporation of the other.²⁰⁸

The same N chemical configurations are revealed by X-ray absorption spectroscopy (XAS), as shown in Figure 3.3(g). The XAS results also confirmed that N, S co-doping yielded the high content of graphitic N (For detailed explanations of XAS results, refer to section 3.5.7). Thus, in CNO, the highly curved local structure may get relaxed by the presence of S and allows the formation of graphitic-N at 700 °C. This observation is in good agreement with literature reports.⁵² Therefore, these S and N atoms in close proximity may adopt the clustered configuration of dopants visualized in STEM images of this study

(Figure 3.2(b)).^{52, 77} The concerted arrangement of S and graphitic-N may also generate active sites for the adsorption of CO₂ by increasing spin and charge densities.^{166, 168}

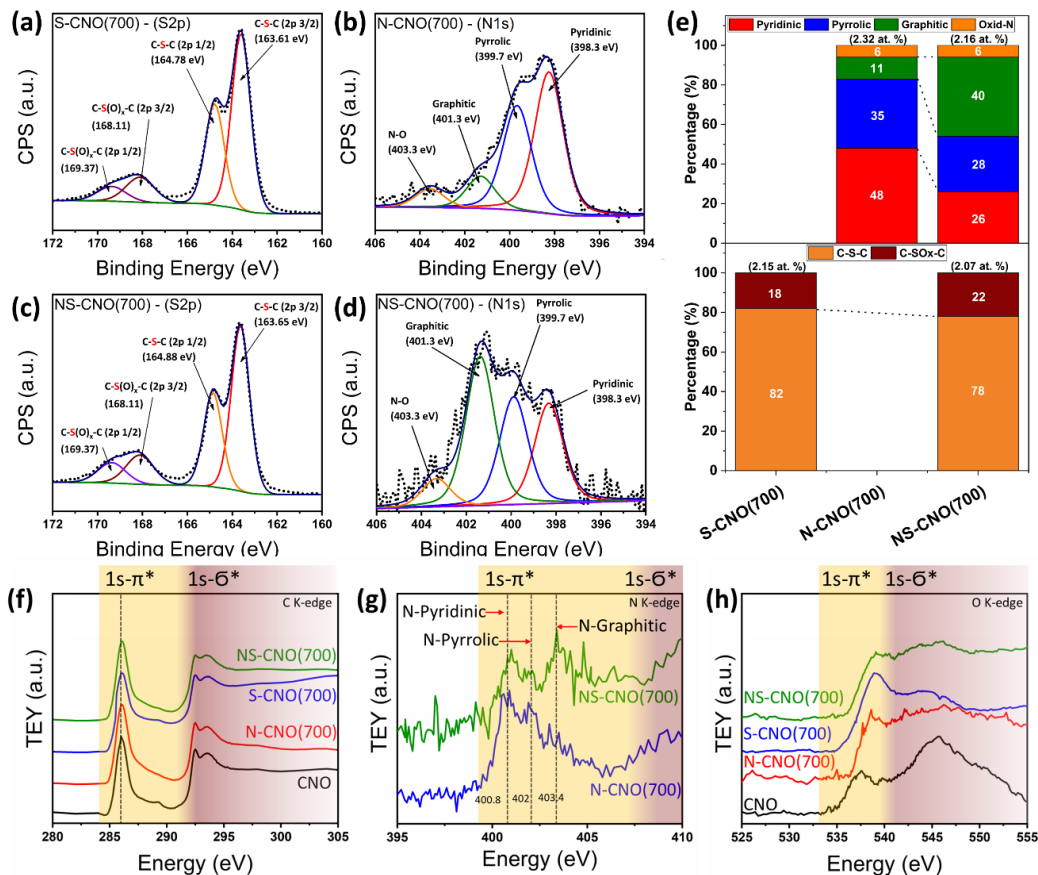
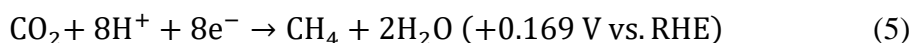
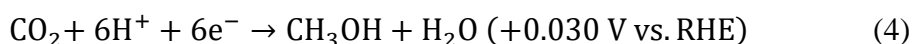
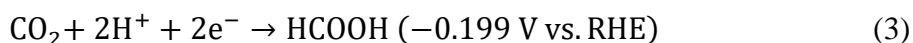
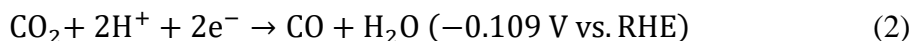


Figure 3. 3 High-resolution XPS characterization of (a) S-CNO(700)-(S2p), (b) N-CNO(700)-(N1s), (c) NS-CNO(700)-(S2p), (d) NS-CNO(700)-(N1s), (e) calculated percentages of N and S configurations and X-ray Absorption Spectroscopy (XAS) of (f) C K-edge, (g) N K-edge and (h) O K-edge of samples.

3.3.3 Electrochemical Characterization

Electrochemical characterizations were performed in a customized H-cell (Figure S3.9). Figure 3.4 presents cyclic voltammetric (CV) curves recorded when 0.1 M KHCO₃ solution was saturated with CO₂ or N₂. All doped CNOs display significantly larger cathodic currents with CO₂ than N₂ clearly proving their activity for CERR, while the

undoped CNO has a poor activity. These observations suggest that N and S dopants play a key role in promoting activity for CERR. NS-CNO(700) shows the highest current density with the lowest overpotential among all samples. Cathodic currents in CVs could originate from one or a combination of reactions listed below.¹³²



where the reaction (1) is for hydrogen evolution, and the reactions (2-5) produce various products from CO₂.

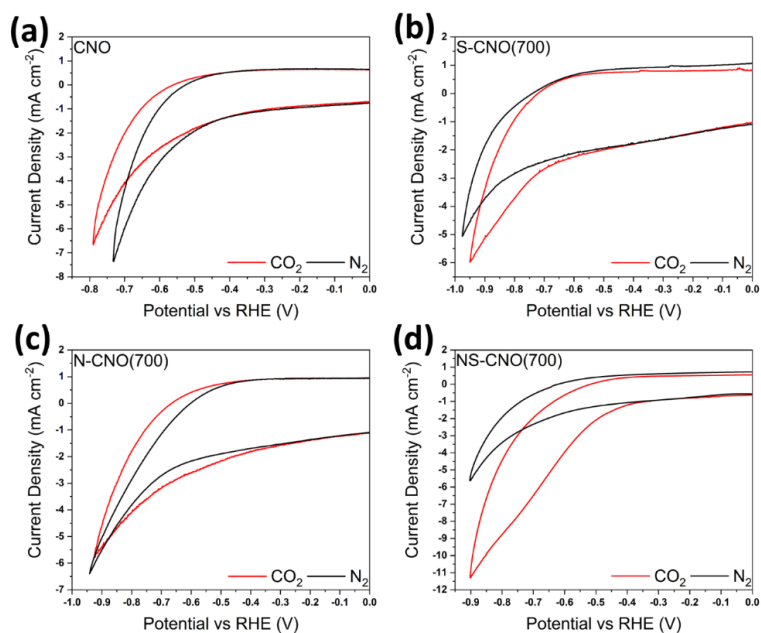
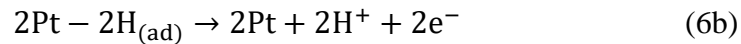


Figure 3. 4 Cyclic voltammograms of (a) pristine CNO, (b) S-CNO(700), (c) N-CNO(700), and (d) NS-CNO(700) in aqueous electrolyte saturated with CO₂ gas at the scan rate of 50 mV s⁻¹. For the comparison, cyclic voltammogram of each catalyst was also recorded in saturated N₂.

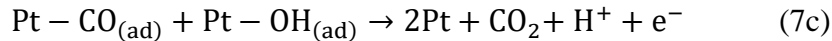
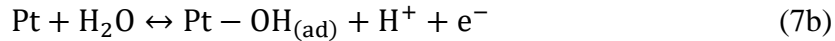
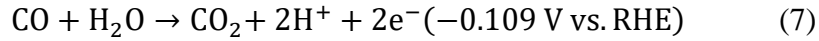
We employed a rotating-ring-disk-electrode (RRDE) technique as an *in-situ* probe of hydrogen evolution reaction (HER) and CERR. The RRDE technique is commonly used to determine the kinetics of electrochemical systems, including ORR.²⁰⁹ The RRDE used in this work is a double-working electrode where a catalyst is on the center glassy carbon disk, and a Pt is on the outer ring. With a convectional flow by the RRDE rotation, produced H₂ and CO from the catalyst are captured by the Pt ring. Until now, the RRDE technique has not been extensively applied to CERR.²¹⁰ This study demonstrates that the RRDE technique is a viable method to screen catalytic materials rapidly. Furthermore, due to the sensitivity of this technique, the onset potential for CERR can be determined accurately. RRDE CVs recorded with undoped and doped CNOs are shown in Figure 3.5.

H₂ generated by a catalyst through hydrogen evolution reaction (HER) can be adsorbed on the Pt ring (reaction (6a)). The adsorbed hydrogen can be desorbed into protons (reaction (6b)). This oxidation process is indicated by the positive anodic current.²¹¹



CNO, S-CNO(700), and N-CNO(700) show clear HER activities by revealing hydrogen oxidation currents in the CVs (Figure 3.5(a) – (c)). In other words, the upshift of CV curve is observed for these catalysts at low overpotentials, indicating predominant HER at low overpotentials.

The production of CO by a catalyst is probed by oxidation ring currents in CVs (Figure 3.5). These symmetric oxidation currents are due to the stripping of CO molecules adsorbed on the Pt ring. The detailed process of CO stripping is shown as follows.^{211, 212}



Although the thermodynamic potential of CO stripping to CO₂ shown in reaction (7) is closer to that of HER (reaction (6)), CO stripping is kinetically sluggish, so it requires a large overpotential as shown in Figure 3.5.^{212, 213} In NS-CNO(700), three definite peaks emerge in the oxidative sweep between 0.4 V and 1.1 V (Figure 3.5(d)). These peaks are labeled as peaks (i), (ii), and (iii). The peak (i) is so-called a prepeak, and the peak (ii) and (iii) are primary CO stripping peaks.²¹³ The prepeak current is recorded at unusually low overpotential, and it is attributable to the oxidation and rearrangement of CO adlayer on Pt when the adlayer is formed with very high coverage.^{213, 214} The peaks (ii) and (iii) originate from normal CO stripping events occurring at two morphological Pt sites i.e., terrace and step sites, respectively.²¹⁵ The absence of prepeak in CNO, S-CNO(700), and N-CNO(700) indicate that those samples have a low activity towards the CO production at the potential range (-0.10 V to -0.50 V vs. RHE). Also, the peak (ii) in Figure 3.5(d) is gradually shifted with more negative disk potential. This shift is due to the switch of CO adsorption geometry on Pt from “bridge” to “top” as the concentration of CO influx increases.²¹⁶ The CO onset

for NS-CNO(700) is about -0.2 V vs. RHE by the first appearance of peak (ii) in Figure 3.5(d).

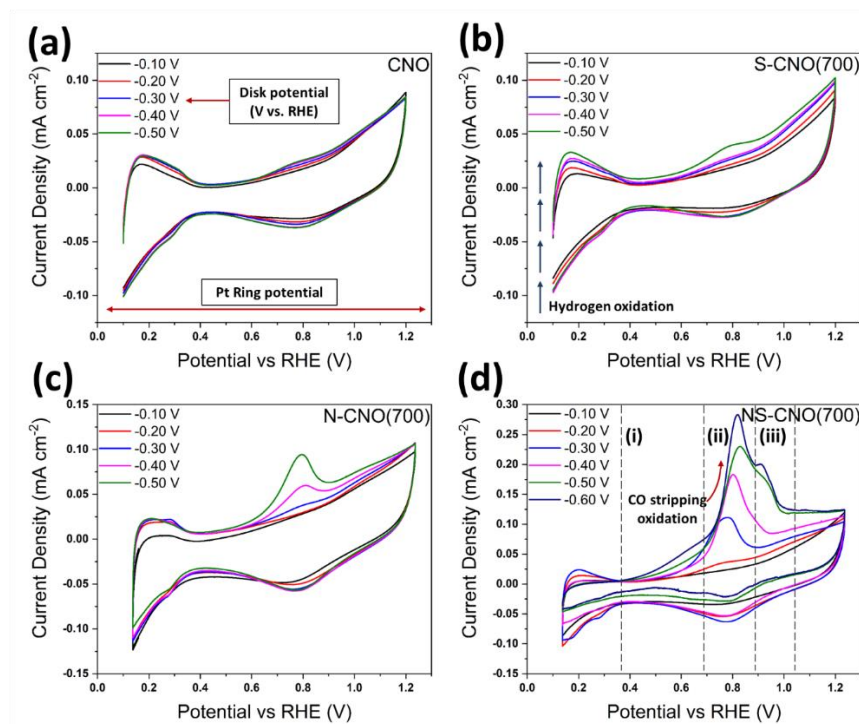


Figure 3. 5 RRDE measurements of (a) CNO, (b) S-CNO(700), (c) N-CNO(700), and (d) NS-CNO(700) to determine the onset potential of CO formation in the presence of CO₂ gas at a scan rate of 50 mV s⁻¹(1000 rpm). The potential at the Pt ring was scanned from 0.10 V to 1.20 V (vs. RHE), while a fixed potential was held at the disk.

Faradaic efficiencies (FE's) of each catalyst were determined by quantifying the products of CERR electrolysis. The electrolysis was conducted by holding potential at the WE while an electrolyte (0.1 M KHCO₃ saturated with CO₂) was circulated through an electrochemical cell by a peristaltic pump at the rate of 5 ml min⁻¹. After the electrolysis, gaseous products were quantified by gas chromatography (GC), and liquid products were quantified by ¹H NMR. CO and H₂ gases were major gaseous products, and a small quantity of CH₄ was also detected. Formic acid was the only liquid product.

FE's (%) of four catalysts for products H₂, CO, HCOOH, and CH₄ at the applied potential are summarized in Figure 3.6. Pristine CNO has no activity towards CERR as it only generates H₂. All doped CNOs have enhanced catalytic activities. S-CNO(700) generates HCOOH (the maximal FE (FE_{max}) = 15 % at -0.80 V), CO (FE_{max} = 24 % at -1.1 V), and CH₄ (FE_{max} = 5 % at -0.90 V), but its performance is inferior to N-CNO(700) and NS-CNO(700). Notably, N-CNO(700) shows high selectivity for HCOOH over CO. HCOOH starts being generated at -0.50 V vs. RHE, and FE_{max}(HCOOH) reaches 55 % at -0.70 V. The generation of CO is limited (FE <20 %) in this potential range. Most importantly, NS-CNO(700) shows the best performance for CO generation with a remarkable selectivity and a low overpotential. This observation is consistent with the RRDE results. CO formation is dominant in the potential window between -0.4 V and -0.8 V, and its FE_{max} reaches 82 % at -0.50 V vs. RHE. The FE's of N, S-CNOs prepared at 600 °C and 800 °C are presented in section 3.5.9.

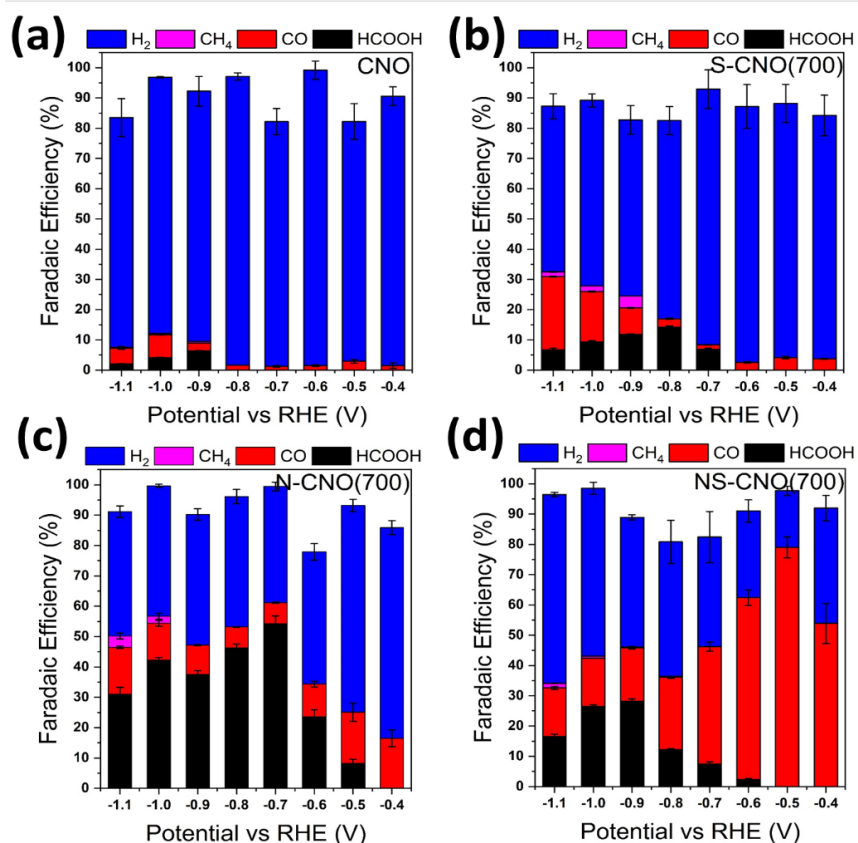


Figure 3. 6 Faradaic efficiencies for gaseous and liquid products in (a) CNO, (b) S-CNO(700), (c) N-CNO(700), and (d) NS-CNO(700)

Previous articles reported the poor CERR activity of S-doped carbon for CO production (FE < 2 %).^{59, 171, 217} In this study, S-CNO(700) shows a moderate activity towards CO (FE_{max} > 20 %) and HCOOH (FE_{max} ~ 15 %). Although S and C have similar electronegativity, C atom bonded to S holds a negative charge due to two extra valance electrons donated from S atoms.²¹⁸ Furthermore, the curved morphology of CNOs pushing electron density outward and stabilizes the adsorption of CO₂ molecules and creates higher CERR activity than S-doped graphene reported in the literature.¹⁷⁵ It is noteworthy that with the increased potential, the major product changes from HCOOH to CO. This switch may occur due to the presence of two active sites associated with S dopants.²¹⁹ A similar

switch in products, HCOOH and CO, was previously attributed to two active sites, α -phase and β -phase of palladium-hydrides.²¹⁹ In a different study, this switchable performance was also noted in PTFE treated copper with surface aerophilic and superhydrophobic properties.²²⁰

N-CNO(700) and NS-CNO(700) demonstrate unique reaction pathways for CERR. N-CNO(700) is efficient in producing HCOOH, while NS-CNO(700) is highly selective towards CO production. These differences imply that the reactions involve two different active sites. Based on XPS and XAS results, N-CNO(700) has plenty of pyridinic-N and pyrrolic-N sites that may be selective towards the HCOOH pathway (Refer to section 3.5.9). Conversely, NS-CNO(700) has the maximal contents of graphitic-N and C-S-C (sulfide). The synergistic effect of graphitic-N and sulfide groups in proximity seems to generate a highly selective route to CO production. This argument is well supported by our theoretical calculations in the next section.

3.3.4 Theoretical evaluation of the activity of NS-CNO catalyst

To provide valuable insights into catalytic sites for CO production, computational tools are developed and implemented to establish a structure-activity relation. Based on the information provided by STEM images, FT-IR and XPS, 4378 chemically unique atomic models of various defects are generated with C₆₀ as the base structure. A computational workflow has been developed using semi-empirical PM7 Hamiltonian to perform energetic calculation, geometric optimization, and frequency analysis.¹⁷⁷⁻¹⁷⁹ With pre-defined reaction intermediates, such a workflow can evaluate important descriptors of reaction energetics, e.g., adsorption energies, free energy changes (supplementary information section 3.5.11).

Following previous studies, CO evolution is assumed to occur through two steps: (i) the formation of surface-adsorbed *COOH and (ii) the formation of CO, as shown in Figure 3.7.^{5, 20, 221, 222} The reaction route to CO production is highlighted in yellow in Figure 3.7. Knowing the intermediates on the reaction pathway, free energy changes between intermediates can be used to estimate electrocatalysis performance.⁵

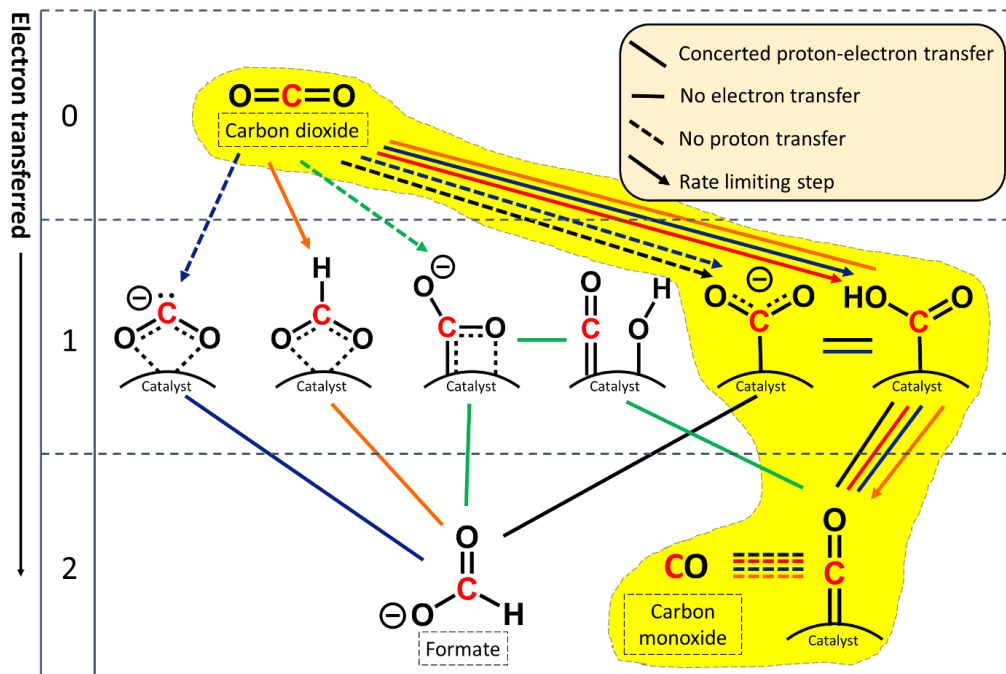


Figure 3. 7 Possible mechanistic pathways of CO₂ reduction to CO and HCOOH. Legend at the top-right indicates the implication of the lines that connecting intermediates: Blue-Kortlever et al.,²²³ Orange-Feaster et al.,²²¹ Green-Chernyshova et al.,²²⁴ Black-Hori et al.,¹⁶⁰ Red-Peterson et al.,¹⁵⁴ Adapted from the mechanistic pathway by Chorkendorff et al.⁶

As implemented in the CHE model,^{154, 180} MIG, the largest free energy increment between neighboring minima along the reaction pathway, can be considered as the infimum of onset potential. This method is used to identify the 50 most active (lowest MIG) configurations for CO production, as shown in Figure 3.8(a), where the stoichiometry of defect structure is represented by bar colors (blue: N-doped only, yellow: S-doped only, red: N, S co-doped) and the first eight configurations are shown in Figure S3.11 with adsorption site haloed. From Figure S3.11, most of the active configurations are N, S co-doped, which is in a good agreement with experimental results where co-doped samples show the least cathodic onset potential. Specifically, the highest active domain of configuration 1 (Figure S3.11) consists of graphitic N and sulfide functional groups further

confirming synergistic effect of N and S. Furthermore, the CO onset potential determined for NS-CNO by theoretical calculations (~ -0.25 V vs. RHE) falls closer to that of determined by the RRDE technique (~ -0.2 V vs. RHE). In Figure 3.8(b), free energy changes for CO and COOH desorption processes in different configurations are plotted as colored scatters, where the configurations not shown in Figure 3.8(a) are denoted by gray scatters. It is apparent that the superiority of the configurations in Figure 8(a) originates from moderately strong adsorption for *COOH and weak adsorption for *CO.

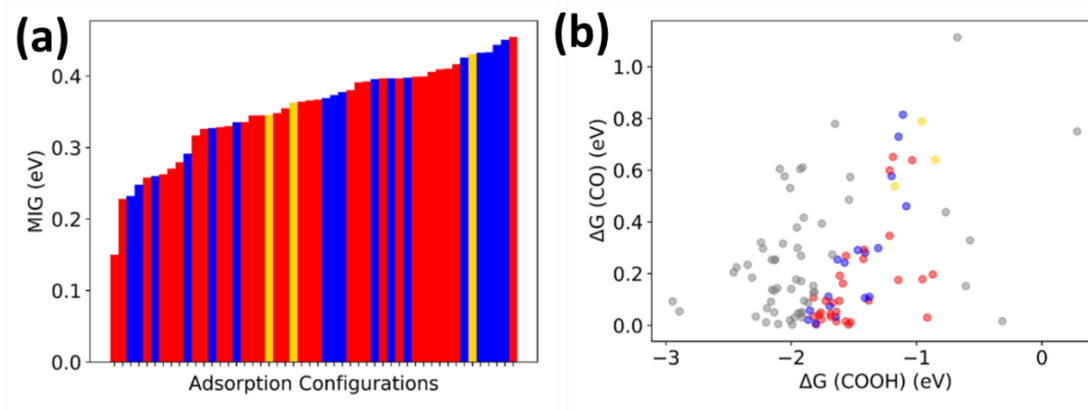


Figure 3. 8 (a) Colored bar chart of the 50 lowest MIG calculated based on different configurations. The bars are colored blue, red, yellow for N-doped, N, S-doped, S-doped structures, respectively. (b) A colored scatter plot of free energy changes in CO/COOH desorption processes for various configurations, where a color code is inherited from (a) except that the gray markers denote the configurations excluded from the bar chart.

3.3.5 Performance Comparison

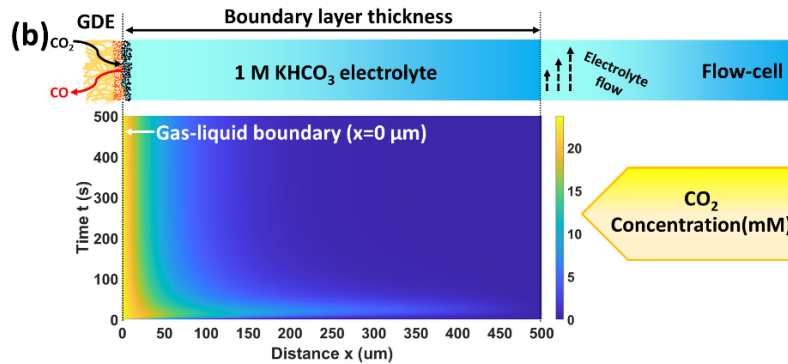
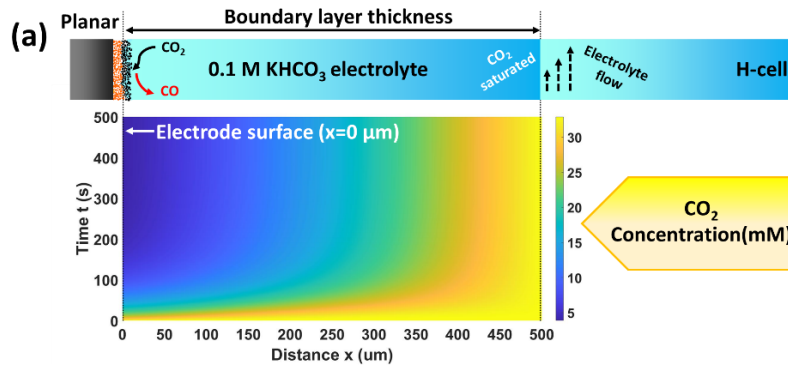
The durability of NS-CNO(700) was evaluated in prolonged electrolysis (Figure 3.9(c)). CERR was performed for 30 hours in 1 M KHCO_3 electrolyte with a modified flow-type electrolysis cell (Figure S3.9, bottom). In this cell, the cathode catalyst is deposited on a gas-diffusion electrode (GDE) to overcome the slow mass transfer of CO_2 and to transport CO_2 to the catalyst-electrolyte interface efficiently. The differences in CO_2

mass transfer rates between H-cell and GDE cells were modeled via the reaction-diffusion model (Figure 3.9(a)-(b)), refer appendix for more details. The CO₂ concentration under operating conditions of H-cell is significantly depleted in the vicinity of the electrode (Figure 3.9(a)), whereas on the GDE electrode, high CO₂ concentration is maintained (Figure 3.9(b)) even at high current densities. Therefore, GDE configuration enhances the selectivity towards CERR, resulting in high activity at low overpotential.^{183, 225, 226} After a noticeable decay in activity during the first 2 hours, NS-CNO(700) demonstrates a stable performance for 20 hours: partial current density for CO production is -10.8 mA cm⁻², and the FE is 91 % at the overpotential of 0.39 V. After 20 hours, the current density becomes irregular due to an electrolyte flooding in the gas diffusion layer.

After 30-hour electrolysis, the cell was disassembled, and XPS analysis was performed to track the deterioration of the catalyst (see supplementary information section 3.5.12). Figure S3.13 presents the XPS results for NS-CNO(700) before and after the durability test. Clearly, the contents of both N and S are decreased after electrolysis. The reduction of the N content is relatively small (from 1.9 at. % to 1.6 at. %, Figure S3.13 (a-b)). High-resolution N1s XPS spectra (Figure S3.13 (c-d)) suggest that graphitic N is intact, but pyridinic N is more vulnerable and changes to pyridonic and pyridinic-COOH. A similar deterioration of pyridinic N was previously reported.^{55, 227} Our discovery implies that graphitic N may involve with S sites and play a pivotal role in CERR instead of pyridinic-N or pyrrolic-N sites for the generation of CO, which is in a good agreement with our theoretical results. In contrast to the relatively minor damages in N configurations, the changes in S configurations are more severe (reduction from 1.9 at. % to 1.3 at. %) due to

oxidation. The observed activity loss during the first 2 hours of electrolysis may be due to the loss of N and S dopants.⁵⁹

In Figure 3.9(d), the performance of NS-CNO(700) is compared with other metal-free catalysts reported in the literature. Overall, NS-CNO(700) exhibits a remarkable performance with very low overpotential and a high FE for CO production, outperforming most of the other metal-free catalysts. However, the CERR partial current density of NS-CNO(700) is lower than many metal-based catalysts, even with the integration of gas-diffusion electrodes (see supplementary information section 3.5.13). Possibly, the main reason for the lower current density is the low concentration of active sites since the atomic percentage of dopants is limited to ~2%.¹⁵⁸ To tackle this challenge, progress needs to be made in catalyst synthesis to amplifying catalytic sites.²²⁸ Furthermore, the precise engineering of interfaces and the component interactions of the GDE will also assist in boosting the overall current density.



(c) NS-CNO(700) durability in 1M KHCO_3 (GDE config)

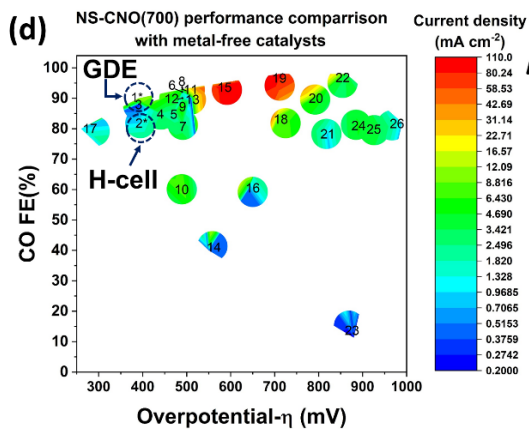
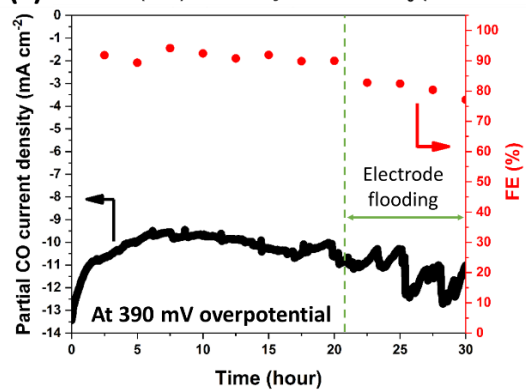


Figure 3. 9 (a) Availability of CO₂ in 0.1 M KHCO₃ (H-cell configuration at -0.92 mA cm⁻² current density, x=0 represents the surface of the planar electrode), (b) availability of CO₂ in 1 M KHCO₃ (GDE configuration at -12 mA cm⁻² current density, x=0 refers to the base of the GDE where gas-liquid boundary exists), (c) durability test of NS-CNO(700) and (d) performance comparison of NS-CNO(700) electrode with other CO generating metal-free catalysts (numbers refer to the catalysts listed in Table 3.2, The magnitude of the current density at each data point is represented by various color intensities).

Table 3. 2 Performance comparison of NS-CNO(700) electrode with other CO generating metal-free catalysts (The table summarizes experimental conditions and the details of the performance for each catalyst)

No	Catalyst	Electrolyte	Testing condition	η / mV	FE/%	Current density / mA cm ⁻²	Durability/ hr	Reference
1	NS-CNO(700) N, S co-doped carbon nano onions	1 M KHCO ₃	Flow-cell GDE Electrolyte flow rate-5 ml min ⁻¹	390	91	10.8	20	This work*
2	NS-CNO(700) N, S co-doped carbon nano onions	0.1 M KHCO ₃	H-cell Electrolyte flow rate-5 ml min ⁻¹	390	82	0.92	-	This work*
3	CN-H-CNTs Steam etched nitrogen-doped carbon nanotube	0.1 M KHCO ₃	H-cell	390	88	0.25	6.7	Cui et al. ⁵⁷
4	NS-CNSs-1000 N,S - doped carbon nanosheet	0.5 M KHCO ₃	H-cell	440	85	2.5	20	Wang et al. ²²⁹
5	NG-800 N-doped three-Dimensional Graphene Foam	0.1 M KHCO ₃	Flow-cell GDE	470	85	1.8	5	Wu et al. ⁵⁴
6	NS-C-900 N,S co-doped carbon layers	0.1 M KHCO ₃	H-cell (Stirring)	490	92	2.63	20	Pan et al. ⁵⁹
7	NRMC-900-3 Mesoporous Carbon Catalyst	0.1 M KHCO ₃	H-cell	490	81	2.9	10	Daiyan et al. ¹³³
8	NSCNW-3 N,S -dual doped carbon nanoweb	0.1 M KHCO ₃	H-cell	490	93	5.9	20	Han et al. ¹⁷⁰
9	N-GRW_GM2 3D nitrogen-doped graphene nanoribbon networks	0.5 M KHCO ₃	H-cell	490	87.6	~7	10	Liu et al. ²³⁰
10	CF-120 N-doped tubular carbon foam	0.1 M KHCO ₃	H-cell Stir	490	60	~7.5	8	Li et al. ²³¹
11	CNPC-1100 Coal-derived N-doped porous carbon electrocatalyst	0.1 M KHCO ₃	H-cell	490	92	~0.9	8	Li et al. ²³²
12	NF-C-950 N, F-co-doped holey Carbon Layers	0.1 M KHCO ₃	H-cell (Stirring)	490	90	1.9	40	Pan et al. ²³³
13	FC Fluorine-Doped Carbon	0.1 M KHCO ₃	H-cell	510	90	0.23	-	Xie et al. ²³⁴
14	BAX-M-950 N-doped porous carbon catalysis	0.1 M KHCO ₃	H-cell	550	40	0.44	24	Li et al. ²³⁵
15	NSHCF900 N, S co-doped hierarchically porous carbon nanofiber	0.1 M KHCO ₃	H-cell	590	94	103	36	Yang et al. ¹⁶⁹
16	g-C₃N₄/MWCNT Graphitic carbon nitride attached multiwall carbon nano tubes	0.1 M KHCO ₃	H-cell	640	60	0.5	-	Lu et al. ²³⁶
17	NCNT Nitrogen-doped carbon nano tubes	0.1 M KHCO ₃	Flow-cell GDE	260	80	1	10	Wu et al. ⁵³
18	NDC-700 Biomass-derived N doped porous carbon	0.5 M NaHCO ₃ 500 rpm	H-cell	710	84	8	72	Li et al. ²³⁷
19	CN/MWCNT Carbon nitride and multiwall carbon nanotube composite	1M KCl	Flow-cell GDE	710	98	90	-	Jhong et al. ²³⁸
20	NCNT-3-700 N-doped carbon nano tube	0.5 M NaHCO ₃	H-cell	790	90	5.8	60	Xu et al. ⁵⁸

21	NC-900 Metal-Organic-Framework-Mediated Nitrogen-Doped Carbon	0.1 M KHCO ₃	H-cell Electrolyte flow rate 100 ml min ⁻¹	820	78	0.85	-	Wang et al. ²³⁹
22	CNFs N-doped carbon nanofibres	EMIM-BF ₄	Single cell	863	98	~3.5	9	Kumar et al. ²⁴⁰
23	CPSN N,S co-doped nanoporous carbon	0.1 M KHCO ₃	H-cell	880	11.3	0.26	27	Li et al. ¹⁷¹
24	P-OLC-CVD P-doped onion like carbon	0.5 M NaHCO ₃	H-cell	890	81	4.9	27	Liu et al. ¹⁶¹
25	ACN-850 N-doped microporous carbon nano tubes	0.1 M KHCO ₃	Flow-cell GDE	940	80	3.5	-	Sharma et al. ⁹²
26	NDC-4 N-doped ultrananocrystalline diamond	0.1 M KHCO ₃	H-cell	990	82	0.83	-	Wanninayake et al. ⁵

3.4 Summary

For the first time, N, S singly doped and co-doped CNOs were systematically investigated for CERR. All dopants have demonstrated marked and distinctive impacts on CERR activity. The local structures of active sites were strongly influenced by doping temperature and co-dopant. N-CNO(700) and NS-CNO(700) were highly selective towards HCOOH and CO, respectively. In the GDE configuration, NS-CNO(700) showed the best performance for CO production with the highest selectivity of (91 %) at 390 mV overpotential. STEM measurements visualized local structures associated with dopants and defects. XPS and XAS analyses suggested that the synergistic combination of graphitic-N and sulfide configurations in close proximity may be the origin for the pronounced activity of NS-CNO(700), which was further supported by theoretical calculations. Finally, enhanced CO production rate and selectivity were attained with the attachment of gas diffusion electrodes. Which clearly addresses the importance of mass transport effects towards CERR.

3.5 Supplementary information

3.5.1 NMR quantification of formic acid

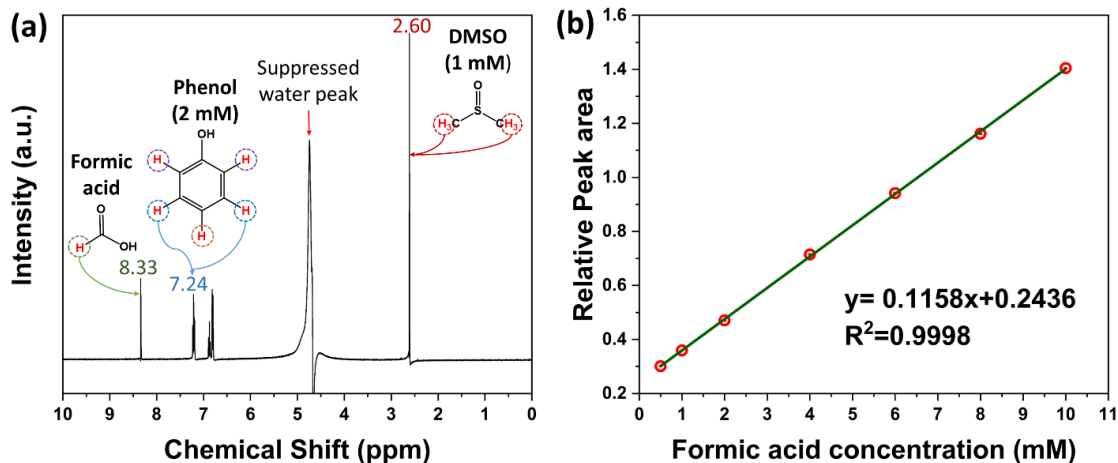


Figure S3. 1 (a) 1D ¹H NMR spectrum of a sample containing the formic acid analyte. (b) a calibration plot of formic acid using phenol as an internal standard (a relative peak area = area of formic acid (peak at 8.33 ppm) / Area of phenol (peak at 7.24 ppm)). Phenol and DMSO are internal standards.

3.5.2 Calculation of faradaic efficiencies (FE's) for liquid and gaseous products

The faradaic efficiency of HCOOH was calculated according to the following equation.

$$\text{Faradaic efficiency} = \frac{e_{\text{output}} \times 100}{e_{\text{input}}} \%$$

$$\text{Faradaic efficiency} = \frac{x \text{ (mol)} \times n_e \times F \times 100\%}{I \text{ (A)} \times t \text{ (s)}}$$

Where,

e_{output} = the number of electrons in moles supplied for the generation of a specific liquid product (mol)

e_{input} = a total number of electrons in moles provided to the electrode during electrolysis (mol)

x = the quantity of a specific liquid product in moles determined by NMR analyses (mol)

n_e = the number of electrons in mol required to obtain 1 mol of formic acid

F = Faraday constant (96485.3329 A s mol⁻¹)

I = The average of chronoamperometric currents recorded during electrolysis (A)

t = Duration of electrolysis (s)

Faradaic efficiency for each gaseous product was calculated according to the following equation.

$$\text{Faradaic efficiency} = \frac{e_{\text{output}} \times 100}{e_{\text{input}}} \%$$

$$\text{Faradaic efficiency} = \frac{x (\text{mol}) \times n_e \times F \times Q (\text{sccm}) \times 100\%}{I (\text{A}) \times V (\text{cm}^3) \times 60}$$

Where,

e_{output} = the number of electrons in moles supplied for the generation of a specific gaseous product (mol)

e_{input} = a total number of electrons in moles provided to the electrode during the collection of V volume of gas (mol)

x = the quantity of specific gaseous product in moles determined by GC analyses (mol)

n_e = the number of electrons required to obtain 1 mol of a specific gaseous product

F = Faraday constant (96485.3329 A s mol⁻¹)

Q = the flow rate of carbon dioxide carrier gas (sccm)

I = the average of chronoamperometric currents recorded during electrolysis (A)

V = The volume of gas injected into GC (cm³)

3.5.3 Raman spectroscopic analysis

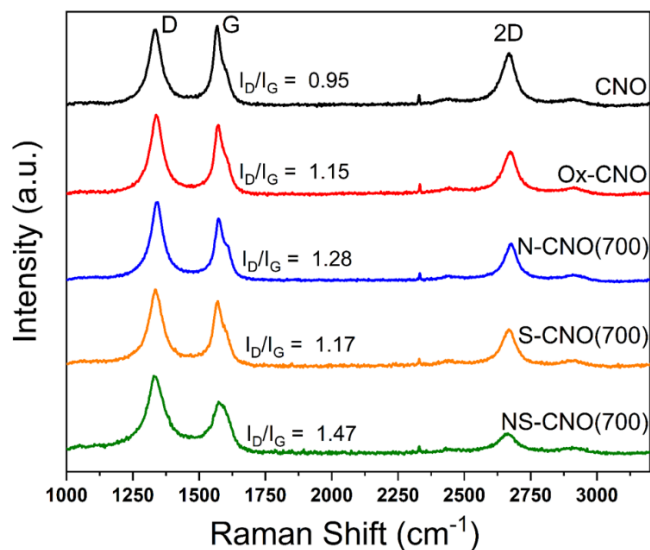


Figure S3. 2 Raman spectra of CNO, Ox-CNO, N-CNO(700), S-CNO(700) and NS-CNO(700).

Table S3. 1 Parameters determined from Raman spectroscopic analysis

Sample	D-band shift (cm ⁻¹)	G-band shift (cm ⁻¹)	2D-band shift (cm ⁻¹)	I _D /I _G	I _{2D} /I _G	2D-band FWHM (cm ⁻¹)
CNO	1336.07	1568.23	2668.55	0.95	0.64	65
Ox-CNO	1337.95	1573.15	2672.66	1.15	0.61	64
N-CNO(700)	1338.81	1572.85	2679.55	1.28	0.59	59
S-CNO(700)	1333.50	1570.84	2667.52	1.17	0.58	66
NS-CNO(700)	1331.46	1573.23	2662.74	1.47	0.41	80

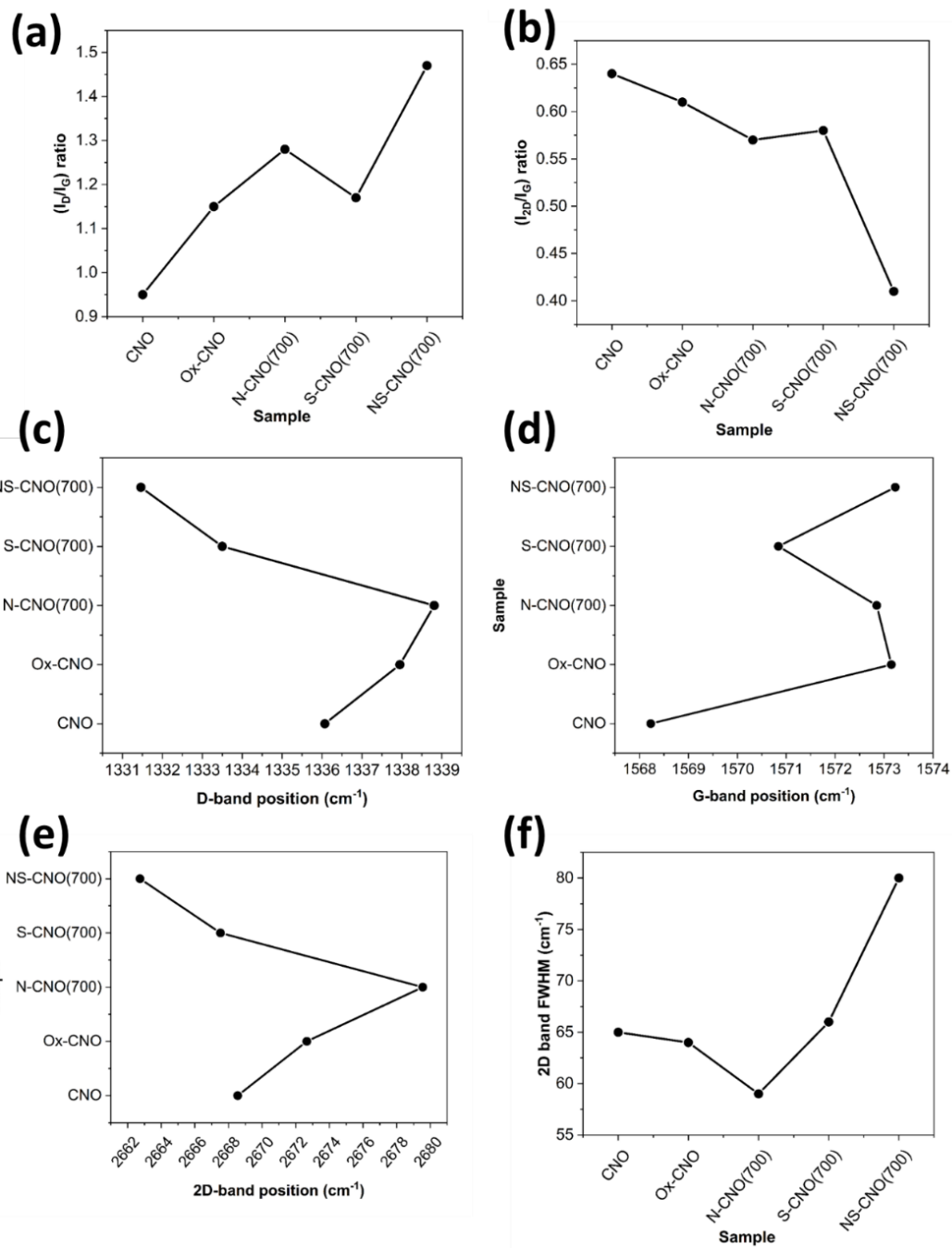


Figure S3. 3 The plots of (a) I_D/I_G , (b) I_{2D}/I_G , (c) D-band position, (d) G-band position, (e) 2D band position, and (f) 2D band FWHM determined from Raman spectra

Raman spectroscopy is a powerful tool to probe defects and electronic structures of carbon materials. The intensity ratio of I_D/I_G represents the degree of a microstructural

disorder in CNOs. Figure S3.3(a) presents the trend of I_D/I_G , showing that doping processes increase the disorder of CNOs, and NS-CNO(700) is the most disordered. Both D and G-band positions are sensitive to structural stress and the types of charge carriers created by heteroatom dopants.²⁴¹⁻²⁴³ It was reported that N and O dopants induced the blue-shift of D-band.^{242, 243} In this work, the D-bands in both Ox-CNOs and N-CNOs are blue-shifted relative to the D band in pristine CNOs, while the D-bands in S-CNOs and NS-CNOs are shifted oppositely (Figure S3.3(c)). The G-band was reported blue-shifted with the increase of charge carrier concentration (both hole and electron). In this work, with respect to pristine CNOs, the blue-shift of G-band is found for in all treated samples (Figure S3.3(d)). Especially, the significant blue-shift of G-band in NS-CNO(700) and Ox-CNOs is found.

Unlike the D-band, the intensity of the 2D band (I_{2D}) is not sensitive to the defects but is sensitive to the charge carrier density.^{193, 196} The I_{2D}/I_G is a measure of charge carrier density, and it is inversely proportional to electron or hole densities²⁴⁴ In this work, NS-CNO(700) shows a significant reduction in the ratio of I_{2D}/I_G ($I_{2D}/I_G = 0.41$) compared to pristine CNO ($I_{2D}/I_G = 0.64$) in Figure S3(b). It indicates the clear n-type nature of NS-CNO(700) due to the large contents of graphitic-N and sulfide-S. Overall, NS-CNO(700) showed a high I_D/I_G ratio and a low I_{2D}/I_G ratio relating to the high number of defects as well as charge carrier density.

The position of 2D-band is sensitive to the type of charges carried by doping. The 2D-band was blue-shifted as the concentration of hole carriers increased. An opposite shift was found as the concentration of electron carriers increased.²⁴⁴ As shown in Figure S3.3(e), both Ox-CNOs and N-CNOs present a blue-shift of the 2D band relative to pristine CNOs, indicating the p-type characters. In contrast, S-CNOs and NS-CNOs show a red-

shifted 2D-band coming from their n-type characters. Since oxygen functional groups withdraw electrons from carbon, Ox-CNO is likely p-type. The situation is more complicated in N-CNOs since mixed N configurations are formed. Pyridinic-N and pyrrolic-N are known to be p-type, while graphitic-N is n-type.²¹⁸ Since pyridinic-N and pyrrolic-N are dominant in N-CNOs (Table S3.2 and Figure S3.6), the blue-shift of 2D-band in N-CNOs (Figure S3.3(e)) is consistent with the literature.⁵² A slight red-shift of the 2D band in S-CNO(700) is due to electrons donated by sulfide-S groups. A further red-shift in NS-CNO(700) is due to the contents of the sulfide-S and graphitic-N group since both groups donate electrons to the carbon host.^{52, 218}

Raman measurements can also be used to determine the Fermi level of a material.²⁴⁵ The full-width at half-maximum (FWHM) of a 2D band in Raman spectra is a measure of the Fermi level.²⁴⁶ For example, the sample with a widened 2D band implies an elevation of the Fermi level and a lowered work function.²⁴⁵ Figure S3.3(f) presents the trend of FWHM's of 2D peaks in all CNOs. Compared to pristine CNOs (FWHM = 65 cm⁻¹), Ox-CNOs present slightly smaller FWHM (FWHM = 64 cm⁻¹). Then, the 2D-band in N-CNO(700) becomes substantially narrower (FWHM= 59 cm⁻¹), implying the lowered Fermi level due to pyridinic-N and pyrrolic-N configurations. In S-CNO(700) and NS-CNO(700), the trend is reversed with FWHM's of 66 and 80 cm⁻¹, respectively. Especially, NS-CNO(700) shows the widest 2D band implying significant electron densities due to dopants, which are available for the interfacial charge transfer process of CERR.

3.5.4 XRD analysis

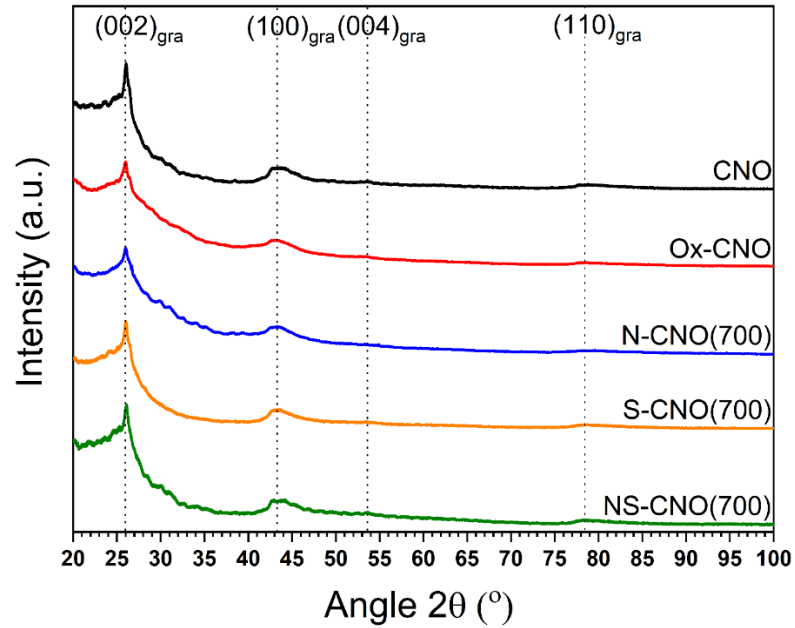


Figure S3. 4 XRD of CNO, Ox-CNO, N-CNO(700), S-CNO(700) and NS-CNO(700).

3.5.5 BET isotherms and pore size distribution

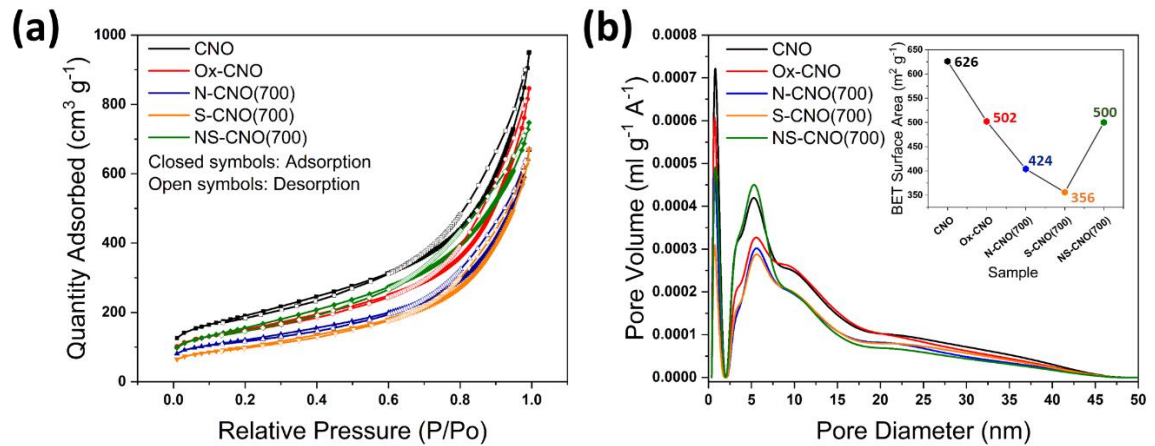


Figure S3. 5 (a) BET isotherms and (b) the pore size distributions of all samples. A plot of BET surface-areas is shown in the inset.

3.5.6 A summary of XPS results

Table S3. 2 A summary of XPS results

Sample	C1s (at. %)	O1s (at. %)	N1s (at. %)	Pyridinic (%)	Pyrrolic (%)	Graphitic (%)	N-O (%)	S2p (at. %)	Sulfide (C-S-C) (%)	C-SOx-C (%)
CNOs	99.04 ± 0.17	0.96 ± 0.16	-	-	-	-	-	-	-	-
Ox-CNOs	93.65 ± 0.35	6.35 ± 0.32	-	-	-	-	-	-	-	-
S-CNOs	96.57 ± 0.39	1.28 ± 0.23	-	-	-	-	-	2.15 ± 0.13	82	18
N-CNOs(600)	96.24 ± 0.60	2.42 ± 0.39	1.34 ± 0.19	46	29	13	12	-	-	-
N-CNOs(700)	96.45 ± 0.47	1.23 ± 0.19	2.32 ± 0.21	48	35	11	6	-	-	-
N-CNOs(800)	98.40 ± 0.30	0.77 ± 0.12	0.83 ± 0.14	43	31	16	10	-	-	-
NS-CNOs(600)	93.02 ± 0.51	2.05 ± 0.20	2.40 ± 0.18	33	33	26	8	2.53 ± 0.16	44	56
NS-CNOs(700)	94.45 ± 0.37	1.32 ± 0.11	2.16 ± 0.13	26	28	40	6	2.07 ± 0.10	78	22
NS-CNOs(800)	97.27 ± 0.41	0.91 ± 0.09	1.03 ± 0.11	28	35	25	12	0.79 ± 0.16	80	20

n=3

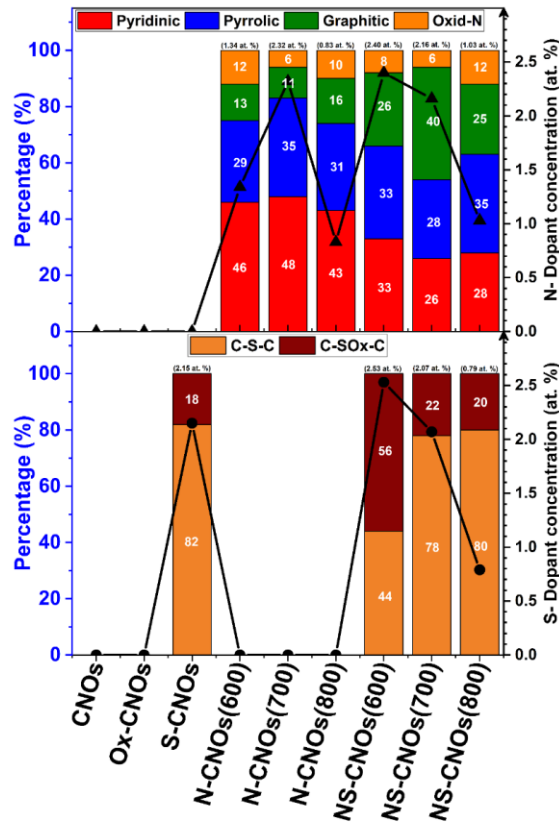


Figure S3. 6 A summary of dopant configurations in all samples determined by XPS analyses

Overall, the annealing temperature is found to influence both contents and chemical configurations of dopants. In N-CNOs, the N content is maximal (2.32 at. %) at 700 °C, and less at 600 °C (1.34 at. %) and 800 °C (0.83 at. %). However, the relative fractions of pyridinic-N, pyrrolic-N, and graphitic-N are similar at any temperature. In NS-CNOs, the maximal contents of both N (2.40 at. %) and S (2.53 at. %) are found at 600 °C. The contents of N and S are less at 700 °C (N, 2.16 at. %; S, 2.07 at. %) and 800 °C (N, 1.03 at. %; S, 0.79 at. %). All NS-CNOs contain more graphitic N than N-CNOs due to the influence of S. Consequently, the highest content of graphitic-N is noted in NS-CNO(700). In NS-CNO(800), the content of graphitic-N becomes less due to the removal of S groups. Unlike N, the chemical configuration of S is significantly influenced by temperature. At 600 °C, the highest portion of oxidized S (C-SO_x-C) (56%) is found. At the temperature of 700 °C or higher, sulfide (C-S-C) becomes dominant (78-80%). This temperature dependence of S configuration may result from the chemical reduction of oxidized S groups by ammonia gas. The two types of functional groups have a significant influence on the electronic properties of a catalyst because oxidized S withdraws electrons while sulfide-S donates electrons to the carbon host.

3.5.7 NEXAFS spectroscopy analysis

C K-edge

Figure 3.3(f), C K-edge spectra exhibit two distinguish adsorption edges. One is starting at 284 eV and the other one at 291 eV relating to the transition to empty π^* and σ^* , respectively.²⁴⁷ The C=C ($1s-\pi^*$) excitation leads to a feature at 286 eV in pristine CNO. Additional bands lying between 286.5 and 290 eV are due to the C-H and C-O/N/S

features.²⁴⁸ We do not see a separate feature for these structures due to the low concentration of dopants. However, the ($1s-\pi^*$) peak maximum shifts to 286.1 eV for the doped samples indicating a slight impact from heteroatoms. The strong feature at 292.5 eV is a well-known excitonic feature in carbon XAS ($1s-\sigma^*$).²⁴⁹ Doping reduces extended conjugation, and usually a single peak around 292.5 eV represents highly doped samples. The presence of a second feature at 293.5 eV represents a highly conjugated structure, which predicts the heteroatom-doping has a minor effect on the conjugation of CNO.

N K-edge

The characteristic of $1s-\pi^*$ excitation of N K-edge (Figure 3.3(g)) exhibits three distinct peaks for N-CNO(700) and NS-CNO(700) from 398 eV to 404 eV. These peaks can be attributed to pyridinic-N, pyrrolic-N, and graphitic-N configurations, respectively.²⁴⁹ We can also notice that the graphitic-N peak intensity of NS-CNO(700) is much higher than that of N-CNO(700). These observations are consistent with XPS results and further confirm the N and S co-doping predominantly generate graphitic-N.

O K-edge

The O $1s-\pi^*$ excitations for C=O are observed at around 535.7 eV for CNO(Figure 3.3(h)). The $1s-\pi^*$ is more prominent and is shifted to slightly higher energy, 536.5 eV for S and N doped CNOs. In addition to the presence of $1s-\pi^*$ C=O transitions, the presence of N and S dopants can introduce the small fraction of N=O and S=O type functional groups. The presence of these dopant moieties would include more O $1s-\pi^*$ transitions and shift this O $1s-\pi^*$ excitations to higher energy. For S-CNO(700), N-CNO(700), and NS-

CNO(700), we see broad peaks from 540-550 eV. These peaks are the combinations of $1s \rightarrow \sigma^*$ transitions in O-C, O-S, and O-N type groups. However, this same feature is narrow and more refined for the CNO, indicating an absence of any sulfur or nitrogen-based oxides.

3.5.8 FT-IR analysis

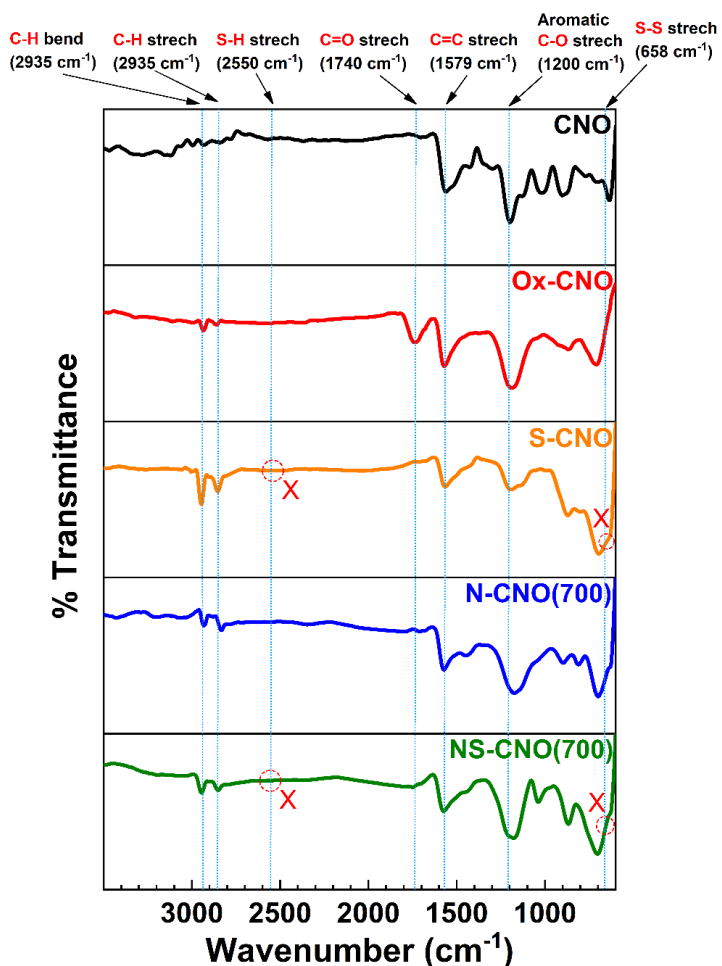


Figure S3. 7 FT-IR spectra of samples of interest

The presence of C-H bending and stretching vibrations in the FT-IR spectra of pristine and all treated CNOs suggests that defects are mostly terminated with hydrogen. Ox-CNOs present a significant increase in C=O stretching mode. In doped CNOs, the

intensity of the C=O stretching mode is suppressed, indicating oxygen functional groups are successfully replaced by heteroatoms. FT-IR can also probe S-H and S-S stretching groups in S-CNO(700) and NS-CNO(700). The absence of S-H and S-S stretching modes further suggests that S configuration in S-CNO(700) and NS-CNO(700) is mainly C-S-C instead of S-H or S-S.

3.5.9 Faradaic efficiencies of N-CNO and NS-CNO prepared at 600 °C and 800 °C

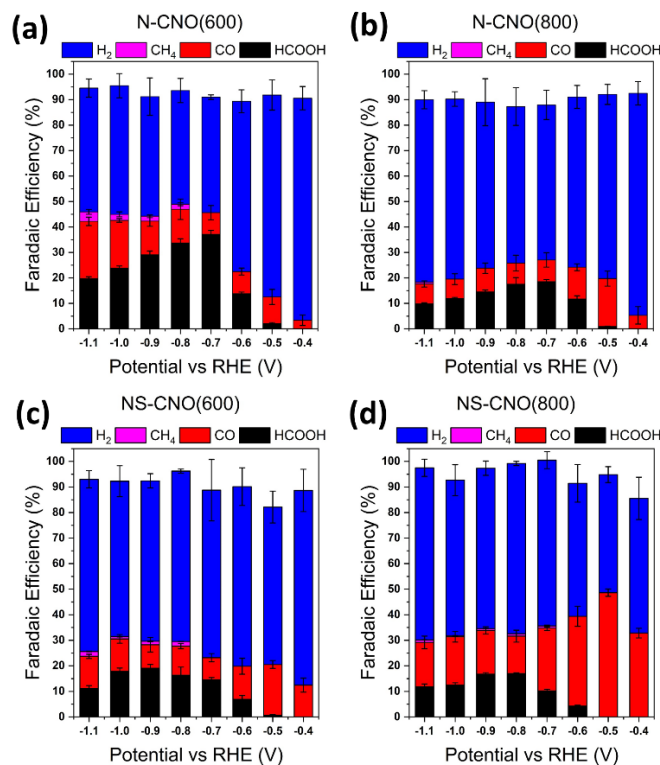


Figure S3. 8 Faradaic efficiencies of N-CNO and NS-CNO prepared at 600 °C and 800 °C.

N-CNO(600) and N-CNO(800) present lower FE's for HCOOH than N-CNO(700). The FE_{max} of HCOOH for N-CNO(600), N-CNO(700), and N-CNO(800) are 37%, 55%, and 19%, respectively. The inferior performances of N-CNO(600) and N-CNO(800) are

due to the lower concentrations of N dopants, more specifically, the lower contents of pyridinic-N and pyrrolic-N sites. Although both pyridinic-N sites act as a Lewis base, the surface passivation of active sites with hydrogen adsorption could block CO₂ adsorption.¹³³ Thus, during the formation of HCOOH, CO₂ may bind to the available Lewis acid sites (carbon atoms next to pyridinic-N/pyrrolic-N) on the catalyst as a Lewis base through its oxygen centers.^{6, 221} Overall, NS-CNO(600) and NS-CNO(800) present worse CERR performances than NS-CNO(700) with the lower FE_{max}'s for CO. The remarkable performance of NS-CNO(700) with the FE_{max} = 82 % is attributed to the high content of graphitic N and sulfide S.

3.5.10 Schematics of the H-cell electrochemical setup and the flow electrochemical setup

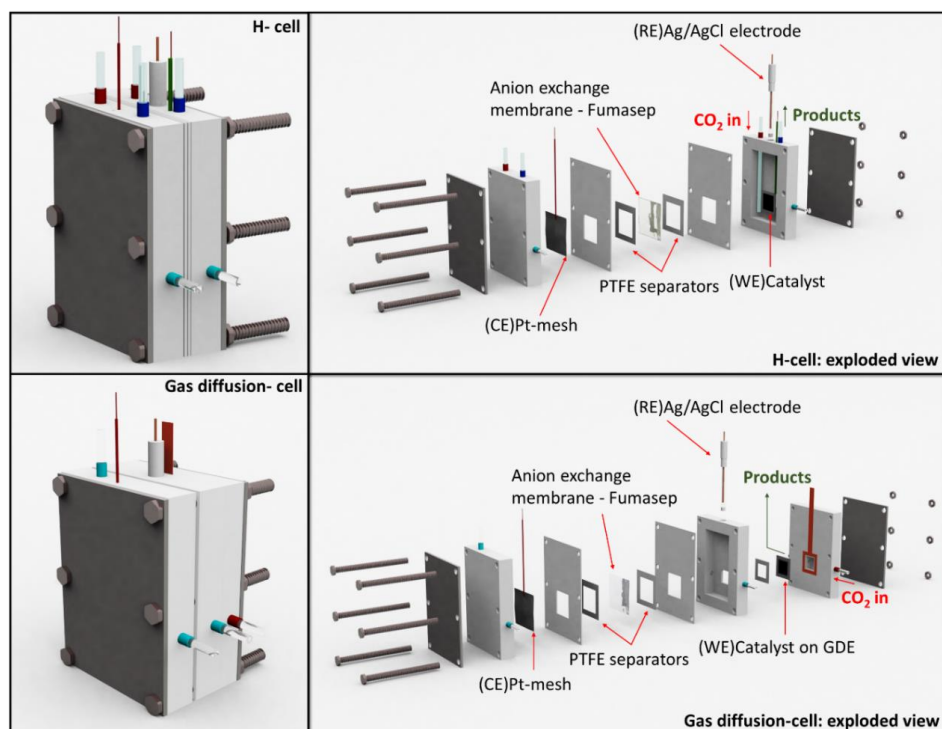


Figure S3. 9 Schematics of a H-cell and a flow-type cell (with gas-diffusion electrodes) used in this study

3.5.11 Computational methods

3.5.11.1 Defect/configuration Generation

While an accurate base structure for CNO simulation should be multi-layered fullerene, we choose C₆₀ as the base structure for generating defects/configurations to limit computation cost. We further note the term ‘defect’ or ‘defect structure’ is used to represent an adsorbent structure, and the term ‘configuration’ stands for a combination of an adsorbent and an adsorbate, thus highlighting the fact that one defect can have multiple adsorption sites (that is, one *defect* can have multiple *configurations*).

Based on XPS, FT-IR, and STEM results, we make the following assumptions for a possible defect:

1. There should be no S-S, N-N, or S-N bond (verified by FT-IR and XPS measurements);
2. The total number of dopants (S or N) should be less than 4 (STEM statistical analysis);
3. The coordination number for N should be 2 or 3;
4. The coordination number for S should be 2;
5. The coordination number for C should be 3;
6. The number of hydrogens should be less than 4;

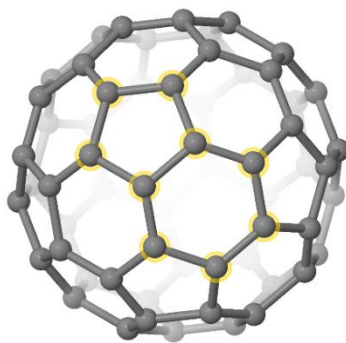


Figure S3. 10 Base structure with 10 sites haloed for defect generation.

In order to generate possible defects, 10 sites (shown in Figure S3.10) on the base structure (C₆₀) are selected and replaced by a combination of C, S, N, or vacancies. The set of possible combinations can be represented by a Cartesian product of 10 four-member sets. After removing unreasonable and duplicate structures, the remaining structures are terminated with hydrogen to eliminate under-coordinated carbon atoms, followed by geometric relaxations. This procedure gives 976 plausible defect structures, and for each defect structure, there could be multiple adsorption sites. We then define an adsorption site on a certain defect that should be at or be adjacent to a dopant. By selecting a defect structure and an adsorption site, a configuration is unambiguously defined. Since the CO desorption step should be spontaneous to allow the reaction, we set a CO adsorption energy cutoff (-0.2 eV), and any configuration with CO adsorption energy lower than this cutoff will be discarded, which drastically reduced the number of configurations need to be considered. For the remaining 1254 configurations, frequency analyses are performed to get thermochemistry data, and any configuration with a negative ΔG (CO desorption) is discarded. Finally, 106 configurations are generated with H_f (heat of formation) and S (entropy) calculated at 298 K.

Structures of the most active configurations

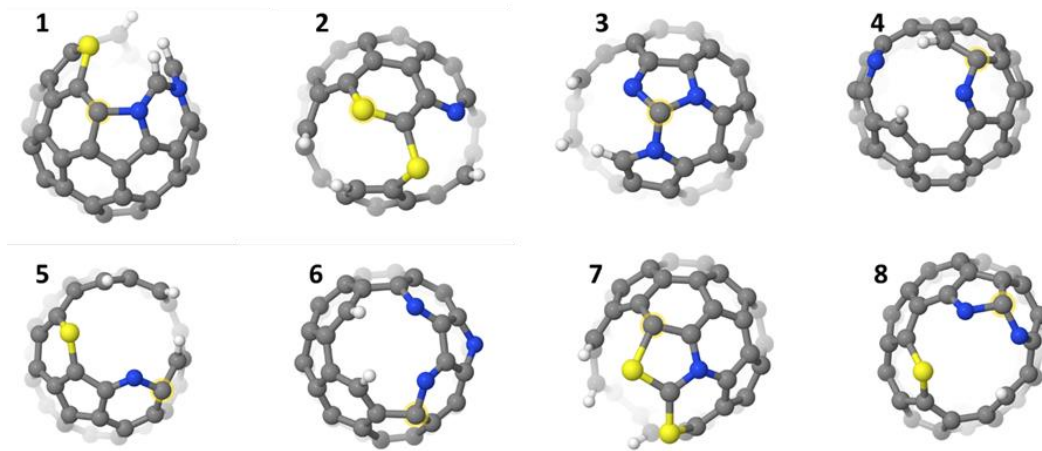


Figure S3. 11 Images of the 8 most active configurations as predicted by the theoretical calculations (activity follows the order 1-high:8-low. Grey, Blue, Yellow and White color represents Carbon, Nitrogen, Sulfur, and Hydrogen. In each structure, the adsorption site is haloed in yellow).

3.5.12 Characterization of a catalyst after electrolysis

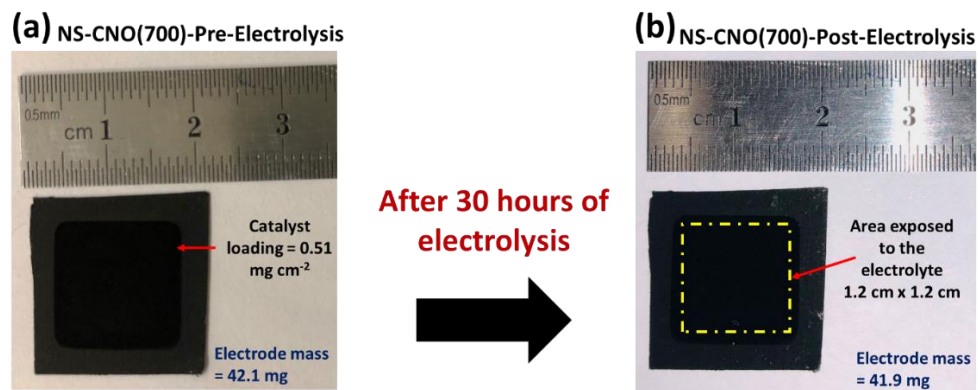


Figure S3. 12 Photographs of NS-CNO(700) before (a) and after 30-hour electrolysis (b)

Figure S3.12 presents the photographs of the same NS-CNO(700) electrode taken before and after 30-hour electrolysis. For the post-electrolysis photograph, the electrode was thoroughly rinsed with DI water to remove adsorbed KHCO_3 and dried at 60°C overnight. The mass of the electrode slightly dropped after electrolysis (mass change < 0.5

%). This mass loss is possibly due to the detachment and dissolution of a catalyst and a binder during 30-hour electrolysis.

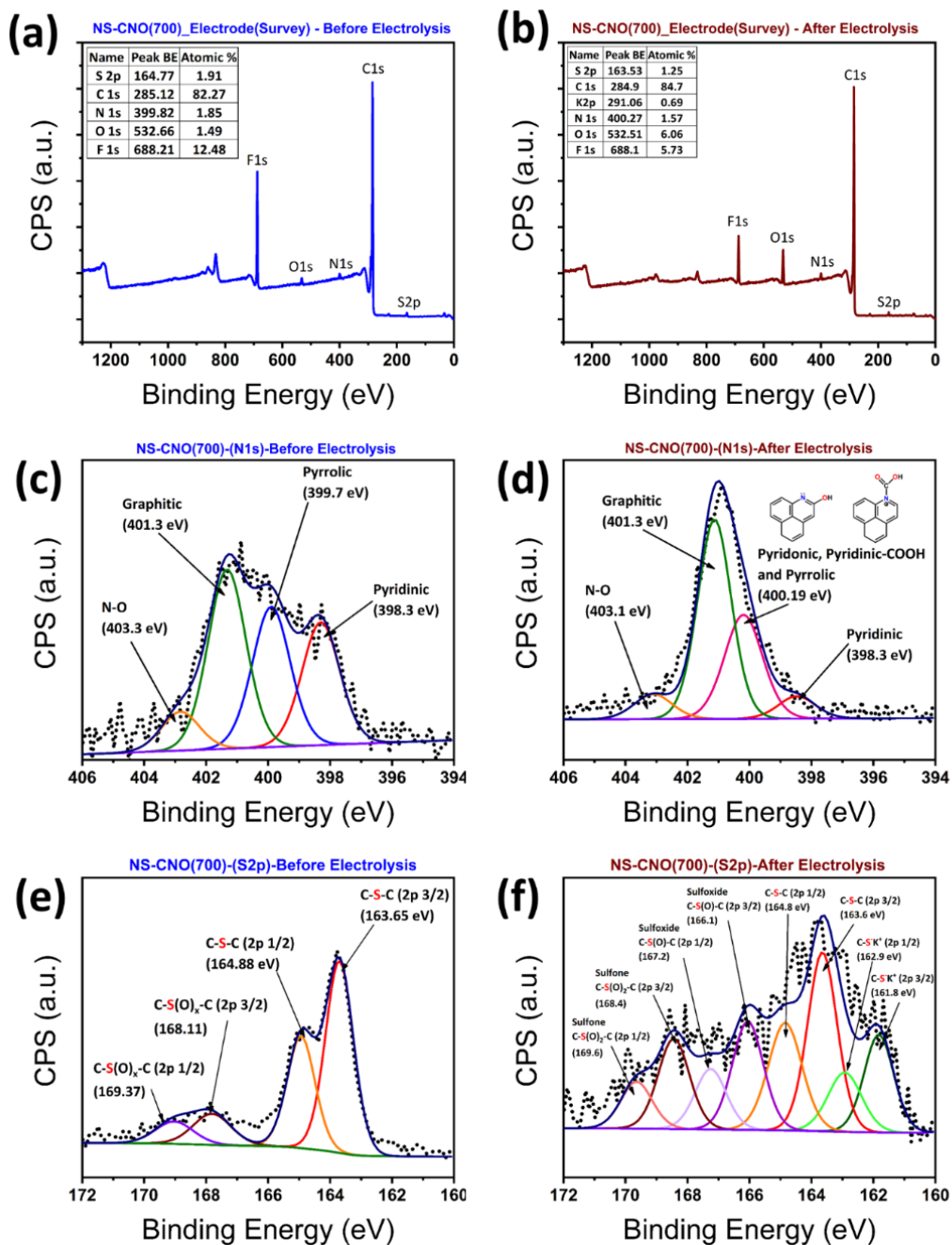


Figure S3. 13 XPS characterizations of NS-CNO(700) before and after electrolysis: XPS survey spectra of before (a) and after electrolysis (b), high-resolution XPS N1s scan before (c) and after electrolysis (d), and high-resolution XPS S2p scan before (e) and after electrolysis (f).

After 30-hour electrolysis, a significant drop in F content is noted due to the removal of the PVDF binder. The O content in the electrode significantly increased (from 1.49 at.% to 6.06 at.%), which is due to the oxidation of C, N, and S during electrolysis. Clearly, pyridinic-N and pyrrolic-N groups are changed to pyridonic, pyridinic-COOH, or pyridinium groups while graphitic-N is largely intact.²⁵⁰ S functional groups experienced more severe changes. Thiophene groups remain similar after electrolysis, but sulfoxide and sulfone groups become dominant.²⁵¹ Also, the ring-opening of sulfide is found and bound with potassium ions.²⁵² This reaction may result from the competing hydrogen evolution occurring on the sulfur sites. However, to decipher the detailed oxidation mechanism of NS-CNO(700), thorough characterizations and in-situ measurements will be conducted in the future.

3.5.13 Comparison of NS-CNO(700) performance with metal-based catalysts

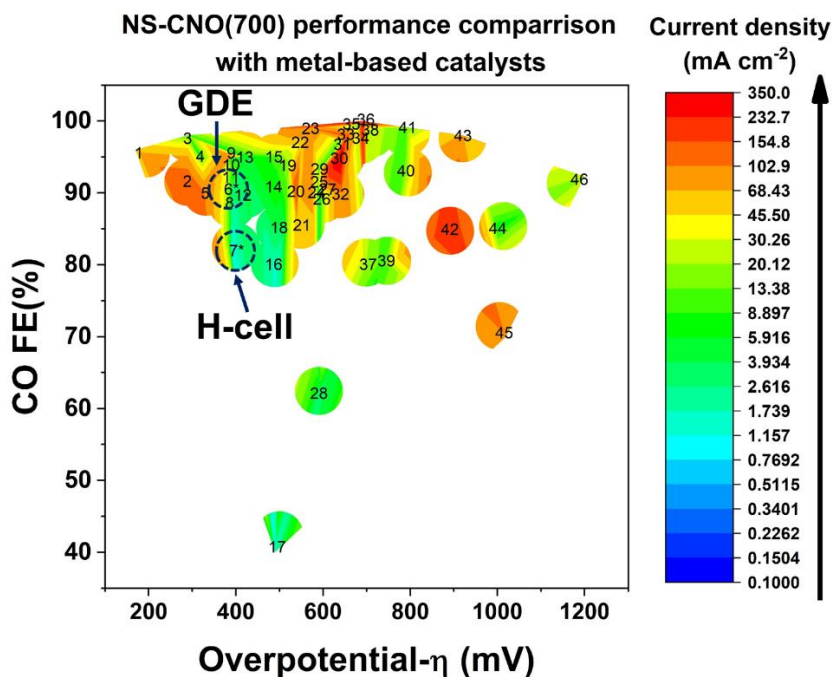


Figure S3. 14 The area plot (top) compares the performance of NS-CNO(700) with metallic catalysts for CO production in terms of FE, overpotential, and current density (The numbers refer to the catalysts listed in Table S3.3). Various color intensities represent the magnitude of the current density at each data point.

Table S3. 3 Performance comparison of NS-CNO(700) electrode with other CO generating catalysts (The table summarizes experimental conditions and the details of the performance for each catalyst)

	Catalyst	Electrolyte	Testing condition	η / mV	FE/ %	Current density / mA cm ⁻²	Durability / hr	Reference
1	Ag powder(100 nm)	EMIMBF4	GDE	170	96	62	7	Rosen et al. ²⁵³
2	C/Ag/PTFE	1 M KOH	GDE	290	90	150	100	Dinh et al. ²²⁶
3	Oxide Au	0.5 M NaHCO ₃	H-cell	290	98	10	8	Chen et al. ¹³⁸
4	Zn-Nx/C	0.5 M KHCO ₃	H-cell	320	95	4.8	75	Yang et al. ²⁵⁴
5	Au/GDL	2 M KOH	GDE	330	90	100	8	Verma et al. ²⁵⁵
6	NS-CNO(700) N, S co-doped carbon nano onions	1 M KHCO ₃	Flow-cell GDE Electrolyte flow rate-5 ml min ⁻¹	390	91	10.8	20	Wanninayake et al.[This work*]

7	NS-CNO(700) N, S co-doped carbon nano onions	0.1 M KHCO ₃	H-cell Electrolyte flow rate-5 ml min ⁻¹	390	82	0.92	-	Wanninayake et al.[This work*]
8	Ag	0.5 M KHCO ₃	H-cell 1200 rpm	390	92	8	2	Lu et al. ¹³⁷
9	Fe ³⁺ -N-C	0.5 M KHCO ₃	GDE	390	95	100	12	Gu et al. ²⁵⁶
10	Fe-N ₄ /CF	0.5 M KHCO ₃	H-cell	390	94. 9	3	60	Zhang et al. ²⁵⁷
11	Fe-ZIF-8 derived Fe-N-C	0.5 M KHCO ₃	H-cell	390	93. 5	15	-	Qin et al. ²⁵⁸
12	Zn-N-G	0.5 M KHCO ₃	H-cell	390	90. 8	3	15	Chen et al. ²⁵⁹
13	FeN/CNF	0.1 M KHCO ₃	H-cell	420	95	4.47	24	Cheng et al. ²⁶⁰
14	Fe-N-C	0.5 M NaHCO ₃	H-cell	490	91	7.6	6	Huan et al. ²⁶¹
15	(Cl,N)-Mn/G	0.5 M KHCO ₃	H-cell	490	95	10	12	Zhang et al. ²⁶²
16	Fe/NG	0.1 M NaHCO ₃	H-cell	490	80	1.5	10	Zhang et al. ²⁶³
17	Cu-rGO	0.1 M NaHCO ₃	Single cell	490	40	1.4	15	Hossain et al. ²⁶⁴
18	Fe-NS-C	0.1 M KHCO ₃	H-cell	510	85	3	-	Dembinska et al.
19	Co-N-C	0.5 M KHCO ₃	H-cell	520	94	18	60	Wang et al. ²⁶⁵
20	C/Ag/PTFE	1 M KHCO ₃	GDE	540	90	160	100	Dinh et al. ²²⁶
21	rGO-PEI-MoS _x	0.5 M NaHCO ₃	H-cell	540	85. 1	55	3	Li et al. ²⁶⁶
22	Ni-NG	0.1 M KHCO ₃	GDE	550	97	50	20	Jiang et al. ²⁶⁷
23	Ni-NCB	0.5 M KHCO ₃	GDE	571	99	100	20	Zheng et al. ²⁶⁸
24	CuO/SnO ₂	0.1 M NaHCO ₃	H-cell	590	90	1.25	5	Schreier et al. ²⁶⁹
25	C-Cu/SnO ₂	0.5 M KHCO ₃	H-cell	590	93	10	-	Li et al. ²⁷⁰
26	Ni-N-Gr	0.1 M KHCO ₃	H-cell	590	90	0.2	5	Su et al. ²⁷¹
27	NiSA-N-CNTs	0.5 M KHCO ₃	H-cell	590	91. 3	23	12	Cheng et al. ²⁷²
28	3D N,P Co-MPC	0.1 M KHCO ₃	H-cell	590	62	3.1	20	Pan et al. ²⁷³
29	Ni-NC@C	0.5 M KHCO ₃	H-cell	590	93	6	24	Jia et al. ²⁷⁴
30	Ag/MWCNT (GDE)	1 M KOH	GDE	640	95	350	-	Sichao et al. ²⁷⁵
31	Ni-N-C	0.1 M KHCO ₃	H-cell	640	97	8.4	9	Pan et al. ²⁷⁶
32	Ag/TiO ₂	1 M KOH	GDE	642	90	101	-	Sichao et al. ²⁷⁷
33	MoS ₂ powder	EMIMBF ₄	H-cell	654	98	130	10	Asadi et al. ²⁷⁸
34	Ni-NSG	0.5 M KHCO ₃	H-cell	680	98	21	100	Yang et al. ²⁷⁹
35	Co-N5/HNPCSs	0.2 M NaHCO ₃	H-cell	680	99. 4	4.5	10	Pan et al. ²⁸⁰
36	Ag/GDL	3 M KOH	GDE	690	100	231	-	Verma et al. ²⁸¹
37	Ag powder(1 um)	0.1 M KHCO ₃	H-cell	700	80	20	7	Delacourt et al. ²⁸²
38	Ni-N-C	0.1 M KHCO ₃	H-cell	700	99	28.6	30	Li et al. ²⁸³
39	h-Zn	0.5 M KHCO ₃	H-cell	740	80	9.5	30	Won et al. ²⁸⁴
40	Ni/N-CHSs	0.5 M KHCO ₃	H-cell	790	93. 1	15	16	Yuan et al. ²⁸⁵
41	Ni@NCNTs	0.5 M KHCO ₃	H-cell	790	99. 1	10	20	Zheng et al. ²⁸⁶
42	Ni-N-C	0.1 M KHCO ₃	GDE	890	85	200	20	Moller et al. ²⁸⁷
43	Ni-N ₄ -C	0.1 M KHCO ₃	H-cell	920	98	71.5	12	Yan et al. ²⁸⁸

44	Polycrystalline Au foil	0.1 M K HCO ₃	H-cell	1000	85	5	-	Hori et al. ¹⁶⁰
45	Ag/GDL	1 M NaHCO ₃	GDE	1020	70	100	25	Salvatore et al. ²⁸⁹
46	Ag/C	0.2 M K ₂ SO ₄	H-cell	1200	92. 3	20	2	Hori et al. ²⁹⁰

CHAPTER 4. CO₂ ELECTROREDUCTION TO MUTICARBON PRODUCTS BY SUPPORTED COPPER ON NITROGEN-DOPED CARBON NANO ONIONS

4.1 Introduction

Electrochemical reduction of CO₂ to value-added chemicals and fuels offers a promising pathway to store renewable electricity. Among various products from CO₂ reduction, ethanol is highly desired since it has high energy density (~27 MJ kg⁻¹). The production of ethanol can leverage its high market price, consistent global demand, and ease of storage to increase economic feasibility.³⁸ Electrochemical conversion of CO₂ to ethanol is, however, a challenging and complicated electrochemical process involving multiple electrons, protons, and intermediates.²⁹¹ Cu-based electrocatalysts are well known for C-C coupling reactions to generate ethylene and ethanol.^{65, 291} Ethylene and ethanol share similar mechanistic pathways with a common intermediate (HOCCH*); therefore, the selectivity of electrochemical CO₂ conversion to ethanol competes with that of ethylene. It is believed that ethylene is formed by the deoxygenation step, where it involves the breakage of the C-O bond of that intermediate.^{6, 38}

Several attempts have been made to steer the CO₂ electroreduction selectivity toward ethanol. Mainly, these strides involve tuning the binding energy of reaction intermediates by silver doping,²⁹² grain boundaries generation²⁹³, defects generation,²⁹⁴ and incorporation of molecular metal catalysis.²⁹¹ These attempts have increased the faradaic efficiency (FE) of ethanol up to 52% and a partial current density (J) up to 160 mA cm⁻² with the cathodic energy efficiency of 31%.³⁸ However, this performance is not sufficient for industrial applications where high selectivity(>80-90%), current density (>300 mA cm⁻²), and stability (>80,000 hrs).^{35, 37} Therefore, it is imperative to discover new electrode architectures and novel catalyst materials for electroreduction to ethanol.³⁷

An electrode architecture is a critical component for the efficient transport of CO₂ to active catalyst sites. Therefore, it is desirable to use catalyst deposited gas diffusion electrodes (GDE), where the diffusion of CO₂ does not limit the reaction.^{295, 296} However, conventional carbon-based GDE used in CO₂ electrolyzers have the limitation of an insufficient CO₂ mass transfer due to flooding of an electrolyte. Therefore, it has been suggested that the electrode durability can be enhanced by adopting polytetrafluoroethylene (PTFE) GDE.⁷¹ In the electrode fabrication, a binder is also used for the integrity of catalyst particles and ionic conductivity. Due to the ionic properties, these binders are also known as ionomers.

The diffusion of CO₂ into catalytic sites is also influenced by the choice of ionomer.¹⁸² In this work, nafion ionomer was used to facilitate the transport of CO₂ to the catalyst.¹⁸² On the other hand, the electronic property of the catalyst is a major factor in controlling the product selectivity in CO₂ electroreduction.⁶ It has been shown that metal catalyst supports immensely modulate the electronic properties of catalysts.⁷² Like various heteroatom doped carbon materials which demonstrated activities for oxygen reduction reaction and CO₂ electroreduction,^{5, 77} N-doped carbon nano onions (N-CNO) can be utilized to tune the interfacial interactions between metal catalysts and reaction intermediates.^{297, 298} Furthermore, these heteroatom defects can promote the nucleation/growth of metallic nanoparticles via strong interactions. Thus, the durability of metallic nanoparticles can be enhanced during CO₂ electroreduction.^{73, 298} However, there is a lack of knowledge on how heteroatom-doped supports influence binding energy of reaction intermediate and the generation of multicarbon products. Furthermore, scalable electrode architectures were rarely studied. In this study, a unique electrode architecture

was accomplished by depositing Cu nanoparticles and N-doped CNOs on Cu-coated PTFE (Figure 4.1). This catalyst resulted in the production of ethanol with the FE of 39% at -0.9 V vs. RHE (which corresponds to the cathodic energy efficiency of 24%), giving the partial current density of -74 mA cm^{-2} for 36 hours. These results provided an insight into the effects of electrode microstructure, heteroatoms, and Cu particles on electrochemical reduction of CO_2 to ethanol.²⁹⁹

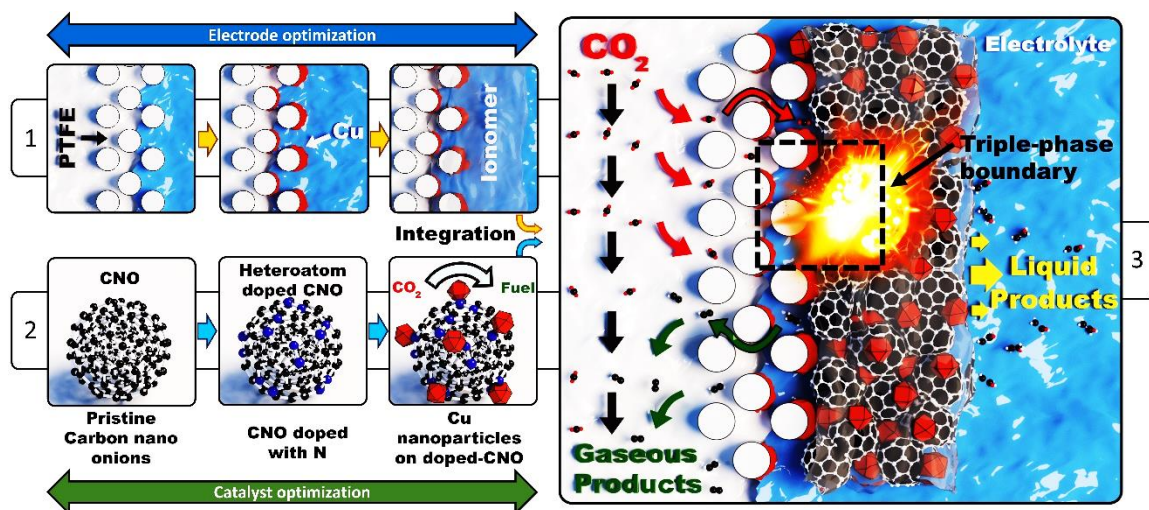


Figure 4. 1 Electrode-catalyst optimization and triple-phase boundary of the integrated system (Carbon, nitrogen, and Cu are denoted as black, blue, and red-orange colors).

4.2 Experimental

4.2.1 Synthesis of nitrogen doped CNOs and supported copper on N-CNOs.

CNOs were treated with a mixture of saturated HNO_3 and DI water (50:50 v:v) at $105 \text{ }^\circ\text{C}$ for 5 hours to produce oxidized CNOs (Ox-CNOs). Then, Ox-CNOs (100 mg) mixed with urea (500 mg) were annealed at $700 \text{ }^\circ\text{C}$ for 3 hours under the flow of argon to produce N-CNOs. The same annealing procedure was used to produce copper incorporated N-CNOs. 377 mg of copper(II) acetate(Sigma-Aldrich 98%) was used as a copper precursor. Interestingly, when undoped CNOs were annealed with Cu precursor, no Cu was

retained on the CNOs, indicating the critical role of N atoms to capture Cu particles. In this work, three types of CNOs were studied for catalytic performances: undoped CNOs, N-doped CNOs prepared at 700 °C (N-CNO(700)), and copper incorporated nitrogen-doped CNOs prepared at 700 °C (N-CNO-Cu(700)).

4.2.2 Preparation of gas diffusion electrodes

First, copper (Cu ~300 nm thick) was sputtered on polytetrafluoroethylene-PTFE (Sterlitech, 450 nm pore size) membranes by a sputter coater (ATC-Orion 5 UHV sputtering system) using a 99.995% pure Cu target. The sputtering rate was maintained at 5 nm min⁻¹ with a base pressure of 7.7 x 10⁻⁸ torr. The resulting electrodes were cut into 2 cm x 2 cm pieces. Then an ionomer stock solution was prepared by adding 310 µl solution of nafion (5 wt %, D520 Nafion™ dispersion, fuelcellstore) to 20 ml of methanol(99.8%, anhydrous, Sigma Aldrich). Finally, 0.8 mg of catalyst (CNO, N-CNO(700), or N-CNO-Cu(700)) was dissolved in an 800 µl of ionomer solution and airbrushed onto 1.2 x 1.2 cm area of the sputtered Cu layer. The final loading of catalyst/ionomer on the Cu-coated PTFE membrane was slightly varied in each airbrushing step and was determined from the electrode mass before and after the airbrushing. Resultant electrodes were denoted as Cu_CNO_Nf, Cu_N-CNO(700)_Nf, and Cu_N-CNO-Cu(700)_Nf, respectively. The term “Nf” indicates the presence of nafion ionomer. A blank Cu-coated PTFE with a layer of nafion airbrushed was denoted as Cu_Nf.

4.2.3 Material characterizations

Morphology, the microstructure of carbon catalyst, copper integrated catalyst, and gas diffusion electrodes were characterized by SEM (Hitachi S-4300) and TEM (FEI Talos F200X). The cross-sectional images of electrodes were obtained by an SEM equipped with a focused ion beam (FIB, Helios Nanolab 660, FEI). The crystallinity and phases of each catalyst were probed by XRD. The elemental composition and chemical state of each sample were analyzed by XPS.

4.2.4 Simulation of local electrode conditions.

Microenvironments and local conditions near catalytic sites, including CO₂ concentration and local pH were simulated by a reaction-diffusion model. In the model, a catalyst layer thickness, catalyst porosity, liquid diffusion thickness, and CO₂ diffusion coefficient in the nafion were estimated as 300 nm, 60%, 500 μm, and $2.5 \times 10^{-5} \text{ dm}^2 \text{ s}^{-1}$,¹⁸² respectively. The liquid diffusion length was approximated to be the thickness of a sealing gasket in the cathode, by assuming that electrolyte is uniformly mixed outside of the sealing gasket. Reaction rate constants and diffusion coefficients were taken from the article by Gupta et al.¹⁸¹ More detailed description of the reaction-diffusion model is shown in the Appendix.

4.2.5 Electrochemical test

4.2.5.1 A flow-type cell configuration.

Electrochemical performances of catalysts were tested in a customized cell with a flow-type configuration, as discussed in chapter 3. Briefly, this flow-type cell is comprised of three chambers for gas, catholyte, and anolyte, respectively. The catalyst side of the GDE is recessed in a squared cavity area of 0.64 cm², which is exposed towards catholyte. CO₂ gas was continuously supplied to the gas chamber at a rate of 50 sccm. The catholyte held 25 ml of electrolyte, and an Ag/AgCl reference electrode was immersed in the catholyte. The anolyte chamber also held 25 ml of electrolyte and was in contact with a Pt-mesh counter electrode. 1 M KOH (Titrisol) in aqueous solution was used for both catholyte and anolyte. Catholyte and anolyte chambers were separated by an anion exchange membrane (Fumasep FAB-PK-130). Both catholyte and anolyte were circulated at the flow rate of 5 ml min⁻¹ using a dual-head peristaltic pump (BINACA PUMPS_MODEL 1001).

4.2.5.2 Electrochemical test and electrolysis.

The electrochemical tests were conducted with a CHI 660D potentiostat. All potentials were relative to the reversible hydrogen electrode (RHE) using the following relation. A local pH on the surface of the catalyst was estimated as 12 from the reaction-diffusion model. This pH was about two units below compared to the bulk pH of 1M KOH.

$$V \text{ vs. (RHE)} = V \text{ vs. (Ag/AgCl)} + 0.222 + 0.059 \times \text{pH} \quad (12)$$

Linear sweep voltammograms (LSV) were obtained under CO₂ at a scan rate of 20 mV s⁻¹. Based on the LSV, the potentials for the electrolysis experiment were determined. The electrolysis experiments were conducted for 30 minutes by applying a constant potential to the WE with respect to RE. During the electrolysis, gas samples were collected every 10 minutes and analyzed by gas chromatography (GC, SRI 8610C, SRI instruments). After the 30 min electrolysis, liquid products were analyzed by NMR (400 MHz Bruker Avance NEO) while using DMSO and phenol as the internal standards.

4.3 Results and discussion

A local environment on the electrode surface was simulated by a reaction-diffusion model using MATLAB programming. Figure 4.2 illustrates a local pH and CO₂ concentration when no current passes through the electrode. The system reaches a steady-state condition in ~20 seconds after its exposure to CO₂ gas. Figure 4.2 (a) suggests that with the pH of ~14 in the bulk solution, the pH is reduced to ~12 right on top of electrode due to the rapid dissolution of CO₂ in KOH. In this configuration, CO₂ travels a short distance into the electrolyte, and it can be utilized before it is converted to bicarbonate.⁷¹ Although this setting is beneficial to induce C-C coupling reactions in the alkaline medium, it utilizes only the small portion of catalyst layers (<2 μm), resulting in low current densities. By applying an ionomer which enhances gas and ion transport to the catalyst layer, CO₂ diffusion length can be increased. The nafion ionomer is a sulfonated tetrafluoroethylene-based fluoropolymer-copolymer. nafion can transport cations as well as gases to the catalyst.¹⁸² Figure 4.2 (b) and (c) highlight the importance of the nafion ionomer. With a 5 μm thick nafion layer, high CO₂ concentration is maintained in the wider range of electrocatalyst as CO₂ diffusion is ~ 165 times faster through the hydrophobic

nafion backbone than in KOH electrolyte.¹⁸² This concept can be used to develop 3D electrode structures leading to high production rates.

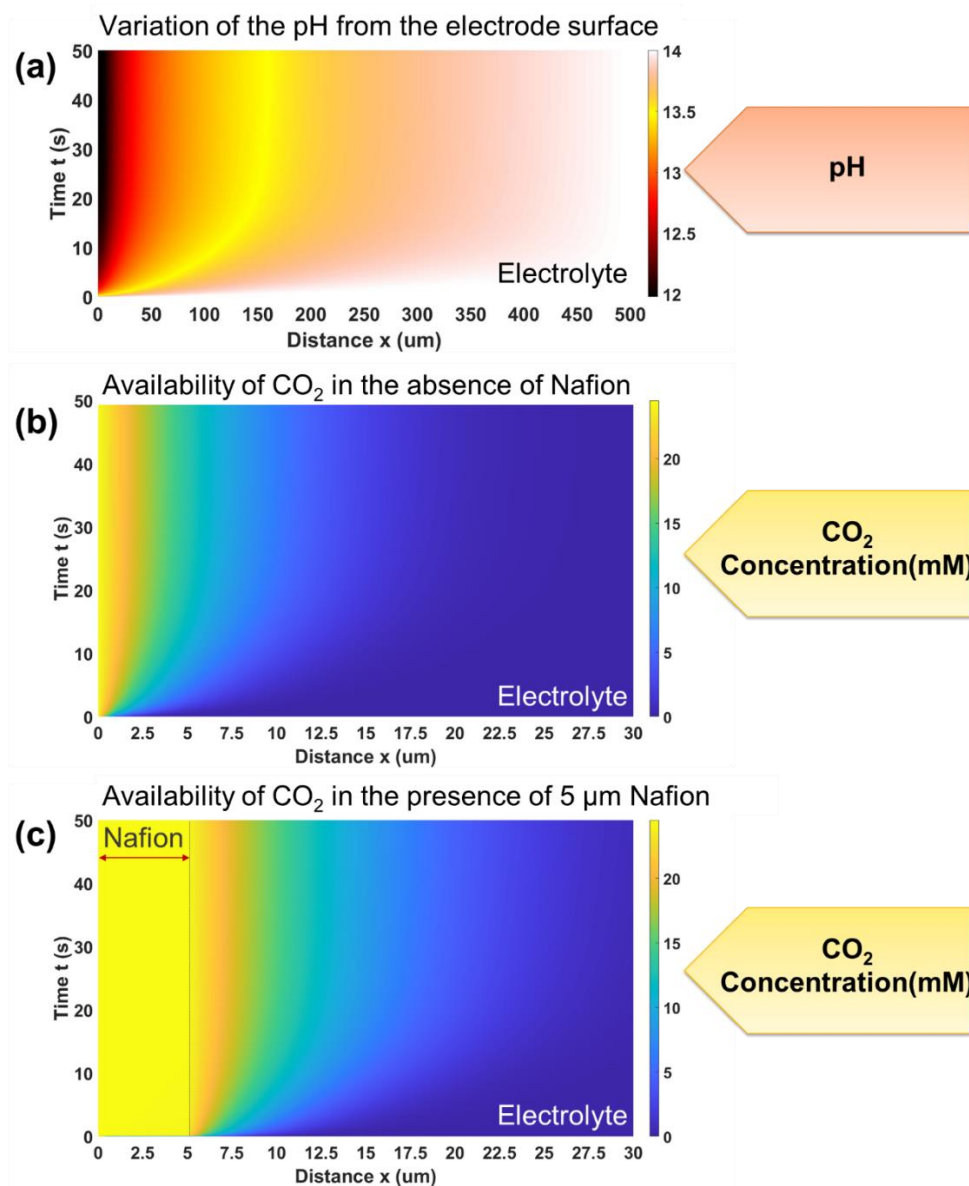


Figure 4. 2 (a) The local pH, (b) CO₂ concentration in the absence of nafion, and (c) CO₂ in the presence of nafion layer (thickness: 5 μm) calculated by a reaction-diffusion model. 0 μm represents the base of the porous electrode, and 500 μm corresponds to the liquid diffusion thickness. The colors indicate the pH or CO₂ concentration.

Motivated by the above findings from the reaction-diffusion model, a gas diffusion electrode was prepared as shown in Figure 4.3. Initially, a 300 nm thick copper layer was

sputtered onto the PTFE membrane. While the copper coating acts as a catalyst, it also helps to maintain high electrical conductivity of the electrode surface (Figure 4.3 (b)). A control sample is prepared by airbrushing a solution of nafion in methanol onto the sputtered copper surface (Figure 4.3 (c)). Nafion has both hydrophobic and hydrophilic domains. When nafion is added to a polar solvent such as methanol, it forms lamellar arrangements where hydrophilic $-\text{SO}_3^-$ groups are exposed to the solvent and $-\text{CF}_2$ hydrophobic groups are pointing toward the center of the lamellar.³⁰⁰ When a nafion ionomer is coated on the electrode, the hydrophilic and hydrophobic domains can transport K^+ ions/bound water and CO_2 gas to the catalyst sites, respectively. Therefore, the extended catalyst layer is prepared by depositing a mixture of ionomer and the catalyst (Figure 4.3 (d)). Interestingly, when the catalyst is in contact with the sputtered copper layer, it forms a unique interface. Digital photographs of each of these electrodes are shown in Figure S4.

1.

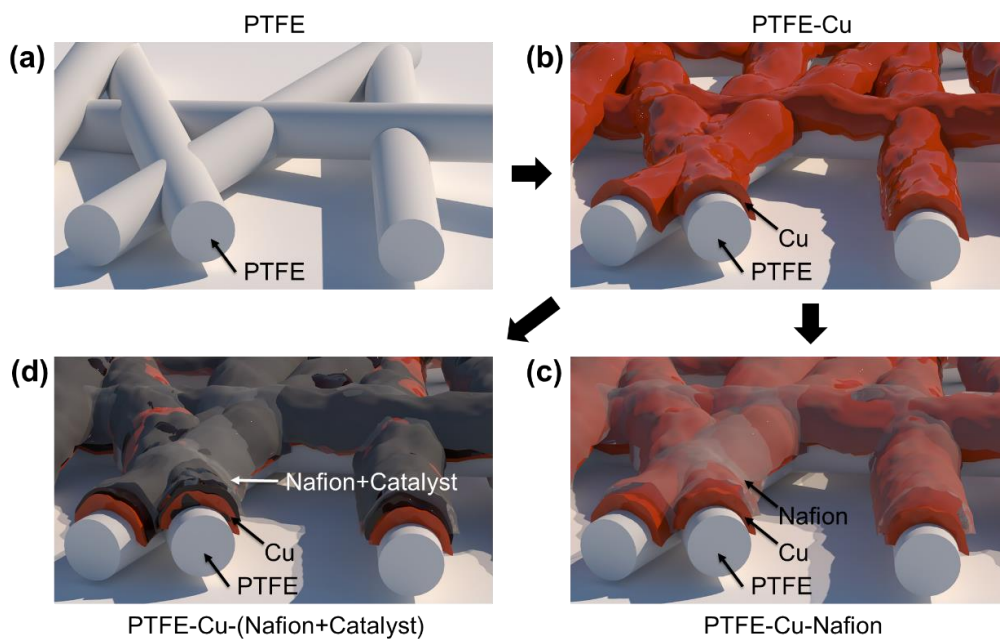


Figure 4. 3 Schematic of the electrode fabrication process.

To probe the electrode microstructure, SEM and TEM characterizations were performed. The SEM images of the PTFE-Cu electrode are shown in Figure 4.4(a). A magnified SEM image of the electrode is in the inset. The SEM images revealed that the Cu is uniformly coated over the PTFE. These images also show a well-preserved porosity of the electrode after the sputtering of Cu, which allows ample room for the diffusion of CO₂ and other gaseous products. Notably, the sputtered copper surface consists of grain-like morphology with grains size ~ 50 nm. The top view SEM image of Cu_N-CNO-Cu(700)_Nf and its cross-sectional SEM image are shown in Figure 4.4 (b) and (c). Based on the cross-sectional SEM image, the catalyst layer thickness is ~ 2 μm for catalyst loading of 0.23 mg cm^{-2} . It is also noted that the sputtered Cu layer is well in contact with the catalyst composite, which is crucial for the interfacial catalyst activity. The small size of CNO assists the uniform coating of catalyst composites on the sputtered Cu. The SEM with energy dispersive x-ray spectroscopy (EDS) has clearly resolved distinct electrode interfaces (Figure 4.4(c), right). The layers of sputtered Cu (300 nm) and Cu and N-CNO composites are resolved in the Cu L series. From the PTFE substrate and nafion ionomer, F is spread over the entire electrode except in the sputtered Cu layer. Pt was coated on the electrode surface to protect the electrode during FIB milling, and it is mapped as Pt M series. A TEM analysis with HAADF-STEM-EDS maps of N-CNO-Cu(700) provides useful insights into the distribution of C, N, and Cu over the catalyst composite (Figure 4.4 (d)). C, N, and Cu are uniformly distributed in the catalyst composite. Notably, high-resolution TEM images show that Cu nanoparticles and N-CNO are in contact. The average size of Cu nanoparticles is ~ 8 nm (a histogram of particle diameters is shown in the inset of Figure 4.4(f)). Due to the strong interaction between Cu and N-CNO, the electronic

structure of Cu is likely to be altered, improving catalytic activities for the CO₂ electroreduction. TEM images of CNO, N-CNO(700), and additional TEM images of N-CNO-Cu(700) are depicted in Figure S4.2. These images suggest that N-doping with N and the deposition of Cu nanoparticles do not alter the curved morphology of CNO.

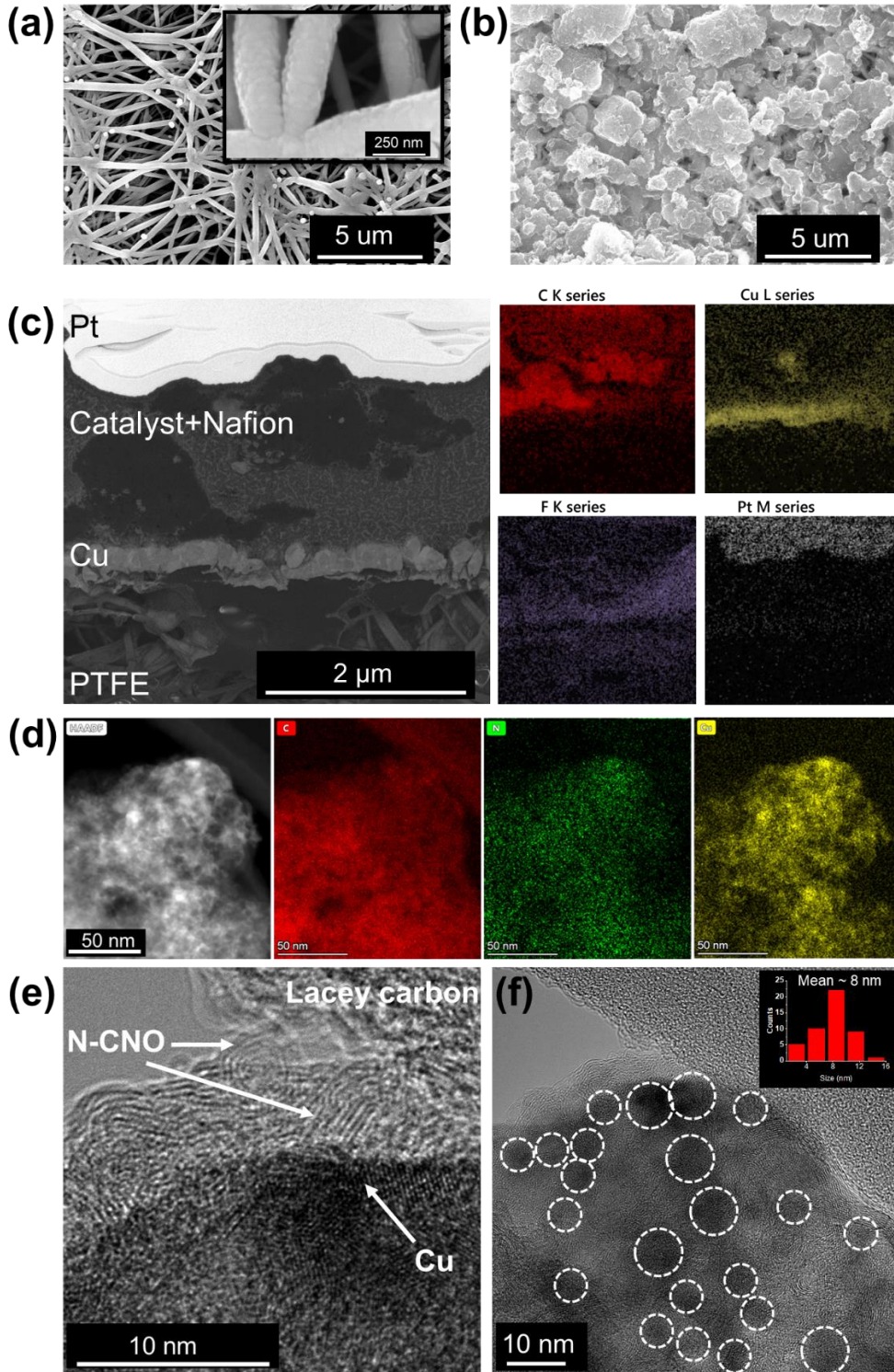


Figure 4. 4 SEM images of (a) PtFE-Cu, (b) a top view of Cu_N-CNO-Cu(700), (c) a cross-sectional image of Cu_N-CNO-Cu(700)_Nf and (d) HAADF-STEM-EDS mapping of N-CNO-Cu(700) and (e)-(f) high resolution TEM images of N-CNO-Cu(700) where circled regions indicate Cu nanoparticles.

In metal-based catalysis, the catalyst activity is a function of the crystalline phase. We conducted XRD measurements to gain insights into the crystalline nature of the sputtered Cu electrode and doped-CNO composite. N-CNO(700) showed characteristic graphitic peaks at 25.8° and 43.3° for (002) and (100) planes, respectively. Figure 4.5 (d) indicates the simulated XRD pattern of Cu. It includes peaks at 2θ angles 43.3° , 50.5° , 74.2° , 89.9° , and 95.2° correspond to (111), (200), (220), (311), and (222) planes, respectively. Both N-CNO-Cu(700) and PTFE_Cu samples have similar crystallinity, while Cu(111) is being the dominant phase. For PTFE_Cu, the calculated average crystallite size of Cu from the Scherrer equation is about ~ 20 nm. In addition, the characteristic Cu peaks, XRD patterns exhibit a graphitic (002) peak for N-CNO-Cu(700), and PTFE/polypropylene(PP) peaks for PTFE membrane.

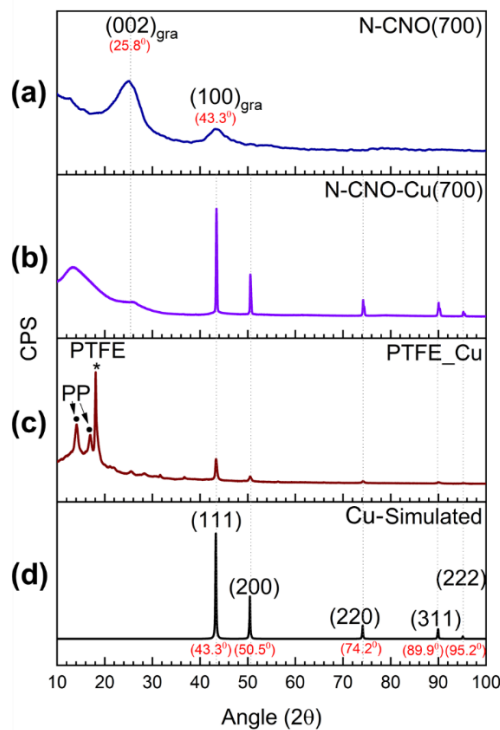


Figure 4. 5 XRD of (a) N-CNO(700), (b) N-CNO-Cu(700), (c) PTFE_Cu and (d) Cu (simulated by Mercury software).³⁰¹

XPS measurements analyze elemental compositions and chemical states of heteroatom dopants and metal catalysts. Table 4.1 summarizes the results of XPS survey scans. The contents of N in N-CNO(700) and N-CNO-Cu(700) are 3.13 at.% and 3.68 at.%, respectively. The high-resolution N1s spectrum of N-CNO(700) is illustrated in Figure 4.6. N peaks were deconvoluted into three peaks at 398.3 eV, 399.7 eV and 401.3 eV for pyridinic (43%), pyrrolic (30%) and graphitic (20%) configurations, respectively.⁵ In N-CNO-Cu(700), the high-resolution N1s spectrum includes an additional peak at 399.0 eV corresponds to N-Cu bonding.³⁰² Simultaneously, pyridinic and pyrrolic contents in N-CNO-Cu(700) are smaller than in N-CNO(700). The decreased content of pyridinic N is attributable to the interaction between pyridinic N and Cu.³⁰² Relative contents of N atoms in N-CNO-Cu(700) for pyridinic, N-Cu, pyrrolic and graphitic are 26%, 44%, 11%, and 11%, respectively. In PTFE_Cu, the majority of sputtered Cu is Cu⁰ (932.4 eV)³⁰³, with a minor portion of Cu²⁺ (934.5 eV) due to surface oxide (Figure 4.6).³⁰² The Cu content in N-CNO-Cu(700) is 2.84 at.%. A high-resolution Cu2p_{3/2} spectrum has two main peaks at 932.4 eV and 933.5 eV, which are assigned to Cu⁰ and Cu-N, respectively (Figure 4.6).³⁰⁴ To figure out whether Cu-N is from surface copper nitride (Cu₃N) or copper nanoparticles in contact with N dopants of N-CNO, acid leaching experiments (5 % HCL for 5 hours) were performed. After acid leaching, copper was mostly eliminated while N content was largely retained, suggesting Cu-N configuration is copper nanoparticles on N-CNO. Furthermore, pyridinic and pyrrolic contents are recovered after acid leaching (Figure S4.2). Both results strongly imply a strong interaction between Cu and N-CNO in N-CNO-Cu(700), in a good agreement with the TEM results. Due to this interaction, the electronic structure of Cu can be efficiently modulated to form catalytic sites.⁷³

Table 4. 1 Elemental composition of CNO-based catalyst/composite.

Sample	C (at. %)	O (at. %)	N (at. %)	Cu (at. %)
CNO	99.12 ± 0.25	0.88 ± 0.23	-	-
N-CNO(700)	95.85 ± 0.18	1.02 ± 0.15	3.13 ± 0.11	-
N-CNO-Cu(700)	91.90 ± 0.17	1.57 ± 0.22	3.68 ± 0.23	2.84 ± 0.31
Acid leached N-CNO-Cu(700)	94.75 ± 0.04	1.50 ± 0.12	3.48 ± 0.17	0.27 ± 0.12

n = 3

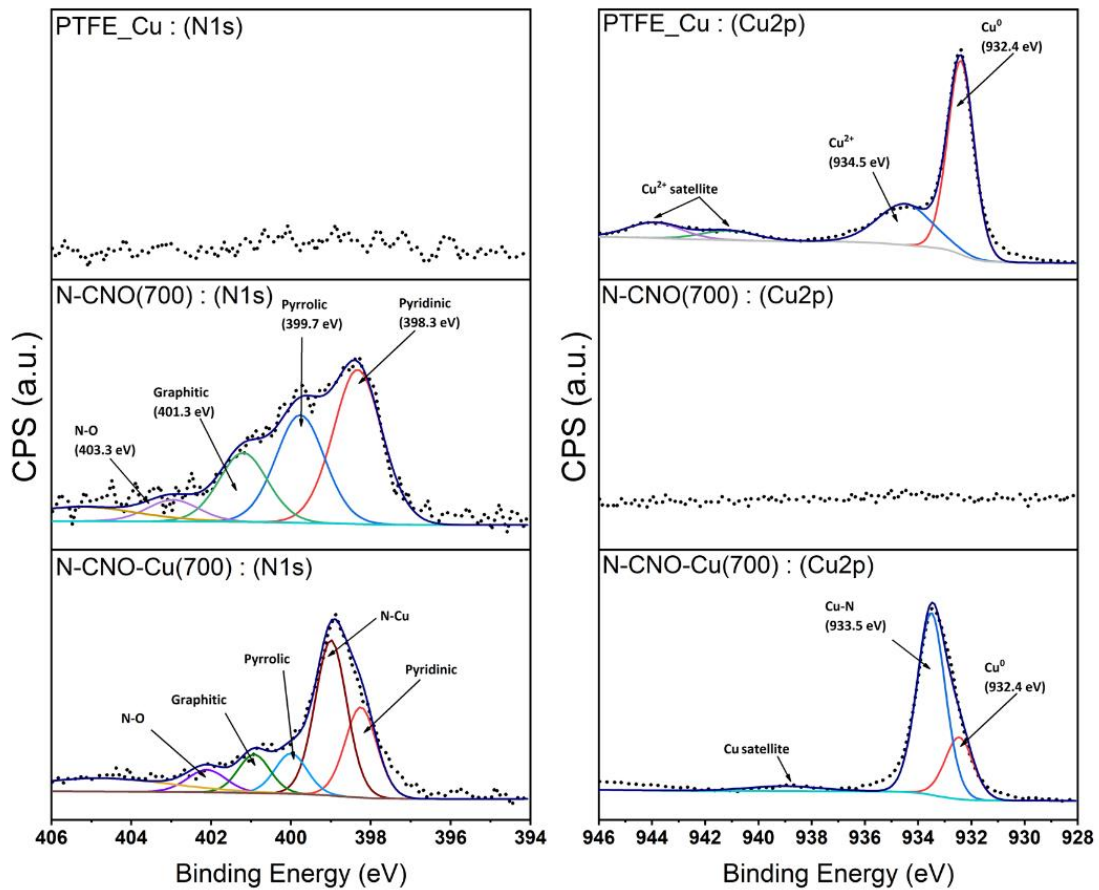


Figure 4. 6 XPS characterization of electrode substrate and catalyst composite.

Electrochemical characterizations were performed in a customized flow cell that is described in chapter 3. Figure 4.7 shows the linear sweep voltammograms (LSV) of four catalysts. In the LSV curves, onset potentials are -0.4, -0.4, -0.3, and -0.15 V vs. RHE for Cu_Nf, Cu_CNO_Nf, Cu_N-CNO(700)_Nf, and Cu_N-CNO-Cu(700)_Nf, respectively. Notably, the highest current densities were acquired with Cu_N-CNO-Cu(700)_Nf, followed by Cu_N-CNO(700)_Nf, indicating the benefit of N-CNO. Cu_CNO_Nf has yielded a lower current density than the unmodified Cu_Nf electrode indicating the undoped CNO impacts electrolysis negatively. To determine the selectivity of each catalyst, the products were further analyzed by GC and $^1\text{H-NMR}$ techniques.

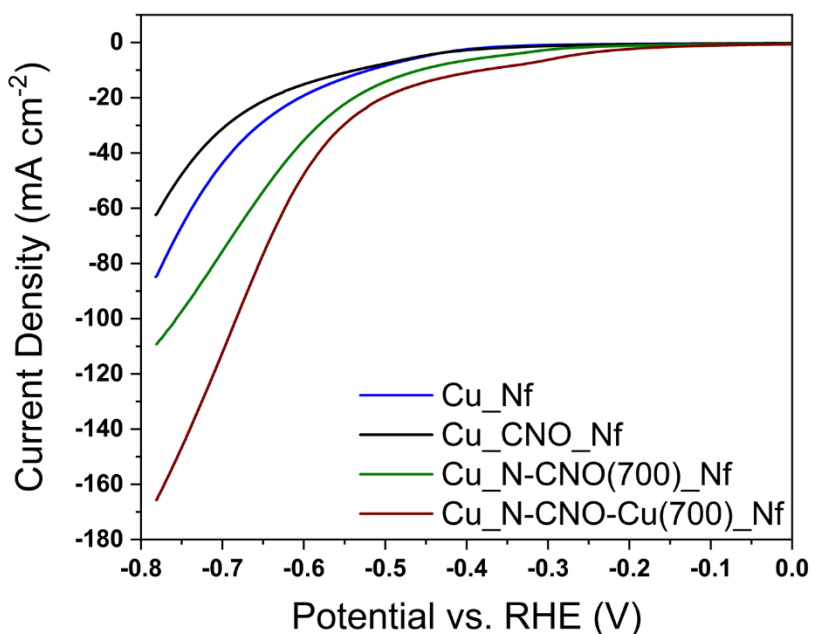


Figure 4. 7 Linear sweep voltammograms of each electrode under CO₂.

Figure 4.8 summarizes the FE's of each electrode. Cu_Nf showed high selectivity toward C₂ products (ethylene and ethanol), exhibiting the C-C coupling capability of Cu.

Specifically, this electrode is highly selective toward ethylene (53% FE) over ethanol (21% FE) at -1.0 V vs. RHE in an agreement with the previous reports.^{71, 182} Cu_CNO_Nf showed a drastic change in product selectivity with the preferential generation of C₁ products such as CO and HCOOH. Both Cu_N-CNO(700)_Nf and Cu_N-CNO-Cu(700)_Nf were more selective toward ethanol than other electrodes. Ethanol FE's of Cu_N-CNO(700)_Nf and Cu_N-CNO-Cu(700)_Nf at -0.9 V vs. RHE were 28% and 39%, respectively. ¹H-NMR results of catholyte after 30-min electrolysis with Cu_N-CNO-Cu(700)_Nf at -0.9 V vs. RHE is shown in Figure S4.3. In both Cu_N-CNO(700)_Nf and Cu_N-CNO-Cu(700), the selectivity for ethylene decreased, indicating the effect of N-CNO. The two electrodes produced more multicarbon products at low overpotentials, demonstrating the synergistic role of N-CNO and Cu in promoting C-C coupling reactions. This effect is further supported by the production of n-propanol (FE: 8.3%) of Cu_N-CNO-Cu(700)_Nf at -0.6 V vs. RHE.

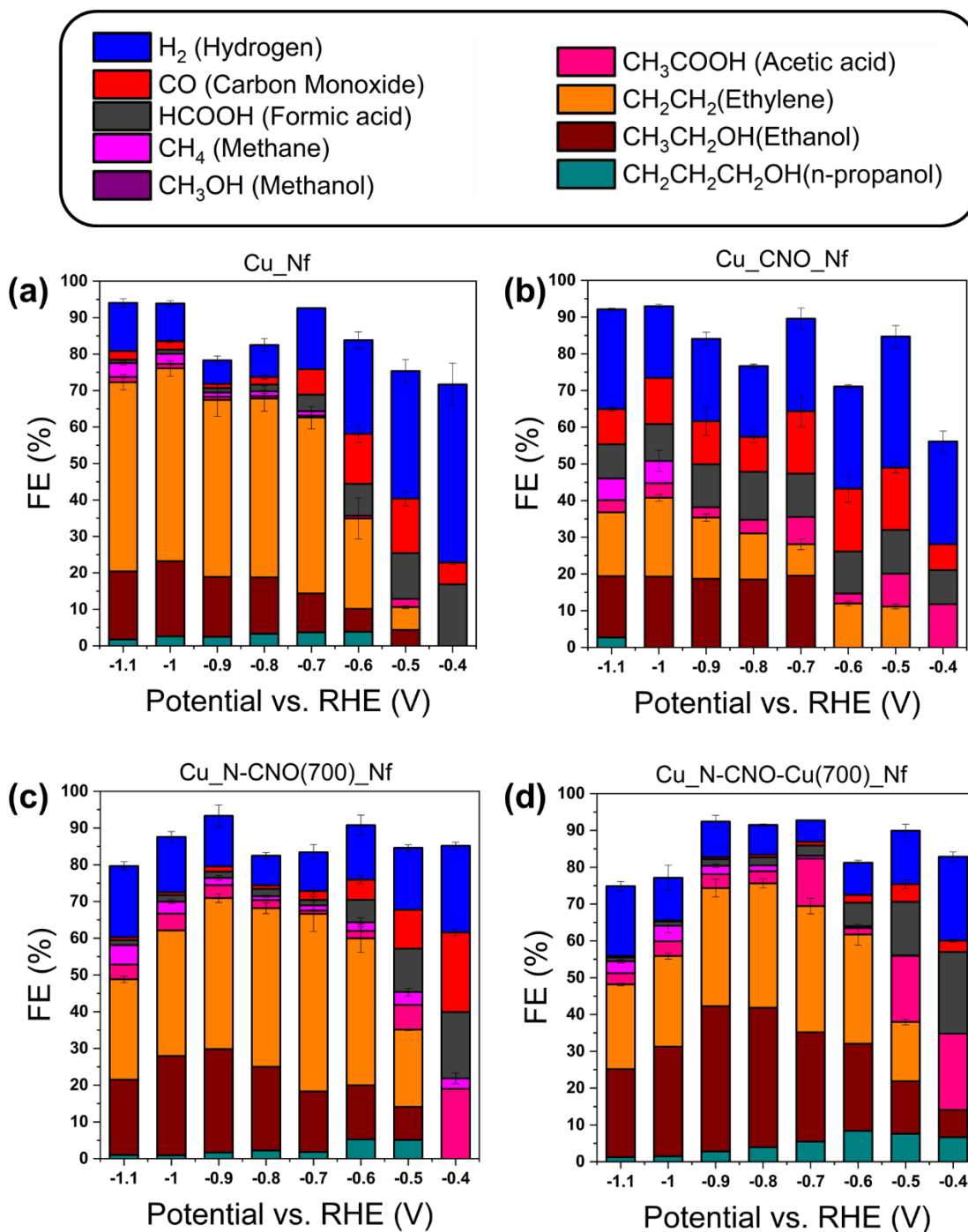


Figure 4. 8 Faradaic efficiencies of (a) Cu_Nf, (b) Cu_CNO_Nf, (c) Cu_N-CNO(700)_Nf and (d) Cu_N-CNO-Cu(700)_Nf.

It is important to understand the factors determining the selectivity of the product.

CO dimerization was reported as the rate-determining step in the pathways of C₂ products

such as ethylene and ethanol.^{71, 305, 306} Dinh et al. computed the binding energy of CO and an energy barrier for CO dimerization on Cu in the presence of hydroxide ions. They claimed that hydroxide ions lowered the binding energy of *CO on Cu and stabilized adsorbed OC-CO intermediate by strong dipole interactions within OC-CO.⁷¹ These collective factors reduced an activation energy barrier for the formation of multicarbon products. This rationale well explains the selectivity of the Cu_Nf electrode towards ethylene and ethanol. However, the selectivity between ethylene and ethanol is mainly determined by the deoxygenation step of the HOCCH* intermediate(Figure 4.9 (a)).³⁸ In this scenario, the selectivity of ethanol increases when the intermediate HOCCH* is stabilized. We propose two origins that increase the production of ethanol: (1) confinement of reacting species in sub-nanometer volumes that act as nanoreactors (Figure 4.9 (b))³⁸ and (2) modulation of electronic properties of Cu by N-CNO to generate new catalytically active sites (Figure 4.9 (c)).^{73, 303} Due to the nanoscopic size of CNO, deposited CNO on sputtered Cu may form sub-nanometer enclosed spaces. In the Cu_CNO_Nf, we observed the decrease of current density and a reduced selectivity for ethylene. This may originate from the blockage of active sites by inactive CNO. Thus, C-C coupling reactions may get hindered, leading to more C₁ products. On the other hand, Cu_N-CNO(700)_Nf increased both ethanol selectivity and current density. N-CNO is rich with pyridinic N that holds a lone pair. It was suggested that electron-donating properties of pyridinic N could stabilize adsorbed *CO intermediates, so enhancing C-C coupling.³⁸ Furthermore, these N groups may stabilize the C-O bond of HOCCH* intermediate while suppressing the deoxygenation step to yield ethanol over ethylene. Intriguingly, Cu_N-CNO-Cu(700) increases both ethanol current density and selectivity. Current density increment is a result of enhanced

catalyst loading aided by the ionomer. However, the selectivity increment attributes to the formation of new catalyst sites between N-CNO and Cu particles. In N-Cu bonds, N-CNO may modulate the electron density of Cu, while tuning the CO binding energy on Cu. This shift increases the chance of OC-CO coupling.³⁰⁷ Besides, the proximal N-CNO may stabilize the C-O bond of HOCCH* intermediate, shifting the reaction selectivity towards ethanol.

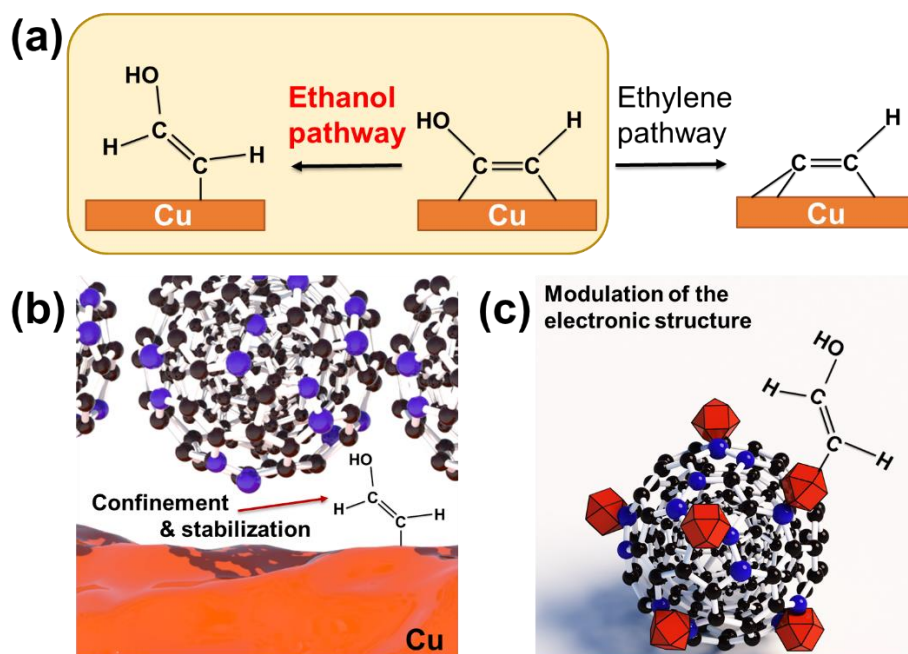


Figure 4. 9 (a) Ethylene vs. ethanol pathways, (b) confinement of reactants between N-CNO and sputtered Cu, and (c) electronic structure modulation of Cu by N-CNO.

Current density (J) and selectivity (FE) are the two most important figures of merits in electrolysis. The FE's and J_{ethanol} of catalysts at -0.9 V vs. RHE are plotted in Figure 4.10(a). By depositing N-CNO-Cu(700) on Cu_Nf, the selectivity of ethanol was enhanced by ~ 2.5 times, and ethanol current density increased by ~ 3 times as compared to Cu_Nf. Figure 4.10(b) shows a correlation between catalyst loading, catalyst thickness, and J_{ethanol} . The J_{ethanol} was gradually raised as the thickness of the catalyst layer become thicker.

However, no apparent gain of current density was observed as the thickness exceeded 5.5 μm . Although the reaction-diffusion model predicted that nafion could transport CO_2 in the long-distance of several microns, CO_2 travel length was limited to 5.5 μm in the presence of catalyst composites. Therefore, more studies should be conducted to decipher the microstructure, ionic conductivity, and gas transport of catalyst composites.

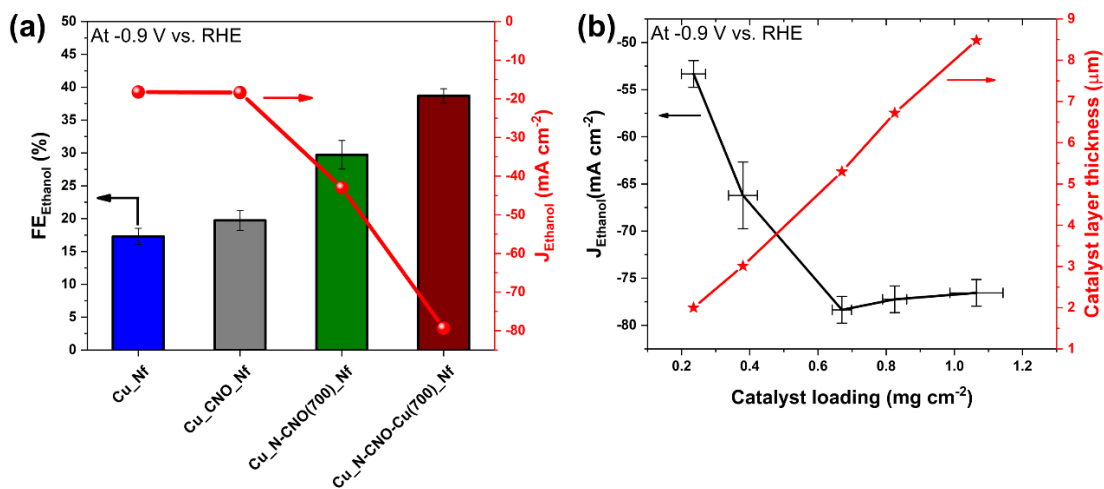


Figure 4.10 (a) Comparison of current density and $\text{FE}_{\text{Ethanol}}$ of all electrodes at -0.9 V vs. RHE and (b) correlation between catalyst loading, catalyst thickness, and $\text{J}_{\text{Ethanol}}$ at -0.9 V vs. RHE of Cu_N-CNO-Cu(700)_Nf electrode.

Finally, the long term durability of Cu_N-CNO-Cu(700)_Nf electrode was studied (Figure 4.11 (a)). The electrode exhibited remarkable durability with ethanol faradaic efficiency of $\sim 39\%$ for 36 hours. The electrode also exhibited a stable ethanol current density, and the current was -74 mA cm^{-2} after 36 hours of electrolysis. These results imply that the modified flow cell with the Cu-PTFE and deposited catalyst layers provides a promising platform for efficient and stable production of ethanol. Figure 4.11 (b) and table 4.2 compare the performance of Cu_N-CNO-Cu(700)_Nf with other electrodes reported in the literature. These results show that this electrode is competent in terms of selectivity and

cathodic energy efficiency. Although the ethanol current density of Cu-N-CNO-Cu(700) does not reach the best value reported (156 mA cm^{-2}) yet, there is plenty of room to further improve it by engineering the electrode architecture.

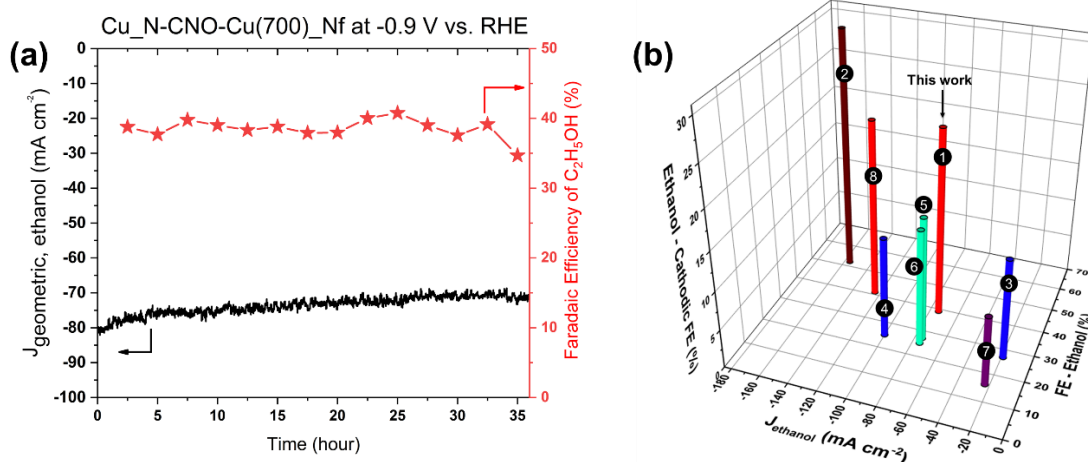


Figure 4. 11 (a) Durability test of Cu_N-CNO-Cu(700)_Nf electrode at -0.9 V vs. RHE and (b) comparison of performance with other reported catalysts that grant current densities $>10 \text{ mA cm}^{-2}$.

Table 4. 2 Comparison of ethanol FE for catalysts with current density higher than 10 mA cm^{-2} .

	Catalyst	J_{ethanol} (Geometric) (mA cm^{-2})	FE _{ethanol} (%)	Cathodic EE _{ethanol} (%)	Reference
1	Cu_N-CNO-Cu(700)_Nf	74	39	24	This work
2	N-C/Cu	156	52	31	Wang et al. ³⁸
3	Boron-doped Cu	19	27	13	Zhou et al. ³⁰⁸
4	Cu ₂ S-Cu	100	25	13	Zhuang et al. ²⁹⁴
5	CuAg	75	25	15	Hoang et al. ²⁹²
6	CuDAT-wire	75	27	16	Hoang et al. ³⁰⁹
7	N-GQD	23	16	9	Wu et al. ⁵⁵
8	Molecule-Cu	124	41	23	Li et al. ²⁹¹

4.4 Summary

In summary, we established a scalable strategy to fabricate an electrode architecture. The modified electrode architecture with the adaptation of PTFE membranes and catalysts resulted in enhanced selectivity and current density of CO₂ electroreduction on Cu electrodes to ethanol. The impact of a nafion ionomer on gas transport was evaluated by the diffusion-reaction model, and that information was used to improve the gas transport properties of the flow-type electrochemical cell. Furthermore, both interfacial and electronic properties of Cu were enhanced by integrating Cu with N-CNO. The XPS analysis of N-CNO_Cu(700) indicated that N-CNO and Cu nanoparticles in the composite were covalently bonded, and pyridinic N groups may play a crucial role in tailoring the electronic properties of Cu. Electrochemical measurements demonstrated that the integration with N-CNO promoted Cu activity in two ways: molecular confinement and modulation of Cu electronic structure. With these synergistic effects, the production of ethanol with 39 % FE was achieved with a partial current density of -74 mA cm⁻². Moreover, the catalyst demonstrated a stable electrolysis performance for 36 hours in an alkaline electrolyte. This work showcases a unique strategy for the efficient production of ethanol from CO₂ with high selectivity and current density. Fundamental understanding of 3-phase interfaces among electrolyte, catalysts as well as innovations of electrode architecture, will make a real breakthrough of the CO₂ reduction technology for commercial applications.

4.5 Supplementary information

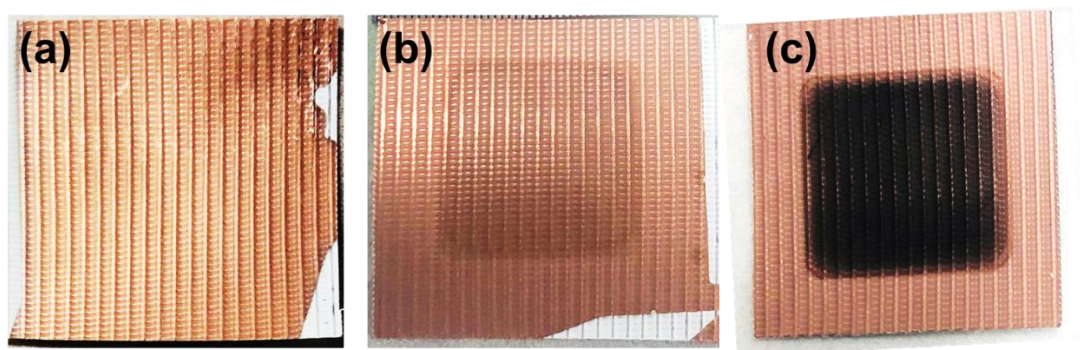


Figure S4. 1 Digital photographs of (a) PTFE-Cu, (b) PTFE-Cu-Nafion, and PTFE-Cu-(Nafion+Catalyst) electrodes.

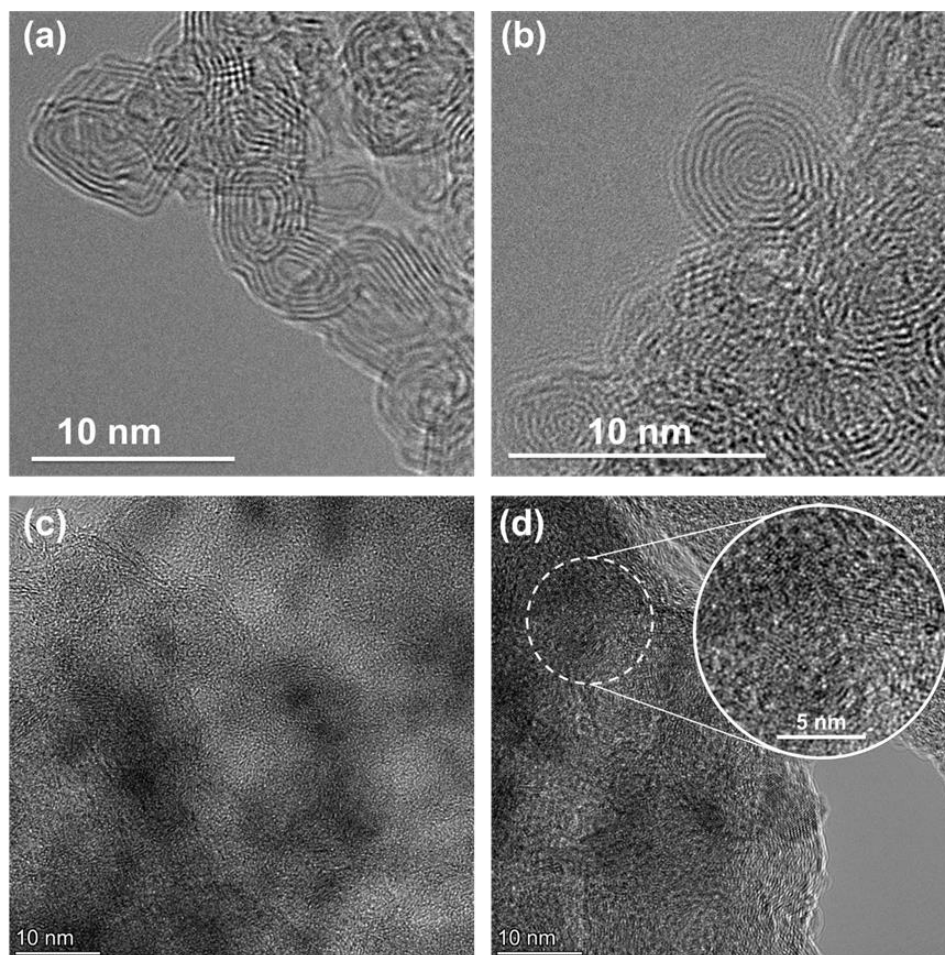


Figure S4. 2 TEM of (a) CNO, (b) N-CNO(700) and (c)-(d) N-CNO-Cu(700), three Cu particles are circled in the inset of (d).

4.5.1 Calculation of crystalline domain size.

The crystalline domain size of copper was calculated using the Scherrer equation.

$$D = \frac{K\lambda}{\beta \cos\theta}$$

Where,

D = Crystallites size (nm)

K = 0.94 (Scherrer constant)- (Assuming spherical particle shape and cubic symmetry)

λ = 0.15406 nm (Wavelength of the X-ray source)

β = FWHM (radians)

θ = Peak position (radians)

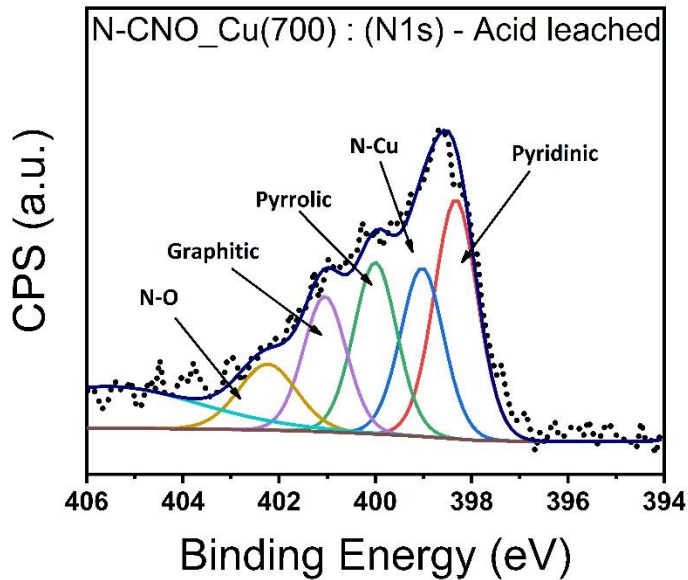


Figure S4. 3 High-resolution XPS of acid leached N-CNO-Cu(700).

Relative percentages of pyridinic, Cu-N, pyrrolic, and graphitic are 30%, 21%, 21%, and 16%, respectively.

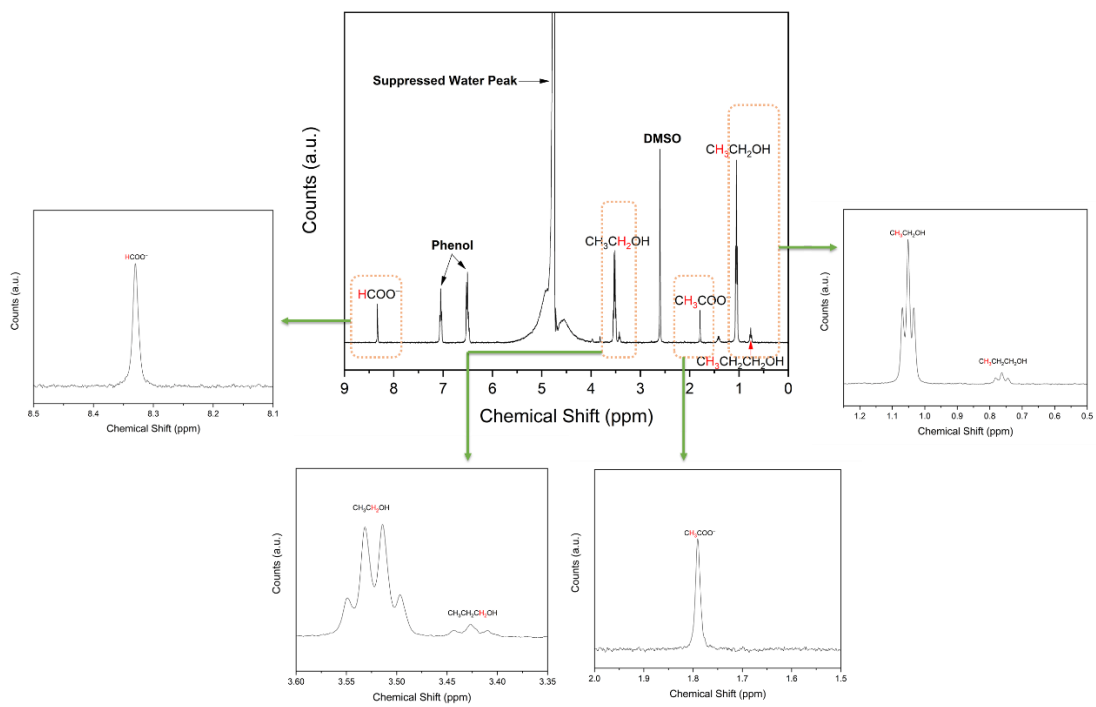


Figure S4. 4 $^1\text{H-NMR}$ of Cu_N-CNO-Cu(700)_{Nf} catholyte after electrolysis at -0.9 V vs. RHE for 30 minutes. DMSO and phenol are internal standards.

CHAPTER 5. CONCLUSIONS AND FUTURE DIRECTIONS

Electrochemical reduction of CO₂ to fuels and chemicals powered by renewable energy presents promising solutions to renewable energy curtailment and detrimental environmental impacts of anthropogenic CO₂. For economically feasible CO₂ conversion technology, however, electrocatalysts should meet stringent requirements, including high energy efficiency (>80-90% FE at <1.8V), high current density (>300 mA cm⁻²), and long-term durability (>80 000 h). So far, the developments of electrocatalysts and reactor systems have been impeded by a lack of fundamental understanding of reaction pathways, local catalyst conditions, and electrode interfaces/interactions.

Heteroatom-doped carbon-based catalysts have been introduced as emerging materials for the CO₂ electroreduction. When the doped carbon is employed as catalyst support, it can modulate the electronic structure of a metal catalyst and enhance the long-term durability of the catalyst. In this thesis, under-investigated metal-free catalysts were investigated. The effects of carbon microstructure and morphology, synergistic co-dopants, and heteroatom-modified support were explored in detail.

The second chapter discusses the effect of nitrogen-doped ultrananocrystalline nanodiamond host structure on the CO₂ electroreduction activity. Nitrogen-containing controlled carbon nanostructures with varying sp²/sp³ ratios were prepared by MACVD. Catalytic activities of nitrogen-doped grain boundaries of ultrananocrystalline nanodiamond vs. multilayer graphite-like structures were systematically studied by experiments and theoretical calculations. Nitrogen atoms in graphitic structure (more-sp²) showed high activity towards the generation of CO over nitrogen in the grain boundaries of UNCD(more-sp³). DFT calculations revealed that these activities are resulting from the

binding energy differences between reaction intermediates. Specifically, grain boundary active sites are poisoned by strong adsorption of CO. However, pyridinic nitrogen in MLG is a strong adsorption site for *COOH, and the adsorption of CO on that site is weak. Consequently, the catalyst produced CO with high selectivity (82% FE). In the future, this work can be expanded to many avenues. First, it is crucial to investigate the active catalyst sites experimentally. As an example, phosphate ions can be used to block pyridinic-N sites before the reaction to probe activity change. This strategy will be used to quantify active sites. Although the MACVD technique generates controlled structures with variable catalytic properties, the current density of the resultant catalyst is low ($<1 \text{ mA cm}^{-2}$) due to limited surface area. The low current is also partly due to the limited mass transfer of CO_2 . Therefore, catalyst structures can be grown on gas diffusion electrodes instead of a Si wafer to increase electrode active area and CO_2 mass transport. Since the activity differences between grain boundary N and MLG pyridinic-N are drastically different, these N groups may alter the electronic structure of metal catalysts. For example, copper nanoparticles can be electrodeposited on NDC-1 and NDC-4 electrodes to generate new catalytic sites and tune product selectivity. Finally, scanning electrochemical microscopy (SECM) techniques can be employed to obtain spatially resolved local electrochemical activities. This approach will provide a deep insight into the structure-performance relationships of catalysts.

The third chapter explored the co-doping of N and S atoms and its impact on CO_2 reduction activity. For the first time, dopant atoms, defects, and associated chemical structures were visualized by STEM techniques. STEM results were coupled with theoretical calculations to identify potential active sites for catalysis. Our results indicated that N-doped CNO and N, S-doped CNO have drastically different catalytic activities. N-

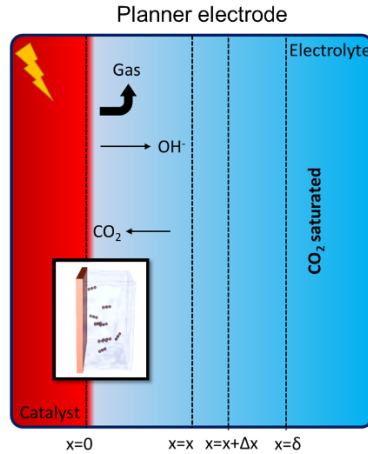
CNO forms HCOOH (55% FE_{\max} at -0.7 V vs. RHE), whereas NS-CNO produces CO (82% FE_{\max} at -0.5 V vs. RHE). Furthermore, we developed a rapid screening method of catalysts by employing the RRDE technique. RRDE measurements revealed that the onset potential of NS-CNO(700) is about -0.2 V vs. RHE, close to the onset potential deduced by theoretical calculations for the potential active domains. For the first time, this work unveils the active domains of the NS-CNO(700) catalyst, which consists of graphitic-N and sulfide configurations. This work also investigated the local environment of the electrode using a reaction-diffusion model. This model predicted that under the H-cell configuration, the reaction suffers from an insufficient mass transport of CO₂ even at low current densities. This limitation was overcome by gas diffusion electrodes, leading to enhanced current density (-10.8 mA cm⁻²) and selectivity toward CO (90% FE) at the overpotential of 290 mV. Although this work is promising as a way to enhance catalyst performance by controlling active sites by engineering heteroatoms, still the performance of the catalyst is inferior to metal-based electrodes. The lower current density of metal-free catalysts is due to the limited number of active sites. In the future, unique strategies should be used to increase the density of the active catalyst domains. Another observation is that the oxidation of N and S functional groups of the catalyst during its operation. Understanding these oxidation mechanisms is crucial to develop more stable catalysts in the future. More specifically, in-situ FTIR/Raman techniques can be employed to probe the chemical degradation of active sites and the reaction intermediates.

The fourth chapter leverages nitrogen doped CNO and Copper nanoparticles to tune catalyst selectivity toward ethanol in the alkaline electrolyte. High ethanol current density, selectivity, and electrode durability were attained by collective modifications of electrode

architecture, interfaces, and the electronic properties of the catalyst. Unlike conventional carbon-based gas diffusion electrodes, Cu deposited PTFE membrane eliminated electrode flooding and maintained unmatched electrode durability. The current density of the electrode was further enhanced by developing a 3D catalyst architecture. This architecture mainly depends on the gas and ion transport behavior of the Nafion ionomer. The reaction-diffusion model indicated that the CO₂ availability could be extended several microns into the porous catalyst by integrating nafion ionomer with catalysts. Most notably, the selectivity towards the production of ethanol was enhanced via tuning the Cu/N-CNO interface by confinement and altering the electronic structure of Cu via direct bonding between N-CNO and Cu. By adopting these concepts, ethanol current density and selectivity were enhanced by 3 times and 2.5 times, respectively, as compared to the unmodified Cu catalyst. Overall, the catalyst exhibited high durability and maintained J_{ethanol} of -74 mA cm^{-2} for more than 30 hours, yielding FE and cathodic energy efficiency of 39% and 24%, respectively. In the future, several other aspects should be explored to increase the current density, selectivity, and stability of the electrode. Although nafion is a good ionic conductor, it is a poor electrical conductor. Therefore, it is worthwhile to test conducting conjugated polymers such as PEDOT:PSS as a binder to get high current densities. Also, it is crucial to understand the gas and ion transport behavior of the polymer once it is mixed with the catalyst. The pore structure, orientation, and arrangement of a polymer that is responsible for gas transport will be characterized by small and wide angle X-ray scattering methods. To elucidate the selectivity of ethanol production, the electronic properties of Cu modulated by heteroatoms will be investigated by DFT calculation in parallel with spectroscopic measurements.

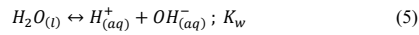
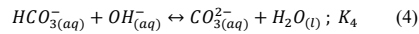
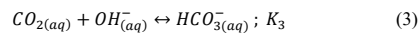
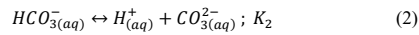
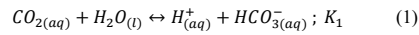
APPENDIX: MODELING LOCAL ELECTRODE CONDITIONS WITH MATLAB
USING REACTION DIFFUSION MODEL

Reaction diffusion model for planar electrode (H-cell configuration)



CO₂ electroreduction is highly sensitive to the local catalytic environment. Therefore, it is crucial to understand the local reaction conditions to deduce reaction mechanisms further.

When CO₂ is dissolved in the electrolyte solution, the following reactions take place.



Reactions (1) and (2) can be ignored at pH > 7 due to the minute constitution of H₂CO₃.

Table of constants at 25 °C, obtained from Gupta et al. under similar electrolyte concentrations.¹⁸¹

	Forward and reverse rate constants	Forward and reverse rate constant values	Equilibrium rate constant
K_1	k_{1f}	$3.71 \times 10^{-2} \text{ s}^{-1}$	$4.27 \times 10^{-7} M$
	k_{1r}	$86970.89 \text{ M}^{-1} \text{ s}^{-1}$	
K_2	k_{2f}	59.44 s^{-1}	$5.623 \times 10^{-11} M$
	k_{2r}	$1.057 \times 10^{12} \text{ M}^{-1} \text{ s}^{-1}$	
K_3	k_{3f}	$5.93 \times 10^3 \text{ M}^{-1} \text{ s}^{-1}$	$4.44 \times 10^7 \text{ M}^{-1}$
	k_{3r}	$1.34 \times 10^{-4} \text{ s}^{-1}$	
K_4	k_{4f}	$1 \times 10^8 \text{ M}^{-1} \text{ s}^{-1}$	$4.66 \times 10^3 \text{ M}^{-1}$
	k_{4r}	$2.15 \times 10^4 \text{ s}^{-1}$	
K_w	k_{wf}	$2.4 \times 10^{-5} \text{ M s}^{-1}$	$1 \times 10^{-14} \text{ M}^2$
	k_{wr}	$2.4 \times 10^9 \text{ M}^{-1} \text{ s}^{-1}$	

With a large electrolyte concentration and the absence of external stirring, the molar flux is given by,

$$J_i = -D_i \frac{\partial C_i}{\partial x}$$

Now, considering the Reaction-diffusion equation, the following time-dependent second order partial differential equation (PDE) is obtained.

$$\frac{\partial C_i}{\partial t} = D_i \frac{\partial^2 C_i}{\partial x^2} + R_i$$

Where,

$$J_i = \text{molar flux} (\text{mol cm}^{-2} \text{ s}^{-1})$$

$$C_i = \text{Concentration}$$

$$D_i = \text{Diffusion Coefficient}$$

$$R_i = \text{Reaction term}$$

Table with diffusion coefficients at 25°C under infinite dilution conditions. Adapted from Gupta et al. and Arquer et al. under similar electrolyte concentrations for identical electrochemical cell system.^{181, 182}

Species	Diffusion coefficient (m ² s ⁻¹)
$CO_{2(aq)}$	1.91×10^{-9}
$H_{(aq)}^+$	9.31×10^{-9}
$HCO_{3(aq)}^-$	0.923×10^{-9}
$CO_{3(aq)}^{2-}$	1.19×10^{-9}
$OH_{(aq)}^-$	5.27×10^{-9}

Now using equilibria reactions, the following PDEs can be written for each species

$$\frac{\partial[CO_{2(aq)}]}{\partial t} = D_{CO_{2(aq)}} \frac{\partial^2[CO_{2(aq)}]}{\partial x^2} - k_{3f}[CO_{2(aq)}][OH_{(aq)}^-] + k_{3r}[HCO_{3(aq)}^-] \quad (1)$$

$$\frac{\partial[HCO_{3(aq)}^-]}{\partial t} = D_{HCO_{3(aq)}^-} \frac{\partial^2[HCO_{3(aq)}^-]}{\partial x^2} + k_{3f}[CO_{2(aq)}][OH_{(aq)}^-] - k_{3r}[HCO_{3(aq)}^-] - k_{4f}[HCO_{3(aq)}^-][OH_{(aq)}^-] + k_{4r}[CO_{3(aq)}^{2-}][H_2O_{(l)}] \quad (2)$$

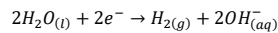
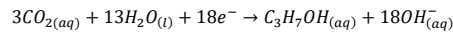
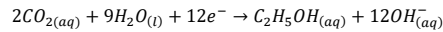
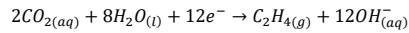
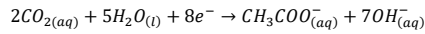
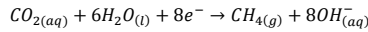
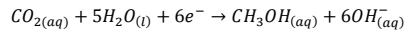
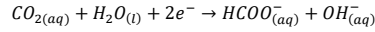
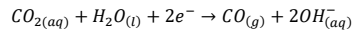
$$\frac{\partial[CO_{3(aq)}^{2-}]}{\partial t} = D_{CO_{3(aq)}^{2-}} \frac{\partial^2[CO_{3(aq)}^{2-}]}{\partial x^2} + k_{4f}[HCO_{3(aq)}^-][OH_{(aq)}^-] - k_{4r}[CO_{3(aq)}^{2-}][H_2O_{(l)}] \quad (3)$$

$$\frac{\partial[OH_{(aq)}^-]}{\partial t} = D_{OH_{(aq)}^-} \frac{\partial^2[OH_{(aq)}^-]}{\partial x^2} - k_{3f}[CO_{2(aq)}][OH_{(aq)}^-] + k_{3r}[HCO_{3(aq)}^-] - k_{4f}[HCO_{3(aq)}^-][OH_{(aq)}^-] + k_{4r}[CO_{3(aq)}^{2-}][H_2O_{(l)}] \quad (4)$$

These coupled time-dependent PDEs (1 to 4) were solved with MATLAB using the following procedure.

1. What are the species consuming/generating at the electrode?
2. At what rate are those species consuming/generating at the electrode?
3. Initial conditions?
4. Boundary conditions?

1. What are the species consuming/generating at the electrode?



From the aforementioned equations, it is clear that $CO_{2(aq)}$ is consumed and $OH_{(aq)}^-$ is generated. Gaseous products and liquid products were ignored as they are not included in the reaction-diffusion equations.

2. At what rate those species are consuming/generating at the electrode?

CO_2 consumption rate per unit area

$$R_{CO_2RR}(\text{mol s}^{-1}\text{m}^{-2}) = \frac{J_{tot}}{F} \left[\left(\frac{nCO_2^{CO(g)} \times FE_{CO(g)}}{ze_{CO(g)}^-} \right) + \left(\frac{nCO_2^{HCOO(aq)} \times FE_{HCOO(aq)}^-}{ze_{HCOO(aq)}^-} \right) + \left(\frac{nCO_2^{CH_3OH(aq)} \times FE_{CH_3OH(aq)}}{ze_{CH_3OH(aq)}^-} \right) + \left(\frac{nCO_2^{CH_4(g)} \times FE_{CH_4(g)}}{ze_{CH_4(g)}^-} \right) \right. \\ \left. + \left(\frac{nCO_2^{CH_3COO(aq)} \times FE_{CH_3COO(aq)}^-}{ze_{CH_3COO(aq)}^-} \right) + \left(\frac{nCO_2^{C_2H_4(g)} \times FE_{C_2H_4(g)}}{ze_{C_2H_4(g)}^-} \right) + \left(\frac{nCO_2^{C_2H_5OH(aq)} \times FE_{C_2H_5OH(aq)}}{ze_{C_2H_5OH(aq)}^-} \right) \right. \\ \left. + \left(\frac{nCO_2^{C_3H_7OH(aq)} \times FE_{C_3H_7OH(aq)}}{ze_{C_3H_7OH(aq)}^-} \right) \right]$$

OH^- generation rate per unit area

$$R_{OH-ER}(\text{mol s}^{-1}\text{m}^{-2}) = \frac{J_{tot}}{F} \left[\left(\frac{nOH_{(aq)}^{CO(g)} \times FE_{CO(g)}}{ze_{CO(g)}^-} \right) + \left(\frac{nOH_{(aq)}^{HCOO(aq)} \times FE_{HCOO(aq)}^-}{ze_{HCOO(aq)}^-} \right) + \left(\frac{nOH_{(aq)}^{CH_3OH(aq)} \times FE_{CH_3OH(aq)}}{ze_{CH_3OH(aq)}^-} \right) + \left(\frac{nOH_{(aq)}^{CH_4(g)} \times FE_{CH_4(g)}}{ze_{CH_4(g)}^-} \right) \right. \\ \left. + \left(\frac{nOH_{(aq)}^{CH_3COO(aq)} \times FE_{CH_3COO(aq)}^-}{ze_{CH_3COO(aq)}^-} \right) + \left(\frac{nOH_{(aq)}^{C_2H_4(g)} \times FE_{C_2H_4(g)}}{ze_{C_2H_4(g)}^-} \right) + \left(\frac{nOH_{(aq)}^{C_2H_5OH(aq)} \times FE_{C_2H_5OH(aq)}}{ze_{C_2H_5OH(aq)}^-} \right) \right. \\ \left. + \left(\frac{nOH_{(aq)}^{C_3H_7OH(aq)} \times FE_{C_3H_7OH(aq)}}{ze_{C_3H_7OH(aq)}^-} \right) \right]$$

Where,

nCO_2 = Number of consumed CO_2 mols

nOH = Number of produced OH^- mols

J_{tot} = Current density from the experiment

FE = Faradaic efficiency

ze^- = Number of electron mols

3. Initial conditions?

At $t = 0$ and $x = x$, at an any given position of the electrolyte

$$[CO_{2(aq)}] = [CO_{2(aq)}]_i$$

$$[HCO_3^-(aq)] = [HCO_3^-(aq)]_i$$

$$[CO_3^{2-}(aq)] = [CO_3^{2-}(aq)]_i$$

$$[OH^-(aq)] = [OH^-(aq)]_i$$

Where,

i, represents initial concentration

4. Boundary conditions?

Left boundary

- At $t > 0$ and $x = 0$, at any given time on the electrode surface, reaction flux

$$D_{CO_2(aq)} \frac{d[CO_2(aq)]}{dx} = -R_{CO_2RR} (\text{mol s}^{-1} \text{m}^{-2})$$

$$D_{OH^-(aq)} \frac{d[OH^-(aq)]}{dx} = R_{OH^-ER} (\text{mol s}^{-1} \text{m}^{-2})$$

$$D_{HCO_3^-(aq)} \frac{d[HCO_3^-(aq)]}{dx} = 0$$

$$D_{CO_3^{2-}(aq)} \frac{d[CO_3^{2-}(aq)]}{dx} = 0$$

Right boundary

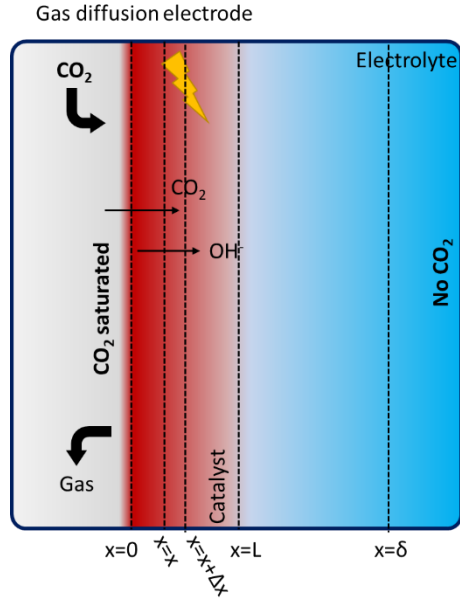
$$[CO_2(aq)] = [CO_2(aq)]_i$$

$$[HCO_3^-(aq)] = [HCO_3^-(aq)]_i$$

$$[CO_3^{2-}(aq)] = [CO_3^{2-}(aq)]_i$$

$$[OH^-(aq)] = [OH^-(aq)]_i$$

Reaction diffusion model for Gas diffusion electrode



For the gas diffusion electrode, similar reaction diffusion equations were used as in H-cell with consumption of CO_2 and generation of OH^- in the catalyst layer.

CO_2 consumption and OH^- generation are assumed to occur homogeneously throughout the entire catalyst layer.

$$\frac{\partial[\text{CO}_2(\text{aq})]}{\partial t} = D_{\text{CO}_2(\text{aq})} \frac{\partial^2[\text{CO}_2(\text{aq})]}{\partial x^2} - k_{3f}[\text{CO}_2(\text{aq})][\text{OH}^-_{(\text{aq})}] + k_{3r}[\text{HCO}_3^-_{(\text{aq})}] - R_{\text{OH}} \quad (1)$$

$$\frac{\partial[\text{HCO}_3^-_{(\text{aq})}]}{\partial t} = D_{\text{HCO}_3^-_{(\text{aq})}} \frac{\partial^2[\text{HCO}_3^-_{(\text{aq})}]}{\partial x^2} + k_{3f}[\text{CO}_2(\text{aq})][\text{OH}^-_{(\text{aq})}] - k_{3r}[\text{HCO}_3^-_{(\text{aq})}] - k_{4f}[\text{HCO}_3^-_{(\text{aq})}][\text{OH}^-_{(\text{aq})}] + k_{4r}[\text{CO}_3^{2-}_{(\text{aq})}][\text{H}_2\text{O}_{(\text{l})}] \quad (2)$$

$$\frac{\partial[\text{CO}_3^{2-}_{(\text{aq})}]}{\partial t} = D_{\text{CO}_3^{2-}_{(\text{aq})}} \frac{\partial^2[\text{CO}_3^{2-}_{(\text{aq})}]}{\partial x^2} + k_{4f}[\text{HCO}_3^-_{(\text{aq})}][\text{OH}^-_{(\text{aq})}] - k_{4r}[\text{CO}_3^{2-}_{(\text{aq})}][\text{H}_2\text{O}_{(\text{l})}] \quad (3)$$

$$\frac{\partial[\text{OH}^-_{(\text{aq})}]}{\partial t} = D_{\text{OH}^-_{(\text{aq})}} \frac{\partial^2[\text{OH}^-_{(\text{aq})}]}{\partial x^2} - k_{3f}[\text{CO}_2(\text{aq})][\text{OH}^-_{(\text{aq})}] + k_{3r}[\text{HCO}_3^-_{(\text{aq})}] - k_{4f}[\text{HCO}_3^-_{(\text{aq})}][\text{OH}^-_{(\text{aq})}] + k_{4r}[\text{CO}_3^{2-}_{(\text{aq})}][\text{H}_2\text{O}_{(\text{l})}] + R_{\text{OH}^-} \quad (4)$$

Similarly, the above coupled PDEs were solved using MATLAB using appropriate boundary conditions. MATLAB codes for the modeling of each electrode are provided below.

MATLAB code for modeling local effects of H-cell electrode of NS-CNO(700) in 0.1

M KHCO₃

```
%clear everything
clc
clear all
%clear everything
%%

% Diffusion coefficients corrected with viscosity of 0.1 M KHCO3 solution

C.DCO2 = 1.674e-7;
C.DHCO3 = 8.09e-8;
C.DCO3 = 1.043e-7; % (dm^2s^-1)
C.DO2 = 4.62e-7;

C.icCO2 = 0.0329;
C.icHCO3 = 0.099; % (mol dm^-3)
C.icCO3 = 3.1e-5;
C.icOH = 6.6e-8;

C.k1f = 5.93e3;
```

```

C.k1r = 1.34e-4;
C.k2f = 1e8;
C.k2r = 2.15e4;

C.L = 0.005; % Distance from the electrode to the liquid boundary (dm)

Current = 0.93; % (mA cm-2)

Time = 600; % seconds

Jtot = Current/10; % (A dm^-2) % Total current density from the experiment

F = 96485.3329; % (A s mol-1)

% Faradaic efficiencies of each product by experiment

FEFCO = 0.82;
FEHCOO = 0.0;
FECH3OH = 0;
FECH4 = 0.0;
FECH3COO = 0;
FEC2H4 = 0.0;
FEC2H5OH = 0;
FEC3H7OH = 0;

C.RCO2 = (Jtot/F) * ((FEFCO/2)+(FEHCOO/2)+(FECH3OH/6)+(FECH4/8)+(2*FECH3COO/8)+(2*FEC2H4/12)+(2*FEC2H5OH/12)+(3*FEC3H7OH/18));
C.ROH = (Jtot/F) * ((FEFCO)+(FEHCOO/2)+(FECH3OH)+(FECH4)+(7*FECH3COO/8)+(FEC2H4)+(FEC2H5OH)+(FEC3H7OH));

%%
x = linspace(0,C.L,500);
t = linspace(0,Time,600);
%%
m = 0;
eqn = @(x,t,u,dudx) diffPDE(x,t,u,dudx,C);
ic = @(x) diffIC(x,C);
bc = @(x1,ul,xr,ur,t) diffBC(x1,ul,xr,ur,t,C);
sol = pdepe(m,eqn,ic,bc,x,t);

%%
cCO2 = sol(:,1);
cHCO3 = sol(:,2);
cCO3 = sol(:,3);
cOH = sol(:,4);

% functions to plot each graph
plotCO2(x,t,cCO2)
plotHCO3(x,t,cHCO3)
plotCO3(x,t,cCO3)
plotpH(x,t,cOH)

%%

function [c,f,s] = diffPDE(x,t,u,dudx,C)

CO2 = u(1);
HCO3 = u(2);
CO3 = u(3);
OH = u(4);

DCO2 = C.DCO2;
DHCO3 = C.DHCO3;
DCO3 = C.DCO3;
DOH = C.DOH;

k1f = C.k1f;
k1r = C.k1r;
k2f = C.k2f;
k2r = C.k2r;

c = [1;1;1;1];
f = [DCO2*dudx(1);DHCO3*dudx(2);DCO3*dudx(3); DOH*dudx(4)];
s = [HCO3*k1r - CO2*OH*k1f; CO2*OH*k1f-HCO3*k1r-HCO3*OH*k2f+CO3*k2r; HCO3*OH*k2f-CO3*k2r; -CO2*OH*k1f+HCO3*k1r-HCO3*OH*k2f+CO3*k2r];

end

function u0 = diffIC(x,C)

icCO2 = C.icCO2;
icHCO3 = C.icHCO3;
icCO3 = C.icCO3;
icOH = C.icOH;

u0=[icCO2; icHCO3; icCO3; icOH];

end

function [p1,q1,pr,qr] = diffBC(x1,ul,xr,ur,t,C)

CO2 = ur(1);
HCO3 = ur(2);
CO3 = ur(3);
OH = ur(4);

icCO2 = C.icCO2;
icHCO3 = C.icHCO3;
icCO3 = C.icCO3;
icOH = C.icOH;

RCO2 = C.RCO2;
ROH = C.ROH;

pr = [CO2 - icCO2; HCO3 - icHCO3; CO3 - icCO3; OH - icOH];
qr = [0; 0; 0; 0];
p1 = [-RCO2; 0; 0; ROH];
q1 = [1; 1; 1; 1];

end

function [] = plotCO2(x,t,cCO2)

figure(1)
surf(x*1e5,t,cCO2*1000)

```

```

title('CO_2')
xlabel('Distance x (um)')
ylabel('Time t (s)')
zlabel('CO_2 Concentration(mM)')

%%%%%%%%%%%%%%%%%%%%%%%%%%%%%%%%%%%%%%%%%%%%%%%%%%%%%%%%%%%%%%%%%%%%%%%% make things look nicer%%%%%%%%%%%%%%%%%%%%%%%%%%%%%%%%%%%%%%%%%%%%%%%%%%%%%%%%%%%%%%%%%%%%%%%%
view(3);
axis on;
light;
lighting phong;
camlight('left');
shading interp;

%%%%%%%%%%%%%%%%%%%%%%%%%%%%%%%%%%%%%%%%%%%%%%%%%%%%%%%%%%%%%%%%%%%%%%%% make things look nicer%%%%%%%%%%%%%%%%%%%%%%%%%%%%%%%%%%%%%%%%%%%%%%%%%%%%%%%%%%%%%%%%%%%%%%%%

end

function [] = plotHCO3(x,t,cHCO3)

figure(2)
surf(x*1e5,t,cHCO3)

title('HCO_3^(-)')
xlabel('Distance x (um)')
ylabel('Time t (s)')
zlabel('HCO_3^(-) Concentration (M)')

view(3);
axis on;
light;
lighting phong;
camlight('left');
shading interp;

end

function [] = plotCO3(x,t,cCO3)

figure(3)
surf(x*1e5,t,cCO3)

title('CO_3^{2-}')
xlabel('Distance x (um)')
ylabel('Time t (s)')
zlabel('CO_3^{2-} Concentration (M)')

view(3);
axis on;
light;
lighting phong;
camlight('left');
shading interp;

end

function [] = plotpH(x,t,cOH)

pOH = -log10(cOH);
pH = 14 - pOH;

figure(4)
X = x*1e5;
surf(X,t,pH)

title('pH')
xlabel('Distance x (um)')
ylabel('Time t (s)')
zlabel('pH')

view(3);
axis on;
light;
lighting phong;
camlight('left');
shading interp;

figure(5)

% cross sectional plot at t = 500s, grid position 500
plot(X, pH(500,:))

title('pH Profile at t = 500 s')
xlabel('Distance x (um)')
ylabel('pH')

end

```

MATLAB code for modeling local effects of GDE of NS-CNO(700) in 1 M KHCO₃

```

%clear everything
clc
clear all
%clear everything
%%

% diffusion coefficients corrected with viscosity of 1M KHCO3 1.145
C.DCO2 = 1.484e-7;
C.DHCO3 = 7.17e-8;
C.DCO3 = 0.925e-7; % (dm^2s^-1)
C.DO2 = 4.09e-7;

% Initial concentration of each species
C.icCO2 = 0.0237;
C.icHCO3 = 0.994; % (mol dm^-3)
C.icCO3 = 0.003;
C.icOH = 2.51e-6;

% Forward and reverse rate constants for equilibrium reactions
C.k1f = 5.93e3;

```

```

C.k1r = 1.34e-4;
C.k2f = 1e8;
C.k2r = 2.15e4;

C.L = 0.005; % Distance from the electrode to the liquid boundary (dm)
C.CL = 1e-6;

JT = 10.8; % Current density mA cm-2
C.Jtot = JT/10; % (A dm^-2) % Total current density from the experiment

F = 96485.3329; % (A s mol-1)

% Faradaic efficiencies of each product by experiment

C.FECO = 0.91;
C.FEHCOO = 0.00;
C.FECH3OH = 0;
C.FECH4 = 0.00;
C.FECH3COO = 0;
C.FEC2H4 = 0.00;
C.FEC2H5OH = 0.0;
C.FEC3H7OH = 0;

FECO = C.FECO;
FEHCOO = C.FEHCOO;
FECH3OH = C.FECH3OH;
FECH4 = C.FECH4;
FECH3COO = C.FECH3COO;
FEC2H4 = C.FEC2H4;
FEC2H5OH = C.FEC2H5OH;
FEC3H7OH = C.FEC3H7OH;

% flux
C.RRco2 = (C.Jtot/F) * ((FECO/2) + (FEHCOO/2) + (FECH3OH/6) + (FECH4/8) + (2*FECH3COO/8) + (2*FEC2H4/12) + (2*FEC2H5OH/12) + (3*FEC3H7OH/18));
C.RROH = (C.Jtot/F) * ((FECO) + (FEHCOO/2) + (FECH3OH) + (FECH4) + (7*FECH3COO/8) + (FEC2H4) + (FEC2H5OH) + (FEC3H7OH));

%%
x = linspace(0,C.L,500);
t = linspace(0,50,500);
m = 0;
eqn = @(x,t,u,dudx) diffPDE(x,t,u,dudx,C);
ic = @(x) diffIC(x,C);
bc = @(xl,ul,xr,ur,t) diffBC(xl,ul,xr,ur,t,C);
sol = pdepe(m,eqn,ic,bc,x,t);

%%
cCO2 = sol(:,:,1);
cHCO3 = sol(:,:,2);
cCO3 = sol(:,:,3);
cOH = sol(:,:,4);

cOH = max(0,cOH);

% functions to plot each graph
plotCO2(x,t,cCO2)
plotHCO3(x,t,cHCO3)
plotCO3(x,t,cCO3)
plotpH(x,t,cOH)

%%

function [c,f,s] = diffPDE(x,t,u,dudx,C)

Jtot = C.Jtot;

FECO = C.FECO;
FEHCOO = C.FEHCOO;
FECH3OH = C.FECH3OH;
FECH4 = C.FECH4;
FECH3COO = C.FECH3COO;
FEC2H4 = C.FEC2H4;
FEC2H5OH = C.FEC2H5OH;
FEC3H7OH = C.FEC3H7OH;

icCO2 = C.icCO2;

CL = C.CL;

if 0 <= x <= CL
    RCO2 = (u(1)/icCO2) * (0.6/CL) * (Jtot/F) * ((FECO/2) + (FEHCOO/2) + (FECH3OH/6) + (FECH4/8) + (2*FECH3COO/8) + (2*FEC2H4/12) + (2*FEC2H5OH/12) + (3*FEC3H7OH/18))
    ROH = (0.6/C.CL) * (Jtot/F) * ((FECO) + (FEHCOO/2) + (FECH3OH) + (FECH4) + (7*FECH3COO/8) + (FEC2H4) + (FEC2H5OH) + (FEC3H7OH))
else
    RCO2 = 0;
    ROH = 0;
end

CO2 = u(1);
HCO3 = u(2);
CO3 = u(3);
OH = u(4);

DCO2 = C.DCO2;
DHCO3 = C.DHCO3;
DCO3 = C.DCO3;
DOH = C.DOH;

k1f = C.k1f;
k1r = C.k1r;
k2f = C.k2f;
k2r = C.k2r;

c = [1;1;1;1];
f = [DCO2*dudx(1); DHCO3*dudx(2); DCO3*dudx(3); DOH*dudx(4)];
s = [HCO3*k1r - CO2*OH*k1f - RCO2; CO2*OH*k1f - HCO3*k1r - HCO3*OH*k2f + CO3*k2r; HCO3*OH*k2f - CO3*k2r; -CO2*OH*k1f + HCO3*k1r - HCO3*OH*k2f + CO3*k2r + ROH];

end

function u0 = diffIC(x,C)

```

```

icCO2 = 0;
icHCO3 = C.icHCO3;
icCO3 = C.icCO3;
icOH = C.icOH;

u0=[icCO2; icHCO3; icCO3; icOH];

end

function [p1,q1,pr,qr] = diffBC(x1,ul,xr,ur,t,C)

CO2r = ur(1);
HCO3r = ur(2);
CO3r = ur(3);
OHR = ur(4);

CO2l = ul(1);
HCO3l = ul(2);
CO3l = ul(3);
OHL = ul(4);

icCO2 = C.icCO2;
icHCO3 = C.icHCO3;
icCO3 = C.icCO3;
icOH = C.icOH;

RRCO2 = C.RRCO2;
RROH = C.RROH;

pr = [CO2r - 0; HCO3r - 0; CO3r - icCO3; OHR - icOH];
qr = [1; 0; 0; 0];
p1 = [CO2l - icCO2; 0; 0; RROH];
q1 = [0; 1; 1; 1];

end

function [] = plotCO2(x,t,cCO2)

figure(1)
ccCO2 = cCO2*1000;
surf(x*1e5,t,cCO2*1000)

title('CO_2')
xlabel('Distance x (um)')
ylabel('Time t (s)')
zlabel('CO_2 Concentration(mM)')

%%%%%%%%%%%% make things look nicer%%%%%%%%%%%%
view(3);
axis on;
light;
lighting phong;
camlight('left');
shading interp;

%%%%%%%%%%%% make things look nicer%%%%%%%%%%%%

figure(2)
% cross sectional plot at t = 25s, grid position 250
semilogy(x*1e5, ccCO2(250,:))

title('CO2 mM Profile at t = 25s')
xlabel('Distance x (um)')
ylabel('mM')

end

function [] = plotHCO3(x,t,cHCO3)

figure(3)
surf(x*1e5,t,cHCO3)

title('HCO_3^-')
xlabel('Distance x (um)')
ylabel('Time t (s)')
zlabel('HCO_3 Concentration (M)')

view(3);
axis on;
light;
lighting phong;
camlight('left');
shading interp;

end

function [] = plotCO3(x,t,cCO3)

figure(4)
surf(x*1e5,t,cCO3)

title('CO_3^(2-)')
xlabel('Distance x (um)')
ylabel('Time t (s)')
zlabel('CO_3^(2-) Concentration (M)')

view(3);
axis on;
light;
lighting phong;
camlight('left');
shading interp;

end

function [] = plotpH(x,t,cOH)

pOH = -log10(cOH);
pH = 14 - pOH;

figure(5)
X = x*1e5;
surf(X,t,pH)

```



```
shading interp;
figure(6)
% cross sectional plot at t = 25s, grid position 250
plot(X, pH(250,:))
title('pH Profile at t = 25s')
xlabel('Distance x (um)')
ylabel('pH')
end
```

MATLAB code for modeling local effects of Cu_N-CNO-Cu(700) in 1M KOH

```

%clear everything
clc
clear all
%clear everything
%%

% Diffusion coefficients of each species, corrected with dynamic viscosity of 1M KOH 1.123
C.DCO2 = 1.514e-7;
C.DHCO3 = 7.31e-8;
C.DCO3 = 0.943e-7; % (dm^2s^-1)
C.DO2 = 4.18e-7;

% Initial concentration of each species.
C.icCO2 = 0.0245;
C.icHCO3 = 0; % (mol dm^-3)
C.icCO3 = 0;
C.icOH = 1;

% Forward and reverse rate constants for equilibria reactions.
C.k1f = 5.93e3;
C.k1r = 1.34e-4;
C.k2f = 1e8;
C.k2r = 2.15e4;

C.L = 0.005; % Distance from the electrode to the liquid boundary (dm)
C.CL = 1e-6; % Thickness of the sputtered Cu layer

JT = 201; % Current density from the experiment (mA cm^-2)
C.Jtot = JT/10; % (A dm^-2) % Total current density from the experiment unit conversion

F = 96485.3329; % (A s mol^-1), Faraday constant

% Faradaic efficiency of each product by experiment, divided by 100
C.FECO = 0.0059;
C.FEFCOO = 0.017;
C.FECH3OH = 0;
C.FECH4 = 0.023;
C.FECH3COO = 0.037;
C.FEC2H4 = 0.33;
C.FEC2H5OH = 0.39;
C.FEC3H7OH = 0.027;

FECO = C.FECO;
FEFCOO = C.FEFCOO;
FECH3OH = C.FECH3OH;
FECH4 = C.FECH4;
FECH3COO = C.FECH3COO;
FEC2H4 = C.FEC2H4;
FEC2H5OH = C.FEC2H5OH;
FEC3H7OH = C.FEC3H7OH;

% Rate of generation and consumption terms
C.RR2CO2 = (C.Jtot/F) * ((FECO/2) + (FEFCOO/2) + (FECH3OH/6) + (FECH4/8) + (2*FECH3COO/8) + (2*FEC2H4/12) + (2*FEC2H5OH/12) + (3*FEC3H7OH/18));
C.RR2OH = (C.Jtot/F) * ((FECO) + (FEFCOO/2) + (FECH3OH) + (FECH4) + (7*FECH3COO/8) + (FEC2H4) + (FEC2H5OH) + (FEC3H7OH));

%%
% define a mesh
x = linspace(0,C.L,500);
t = linspace(0,50,500);
%%
% solving coupled PDE
m = 0;
eqn = @(x,t,u,dudx) diffPDE(x,t,u,dudx,C);
ic = @(x) diffIC(x,C);
bc = @(xl,ul,xr,ur,t) diffBC(xl,ul,xr,ur,t,C);
sol = pdepe(m,eqn,ic,bc,x,t);

%%
% extracting values from solved PDE for each term
cCO2 = sol(:,:,1);
cHCO3 = sol(:,:,2);
cCO3 = sol(:,:,3);
cOH = sol(:,:,4);

% functions to plot each graph
plotCO2(x,t,cCO2)
plotHCO3(x,t,cHCO3)
plotCO3(x,t,cCO3)
plotpH(x,t,cOH)

%%

function [c,f,s] = diffPDE(x,t,u,dudx,C)

Jtot = C.Jtot;

FECO = C.FECO;
FEFCOO = C.FEFCOO;
FECH3OH = C.FECH3OH;
FECH4 = C.FECH4;
FECH3COO = C.FECH3COO;
FEC2H4 = C.FEC2H4;
FEC2H5OH = C.FEC2H5OH;
FEC3H7OH = C.FEC3H7OH;

icCO2 = C.icCO2;

CL = C.CL;

```

```

if 0 <= x <= CL
    RCO2 = (u(1)/icCO2)*(0.6/CL)*(Jtot/F)*((FECO/2)+(FEHCOO/2)+(FECH3OH/6)+(FECH4/8)+(2*FECH3COO/8)+(2*FECH2H4/12)+(2*FECH2H5OH/12)+(3*FECH3TOH/18))
    ROH = (0.6/C.L)*(Jtot/F)*((FECO)+(FEHCOO/2)+(FECH3OH)+(FECH4)+(7*FECH3COO/8)+(FECH2H4)+(FECH2H5OH)+(FECH3TOH))
else
    RCO2 = 0;
    ROH = 0;
end

CO2 = u(1);
HCO3 = u(2);
CO3 = u(3);
OH = u(4);

DCO2 = C.DCO2;
DHCO3 = C.DHCO3;
DCO3 = C.DCO3;
DOH = C.DOH;

k1f = C.k1f;
k1r = C.k1r;
k2f = C.k2f;
k2r = C.k2r;

c = [1;1;1;1];
f = [DCO2*dudx(1);DHCO3*dudx(2);DCO3*dudx(3); DOH*dudx(4)];
s = [HCO3*k1r - CO2*OH*k1f - RCO2 ; CO2*OH*k1f-HCO3*k1r-HCO3*OH*k2f+CO3*k2r; HCO3*OH*k2f-CO3*k2r; -CO2*OH*k1f+HCO3*k1r-HCO3*OH*k2f+CO3*k2r + ROH];

end

function u0 = diffIC(x,C)

icCO2 = 0;
icHCO3 = C.icHCO3;
icCO3 = C.icCO3;
icOH = C.icOH;

u0=[icCO2; icHCO3; icCO3; icOH];

end

function [p1,q1,pr,qr] = diffBC(x1,ul,xr,ur,t,C)

CO2r = ur(1);
HCO3r = ur(2);
CO3r = ur(3);
OHR = ur(4);

CO2l = ul(1);
HCO3l = ul(2);
CO3l = ul(3);
OHL = ul(4);

icCO2 = C.icCO2;
icHCO3 = C.icHCO3;
icCO3 = C.icCO3;
icOH = C.icOH;

RRCO2 = C.RRCO2;
RROH = C.RROH;

pr = [CO2r - 0; HCO3r - 0; CO3r - icCO3; OHR - icOH];
qr = [1; 0; 0; 0];
p1 = [CO2l - icCO2; 0; 0; RROH];
q1 = [0; 1; 1; 1];

end

function [] = plotCO2(x,t,cCO2)

figure(1)
ccCO2 = cCO2*1000;
surf(log10(x*1e5),t,cCO2*1000) % plot x-axis in log scale

title('CO [2]')
xlabel('Distance x (um)')
ylabel('Time t (s)')
zlabel('CO [2] Concentration(mM)')

%%%%%%%%%%%% Adjust graph format %%%%%%%%%%%%%
view(3);
axis on;
light;
lighting phong;
camlight('left');
shading interp;

%%%%%%%%%%%% Adjust graph format %%%%%%%%%%%%%

figure(2)
% cross sectional plot at t = 25s, grid position 250
semilogx(x*1e5, ccCO2(250,:))% plot x-axis in log scale
%plot(x*1e5, ccCO2(250,:))

title('CO2 mM Profile at t = 25s')
xlabel('Distance x (um)')
ylabel('mM')

end

function [] = plotHCO3(x,t,cHCO3)

figure(3)
surf(x*1e5,t,cHCO3)

title('HCO [3]^(-)')
xlabel('Distance x (um)')
ylabel('Time t (s)')
zlabel('HCO [3] Concentration(M)')

%%%%%%%%%%%% Adjust graph format %%%%%%%%%%%%%
view(3);

```

```

axis on;
light;
lighting phong;
camlight('left');
shading interp;

end

function [] = plotCO3(x,t,cCO3)

figure(4)
surf(x*1e5,t,cCO3)

title('CO3(2-)')
xlabel('Distance x (um)')
ylabel('Time t (s)')
zlabel('CO3(2-) Concentration (M)')

%%%%%%%%%%%% Adjust graph format %%%%%%%%%%
view(3);
axis on;
light;
lighting phong;
camlight('left');
shading interp;

end

function [] = plotpH(x,t,cOH)

pOH = -log10(cOH);
pH = 14 - pOH;

figure(5)
X = x*1e5;
surf(X,t,pH)

title('pH')
xlabel('Distance x (um)')
ylabel('Time t (s)')
zlabel('pH')

%%%%%%%%%%%% Adjust graph format %%%%%%%%%%
view(3);
axis on;
light;
lighting phong;
camlight('left');
shading interp;

figure(6)

% cross sectional plot at t = 25s, grid position 250

plot(X, pH(250,:))

title('pH Profile at t = 25s')
xlabel('Distance x (um)')
ylabel('pH')

end

```

REFERENCES

1. EPA Greenhouse Gas Equivalencies Calculator. <https://www.epa.gov/energy/greenhouse-gas-equivalencies-calculator> (accessed 04-20-2020).
2. Lüthi, D.; Le Floch, M.; Bereiter, B.; Blunier, T.; Barnola, J.-M.; Siegenthaler, U.; Raynaud, D.; Jouzel, J.; Fischer, H.; Kawamura, K.; Stocker, T. F., High-resolution carbon dioxide concentration record 650,000–800,000 years before present. *Nature* **2008**, *453* (7193), 379-382.
3. Ritchie, H. R., Max CO₂ and Greenhouse Gas Emissions. In *Our World in Data*, 2020.
4. Li, K.; An, X.; Park, K. H.; Khraisheh, M.; Tang, J., A critical review of CO₂ photoconversion: Catalysts and reactors. *Catalysis Today* **2014**, *224*, 3-12.
5. Wanninayake, N.; Ai, Q.; Zhou, R.; Hoque, M. A.; Herrell, S.; Guzman, M. I.; Risko, C.; Kim, D. Y., Understanding the effect of host structure of nitrogen doped ultrananocrystalline diamond electrode on electrochemical carbon dioxide reduction. *Carbon* **2020**, *157*, 408-419.
6. Nitopi, S.; Bertheussen, E.; Scott, S. B.; Liu, X.; Engstfeld, A. K.; Horch, S.; Seger, B.; Stephens, I. E. L.; Chan, K.; Hahn, C.; Nørskov, J. K.; Jaramillo, T. F.; Chorkendorff, I., Progress and Perspectives of Electrochemical CO₂ Reduction on Copper in Aqueous Electrolyte. *Chemical Reviews* **2019**, *119* (12), 7610-7672.
7. EPA US Carbon Dioxide Emissions. <https://www.epa.gov/ghgemissions/overview-greenhouse-gases#carbon-dioxide> (accessed 07-12-2020).
8. Intergovernmental Panel on Climate, C., *Climate Change 2014: Mitigation of Climate Change: Working Group III Contribution to the IPCC Fifth Assessment Report*. Cambridge University Press: Cambridge, 2015.
9. Lund, H., Chapter 1 - Introduction. In *Renewable Energy Systems (Second Edition)*, Lund, H., Ed. Academic Press: Boston, 2014; pp 1-14.
10. Administration, U. S. E. I. U.S. primary energy consumption by energy source, Monthly Energy Review, April 2020. <https://www.eia.gov/energyexplained/renewable-sources/> (accessed 07-14-2020).
11. statistics, R. e. Share of energy from renewable sources, 2018. https://ec.europa.eu/eurostat/statistics-explained/index.php/Renewable_energy_statistics#:~:text=In%202018%2C%20renewable%20energy%20represented,EU%20reached%208.3%20%25%20in%202018. (accessed 07-14-2020).
12. Pickl, M. J., The renewable energy strategies of oil majors – From oil to energy? *Energy Strategy Reviews* **2019**, *26*, 100370.
13. Bird, L.; Lew, D.; Milligan, M.; Carlini, E. M.; Estanqueiro, A.; Flynn, D.; Gomez-Lazaro, E.; Holttinen, H.; Menemenlis, N.; Orth, A.; Eriksen, P. B.; Smith, J. C.; Soder, L.; Sorensen, P.; Altiparmakis, A.; Yasuda, Y.; Miller, J., Wind and solar energy curtailment: A review of international experience. *Renewable and Sustainable Energy Reviews* **2016**, *65*, 577-586.

14. Frew, B.; Cole, W.; Denholm, P.; Frazier, A. W.; Vincent, N.; Margolis, R., Sunny with a Chance of Curtailment: Operating the US Grid with Very High Levels of Solar Photovoltaics. *iScience* **2019**, *21*, 436-447.
15. Hailye, T. What Will California Do With Too Much Solar? <https://www.kqed.org/science/610026/what-will-california-do-with-too-much-solar> (accessed 07-19-2020).
16. Yan, Z.; Hitt, J. L.; Turner, J. A.; Mallouk, T. E., Renewable electricity storage using electrolysis. *Proceedings of the National Academy of Sciences* **2020**, *117* (23), 12558-12563.
17. Dincer, I.; Ezan, M. A., Energy Storage Methods. In *Heat Storage: A Unique Solution For Energy Systems*, Springer International Publishing: Cham, 2018; pp 35-56.
18. Davis, S. J.; Lewis, N. S.; Shaner, M.; Aggarwal, S.; Arent, D.; Azevedo, I. L.; Benson, S. M.; Bradley, T.; Brouwer, J.; Chiang, Y.-M.; Clack, C. T. M.; Cohen, A.; Doig, S.; Edmonds, J.; Fennell, P.; Field, C. B.; Hannegan, B.; Hodge, B.-M.; Hoffert, M. I.; Ingersoll, E.; Jaramillo, P.; Lackner, K. S.; Mach, K. J.; Mastrandrea, M.; Ogden, J.; Peterson, P. F.; Sanchez, D. L.; Sperling, D.; Stagner, J.; Trancik, J. E.; Yang, C.-J.; Caldeira, K., Net-zero emissions energy systems. *Science* **2018**, *360* (6396), eaas9793.
19. Hepburn, C.; Adlen, E.; Beddington, J.; Carter, E. A.; Fuss, S.; Mac Dowell, N.; Minx, J. C.; Smith, P.; Williams, C. K., The technological and economic prospects for CO₂ utilization and removal. *Nature* **2019**, *575* (7781), 87-97.
20. Sun, Z.; Ma, T.; Tao, H.; Fan, Q.; Han, B., Fundamentals and Challenges of Electrochemical CO₂ Reduction Using Two-Dimensional Materials. *Chem* **2017**, *3* (4), 560-587.
21. Song, C., Global challenges and strategies for control, conversion and utilization of CO₂ for sustainable development involving energy, catalysis, adsorption and chemical processing. *Catalysis Today* **2006**, *115* (1), 2-32.
22. Fan, L.; Xia, C.; Yang, F.; Wang, J.; Wang, H.; Lu, Y., Strategies in catalysts and electrolyzer design for electrochemical CO₂ reduction toward C₂₊ products. *Science Advances* **2020**, *6* (8), eaay3111.
23. Mondal, B.; Song, J.; Neese, F.; Ye, S., Bio-inspired mechanistic insights into CO₂ reduction. *Current Opinion in Chemical Biology* **2015**, *25*, 103-109.
24. Francke, R.; Schille, B.; Roemelt, M., Homogeneously Catalyzed Electroreduction of Carbon Dioxide—Methods, Mechanisms, and Catalysts. *Chemical Reviews* **2018**, *118* (9), 4631-4701.
25. Miessler, G. L.; Fischer, P. J.; Tarr, D. A., *Inorganic chemistry*. 2014.
26. Ludwig, J. R.; Schindler, C. S., Catalyst: Sustainable Catalysis. *Chem* **2017**, *2* (3), 313-316.
27. Krischer, K. S., Elena R., Fundamentals of Electrocatalysis. In *Handbook of Heterogeneous Catalysis*, 2008; pp 1873-1905.
28. Wei, L.; Tian, N.; Zhou, Z. Y.; Jiang, Y. X.; Sun, S. G., Electrocatalyst Preparation by Electrodeposition. In *Encyclopedia of Interfacial Chemistry*, Wandelt, K., Ed. Elsevier: Oxford, 2018; pp 507-520.
29. Pletcher, D., A first course in electrode processes. The Royal Society of Chemistry Publishing: Cambridge: 2009.
30. Brownson, D. A.; Banks, C. E., The handbook of graphene electrochemistry. **2014**.

31. Engel, T.; Reid, P. J., *Thermodynamics, statistical thermodynamics, and kinetics*. Prentice Hall Upper Saddle River, NJ, USA: 2010.
32. Medford, A. J.; Vojvodic, A.; Hummelshøj, J. S.; Voss, J.; Abild-Pedersen, F.; Studt, F.; Bligaard, T.; Nilsson, A.; Nørskov, J. K., From the Sabatier principle to a predictive theory of transition-metal heterogeneous catalysis. *Journal of Catalysis* **2015**, *328*, 36-42.
33. Perez, N., Mass Transport by Diffusion and Migration. In *Electrochemistry and Corrosion Science*, Perez, N., Ed. Springer International Publishing: Cham, 2016; pp 151-197.
34. Cai, W.; Zhao, X.; Liu, C.; Xing, W.; Zhang, J., 2 - Electrode Kinetics of Electron-Transfer Reaction and Reactant Transport in Electrolyte Solution. In *Rotating Electrode Methods and Oxygen Reduction Electrocatalysts*, Xing, W.; Yin, G.; Zhang, J., Eds. Elsevier: Amsterdam, 2014; pp 33-65.
35. Bushuyev, O. S.; De Luna, P.; Dinh, C. T.; Tao, L.; Saur, G.; van de Lagemaat, J.; Kelley, S. O.; Sargent, E. H., What Should We Make with CO₂ and How Can We Make It? *Joule* **2018**, *2* (5), 825-832.
36. Spurgeon, J. M.; Kumar, B., A comparative technoeconomic analysis of pathways for commercial electrochemical CO₂ reduction to liquid products. *Energy & Environmental Science* **2018**, *11* (6), 1536-1551.
37. Kibria, M. G.; Edwards, J. P.; Gabardo, C. M.; Dinh, C.-T.; Seifitokaldani, A.; Sinton, D.; Sargent, E. H., Electrochemical CO₂ Reduction into Chemical Feedstocks: From Mechanistic Electrocatalysis Models to System Design. *Advanced Materials* **2019**, *31* (31), 1807166.
38. Wang, X.; Wang, Z.; García de Arquer, F. P.; Dinh, C.-T.; Ozden, A.; Li, Y. C.; Nam, D.-H.; Li, J.; Liu, Y.-S.; Wicks, J.; Chen, Z.; Chi, M.; Chen, B.; Wang, Y.; Tam, J.; Howe, J. Y.; Proppe, A.; Todorović, P.; Li, F.; Zhuang, T.-T.; Gabardo, C. M.; Kirmani, A. R.; McCallum, C.; Hung, S.-F.; Lum, Y.; Luo, M.; Min, Y.; Xu, A.; O'Brien, C. P.; Stephen, B.; Sun, B.; Ip, A. H.; Richter, L. J.; Kelley, S. O.; Sinton, D.; Sargent, E. H., Efficient electrically powered CO₂-to-ethanol via suppression of deoxygenation. *Nature Energy* **2020**, *5* (6), 478-486.
39. Zheng, T.; Jiang, K.; Wang, H., Recent Advances in Electrochemical CO₂-to-CO Conversion on Heterogeneous Catalysts. *Advanced Materials* **2018**, *30* (48), 1802066.
40. Garg, S.; Li, M.; Weber, A. Z.; Ge, L.; Li, L.; Rudolph, V.; Wang, G.; Rufford, T. E., Advances and challenges in electrochemical CO₂ reduction processes: an engineering and design perspective looking beyond new catalyst materials. *Journal of Materials Chemistry A* **2020**, *8* (4), 1511-1544.
41. Khezri, B.; Fisher, A. C.; Pumera, M., CO₂ reduction: the quest for electrocatalytic materials. *Journal of Materials Chemistry A* **2017**, *5* (18), 8230-8246.
42. Kharisov, B. I.; Kharissova, O. V., General Data on Carbon Allotropes. In *Carbon Allotropes: Metal-Complex Chemistry, Properties and Applications*, Springer International Publishing: Cham, 2019; pp 1-8.
43. Bianco, A.; Chen, Y.; Chen, Y.; Ghoshal, D.; Hurt, R. H.; Kim, Y. A.; Koratkar, N.; Meunier, V.; Terrones, M., A carbon science perspective in 2018: Current achievements and future challenges. *Carbon* **2018**, *132*, 785-801.

44. Mohamed, A. G. A.; Huang, Y.; Xie, J.; Borse, R. A.; Parameswaram, G.; Wang, Y., Metal-free sites with multidimensional structure modifications for selective electrochemical CO₂ reduction. *Nano Today* **2020**, *33*, 100891.
45. Rodríguez-reinoso, F., The role of carbon materials in heterogeneous catalysis. *Carbon* **1998**, *36* (3), 159-175.
46. Liu, Y.; Chen, S.; Quan, X.; Yu, H., Efficient Electrochemical Reduction of Carbon Dioxide to Acetate on Nitrogen-Doped Nanodiamond. *Journal of the American Chemical Society* **2015**, *137* (36), 11631-11636.
47. Liu, Y.; Zhang, Y.; Cheng, K.; Quan, X.; Fan, X.; Su, Y.; Chen, S.; Zhao, H.; Zhang, Y.; Yu, H.; Hoffmann, M. R., Selective Electrochemical Reduction of Carbon Dioxide to Ethanol on a Boron- and Nitrogen-Co-doped Nanodiamond. *Angewandte Chemie International Edition* **2017**, *56* (49), 15607-15611.
48. Tomisaki, M.; Kasahara, S.; Natsui, K.; Ikemiya, N.; Einaga, Y., Switchable Product Selectivity in the Electrochemical Reduction of Carbon Dioxide Using Boron-Doped Diamond Electrodes. *Journal of the American Chemical Society* **2019**, *141* (18), 7414-7420.
49. Wei, D.; Liu, Y.; Wang, Y.; Zhang, H.; Huang, L.; Yu, G., Synthesis of N-Doped Graphene by Chemical Vapor Deposition and Its Electrical Properties. *Nano Letters* **2009**, *9* (5), 1752-1758.
50. Sandoval, S.; Tobias, G., Tuning the Nature of N-Based Groups From N-Containing Reduced Graphene Oxide: Enhanced Thermal Stability Using Post-Synthesis Treatments. *Nanomaterials* **2020**, *10* (8), 1451.
51. Jalili, S.; Vaziri, R., Study of the electronic properties of Li-intercalated nitrogen doped graphite. *Molecular Physics* **2011**, *109* (5), 687-694.
52. Wang, X.; Sun, G.; Routh, P.; Kim, D.-H.; Huang, W.; Chen, P., Heteroatom-doped graphene materials: syntheses, properties and applications. *Chemical Society Reviews* **2014**, *43* (20), 7067-7098.
53. Wu, J.; Yadav, R. M.; Liu, M.; Sharma, P. P.; Tiwary, C. S.; Ma, L.; Zou, X.; Zhou, X.-D.; Yakobson, B. I.; Lou, J.; Ajayan, P. M., Achieving Highly Efficient, Selective, and Stable CO₂ Reduction on Nitrogen-Doped Carbon Nanotubes. *ACS Nano* **2015**, *9* (5), 5364-5371.
54. Wu, J.; Liu, M.; Sharma, P. P.; Yadav, R. M.; Ma, L.; Yang, Y.; Zou, X.; Zhou, X.-D.; Vajtai, R.; Yakobson, B. I.; Lou, J.; Ajayan, P. M., Incorporation of Nitrogen Defects for Efficient Reduction of CO₂ via Two-Electron Pathway on Three-Dimensional Graphene Foam. *Nano Letters* **2016**, *16* (1), 466-470.
55. Wu, J.; Ma, S.; Sun, J.; Gold, J. I.; Tiwary, C.; Kim, B.; Zhu, L.; Chopra, N.; Odeh, I. N.; Vajtai, R.; Yu, A. Z.; Luo, R.; Lou, J.; Ding, G.; Kenis, P. J. A.; Ajayan, P. M., A metal-free electrocatalyst for carbon dioxide reduction to multi-carbon hydrocarbons and oxygenates. *Nature Communications* **2016**, *7* (1), 13869.
56. Liu, Y.; Zhao, J.; Cai, Q., Pyrrolic-nitrogen doped graphene: a metal-free electrocatalyst with high efficiency and selectivity for the reduction of carbon dioxide to formic acid: a computational study. *Physical Chemistry Chemical Physics* **2016**, *18* (7), 5491-5498.
57. Cui, X.; Pan, Z.; Zhang, L.; Peng, H.; Zheng, G., Selective Etching of Nitrogen-Doped Carbon by Steam for Enhanced Electrochemical CO₂ Reduction. *Advanced Energy Materials* **2017**, *7* (22), 1701456.

58. Xu, J.; Kan, Y.; Huang, R.; Zhang, B.; Wang, B.; Wu, K.-H.; Lin, Y.; Sun, X.; Li, Q.; Centi, G.; Su, D., Revealing the Origin of Activity in Nitrogen-Doped Nanocarbons towards Electrocatalytic Reduction of Carbon Dioxide. *ChemSusChem* **2016**, *9* (10), 1085-1089.
59. Pan, F.; Li, B.; Deng, W.; Du, Z.; Gang, Y.; Wang, G.; Li, Y., Promoting electrocatalytic CO₂ reduction on nitrogen-doped carbon with sulfur addition. *Applied Catalysis B: Environmental* **2019**, *252*, 240-249.
60. Hori, Y., Electrochemical CO₂ Reduction on Metal Electrodes, in "Modern Aspects of Electrochemistry 42", Eds. CG Vayenas, RE White, ME Gamboa-Aldeco. Springer New York, New York: 2008.
61. Zheng, X.; De Luna, P.; García de Arquer, F. P.; Zhang, B.; Becknell, N.; Ross, M. B.; Li, Y.; Banis, M. N.; Li, Y.; Liu, M.; Voznyy, O.; Dinh, C. T.; Zhuang, T.; Stadler, P.; Cui, Y.; Du, X.; Yang, P.; Sargent, E. H., Sulfur-Modulated Tin Sites Enable Highly Selective Electrochemical Reduction of CO₂ to Formate. *Joule* **2017**, *1* (4), 794-805.
62. Ma, M.; Trzeźniewski, B. J.; Xie, J.; Smith, W. A., Selective and Efficient Reduction of Carbon Dioxide to Carbon Monoxide on Oxide-Derived Nanostructured Silver Electrocatalysts. *Angewandte Chemie International Edition* **2016**, *55* (33), 9748-9752.
63. Jiang, K.; Siahrostami, S.; Akey, A. J.; Li, Y.; Lu, Z.; Lattimer, J.; Hu, Y.; Stokes, C.; Gangishetty, M.; Chen, G.; Zhou, Y.; Hill, W.; Cai, W.-B.; Bell, D.; Chan, K.; Nørskov, J. K.; Cui, Y.; Wang, H., Transition-Metal Single Atoms in a Graphene Shell as Active Centers for Highly Efficient Artificial Photosynthesis. *Chem* **2017**, *3* (6), 950-960.
64. Ju, W.; Bagger, A.; Hao, G.-P.; Varela, A. S.; Sinev, I.; Bon, V.; Roldan Cuenya, B.; Kaskel, S.; Rossmeisl, J.; Strasser, P., Understanding activity and selectivity of metal-nitrogen-doped carbon catalysts for electrochemical reduction of CO₂. *Nature Communications* **2017**, *8* (1), 944.
65. Kuhl, K. P.; Cave, E. R.; Abram, D. N.; Jaramillo, T. F., New insights into the electrochemical reduction of carbon dioxide on metallic copper surfaces. *Energy & Environmental Science* **2012**, *5* (5), 7050-7059.
66. Li, C. W.; Kanan, M. W., CO₂ Reduction at Low Overpotential on Cu Electrodes Resulting from the Reduction of Thick Cu₂O Films. *Journal of the American Chemical Society* **2012**, *134* (17), 7231-7234.
67. Raciti, D.; Livi, K. J.; Wang, C., Highly Dense Cu Nanowires for Low-Overpotential CO₂ Reduction. *Nano Letters* **2015**, *15* (10), 6829-6835.
68. Cao, L.; Raciti, D.; Li, C.; Livi, K. J. T.; Rottmann, P. F.; Hemker, K. J.; Mueller, T.; Wang, C., Mechanistic Insights for Low-Overpotential Electroreduction of CO₂ to CO on Copper Nanowires. *ACS Catalysis* **2017**, *7* (12), 8578-8587.
69. Kibria, M. G.; Dinh, C.-T.; Seifitokaldani, A.; De Luna, P.; Burdyny, T.; Quintero-Bermudez, R.; Ross, M. B.; Bushuyev, O. S.; García de Arquer, F. P.; Yang, P.; Sinton, D.; Sargent, E. H., A Surface Reconstruction Route to High Productivity and Selectivity in CO₂ Electroreduction toward C₂+ Hydrocarbons. *Advanced Materials* **2018**, *30* (49), 1804867.

70. Handoko, A. D.; Chan, K. W.; Yeo, B. S., $-CH_3$ Mediated Pathway for the Electroreduction of CO_2 to Ethane and Ethanol on Thick Oxide-Derived Copper Catalysts at Low Overpotentials. *ACS Energy Letters* **2017**, *2* (9), 2103-2109.
71. Dinh, C.-T.; Burdyny, T.; Kibria, M. G.; Seifitokaldani, A.; Gabardo, C. M.; García de Arquer, F. P.; Kiani, A.; Edwards, J. P.; De Luna, P.; Bushuyev, O. S.; Zou, C.; Quintero-Bermudez, R.; Pang, Y.; Sinton, D.; Sargent, E. H., CO_2 electroreduction to ethylene via hydroxide-mediated copper catalysis at an abrupt interface. *Science* **2018**, *360* (6390), 783-787.
72. Navalon, S.; Dhakshinamoorthy, A.; Alvaro, M.; Garcia, H., Metal nanoparticles supported on two-dimensional graphenes as heterogeneous catalysts. *Coordination Chemistry Reviews* **2016**, *312*, 99-148.
73. Song, Y.; Peng, R.; Hensley, D. K.; Bonnesen, P. V.; Liang, L.; Wu, Z.; Meyer III, H. M.; Chi, M.; Ma, C.; Sumpter, B. G.; Rondinone, A. J., High-Selectivity Electrochemical Conversion of CO_2 to Ethanol using a Copper Nanoparticle/N-Doped Graphene Electrode. *ChemistrySelect* **2016**, *1* (19), 6055-6061.
74. Hernandez-Aldave, S.; Andreoli, E., Fundamentals of Gas Diffusion Electrodes and Electrolysers for Carbon Dioxide Utilisation: Challenges and Opportunities. *Catalysts* **2020**, *10* (6), 713.
75. Burdyny, T.; Smith, W. A., CO_2 reduction on gas-diffusion electrodes and why catalytic performance must be assessed at commercially-relevant conditions. *Energy & Environmental Science* **2019**, *12* (5), 1442-1453.
76. Haynes, W. M., *CRC handbook of chemistry and physics*. CRC press: 2014.
77. Thomas, M. P.; Wanninayake, N.; De Alwis Goonatileke, M.; Kim, D. Y.; Guiton, B. S., Direct imaging of heteroatom dopants in catalytic carbon nano-onions. *Nanoscale* **2020**, *12* (10), 6144-6152.
78. Raupach, M. R.; Marland, G.; Ciais, P.; Le Quere, C.; Canadell, J. G.; Klepper, G.; Field, C. B., Global and regional drivers of accelerating CO_2 emissions. *Proc Natl Acad Sci U S A* **2007**, *104* (24), 10288-93.
79. Scheffer, M.; Brovkin, V.; Cox, P. M., Positive feedback between global warming and atmospheric CO_2 concentration inferred from past climate change. *Geophysical Research Letters* **2006**, *33* (10).
80. Kuhl, K. P.; Hatsukade, T.; Cave, E. R.; Abram, D. N.; Kibsgaard, J.; Jaramillo, T. F., Electrocatalytic Conversion of Carbon Dioxide to Methane and Methanol on Transition Metal Surfaces. *Journal of the American Chemical Society* **2014**, *136* (40), 14107-14113.
81. Wu, J.; Zhou, X.-D., Catalytic conversion of CO_2 to value added fuels: Current status, challenges, and future directions. *Chinese Journal of Catalysis* **2016**, *37* (7), 999-1015.
82. Jovanov, Z. P.; Hansen, H. A.; Varela, A. S.; Malacrida, P.; Peterson, A. A.; Nørskov, J. K.; Stephens, I. E. L.; Chorkendorff, I., Opportunities and challenges in the electrocatalysis of CO_2 and CO reduction using bifunctional surfaces: A theoretical and experimental study of Au-Cd alloys. *Journal of Catalysis* **2016**, *343* (Supplement C), 215-231.
83. Wu, J.; Risalvato, F. G.; Ke, F.-S.; Pellechia, P. J.; Zhou, X.-D., Electrochemical Reduction of Carbon Dioxide I. Effects of the Electrolyte on the Selectivity and Activity with Sn Electrode. *Journal of The Electrochemical Society* **2012**, *159* (7), F353-F359.

84. Kondratenko, E. V.; Mul, G.; Baltrusaitis, J.; Larrazabal, G. O.; Perez-Ramirez, J., Status and perspectives of CO₂ conversion into fuels and chemicals by catalytic, photocatalytic and electrocatalytic processes. *Energy & Environmental Science* **2013**, *6* (11), 3112-3135.
85. Duan, X.; Xu, J.; Wei, Z.; Ma, J.; Guo, S.; Wang, S.; Liu, H.; Dou, S., Metal-Free Carbon Materials for CO₂ Electrochemical Reduction. *Advanced Materials* **2017**, *29* (41), 1701784.
86. Chai, G.-L.; Guo, Z.-X., Highly effective sites and selectivity of nitrogen-doped graphene/CNT catalysts for CO₂ electrochemical reduction. *Chemical Science* **2016**, *7* (2), 1268-1275.
87. Zhu, D. D.; Liu, J. L.; Qiao, S. Z., Recent Advances in Inorganic Heterogeneous Electrocatalysts for Reduction of Carbon Dioxide. *Advanced Materials* **2016**, *28* (18), 3423-3452.
88. Shcherban, N. D.; Filonenko, S. M.; Ovcharov, M. L.; Mishura, A. M.; Skoryk, M. A.; Aho, A.; Murzin, D. Y., Simple method for preparing of sulfur-doped graphitic carbon nitride with superior activity in CO₂ photoreduction. *ChemistrySelect* **2016**, *1* (15), 4987-4993.
89. Sreekanth, N.; Nazrulla, M. A.; Vineesh, T. V.; Sailaja, K.; Phani, K. L., Metal-free boron-doped graphene for selective electroreduction of carbon dioxide to formic acid/formate. *Chemical Communications* **2015**, *51* (89), 16061-16064.
90. Yang, N.; Waldvogel, S. R.; Jiang, X., Electrochemistry of Carbon Dioxide on Carbon Electrodes. *ACS Applied Materials & Interfaces* **2016**, *8* (42), 28357-28371.
91. Wu, J.; Yadav, R. M.; Liu, M.; Sharma, P. P.; Tiwary, C. S.; Ma, L.; Zou, X.; Zhou, X. D.; Yakobson, B. I.; Lou, J.; Ajayan, P. M., Achieving Highly Efficient, Selective, and Stable CO₂ Reduction on Nitrogen-Doped Carbon Nanotubes. *ACS Nano* **2015**, *9* (5), 5364-71.
92. Sharma, P. P.; Wu, J.; Yadav, R. M.; Liu, M.; Wright, C. J.; Tiwary, C. S.; Yakobson, B. I.; Lou, J.; Ajayan, P. M.; Zhou, X.-D., Nitrogen-Doped Carbon Nanotube Arrays for High-Efficiency Electrochemical Reduction of CO₂: On the Understanding of Defects, Defect Density, and Selectivity. *Angewandte Chemie International Edition* **2015**, *54* (46), 13701-13705.
93. Natsui, K.; Iwakawa, H.; Ikemiya, N.; Nakata, K.; Einaga, Y., Stable and Highly Efficient Electrochemical Production of Formic Acid from Carbon Dioxide Using Diamond Electrodes. *Angewandte Chemie International Edition* **2018**, *57* (10), 2639-2643.
94. Islam, S. Z.; Reed, A.; Nagpure, S.; Wanninayake, N.; Browning, J. F.; Strzalka, J.; Kim, D. Y.; Rankin, S. E., Hydrogen incorporation by plasma treatment gives mesoporous black TiO₂ thin films with visible photoelectrochemical water oxidation activity. *Microporous and Mesoporous Materials* **2018**, *261* (Supplement C), 35-43.
95. Islam, S. Z.; Reed, A.; Wanninayake, N.; Kim, D. Y.; Rankin, S. E., Remarkable Enhancement of Photocatalytic Water Oxidation in N₂/Ar Plasma Treated, Mesoporous TiO₂ Films. *The Journal of Physical Chemistry C* **2016**, *120* (26), 14069-14081.
96. Britz, D., 100% ir compensation by damped positive feedback. *Electrochimica Acta* **1980**, *25* (11), 1449-1452.
97. Aguirre, M. E.; Zhou, R.; Eugene, A. J.; Guzman, M. I.; Grela, M. A., Cu₂O/TiO₂ heterostructures for CO₂ reduction through a direct Z-scheme: Protecting Cu₂O from photocorrosion. *Applied Catalysis B: Environmental* **2017**, *217*, 485-493.

98. Bo, Z.; Yang, Y.; Chen, J.; Yu, K.; Yan, J.; Cen, K., Plasma-enhanced chemical vapor deposition synthesis of vertically oriented graphene nanosheets. *Nanoscale* **2013**, *5* (12), 5180-5204.
99. Auciello, O.; Sumant, A. V., Status review of the science and technology of ultrananocrystalline diamond (UNCD™) films and application to multifunctional devices. *Diamond and Related Materials* **2010**, *19* (7), 699-718.
100. May, P. W.; Smith, J. A.; Mankelevich, Y. A., Deposition of NCD films using hot filament CVD and Ar/CH₄/H₂ gas mixtures. *Diamond and Related Materials* **2006**, *15* (2), 345-352.
101. Birrell, J.; Carlisle, J. A.; Auciello, O.; Gruen, D. M.; Gibson, J. M., Morphology and electronic structure in nitrogen-doped ultrananocrystalline diamond. *Applied Physics Letters* **2002**, *81* (12), 2235-2237.
102. Bhattacharyya, S.; Auciello, O.; Birrell, J.; Carlisle, J. A.; Curtiss, L. A.; Goyette, A. N.; Gruen, D. M.; Krauss, A. R.; Schlueter, J.; Sumant, A.; Zapol, P., Synthesis and characterization of highly-conducting nitrogen-doped ultrananocrystalline diamond films. *Applied Physics Letters* **2001**, *79* (10), 1441-1443.
103. Tzeng, Y.; Yeh, S.; Fang, W. C.; Chu, Y., Nitrogen-incorporated ultrananocrystalline diamond and multi-layer-graphene-like hybrid carbon films. **2014**, *4*, 4531.
104. Cheng, C. Y.; Teii, K., Control of the Growth Regimes of Nanodiamond and Nanographite in Microwave Plasmas. *IEEE Transactions on Plasma Science* **2012**, *40* (7), 1783-1788.
105. Teii, K.; Shimada, S.; Nakashima, M.; Chuang, A. T. H., Synthesis and electrical characterization of n-type carbon nanowalls. *Journal of Applied Physics* **2009**, *106* (8), 084303.
106. Takeuchi, W.; Ura, M.; Hiramatsu, M.; Tokuda, Y.; Kano, H.; Hori, M., Electrical conduction control of carbon nanowalls. *Applied Physics Letters* **2008**, *92* (21), 213103.
107. Zapol, P.; Sternberg, M.; Curtiss, L. A.; Frauenheim, T.; Gruen, D. M., Tight-binding molecular-dynamics simulation of impurities in ultrananocrystalline diamond grain boundaries. *Physical Review B* **2001**, *65* (4), 045403.
108. Sankaran, K. J.; Kurian, J.; Chen, H. C.; Dong, C. L.; Lee, C. Y.; Tai, N. H.; Lin, I. N., Origin of a needle-like granular structure for ultrananocrystalline diamond films grown in a N₂/CH₄ plasma. *Journal of Physics D: Applied Physics* **2012**, *45* (36), 365303.
109. Kumar, A.; Ann Lin, P.; Xue, A.; Hao, B.; Khin Yap, Y.; Sankaran, R. M., Formation of nanodiamonds at near-ambient conditions via microplasma dissociation of ethanol vapour. *Nature Communications* **2013**, *4* (1), 2618.
110. Klinger, M., More features, more tools, more CrysTBox. *Journal of Applied Crystallography* **2017**, *50* (4), 1226-1234.
111. Shenderova, O. A.; Gruen, D. M., *Ultrananocrystalline diamond: synthesis, properties and applications*. William Andrew: 2012.
112. Andrea Carlo, F.; Robertson, J., Raman Spectroscopy of Amorphous, Nanostructured, Diamond-like Carbon, and Nanodiamond. *Philosophical Transactions: Mathematical, Physical and Engineering Sciences* **2004**, *362* (1824), 2477-2512.
113. Takehiko, O.; Masaaki, Y.; Akira, H.; Minoru, T., Raman Analysis of trans - Polyacetylene Chains in Hydrogenated Amorphous Carbon Films. *Japanese Journal of Applied Physics* **2007**, *46* (2R), 756.

114. Beams, R.; Gustavo Cançado, L.; Novotny, L., Raman characterization of defects and dopants in graphene. *Journal of Physics: Condensed Matter* **2015**, *27* (8), 083002.
115. Rolim, G. K.; Corrêa, S. A.; Galves, L. A.; Lopes, J. M. J.; Soares, G. V.; Radtke, C., Chemical and morphological modifications of single layer graphene submitted to annealing in water vapor. *Applied Surface Science* **2018**, *427* (Part B), 825-829.
116. Rani, R.; Panda, K.; Kumar, N.; Titovich, K. A.; Ivanovich, K. V.; Vyacheslavovich, S. A.; Lin, I. N., Tribological Properties of Ultrananocrystalline Diamond Films: Mechanochemical Transformation of Sliding Interfaces. *Scientific Reports* **2018**, *8* (1), 283.
117. Kaciulis, S., Spectroscopy of carbon: from diamond to nitride films. *Surface and Interface Analysis* **2012**, *44* (8), 1155-1161.
118. Shigemoto, A.; Amano, T.; Yamamoto, R., Work function measurements of vanadium doped diamond-like carbon films by ultraviolet photoelectron spectroscopy. *arXiv preprint arXiv:1402.1911* **2014**.
119. Shchukarev, A.; Korolkov, D., XPS Study of group IA carbonates. In *Open Chemistry*, 2004; Vol. 2, p 347.
120. Xing, Z.; Ju, Z.; Zhao, Y.; Wan, J.; Zhu, Y.; Qiang, Y.; Qian, Y., One-pot hydrothermal synthesis of Nitrogen-doped graphene as high-performance anode materials for lithium ion batteries. *Scientific Reports* **2016**, *6*, 26146.
121. Zhang, C.; Hao, R.; Liao, H.; Hou, Y., Synthesis of amino-functionalized graphene as metal-free catalyst and exploration of the roles of various nitrogen states in oxygen reduction reaction. *Nano Energy* **2013**, *2* (1), 88-97.
122. Birrell, J.; Gerbi, J. E.; Auciello, O.; Gibson, J. M.; Gruen, D. M.; Carlisle, J. A., Bonding structure in nitrogen doped ultrananocrystalline diamond. *Journal of Applied Physics* **2003**, *93* (9), 5606-5612.
123. Murata, Y.; Nakayama, R.; Ichihara, F.; Ono, H.; Choo, C.-K.; Tanaka, K., Effects of nitrogen substitution in amorphous carbon films on electronic structure and surface reactivity studied with x-ray and ultra-violet photoelectron spectroscopies. *Journal of Applied Physics* **2017**, *121* (9), 095302.
124. Song, C.; Kim, S., Preparation and Electrochemical Characterization of Pt-Supported Flake-like Graphitic Carbon Nitride on Reduced Graphene Oxide as Fuel Cell Catalysts. *Journal of The Electrochemical Society* **2015**, *162* (10), F1181-F1190.
125. Yu, Y.; Zhang, H.; Cui, S., Fabrication of robust multilayer films by triggering the coupling reaction between phenol and primary amine groups with visible light irradiation. *Nanoscale* **2011**, *3* (9), 3819-3824.
126. Graf, N.; Yegen, E.; Gross, T.; Lippitz, A.; Weigel, W.; Krakert, S.; Terfort, A.; Unger, W. E. S., XPS and NEXAFS studies of aliphatic and aromatic amine species on functionalized surfaces. *Surface Science* **2009**, *603* (18), 2849-2860.
127. Tan, K. L.; Tan, B. T. G.; Kang, E. T.; Neoh, K. G., X-ray photoelectron spectroscopy studies of the chemical structure of polyaniline. *Physical Review B* **1989**, *39* (11), 8070-8073.
128. Xing, T.; Zheng, Y.; Li, L. H.; Cowie, B. C. C.; Gunzelmann, D.; Qiao, S. Z.; Huang, S.; Chen, Y., Observation of Active Sites for Oxygen Reduction Reaction on Nitrogen-Doped Multilayer Graphene. *ACS Nano* **2014**, *8* (7), 6856-6862.

129. Xing, T.; Sunarso, J.; Yang, W.; Yin, Y.; Glushenkov, A. M.; Li, L. H.; Howlett, P. C.; Chen, Y., Ball milling: a green mechanochemical approach for synthesis of nitrogen doped carbon nanoparticles. *Nanoscale* **2013**, *5* (17), 7970-7976.
130. Pan, F.; Jin, J.; Fu, X.; Liu, Q.; Zhang, J., Advanced Oxygen Reduction Electrocatalyst Based on Nitrogen-Doped Graphene Derived from Edible Sugar and Urea. *ACS Applied Materials & Interfaces* **2013**, *5* (21), 11108-11114.
131. Kabir, S.; Artyushkova, K.; Serov, A.; Kiefer, B.; Atanassov, P., Binding energy shifts for nitrogen-containing graphene-based electrocatalysts – experiments and DFT calculations. *Surface and Interface Analysis* **2016**, *48* (5), 293-300.
132. Lu, X.; Leung, D. Y. C.; Wang, H.; Leung, M. K. H.; Xuan, J., Electrochemical Reduction of Carbon Dioxide to Formic Acid. **2014**, *1* (5), 836-849.
133. Daiyan, R.; Tan, X.; Chen, R.; Saputera, W. H.; Tahini, H. A.; Lovell, E.; Ng, Y. H.; Smith, S. C.; Dai, L.; Lu, X.; Amal, R., Electroreduction of CO₂ to CO on a Mesoporous Carbon Catalyst with Progressively Removed Nitrogen Moieties. *ACS Energy Letters* **2018**, *3* (9), 2292-2298.
134. Song, Y.; Peng, R.; Hensley, D. K.; Bonnesen, P. V.; Liang, L.; Wu, Z.; Meyer, H. M.; Chi, M.; Ma, C.; Sumpter, B. G.; Rondinone, A. J., High-Selectivity Electrochemical Conversion of CO₂ to Ethanol using a Copper Nanoparticle/N-Doped Graphene Electrode. *ChemistrySelect* **2016**, *1* (19), 6055-6061.
135. Hatsukade, T.; Kuhl, K. P.; Cave, E. R.; Abram, D. N.; Jaramillo, T. F., Insights into the electrocatalytic reduction of CO₂ on metallic silver surfaces. *Physical Chemistry Chemical Physics* **2014**, *16* (27), 13814-13819.
136. Bennett, J. A.; Wang, J.; Show, Y.; Swain, G. M., Effect of sp²-Bonded Nondiamond Carbon Impurity on the Response of Boron-Doped Polycrystalline Diamond Thin-Film Electrodes. *Journal of The Electrochemical Society* **2004**, *151* (9), E306-E313.
137. Lu, Q.; Rosen, J.; Zhou, Y.; Hutchings, G. S.; Kimmel, Y. C.; Chen, J. G.; Jiao, F., A selective and efficient electrocatalyst for carbon dioxide reduction. *Nature Communications* **2014**, *5* (1), 3242.
138. Chen, Y.; Li, C. W.; Kanan, M. W., Aqueous CO₂ Reduction at Very Low Overpotential on Oxide-Derived Au Nanoparticles. *Journal of the American Chemical Society* **2012**, *134* (49), 19969-19972.
139. Pandey, K. C., New dimerized-chain model for the reconstruction of the diamond (111)-(2 × 2) surface. *Physical Review B* **1982**, *25* (6), 4338-4341.
140. Zhang, Y.; Liu, J.; Wei, Z.; Liu, Q.; Wang, C.; Ma, J., Electrochemical CO₂ reduction over nitrogen-doped SnO₂ crystal surfaces. *Journal of energy chemistry* **2019**, *33*, 22-30.
141. Yang, Y.; Liu, J.; Wei, Z.; Wang, S.; Ma, J., Transition metal-dinitrogen complex embedded graphene for nitrogen reduction reaction. *ChemCatChem* **2019**, *11* (12), 2821-2827.
142. Alfonso, D. R.; Tafen, D. N.; Kauffmann, D. R., First-principles modeling in heterogeneous electrocatalysis. *Catalysts* **2018**, *8* (10), 424.
143. McCrory, C. C.; Jung, S.; Peters, J. C.; Jaramillo, T. F., Benchmarking heterogeneous electrocatalysts for the oxygen evolution reaction. *Journal of the American Chemical Society* **2013**, *135* (45), 16977-16987.

144. Kresse, G., G. kresse and d. joubert, phys. rev. b 59, 1758 (1999). *Phys. Rev. B* **1999**, 59, 1758.
145. Kresse, G.; Furthmüller, J., Efficient iterative schemes for ab initio total-energy calculations using a plane-wave basis set. *Physical Review B* **1996**, 54 (16), 11169-11186.
146. Kresse, G.; Furthmüller, J., Efficiency of ab-initio total energy calculations for metals and semiconductors using a plane-wave basis set. *Computational materials science* **1996**, 6 (1), 15-50.
147. Kresse, G.; Hafner, J., Ab initio molecular dynamics for open-shell transition metals. *Physical Review B* **1993**, 48 (17), 13115.
148. Perdew, J. P.; Chevary, J. A.; Vosko, S. H.; Jackson, K. A.; Pederson, M. R.; Singh, D. J.; Fiolhais, C., Atoms, molecules, solids, and surfaces: Applications of the generalized gradient approximation for exchange and correlation. *Physical review B* **1992**, 46 (11), 6671.
149. Blöchl, P. E., Projector augmented-wave method. *Physical review B* **1994**, 50 (24), 17953.
150. Grimme, S.; Ehrlich, S.; Goerigk, L., Effect of the damping function in dispersion corrected density functional theory. *Journal of computational chemistry* **2011**, 32 (7), 1456-1465.
151. Grimme, S.; Antony, J.; Ehrlich, S.; Krieg, H., A consistent and accurate ab initio parametrization of density functional dispersion correction (DFT-D) for the 94 elements H-Pu. *The Journal of chemical physics* **2010**, 132 (15), 154104.
152. Mathew, K.; Kolluru, V. C.; Mula, S.; Steinmann, S. N.; Hennig, R. G., Implicit self-consistent electrolyte model in plane-wave density-functional theory. *The Journal of Chemical Physics* **2019**, 151 (23), 234101.
153. Mathew, K.; Sundararaman, R.; Letchworth-Weaver, K.; Arias, T.; Hennig, R. G., Implicit solvation model for density-functional study of nanocrystal surfaces and reaction pathways. *The Journal of chemical physics* **2014**, 140 (8), 084106.
154. Peterson, A. A.; Abild-Pedersen, F.; Studt, F.; Rossmeisl, J.; Nørskov, J. K., How copper catalyzes the electroreduction of carbon dioxide into hydrocarbon fuels. *Energy & Environmental Science* **2010**, 3 (9), 1311-1315.
155. Johnson III, R. D., NIST Computational Chemistry Comparison and Benchmark Database, NIST Standard Reference Database Number 101 Release 18, 2016. See the following: <https://cccbdb.nist.gov> **2015**.
156. Jones, G.; Jakobsen, J. G.; Shim, S. S.; Kleis, J.; Andersson, M. P.; Rossmeisl, J.; Abild-Pedersen, F.; Bligaard, T.; Helveg, S.; Hinnemann, B., First principles calculations and experimental insight into methane steam reforming over transition metal catalysts. *Journal of Catalysis* **2008**, 259 (1), 147-160.
157. Theaker, N.; Strain, J. M.; Kumar, B.; Brian, J. P.; Kumari, S.; Spurgeon, J. M., Heterogeneously catalyzed two-step cascade electrochemical reduction of CO₂ to ethanol. *Electrochimica Acta* **2018**, 274, 1-8.
158. Wu, J.; Sharifi, T.; Gao, Y.; Zhang, T.; Ajayan, P. M., Emerging Carbon-Based Heterogeneous Catalysts for Electrochemical Reduction of Carbon Dioxide into Value-Added Chemicals. **2019**, 31 (13), 1804257.
159. Verma, S.; Lu, S.; Kenis, P. J. A., Co-electrolysis of CO₂ and glycerol as a pathway to carbon chemicals with improved techno-economics due to low electricity consumption. *Nature Energy* **2019**, 4 (6), 466-474.

160. Hori, Y.; Wakebe, H.; Tsukamoto, T.; Koga, O., Electrocatalytic process of CO selectivity in electrochemical reduction of CO₂ at metal electrodes in aqueous media. *Electrochimica Acta* **1994**, *39* (11), 1833-1839.
161. Liu, T.; Ali, S.; Lian, Z.; Si, C.; Su, D. S.; Li, B., Phosphorus-doped onion-like carbon for CO₂ electrochemical reduction: the decisive role of the bonding configuration of phosphorus. *Journal of Materials Chemistry A* **2018**, *6* (41), 19998-20004.
162. Liu, S.; Yang, H.; Huang, X.; Liu, L.; Cai, W.; Gao, J.; Li, X.; Zhang, T.; Huang, Y.; Liu, B., Identifying Active Sites of Nitrogen-Doped Carbon Materials for the CO₂ Reduction Reaction. **2018**, *28* (21), 1800499.
163. Cui, X.; Pan, Z.; Zhang, L.; Peng, H.; Zheng, G., Selective Etching of Nitrogen-Doped Carbon by Steam for Enhanced Electrochemical CO₂ Reduction. **2017**, *7* (22), 1701456.
164. Xu, J.; Kan, Y.; Huang, R.; Zhang, B.; Wang, B.; Wu, K.-H.; Lin, Y.; Sun, X.; Li, Q.; Centi, G.; Su, D., Revealing the Origin of Activity in Nitrogen-Doped Nanocarbons towards Electrocatalytic Reduction of Carbon Dioxide. **2016**, *9* (10), 1085-1089.
165. Cui, H.; Guo, Y.; Guo, L.; Wang, L.; Zhou, Z.; Peng, Z., Heteroatom-doped carbon materials and their composites as electrocatalysts for CO₂ reduction. *Journal of Materials Chemistry A* **2018**, *6* (39), 18782-18793.
166. Chen, J.-F.; Mao, Y.; Wang, H.-F.; Hu, P., Theoretical Study of Heteroatom Doping in Tuning the Catalytic Activity of Graphene for Triiodide Reduction. *ACS Catalysis* **2016**, *6* (10), 6804-6813.
167. Denis, P. A., Band gap opening of monolayer and bilayer graphene doped with aluminium, silicon, phosphorus, and sulfur. *Chemical Physics Letters* **2010**, *492* (4), 251-257.
168. Liang, J.; Jiao, Y.; Jaroniec, M.; Qiao, S. Z., Sulfur and Nitrogen Dual-Doped Mesoporous Graphene Electrocatalyst for Oxygen Reduction with Synergistically Enhanced Performance. *Angewandte Chemie International Edition* **2012**, *51* (46), 11496-11500.
169. Yang, H.; Wu, Y.; Lin, Q.; Fan, L.; Chai, X.; Zhang, Q.; Liu, J.; He, C.; Lin, Z., Composition Tailoring via N and S Co-doping and Structure Tuning by Constructing Hierarchical Pores: Metal-Free Catalysts for High-Performance Electrochemical Reduction of CO₂. *Angewandte Chemie* **2018**, *130* (47), 15702-15706.
170. Han, H.; Park, S.; Jang, D.; Lee, S.; Kim, W. B., Electrochemical Reduction of CO₂ to CO by N,S Dual-Doped Carbon Nanoweb Catalysts. *ChemSusChem* **2019**, *n/a* (n/a).
171. Li, W.; Seredych, M.; Rodríguez-Castellón, E.; Bandoz, T. J., Metal-free Nanoporous Carbon as a Catalyst for Electrochemical Reduction of CO₂ to CO and CH₄. **2016**, *9* (6), 606-616.
172. Li, G.; Qin, Y.; Wu, Y.; Pei, L.; Hu, Q.; Yang, H.; Zhang, Q.; Liu, J.; He, C., Nitrogen and sulfur dual-doped high-surface-area hollow carbon nanospheres for efficient CO₂ reduction. *Chinese Journal of Catalysis* **2020**, *41* (5), 830-838.
173. McDonough, J. K.; Gogotsi, Y., Carbon Onions: Synthesis and Electrochemical Applications. **2013**, *22* (3), 61-66.
174. Haddon, R. C., Chemistry of the Fullerenes: The Manifestation of Strain in a Class of Continuous Aromatic Molecules. *Science* **1993**, *261* (5128), 1545-1550.

175. Martin, J. W.; Slavchov, R. I.; Yapp, E. K. Y.; Akroyd, J.; Mosbach, S.; Kraft, M., The Polarization of Polycyclic Aromatic Hydrocarbons Curved by Pentagon Incorporation: The Role of the Flexoelectric Dipole. *The Journal of Physical Chemistry C* **2017**, *121* (48), 27154-27163.
176. Pan, X.; Bao, X., The Effects of Confinement inside Carbon Nanotubes on Catalysis. *Accounts of Chemical Research* **2011**, *44* (8), 553-562.
177. Stewart, J. J., MOPAC: a semiempirical molecular orbital program. *Journal of computer-aided molecular design* **1990**, *4* (1), 1-103.
178. MOPAC, J., Stewart, Stewart Computational Chemistry, Colorado Springs, CO, USA, 2016. *There is no corresponding record for this reference.[Google Scholar]*.
179. Stewart, J. J., Optimization of parameters for semiempirical methods VI: more modifications to the NDDO approximations and re-optimization of parameters. *Journal of molecular modeling* **2013**, *19* (1), 1-32.
180. Nørskov, J. K.; Rossmeisl, J.; Logadottir, A.; Lindqvist, L.; Kitchin, J. R.; Bligaard, T.; Jonsson, H., Origin of the overpotential for oxygen reduction at a fuel-cell cathode. *The Journal of Physical Chemistry B* **2004**, *108* (46), 17886-17892.
181. Gupta, N.; Gattrell, M.; MacDougall, B., Calculation for the cathode surface concentrations in the electrochemical reduction of CO₂ in KHCO₃ solutions. *Journal of Applied Electrochemistry* **2006**, *36* (2), 161-172.
182. García de Arquer, F. P.; Dinh, C.-T.; Ozden, A.; Wicks, J.; McCallum, C.; Kirmani, A. R.; Nam, D.-H.; Gabardo, C.; Seifitokaldani, A.; Wang, X.; Li, Y. C.; Li, F.; Edwards, J.; Richter, L. J.; Thorpe, S. J.; Sinton, D.; Sargent, E. H., CO₂ electrolysis to multicarbon products at activities greater than 1 A cm⁻². *Science* **2020**, *367* (6478), 661-666.
183. Dinh, C.-T.; Burdyny, T.; Kibria, M. G.; Seifitokaldani, A.; Gabardo, C. M.; García de Arquer, F. P.; Kiani, A.; Edwards, J. P.; De Luna, P.; Bushuyev, O. S.; Zou, C.; Quintero-Bermudez, R.; Pang, Y.; Sinton, D.; Sargent, E. H., CO₂ electroreduction to ethylene via hydroxide-mediated copper catalysis at an abrupt interface. **2018**, *360* (6390), 783-787.
184. Zeiger, M.; Jäckel, N.; Aslan, M.; Weingarh, D.; Presser, V., Understanding structure and porosity of nanodiamond-derived carbon onions. *Carbon* **2015**, *84*, 584-598.
185. Zeiger, M.; Jäckel, N.; Mochalin, V. N.; Presser, V., Review: carbon onions for electrochemical energy storage. *Journal of Materials Chemistry A* **2016**, *4* (9), 3172-3196.
186. Zheng, B.; Cai, X.-L.; Zhou, Y.; Xia, X.-H., Pure Pyridinic Nitrogen-Doped Single-Layer Graphene Catalyzes Two-Electron Transfer Process of Oxygen Reduction Reaction. **2016**, *3* (12), 2036-2042.
187. Kanai, Y.; Khalap, V. R.; Collins, P. G.; Grossman, J. C., Atomistic Oxidation Mechanism of a Carbon Nanotube in Nitric Acid. *Physical Review Letters* **2010**, *104* (6), 066401.
188. Li, X.; Wang, H.; Robinson, J. T.; Sanchez, H.; Diankov, G.; Dai, H., Simultaneous Nitrogen Doping and Reduction of Graphene Oxide. *Journal of the American Chemical Society* **2009**, *131* (43), 15939-15944.
189. Yim, S. D.; Kim, S. J.; Baik, J. H.; Nam, I. S.; Mok, Y. S.; Lee, J.-H.; Cho, B. K.; Oh, S. H., Decomposition of Urea into NH₃ for the SCR Process. *Industrial & Engineering Chemistry Research* **2004**, *43* (16), 4856-4863.

190. Mou, Z.; Chen, X.; Du, Y.; Wang, X.; Yang, P.; Wang, S., Forming mechanism of nitrogen doped graphene prepared by thermal solid-state reaction of graphite oxide and urea. *Applied Surface Science* **2011**, 258 (5), 1704-1710.
191. Wang, Z. D.; Yoshida, M.; George, B., Theoretical study on the thermal decomposition of thiourea. *Computational and Theoretical Chemistry* **2013**, 1017, 91-98.
192. Krishna, R.; Jones, A. N.; McDermott, L.; Marsden, B. J., Neutron irradiation damage of nuclear graphite studied by high-resolution transmission electron microscopy and Raman spectroscopy. *Journal of Nuclear Materials* **2015**, 467, 557-565.
193. Ferrari, A. C.; Basko, D. M., Raman spectroscopy as a versatile tool for studying the properties of graphene. *Nature Nanotechnology* **2013**, 8, 235.
194. Kolagatla, S.; Subramanian, P.; Schechter, A., Nanoscale mapping of catalytic hotspots on Fe, N-modified HOPG by scanning electrochemical microscopy-atomic force microscopy. *Nanoscale* **2018**, 10 (15), 6962-6970.
195. Roy, D.; Chhowalla, M.; Wang, H.; Sano, N.; Alexandrou, I.; Clyne, T. W.; Amaratunga, G. A. J., Characterisation of carbon nano-onions using Raman spectroscopy. *Chemical Physics Letters* **2003**, 373 (1), 52-56.
196. Cançado, L. G.; Jorio, A.; Ferreira, E. H. M.; Stavale, F.; Achete, C. A.; Capaz, R. B.; Moutinho, M. V. O.; Lombardo, A.; Kulmala, T. S.; Ferrari, A. C., Quantifying Defects in Graphene via Raman Spectroscopy at Different Excitation Energies. *Nano Letters* **2011**, 11 (8), 3190-3196.
197. Tomita, S.; Burian, A.; Dore, J. C.; LeBolloch, D.; Fujii, M.; Hayashi, S., Diamond nanoparticles to carbon onions transformation: X-ray diffraction studies. *Carbon* **2002**, 40 (9), 1469-1474.
198. ALOthman, Z. A., A Review: Fundamental Aspects of Silicate Mesoporous Materials. *Materials* **2012**, 5 (12), 2874-2902.
199. Thommes, M., Physical Adsorption Characterization of Nanoporous Materials. **2010**, 82 (7), 1059-1073.
200. Lee, M.; Seo, Y.; Shin, H. S.; Jo, C.; Ryoo, R., Anatase TiO₂ nanosheets with surface acid sites for Friedel–Crafts alkylation. *Microporous and Mesoporous Materials* **2016**, 222, 185-191.
201. Mykhailiv, O.; Zubyk, H.; Plonska-Brzezinska, M. E., Carbon nano-onions: Unique carbon nanostructures with fascinating properties and their potential applications. *Inorganica Chimica Acta* **2017**, 468, 49-66.
202. Zhao, L.; He, R.; Rim, K. T.; Schiros, T.; Kim, K. S.; Zhou, H.; Gutiérrez, C.; Chockalingam, S. P.; Arguello, C. J.; Pálová, L.; Nordlund, D.; Hybertsen, M. S.; Reichman, D. R.; Heinz, T. F.; Kim, P.; Pinczuk, A.; Flynn, G. W.; Pasupathy, A. N., Visualizing Individual Nitrogen Dopants in Monolayer Graphene. **2011**, 333 (6045), 999-1003.
203. Hashim, D. P.; Narayanan, N. T.; Romo-Herrera, J. M.; Cullen, D. A.; Hahm, M. G.; Lezzi, P.; Suttle, J. R.; Kelkhoff, D.; Muñoz-Sandoval, E.; Ganguli, S.; Roy, A. K.; Smith, D. J.; Vajtai, R.; Sumpter, B. G.; Meunier, V.; Terrones, H.; Terrones, M.; Ajayan, P. M., Covalently bonded three-dimensional carbon nanotube solids via boron induced nanojunctions. *Scientific Reports* **2012**, 2, 363.
204. Romo-Herrera, J. M.; Sumpter, B. G.; Cullen, D. A.; Terrones, H.; Cruz-Silva, E.; Smith, D. J.; Meunier, V.; Terrones, M., An Atomistic Branching Mechanism for Carbon Nanotubes: Sulfur as the Triggering Agent. **2008**, 47 (16), 2948-2953.

205. Quan, B.; Yu, S.-H.; Chung, D. Y.; Jin, A.; Park, J. H.; Sung, Y.-E.; Piao, Y., Single Source Precursor-based Solvothermal Synthesis of Heteroatom-doped Graphene and Its Energy Storage and Conversion Applications. *Scientific Reports* **2014**, *4*, 5639.
206. Zhang, X.; Gao, X.; Wu, Z.; Zhu, M.; Jiang, Q.; Zhou, S.; Huang, Y.; Rao, Z. J. I., High-capacitance supercapacitor based on nitrogen-doped porous carbons-sandwiched graphene hybrid frameworks. **2019**.
207. Xu, X.; Sun, Z.; Chua, D. H. C.; Pan, L., Novel nitrogen doped graphene sponge with ultrahigh capacitive deionization performance. *Scientific Reports* **2015**, *5*, 11225.
208. Wang, T.; Wang, L.-X.; Wu, D.-L.; Xia, W.; Jia, D.-Z., Interaction between Nitrogen and Sulfur in Co-Doped Graphene and Synergetic Effect in Supercapacitor. *Scientific Reports* **2015**, *5*, 9591.
209. Kuiken, H. K.; Bakkers, E. P. A. M.; Ligthart, H.; Kelly, J. J., The Rotating Ring-Ring Electrode. Theory and Experiment. **2000**, *147* (3), 1110-1116.
210. Zhu, X.; Gupta, K.; Bersani, M.; Darr, J. A.; Shearing, P. R.; Brett, D. J. L., Electrochemical reduction of carbon dioxide on copper-based nanocatalysts using the rotating ring-disc electrode. *Electrochimica Acta* **2018**, *283*, 1037-1044.
211. Grgur, B. N.; Markovic, N. M.; Ross, P. N., Electrooxidation of H₂, CO, and H₂/CO Mixtures on a Well-Characterized Pt₇₀Mo₃₀ Bulk Alloy Electrode. *The Journal of Physical Chemistry B* **1998**, *102* (14), 2494-2501.
212. Wendt, H.; Spinacé, E. V.; Oliveira Neto, A.; Linardi, M., Electrocatalysis and electrocatalysts for low temperature fuel cells: fundamentals, state of the art, research and development %J Química Nova. **2005**, *28*, 1066-1075.
213. McPherson, I. J.; Ash, P. A.; Jones, L.; Varambhia, A.; Jacobs, R. M. J.; Vincent, K. A., Electrochemical CO Oxidation at Platinum on Carbon Studied through Analysis of Anomalous in Situ IR Spectra. *The Journal of Physical Chemistry C* **2017**, *121* (32), 17176-17187.
214. Cuesta, A.; Couto, A.; Rincón, A.; Pérez, M. C.; López-Cudero, A.; Gutiérrez, C., Potential dependence of the saturation CO coverage of Pt electrodes: The origin of the pre-peak in CO-stripping voltammograms. Part 3: Pt(poly). *Journal of Electroanalytical Chemistry* **2006**, *586* (2), 184-195.
215. Guerin, S.; Hayden, B. E.; Lee, C. E.; Mormiche, C.; Owen, J. R.; Russell, A. E.; Theobald, B.; Thompsett, D., Combinatorial Electrochemical Screening of Fuel Cell Electrocatalysts. *Journal of Combinatorial Chemistry* **2004**, *6* (1), 149-158.
216. Kalhara Gunasooriya, G. T. K.; Saeys, M., CO Adsorption Site Preference on Platinum: Charge Is the Essence. *ACS Catalysis* **2018**, *8* (5), 3770-3774.
217. Li, W.; Bandosz, T. J., Role of Heteroatoms in S,N-Codoped Nanoporous Carbon Materials in CO₂ (Photo)electrochemical Reduction. **2018**, *11* (17), 2987-2999.
218. Lee, J. H.; Kwon, S. H.; Kwon, S.; Cho, M.; Kim, K. H.; Han, T. H.; Lee, S. G., Tunable Electronic Properties of Nitrogen and Sulfur Doped Graphene: Density Functional Theory Approach. **2019**, *9* (2), 268.
219. Gao, D.; Zhou, H.; Cai, F.; Wang, D.; Hu, Y.; Jiang, B.; Cai, W.-B.; Chen, X.; Si, R.; Yang, F.; Miao, S.; Wang, J.; Wang, G.; Bao, X. J. N. R., Switchable CO₂ electroreduction via engineering active phases of Pd nanoparticles. **2017**, *10* (6), 2181-2191.

220. Zhang, Y.; Cai, Z.; Zhao, Y.; Wen, X.; Xu, W.; Zhong, Y.; Bai, L.; Liu, W.; Zhang, Y.; Zhang, Y.; Kuang, Y.; Sun, X., Superaerophilic copper nanowires for efficient and switchable CO₂ electroreduction. *Nanoscale Horizons* **2019**, *4* (2), 490-494.
221. Feaster, J. T.; Shi, C.; Cave, E. R.; Hatsukade, T.; Abram, D. N.; Kuhl, K. P.; Hahn, C.; Nørskov, J. K.; Jaramillo, T. F., Understanding selectivity for the electrochemical reduction of carbon dioxide to formic acid and carbon monoxide on metal electrodes. *Acs Catalysis* **2017**, *7* (7), 4822-4827.
222. Kortlever, R.; Shen, J.; Schouten, K. J. P.; Calle-Vallejo, F.; Koper, M. T., Catalysts and reaction pathways for the electrochemical reduction of carbon dioxide. *The journal of physical chemistry letters* **2015**, *6* (20), 4073-4082.
223. Kortlever, R.; Shen, J.; Schouten, K. J. P.; Calle-Vallejo, F.; Koper, M. T. M., Catalysts and Reaction Pathways for the Electrochemical Reduction of Carbon Dioxide. *The Journal of Physical Chemistry Letters* **2015**, *6* (20), 4073-4082.
224. Chernyshova, I. V.; Somasundaran, P.; Ponnurangam, S., On the origin of the elusive first intermediate of CO₂ electroreduction. *Proceedings of the National Academy of Sciences* **2018**, *115* (40), E9261-E9270.
225. Ma, S.; Luo, R.; Moniri, S.; Lan, Y.; Kenis, P. J. A., Efficient Electrochemical Flow System with Improved Anode for the Conversion of CO₂ to CO. **2014**, *161* (10), F1124-F1131.
226. Dinh, C.-T.; García de Arquer, F. P.; Sinton, D.; Sargent, E. H., High Rate, Selective, and Stable Electroreduction of CO₂ to CO in Basic and Neutral Media. *ACS Energy Letters* **2018**, *3* (11), 2835-2840.
227. Fernandes, D. M.; Peixoto, A. F.; Freire, C., Nitrogen-doped metal-free carbon catalysts for (electro)chemical CO₂ conversion and valorisation. *Dalton Transactions* **2019**, *48* (36), 13508-13528.
228. Gabardo, C. M.; Seifitokaldani, A.; Edwards, J. P.; Dinh, C.-T.; Burdyny, T.; Kibria, M. G.; O'Brien, C. P.; Sargent, E. H.; Sinton, D., Combined high alkalinity and pressurization enable efficient CO₂ electroreduction to CO. *Energy & Environmental Science* **2018**, *11* (9), 2531-2539.
229. Wang, G.; Liu, M.; Jia, J.; Xu, H.; Zhao, B.; Lai, K.; Tu, C.; Wen, Z., Nitrogen and Sulfur Co-doped Carbon Nanosheets for Electrochemical Reduction of CO₂. *ChemCatChem* **2020**, *12* (8), 2203-2208.
230. Liu, S.; Yang, H.; Huang, X.; Liu, L.; Cai, W.; Gao, J.; Li, X.; Zhang, T.; Huang, Y.; Liu, B., Identifying Active Sites of Nitrogen-Doped Carbon Materials for the CO₂ Reduction Reaction. *Advanced Functional Materials* **2018**, *28* (21), 1800499.
231. Li, H.; Xiao, N.; Wang, Y.; Li, C.; Ye, X.; Guo, Z.; Pan, X.; Liu, C.; Bai, J.; Xiao, J.; Zhang, X.; Zhao, S.; Qiu, J., Nitrogen-doped tubular carbon foam electrodes for efficient electroreduction of CO₂ to syngas with potential-independent CO/H₂ ratios. *Journal of Materials Chemistry A* **2019**, *7* (32), 18852-18860.
232. Li, C.; Wang, Y.; Xiao, N.; Li, H.; Ji, Y.; Guo, Z.; Liu, C.; Qiu, J., Nitrogen-doped porous carbon from coal for high efficiency CO₂ electrocatalytic reduction. *Carbon* **2019**, *151*, 46-52.
233. Pan, F.; Li, B.; Xiang, X.; Wang, G.; Li, Y., Efficient CO₂ Electroreduction by Highly Dense and Active Pyridinic Nitrogen on Holey Carbon Layers with Fluorine Engineering. *ACS Catalysis* **2019**, *9* (3), 2124-2133.

234. Xie, J.; Zhao, X.; Wu, M.; Li, Q.; Wang, Y.; Yao, J., Metal-Free Fluorine-Doped Carbon Electrocatalyst for CO₂ Reduction Outcompeting Hydrogen Evolution. *Angewandte Chemie International Edition* **2018**, *57* (31), 9640-9644.
235. Li, W.; Herkt, B.; Seredych, M.; Bando, T. J., Pyridinic-N groups and ultramicropore nanoreactors enhance CO₂ electrochemical reduction on porous carbon catalysts. *Applied Catalysis B: Environmental* **2017**, *207*, 195-206.
236. Lu, X.; Tan, T. H.; Ng, Y. H.; Amal, R., Highly Selective and Stable Reduction of CO₂ to CO by a Graphitic Carbon Nitride/Carbon Nanotube Composite Electrocatalyst. *Chemistry – A European Journal* **2016**, *22* (34), 11991-11996.
237. Li, F.; Xue, M.; Knowles, G. P.; Chen, L.; MacFarlane, D. R.; Zhang, J., Porous nitrogen-doped carbon derived from biomass for electrocatalytic reduction of CO₂ to CO. *Electrochimica Acta* **2017**, *245*, 561-568.
238. Jhong, H.-R. M.; Tornow, C. E.; Smid, B.; Gewirth, A. A.; Lyth, S. M.; Kenis, P. J. A., A Nitrogen-Doped Carbon Catalyst for Electrochemical CO₂ Conversion to CO with High Selectivity and Current Density. **2017**, *10* (6), 1094-1099.
239. Wang, R.; Sun, X.; Ould-Chikh, S.; Osadchii, D.; Bai, F.; Kapteijn, F.; Gascon, J., Metal-Organic-Framework-Mediated Nitrogen-Doped Carbon for CO₂ Electrochemical Reduction. *ACS Applied Materials & Interfaces* **2018**, *10* (17), 14751-14758.
240. Kumar, B.; Asadi, M.; Pisasale, D.; Sinha-Ray, S.; Rosen, B. A.; Haasch, R.; Abiade, J.; Yarin, A. L.; Salehi-Khojin, A., Renewable and metal-free carbon nanofibre catalysts for carbon dioxide reduction. *Nature Communications* **2013**, *4* (1), 2819.
241. Liu, H.; Liu, Y.; Zhu, D., Chemical doping of graphene. *Journal of Materials Chemistry* **2011**, *21* (10), 3335-3345.
242. Zafar, Z.; Ni, Z. H.; Wu, X.; Shi, Z. X.; Nan, H. Y.; Bai, J.; Sun, L. T., Evolution of Raman spectra in nitrogen doped graphene. *Carbon* **2013**, *61*, 57-62.
243. Sundramoorthy, A. K.; Gunasekaran, S., Partially Oxidized Graphene/Metallic Single-Walled Carbon Nanotubes Film-Coated Electrode for Nanomolar Detection of Dopamine. *Electroanalysis* **2015**, *27* (8), 1811-1816.
244. Das, A.; Pisana, S.; Chakraborty, B.; Piscanec, S.; Saha, S. K.; Waghmare, U. V.; Novoselov, K. S.; Krishnamurthy, H. R.; Geim, A. K.; Ferrari, A. C.; Sood, A. K., Monitoring dopants by Raman scattering in an electrochemically top-gated graphene transistor. *Nature Nanotechnology* **2008**, *3* (4), 210-215.
245. Singh, A. K.; Yasri, N.; Karan, K.; Roberts, E. P. L., Electrocatalytic Activity of Functionalized Carbon Paper Electrodes and Their Correlation to the Fermi Level Derived from Raman Spectra. *ACS Applied Energy Materials* **2019**, *2* (3), 2324-2336.
246. Li, Y., *Probing the response of two-dimensional crystals by optical spectroscopy*. Springer: 2015.
247. Morant, C.; Torres, R.; Jimenez, I.; Sanz, J. M.; Elizalde, E., Characterization of Nitrogen-Doped Carbon Nanotubes by Atomic Force Microscopy, X-ray Photoelectron Spectroscopy and X-ray Absorption Near Edge Spectroscopy. *Journal of Nanoscience and Nanotechnology* **2009**, *9* (6), 3633-3638.
248. Latham, K. G.; Simone, M. I.; Dose, W. M.; Allen, J. A.; Donne, S. W., Synchrotron based NEXAFS study on nitrogen doped hydrothermal carbon: Insights into surface functionalities and formation mechanisms. *Carbon* **2017**, *114*, 566-578.

249. Schultz, B. J.; Dennis, R. V.; Aldinger, J. P.; Jaye, C.; Wang, X.; Fischer, D. A.; Cartwright, A. N.; Banerjee, S., X-ray absorption spectroscopy studies of electronic structure recovery and nitrogen local structure upon thermal reduction of graphene oxide in an ammonia environment. *RSC Advances* **2014**, *4* (2), 634-644.
250. Jain, D.; Zhang, Q.; Hightower, J.; Gustin, V.; Asthagiri, A.; Ozkan, U. S., Changes in Active Sites on Nitrogen-Doped Carbon Catalysts Under Oxygen Reduction Reaction: A Combined Post-Reaction Characterization and DFT Study. *ChemCatChem* **2019**, *11* (24), 5945-5950.
251. Tang, L.; Wang, S.; Zhu, X.; Guan, Y.; Chen, S.; Tao, X.; He, H., Feasibility study of reduction removal of thiophene sulfur in coal. *Fuel* **2018**, *234*, 1367-1372.
252. Liu, X.-P.; Deng, K.; Wei, Q.; Liang, M.-h.; Zhang, Z.-J.; Jiang, P., Self-assembly of trithia-9-crown-3 and octathia-24-crown-8 on Au(111) surfaces. *RSC Advances* **2016**, *6* (85), 81726-81730.
253. Rosen, B. A.; Salehi-Khojin, A.; Thorson, M. R.; Zhu, W.; Whipple, D. T.; Kenis, P. J. A.; Masel, R. I., Ionic Liquid-Mediated Selective Conversion of CO₂ to CO at Low Overpotentials. *Science* **2011**, *334* (6056), 643-644.
254. Yang, F.; Song, P.; Liu, X.; Mei, B.; Xing, W.; Jiang, Z.; Gu, L.; Xu, W., Highly Efficient CO₂ Electroreduction on ZnN₄-based Single-Atom Catalyst. *Angewandte Chemie International Edition* **2018**, *57* (38), 12303-12307.
255. Verma, S.; Hamasaki, Y.; Kim, C.; Huang, W.; Lu, S.; Jhong, H.-R. M.; Gewirth, A. A.; Fujigaya, T.; Nakashima, N.; Kenis, P. J. A., Insights into the Low Overpotential Electroreduction of CO₂ to CO on a Supported Gold Catalyst in an Alkaline Flow Electrolyzer. *ACS Energy Letters* **2018**, *3* (1), 193-198.
256. Gu, J.; Hsu, C.-S.; Bai, L.; Chen, H. M.; Hu, X., Atomically dispersed Fe³⁺ sites catalyze efficient CO₂ electroreduction to CO. *Science* **2019**, *364* (6445), 1091-1094.
257. Zhang, Z.; Ma, C.; Tu, Y.; Si, R.; Wei, J.; Zhang, S.; Wang, Z.; Li, J.-F.; Wang, Y.; Deng, D., Multiscale carbon foam confining single iron atoms for efficient electrocatalytic CO₂ reduction to CO. *Nano Research* **2019**, *12* (9), 2313-2317.
258. Qin, X.; Zhu, S.; Xiao, F.; Zhang, L.; Shao, M., Active Sites on Heterogeneous Single-Iron-Atom Electrocatalysts in CO₂ Reduction Reaction. *ACS Energy Letters* **2019**, *4* (7), 1778-1783.
259. Chen, Z.; Mou, K.; Yao, S.; Liu, L., Zinc-Coordinated Nitrogen-Codoped Graphene as an Efficient Catalyst for Selective Electrochemical Reduction of CO₂ to CO. *ChemSusChem* **2018**, *11* (17), 2944-2952.
260. Cheng, Q.; Mao, K.; Ma, L.; Yang, L.; Zou, L.; Zou, Z.; Hu, Z.; Yang, H., Encapsulation of Iron Nitride by Fe-N-C Shell Enabling Highly Efficient Electroreduction of CO₂ to CO. *ACS Energy Letters* **2018**, *3* (5), 1205-1211.
261. Huan, T. N.; Ranjbar, N.; Rousse, G.; Sougrati, M.; Zitolo, A.; Mougél, V.; Jaouen, F.; Fontecave, M., Electrochemical Reduction of CO₂ Catalyzed by Fe-N-C Materials: A Structure-Selectivity Study. *ACS Catalysis* **2017**, *7* (3), 1520-1525.
262. Zhang, B.; Zhang, J.; Shi, J.; Tan, D.; Liu, L.; Zhang, F.; Lu, C.; Su, Z.; Tan, X.; Cheng, X.; Han, B.; Zheng, L.; Zhang, J., Manganese acting as a high-performance heterogeneous electrocatalyst in carbon dioxide reduction. *Nature Communications* **2019**, *10* (1), 2980.
263. Zhang, C.; Yang, S.; Wu, J.; Liu, M.; Yazdi, S.; Ren, M.; Sha, J.; Zhong, J.; Nie, K.; Jalilov, A. S.; Li, Z.; Li, H.; Yakobson, B. I.; Wu, Q.; Ringe, E.; Xu, H.;

- Ajayan, P. M.; Tour, J. M., Electrochemical CO₂ Reduction with Atomic Iron-Dispersed on Nitrogen-Doped Graphene. *Advanced Energy Materials* **2018**, *8* (19), 1703487.
264. Hossain, M. N.; Wen, J.; Chen, A., Unique copper and reduced graphene oxide nanocomposite toward the efficient electrochemical reduction of carbon dioxide. *Scientific Reports* **2017**, *7* (1), 3184.
265. Wang, X.; Chen, Z.; Zhao, X.; Yao, T.; Chen, W.; You, R.; Zhao, C.; Wu, G.; Wang, J.; Huang, W.; Yang, J.; Hong, X.; Wei, S.; Wu, Y.; Li, Y., Regulation of Coordination Number over Single Co Sites: Triggering the Efficient Electroreduction of CO₂. *Angewandte Chemie International Edition* **2018**, *57* (7), 1944-1948.
266. Li, F.; Zhao, S.-F.; Chen, L.; Khan, A.; MacFarlane, D. R.; Zhang, J., Polyethylenimine promoted electrocatalytic reduction of CO₂ to CO in aqueous medium by graphene-supported amorphous molybdenum sulphide. *Energy & Environmental Science* **2016**, *9* (1), 216-223.
267. Jiang, K.; Siahrostami, S.; Zheng, T.; Hu, Y.; Hwang, S.; Stavitski, E.; Peng, Y.; Dynes, J.; Gangisetty, M.; Su, D.; Attenkofer, K.; Wang, H., Isolated Ni single atoms in graphene nanosheets for high-performance CO₂ reduction. *Energy & Environmental Science* **2018**, *11* (4), 893-903.
268. Zheng, T.; Jiang, K.; Ta, N.; Hu, Y.; Zeng, J.; Liu, J.; Wang, H., Large-Scale and Highly Selective CO₂ Electrocatalytic Reduction on Nickel Single-Atom Catalyst. *Joule* **2019**, *3* (1), 265-278.
269. Schreier, M.; Héroguel, F.; Steier, L.; Ahmad, S.; Luterbacher, J. S.; Mayer, M. T.; Luo, J.; Grätzel, M., Solar conversion of CO₂ to CO using Earth-abundant electrocatalysts prepared by atomic layer modification of CuO. *Nature Energy* **2017**, *2* (7), 17087.
270. Li, Q.; Fu, J.; Zhu, W.; Chen, Z.; Shen, B.; Wu, L.; Xi, Z.; Wang, T.; Lu, G.; Zhu, J.-j.; Sun, S., Tuning Sn-Catalysis for Electrochemical Reduction of CO₂ to CO via the Core/Shell Cu/SnO₂ Structure. *Journal of the American Chemical Society* **2017**, *139* (12), 4290-4293.
271. Su, P.; Iwase, K.; Nakanishi, S.; Hashimoto, K.; Kamiya, K., Nickel-Nitrogen-Modified Graphene: An Efficient Electrocatalyst for the Reduction of Carbon Dioxide to Carbon Monoxide. *Small* **2016**, *12* (44), 6083-6089.
272. Cheng, Y.; Zhao, S.; Johannessen, B.; Veder, J.-P.; Saunders, M.; Rowles, M. R.; Cheng, M.; Liu, C.; Chisholm, M. F.; De Marco, R.; Cheng, H.-M.; Yang, S.-Z.; Jiang, S. P., Atomically Dispersed Transition Metals on Carbon Nanotubes with Ultrahigh Loading for Selective Electrochemical Carbon Dioxide Reduction. *Advanced Materials* **2018**, *30* (13), 1706287.
273. Pan, F.; Liang, A.; Duan, Y.; Liu, Q.; Zhang, J.; Li, Y., Self-growth-templating synthesis of 3D N,P,Co-doped mesoporous carbon frameworks for efficient bifunctional oxygen and carbon dioxide electroreduction. *Journal of Materials Chemistry A* **2017**, *5* (25), 13104-13111.
274. Jia, M.; Choi, C.; Wu, T.-S.; Ma, C.; Kang, P.; Tao, H.; Fan, Q.; Hong, S.; Liu, S.; Soo, Y.-L.; Jung, Y.; Qiu, J.; Sun, Z., Carbon-supported Ni nanoparticles for efficient CO₂ electroreduction. *Chemical Science* **2018**, *9* (47), 8775-8780.
275. Ma, S.; Luo, R.; Gold, J. I.; Yu, A. Z.; Kim, B.; Kenis, P. J. A., Carbon nanotube containing Ag catalyst layers for efficient and selective reduction of carbon dioxide. *Journal of Materials Chemistry A* **2016**, *4* (22), 8573-8578.

276. Pan, F.; Deng, W.; Justiniano, C.; Li, Y., Identification of champion transition metals centers in metal and nitrogen-codoped carbon catalysts for CO₂ reduction. *Applied Catalysis B: Environmental* **2018**, *226*, 463-472.
277. Ma, S.; Lan, Y.; Perez, G. M. J.; Moniri, S.; Kenis, P. J. A., Silver Supported on Titania as an Active Catalyst for Electrochemical Carbon Dioxide Reduction. *ChemSusChem* **2014**, *7* (3), 866-874.
278. Asadi, M.; Kumar, B.; Behranginia, A.; Rosen, B. A.; Baskin, A.; Reppin, N.; Pisasale, D.; Phillips, P.; Zhu, W.; Haasch, R.; Klie, R. F.; Král, P.; Abiade, J.; Salehi-Khojin, A., Robust carbon dioxide reduction on molybdenum disulphide edges. *Nature Communications* **2014**, *5* (1), 4470.
279. Yang, H. B.; Hung, S.-F.; Liu, S.; Yuan, K.; Miao, S.; Zhang, L.; Huang, X.; Wang, H.-Y.; Cai, W.; Chen, R.; Gao, J.; Yang, X.; Chen, W.; Huang, Y.; Chen, H. M.; Li, C. M.; Zhang, T.; Liu, B., Atomically dispersed Ni(i) as the active site for electrochemical CO₂ reduction. *Nature Energy* **2018**, *3* (2), 140-147.
280. Pan, Y.; Lin, R.; Chen, Y.; Liu, S.; Zhu, W.; Cao, X.; Chen, W.; Wu, K.; Cheong, W.-C.; Wang, Y.; Zheng, L.; Luo, J.; Lin, Y.; Liu, Y.; Liu, C.; Li, J.; Lu, Q.; Chen, X.; Wang, D.; Peng, Q.; Chen, C.; Li, Y., Design of Single-Atom Co–N₅ Catalytic Site: A Robust Electrocatalyst for CO₂ Reduction with Nearly 100% CO Selectivity and Remarkable Stability. *Journal of the American Chemical Society* **2018**, *140* (12), 4218-4221.
281. Verma, S.; Lu, X.; Ma, S.; Masel, R. I.; Kenis, P. J. A., The effect of electrolyte composition on the electroreduction of CO₂ to CO on Ag based gas diffusion electrodes. *Physical Chemistry Chemical Physics* **2016**, *18* (10), 7075-7084.
282. Charles, D.; Paul, L. R.; John, B. K.; John, S. N., Design of an Electrochemical Cell Making Syngas (CO + H₂) from CO and H₂O Reduction at Room Temperature. *Journal of Electrochemical Society* **2007**, *155*, B42-B49.
283. Li, X.; Bi, W.; Chen, M.; Sun, Y.; Ju, H.; Yan, W.; Zhu, J.; Wu, X.; Chu, W.; Wu, C.; Xie, Y., Exclusive Ni–N₄ Sites Realize Near-Unity CO Selectivity for Electrochemical CO₂ Reduction. *Journal of the American Chemical Society* **2017**, *139* (42), 14889-14892.
284. Won, D. H.; Shin, H.; Koh, J.; Chung, J.; Lee, H. S.; Kim, H.; Woo, S. I., Highly Efficient, Selective, and Stable CO₂ Electroreduction on a Hexagonal Zn Catalyst. *Angewandte Chemie International Edition* **2016**, *55* (32), 9297-9300.
285. Yuan, C.-Z.; Li, H.-B.; Jiang, Y.-F.; Liang, K.; Zhao, S.-J.; Fang, X.-X.; Ma, L.-B.; Zhao, T.; Lin, C.; Xu, A.-W., Tuning the activity of N-doped carbon for CO₂ reduction via in situ encapsulation of nickel nanoparticles into nano-hybrid carbon substrates. *Journal of Materials Chemistry A* **2019**, *7* (12), 6894-6900.
286. Zheng, W.; Guo, C.; Yang, J.; He, F.; Yang, B.; Li, Z.; Lei, L.; Xiao, J.; Wu, G.; Hou, Y., Highly active metallic nickel sites confined in N-doped carbon nanotubes toward significantly enhanced activity of CO₂ electroreduction. *Carbon* **2019**, *150*, 52-59.
287. Möller, T.; Ju, W.; Bagger, A.; Wang, X.; Luo, F.; Ngo Thanh, T.; Varela, A. S.; Rossmeisl, J.; Strasser, P., Efficient CO₂ to CO electrolysis on solid Ni–N–C catalysts at industrial current densities. *Energy & Environmental Science* **2019**, *12* (2), 640-647.
288. Yan, C.; Li, H.; Ye, Y.; Wu, H.; Cai, F.; Si, R.; Xiao, J.; Miao, S.; Xie, S.; Yang, F.; Li, Y.; Wang, G.; Bao, X., Coordinatively unsaturated nickel–nitrogen sites

- towards selective and high-rate CO₂ electroreduction. *Energy & Environmental Science* **2018**, *11* (5), 1204-1210.
289. Salvatore, D. A.; Weekes, D. M.; He, J.; Dettelbach, K. E.; Li, Y. C.; Mallouk, T. E.; Berlinguette, C. P., Electrolysis of Gaseous CO₂ to CO in a Flow Cell with a Bipolar Membrane. *ACS Energy Letters* **2018**, *3* (1), 149-154.
290. Hori, Y.; Ito, H.; Okano, K.; Nagasu, K.; Sato, S., Silver-coated ion exchange membrane electrode applied to electrochemical reduction of carbon dioxide. *Electrochimica Acta* **2003**, *48* (18), 2651-2657.
291. Li, F.; Li, Y. C.; Wang, Z.; Li, J.; Nam, D.-H.; Lum, Y.; Luo, M.; Wang, X.; Ozden, A.; Hung, S.-F.; Chen, B.; Wang, Y.; Wicks, J.; Xu, Y.; Li, Y.; Gabardo, C. M.; Dinh, C.-T.; Wang, Y.; Zhuang, T.-T.; Sinton, D.; Sargent, E. H., Cooperative CO₂-to-ethanol conversion via enriched intermediates at molecule–metal catalyst interfaces. *Nature Catalysis* **2020**, *3* (1), 75-82.
292. Hoang, T. T. H.; Verma, S.; Ma, S.; Fister, T. T.; Timoshenko, J.; Frenkel, A. I.; Kenis, P. J. A.; Gewirth, A. A., Nanoporous Copper–Silver Alloys by Additive-Controlled Electrodeposition for the Selective Electroreduction of CO₂ to Ethylene and Ethanol. *Journal of the American Chemical Society* **2018**, *140* (17), 5791-5797.
293. Li, C. W.; Ciston, J.; Kanan, M. W., Electroreduction of carbon monoxide to liquid fuel on oxide-derived nanocrystalline copper. *Nature* **2014**, *508* (7497), 504-507.
294. Zhuang, T.-T.; Liang, Z.-Q.; Seifitokaldani, A.; Li, Y.; De Luna, P.; Burdyny, T.; Che, F.; Meng, F.; Min, Y.; Quintero-Bermudez, R.; Dinh, C. T.; Pang, Y.; Zhong, M.; Zhang, B.; Li, J.; Chen, P.-N.; Zheng, X.-L.; Liang, H.; Ge, W.-N.; Ye, B.-J.; Sinton, D.; Yu, S.-H.; Sargent, E. H., Steering post-C–C coupling selectivity enables high efficiency electroreduction of carbon dioxide to multi-carbon alcohols. *Nature Catalysis* **2018**, *1* (6), 421-428.
295. Fan, L.; Xia, C.; Yang, F.; Wang, J.; Wang, H.; Lu, Y., Strategies in catalysts and electrolyzer design for electrochemical CO₂ reduction toward C₂₊ products. *Science Advances* **2020**, *6* (8), eaay3111.
296. Higgins, D.; Hahn, C.; Xiang, C.; Jaramillo, T. F.; Weber, A. Z., Gas-Diffusion Electrodes for Carbon Dioxide Reduction: A New Paradigm. *ACS Energy Letters* **2019**, *4* (1), 317-324.
297. Pan, F.; Zhang, H.; Liu, K.; Cullen, D.; More, K.; Wang, M.; Feng, Z.; Wang, G.; Wu, G.; Li, Y., Unveiling Active Sites of CO₂ Reduction on Nitrogen-Coordinated and Atomically Dispersed Iron and Cobalt Catalysts. *ACS Catalysis* **2018**, *8* (4), 3116-3122.
298. Yuan, J.; Yang, M.-P.; Zhi, W.-Y.; Wang, H.; Wang, H.; Lu, J.-X., Efficient electrochemical reduction of CO₂ to ethanol on Cu nanoparticles decorated on N-doped graphene oxide catalysts. *Journal of CO₂ Utilization* **2019**, *33*, 452-460.
299. Jhong, H.-R. M.; Ma, S.; Kenis, P. J. A., Electrochemical conversion of CO₂ to useful chemicals: current status, remaining challenges, and future opportunities. *Current Opinion in Chemical Engineering* **2013**, *2* (2), 191-199.
300. da Silva, J. S.; Carvalho, S. G. M.; da Silva, R. P.; Tavares, A. C.; Schade, U.; Puskar, L.; Fonseca, F. C.; Matos, B. R., SAXS signature of the lamellar ordering of ionic domains of perfluorinated sulfonic-acid ionomers by electric and magnetic field-assisted casting. *Physical Chemistry Chemical Physics* **2020**, *22* (24), 13764-13779.

301. Macrae, C. F.; Sovago, I.; Cottrell, S. J.; Galek, P. T.; McCabe, P.; Pidcock, E.; Platings, M.; Shields, G. P.; Stevens, J. S.; Towler, M., Mercury 4.0: from visualization to analysis, design and prediction. *Journal of Applied Crystallography* **2020**, *53* (1), 226-235.
302. Bulushev, D. A.; Chuvilin, A. L.; Sobolev, V. I.; Stolyarova, S. G.; Shubin, Y. V.; Asanov, I. P.; Ishchenko, A. V.; Magnani, G.; Riccò, M.; Okotrub, A. V.; Bulusheva, L. G., Copper on carbon materials: stabilization by nitrogen doping. *Journal of Materials Chemistry A* **2017**, *5* (21), 10574-10583.
303. Karapinar, D.; Huan, N. T.; Ranjbar Sahraie, N.; Li, J.; Wakerley, D.; Touati, N.; Zanna, S.; Taverna, D.; Galvão Tizei, L. H.; Zitolo, A.; Jaouen, F.; Mougél, V.; Fontecave, M., Electroreduction of CO₂ on Single-Site Copper-Nitrogen-Doped Carbon Material: Selective Formation of Ethanol and Reversible Restructuration of the Metal Sites. *Angewandte Chemie International Edition* **2019**, *58* (42), 15098-15103.
304. Zhao, X.; Li, F.; Wang, R.; Seo, J.-M.; Choi, H.-J.; Jung, S.-M.; Mahmood, J.; Jeon, I.-Y.; Baek, J.-B., Controlled Fabrication of Hierarchically Structured Nitrogen-Doped Carbon Nanotubes as a Highly Active Bifunctional Oxygen Electrocatalyst. *Advanced Functional Materials* **2017**, *27* (9), 1605717.
305. Xiao, H.; Cheng, T.; Goddard, W. A.; Sundararaman, R., Mechanistic Explanation of the pH Dependence and Onset Potentials for Hydrocarbon Products from Electrochemical Reduction of CO on Cu (111). *Journal of the American Chemical Society* **2016**, *138* (2), 483-486.
306. Goodpaster, J. D.; Bell, A. T.; Head-Gordon, M., Identification of Possible Pathways for C–C Bond Formation during Electrochemical Reduction of CO₂: New Theoretical Insights from an Improved Electrochemical Model. *The Journal of Physical Chemistry Letters* **2016**, *7* (8), 1471-1477.
307. Liu, C.; Lourenço, M. P.; Hedström, S.; Cavalca, F.; Diaz-Morales, O.; Duarte, H. A.; Nilsson, A.; Pettersson, L. G. M., Stability and Effects of Subsurface Oxygen in Oxide-Derived Cu Catalyst for CO₂ Reduction. *The Journal of Physical Chemistry C* **2017**, *121* (45), 25010-25017.
308. Zhou, Y.; Che, F.; Liu, M.; Zou, C.; Liang, Z.; De Luna, P.; Yuan, H.; Li, J.; Wang, Z.; Xie, H.; Li, H.; Chen, P.; Bladt, E.; Quintero-Bermudez, R.; Sham, T.-K.; Bals, S.; Hofkens, J.; Sinton, D.; Chen, G.; Sargent, E. H., Dopant-induced electron localization drives CO₂ reduction to C₂ hydrocarbons. *Nature Chemistry* **2018**, *10* (9), 974-980.
309. Hoang, T. T. H.; Ma, S.; Gold, J. I.; Kenis, P. J. A.; Gewirth, A. A., Nanoporous Copper Films by Additive-Controlled Electrodeposition: CO₂ Reduction Catalysis. *ACS Catalysis* **2017**, *7* (5), 3313-3321.

VITA

NAMAL WANNINAYAKE

Education

BSc, Chemistry, Physics, Computer Science
University of Peradeniya, Kandy. 2013
Sri Lanka

Awards

Outstanding Poster Award 2019
Materials Research Society, Materials Networking Day Lexington, KY

Philip L. Walker Award 2019
American Carbon Society, International Carbon Conference Lexington, KY

235th ECS meeting Travel Award 2019
Electrochemical Society, Energy Technology Division Dallas, TX

Top Student Research Presentation Award 2019
National Science Foundation, EPSCoR super collider event Lexington, KY

Student Poster Award (Energy Category) 2018
North American Membrane Society meeting Lexington, KY

Next Generation Electrochemistry (NGenE) 2018
Summer Institute Scholarship Chicago, IL
UIC Energy Initiative - University of Illinois at Chicago

Outstanding Poster Award 2018
Society of Postdoctoral Scholars, Fourth Annual Lexington, KY
Postdoctoral Research Symposium

Experimental Program to Stimulate Competitive 2016
Research Fellowship, National Science Foundation, EPSCoR Lexington, KY

Fast Start Award 2015
Outstanding initial overall progress towards the PhD Lexington, KY
Department of Chemistry, University of Kentucky

Publications

Wanninayake, N.; Ai, Q.; Zhou, R.; Hoque, M.; Herrell, S.; Guzman, M.; Risko, C.; Kim, D. Understanding the effect of host structure of nitrogen doped

ultrananocrystalline diamond electrode on electrochemical carbon dioxide reduction. *Carbon* **2020**, *157*, 408-419.

Thomas, M.*; **Wanninayake, N.***; De Alwis Goonatilleke, M.; Kim, D.; Guiton, B. Direct imaging of heteroatom dopants in catalytic carbon nano-ions. *Nanoscale* **2020**, *12*, 6144-6152. (Equal contribution*)

Beasley, C.; Kumaran Gnanamani, M.; Santillan-Jimenez, E.; Martinelli, M.; Shafer, W.; Hopps, S.; **Wanninayake, N.**; Kim, D. Effect of Metal Work Function on Hydrogen Production from Photocatalytic Water Splitting with MTiO₂ Catalysts. *ChemistrySelect* **2020**, *5*, 1013-1019.

Beasley, C.; Gnanamani, M.; Martinelli, M.; Góra-Marek, K.; Hamano, K.; Shafer, W.; **Wanninayake, N.**; Kim, D. Dehydration of 1,5-Pentanediol over ZrO₂-ZnO Mixed Oxides. *ChemistrySelect* **2019**, *4*, 3123-3130.

Khan, M.; Islam, S.; Nagpure, S.; He, Y.; **Wanninayake, N.**; Palmer, R.; Strzalka, J.; Kim, D.; Knutson, B.; Rankin, S. Epitaxial Formation Mechanism of Multilayer TiO₂ Films with Ordered Accessible Vertical Nanopores by Evaporation-Driven Assembly. *The Journal of Physical Chemistry C* **2019**, *124*, 1958-1972.

Pillar-Little, T.; **Wanninayake, N.**; Nease, L.; Heidary, D.; Glazer, E.; Kim, D. Superior photodynamic effect of carbon quantum dots through both type I and type II pathways: Detailed comparison study of top-down-synthesized and bottom-up-synthesized carbon quantum dots. *Carbon* **2018**, *140*, 616-623.

Colburn, A.; **Wanninayake, N.**; Kim, D.; Bhattacharyya, D. Cellulose-graphene quantum dot composite membranes using ionic liquid. *Journal of Membrane Science* **2018**, *556*, 293-302.

Islam, S.; Reed, A.; Nagpure, S.; **Wanninayake, N.**; Browning, J.; Strzalka, J.; Kim, D.; Rankin, S. Hydrogen incorporation by plasma treatment gives mesoporous black TiO₂ thin films with visible photoelectrochemical water oxidation activity. *Microporous and Mesoporous Materials* **2018**, *261*, 35-43.

Li, W.; Zhang, Y.; Das, L.; Wang, Y.; Li, M.; **Wanninayake, N.**; Pu, Y.; Kim, D.; Cheng, Y.; Ragauskas, A. et al. Linking lignin source with structural and electrochemical properties of lignin-derived carbon materials. *RSC Advances* **2018**, *8*, 38721-38732.

Islam, S.; Reed, A.; **Wanninayake, N.**; Kim, D.; Rankin, S. Remarkable Enhancement of Photocatalytic Water Oxidation in N₂/Ar Plasma Treated, Mesoporous TiO₂ Films. *The Journal of Physical Chemistry C* **2016**, *120*, 14069-14081.